

Dissertation
submitted to the
Combined Faculty of Mathematics, Engineering and Natural Sciences
of Heidelberg University, Germany
for the degree of
Doctor of Natural Sciences

Put forward by

Peter Rodenkirch

born in Nastätten (Germany)

Oral examination: 25th of May, 2022

Signatures of Planet-Disk Interaction and Disk Winds

A numerical study of gas and dust dynamics in protoplanetary disks under the influence of planets and winds

Referees:

Prof. Dr. Cornelis P. Dullemond

Prof. Dr. Ralf Klessen

For my wife Imane

Contents

Contents	I
1 Introduction	1
1.1 Historical developments	1
1.2 Observational data	2
1.3 Theory of protoplanetary disk evolution	5
1.3.1 General evolution of disks	5
1.3.2 Disk gas structure & dynamics	6
1.3.3 Magnetohydrodynamics	8
1.3.4 Angular momentum transport & turbulence	11
1.3.5 Dust dynamics	14
1.3.6 Planet-disk interaction	16
1.3.7 Disk winds	19
1.4 Motivation and aims of this thesis	30
2 Dust dynamics in planet-disk interaction	33
2.1 Motivation	33
2.2 Model	36
2.2.1 Basic equations	36
2.2.2 Disk model	38
2.2.3 Boundary conditions	39
2.2.4 Code setup and parameters	39
2.2.5 Radiative transfer model and post-processing	41
2.3 Results	43
2.3.1 Dust substructure overview	45
2.3.2 Rings	45
2.3.3 Surface density estimation	48
2.3.4 Secondary planet mass	49
2.3.5 Asymmetries	50
2.3.6 Synthetic images	56
2.4 Resolution study	61
2.5 Dust temperatures	61
2.6 Discussion	62
2.6.1 Comparison to previous works	62
2.6.2 Model assumptions	64

2.7	Conclusion	65
3	Dust entrainment in magnetically and thermally driven disk winds	67
3.1	Motivation	67
3.2	Model	68
3.2.1	Basic equations	69
3.2.2	Disk model	70
3.2.3	Super time stepping	75
3.2.4	Boundary conditions	78
3.2.5	Radiative transfer model and post-processing	79
3.3	Results	80
3.3.1	Parameters & normalization	80
3.3.2	Gas flow structure	81
3.3.3	Dust flow structure	83
3.3.4	Maximum grain size and flow angle	87
3.3.5	Wind launching surface	89
3.3.6	Gas and dust streamlines	92
3.3.7	Dust temperature estimate	93
3.3.8	Ionization fraction	95
3.3.9	Synthetic observations	95
3.4	Discussion	98
3.5	Conclusion	99
4	Accretion phenomena in transition disks	101
4.1	Motivation	101
4.2	Numerical model & parameters	103
4.3	Results	103
4.3.1	Magnetic field profile	103
4.3.2	Gas dynamics	106
4.3.3	Accretion rates	110
4.3.4	Parameter study	112
4.4	Discussion	114
4.5	Conclusion	115
5	Conclusions and Outlook	117
	List of Figures	122
	List of Tables	123
	List of publications	125
	Bibliography	127

Abstract

Protoplanetary disks, consisting of gas and dust, are thought to be the birthplace of planets. Recent observations have revealed a multitude of substructures in the dust continuum and scattered light emission. It is unclear if these gaps, rings and asymmetries are signposts of embedded planets interacting with their surroundings, or if different physical mechanisms, such as hydrodynamic instabilities, interactions with magnetic fields and disk winds could be the origin. Observations indicate that the lifetime of protoplanetary disks is limited to several million years and it is debated whether accretion due to turbulent processes, planet-disk interaction or disk winds might be the driving factor of disk dispersal. In this work a suite of numerical (magneto-)hydrodynamical simulations of planet-disk interaction as well as photoevaporation and magnetically driven disk winds was carried out. We found that asymmetries observed in the dust continuum can indicate the presence of an embedded planet, containing several earth masses of dust. Furthermore, we found that dust can efficiently be entrained in both thermal and magnetic disk winds, being potentially observable and assisting the identification of the physics driving the wind. Extending the wind models to transition disks revealed accretion rates compatible with recent observations with a similar dependence on the disk mass.

Zusammenfassung

Es wird angenommen, dass protoplanetare Scheiben, bestehend aus Gas und Staub, Geburtsstätten von Planeten sind. Aktuelle Beobachtungen zeigen eine Vielfalt von Strukturen in der Staubkontinuumemission und im nahen infraroten Bereich. Es ist bislang unklar, ob diese Lücken, Ringe und Asymmetrien Zeichen von mit ihrer Umgebung interagierenden Planeten sind oder ob andere physikalische Vorgänge, wie hydrodynamische Instabilitäten, Wechselwirkung mit Magnetfeldern oder Scheibenwinde, dafür verantwortlich sind. Beobachtungen weisen darauf hin, dass protoplanetare Scheiben nur einige Millionen Jahre überdauern und es wird diskutiert, ob Akkretion durch Turbulenz, die Wechselwirkung von Planeten mit der Scheibe oder Winde der dominante Prozess der Auflösung der Scheiben sind. In dieser Arbeit wurden eine Reihe von numerischen (magneto-)hydrodynamischen Simulationen von Planeten-Scheiben Wechselwirkung, sowie auch Photoevaporation und magnetische Scheibenwinde durchgeführt. Wir konnten zeigen, dass die beobachteten Asymmetrien mehrere Erdmassen an Staub einfangen und die Existenz eines in der Scheibe eingebetteten Planeten bedeuten können. Darüber hinaus, deuten die Ergebnisse darauf hin, dass Staub effizient in sowohl thermischen als auch magnetisch getriebenen Winden transportiert werden kann und durch Beobachtungen der Staubemission zwischen diesen beiden Windtypen unterschieden werden könnte. Die Akkretionsraten der Simulationen von Scheiben mit einer inneren, praktisch gasfreien Region decken sich mit den beobachteten Werten.

Introduction

One of the most prominent questions throughout of the history of human civilization is the origin of the planet earth and the celestial bodies visible in the night sky. In the field of planet formation the current evidence points towards the following mechanism:

The general picture is that vast agglomerations of molecular hydrogen called *Giant Molecular Clouds* (GMCs) become gravitationally unstable as soon as their mass exceeds the *Jeans Mass* (Jeans, 1902). With a non-zero angular momentum of the initial GMC, the collapsing cloud flattens along the angular momentum vector and forms a *protoplanetary disk* (PPD), containing a significant amount of dust originating from the *interstellar medium* (ISM). Through the interaction of gas and dust, as well as coagulation and fragmentation of the dust grains, the microscopic particles grow into pebbles and subsequently form planetesimals, planetary embryos and eventually planets.

Significant progress in developing a consistent theory of this process that is in agreement with the current observations has been made throughout the last decades. The complex nature of a protoplanetary disk, including physical processes interacting over several orders of magnitude, such as radiation physics, magneto-hydrodynamics, dust dynamics as well as complex chemistry has prevented the formulation of a clear and concise picture of planet formation starting from the cloud collapse and ending with the final planetary system.

The following sections aim to present the current state of the observational data and to provide a general overview of the physical processes relevant for the projects presented in this thesis.

1.1 Historical developments

With the dawn of modern physics and astronomy, made possible by the formulation of classical mechanics in the seminal work *Philosophiae Naturalis Principia Mathematica* by Isaac Newton (Newton, 1687), the question of the origin of our solar system has been started to be examined quantitatively.

But even before, the movement of celestial bodies was described phenomenologically Nicolaus Copernicus, Tycho Brahe, Johannes Kepler, and Galileo Galilei, advocating a heliocentric world view. Later in the 18th century Immanuel Kant postulated the *nebula hypothesis* (Kant, 1755) which states that stars and the surrounding planetary systems form from large clouds collapsing under their own gravitation into protoplanetary disks. Kant also remarkably proposed the galaxies in the form of an extended agglom-

eration of a large number of stars at a far distance, addressing the observations of faint nebulous objects at that time.

A similar theory about the formation of planets was described in by Laplace in his work *Exposition du système du monde* (Laplace, 1796). Safronov (1972) laid the groundwork for modern planet formation theory. It turns out that less than one percent of the total angular momentum of our solar system is contained in the rotation of the sun, whereas the remaining part is conserved in the orbital motions of the planets (Ray, 2012). This observations was coined as the “angular momentum problem”, discussed by Mestel (1965a,b) in detail. In some way the central star has to lose the majority of its angular momentum and the lack of plausible explanations for this phenomenon contested the nebular hypothesis. Alternative theories were developed, notably the capture hypothesis (Shmidt, 1944; Woolfson, 1964) in which the central star sweeps up material from the ambient medium. With such a theory the aligned angular momentum vectors of both the central star and the planets in our solar system would not necessarily be the natural outcome.

The angular momentum problem can be solved by considering the effect of magnetic fields during the star formation process and the subsequent evolution of the surrounding disk. Close to the star the ambient gas is sufficiently ionized so that the magnetic field can be considered to be “frozen in”. Up to a point called *Alfvén radius* the magnetic pressure dominates over the thermal pressure and the magnetic field originating from the star can be imagined as rigid wires. Stellar winds flow in the field direction within this magnetically dominated region like beads on a wire and thus extract angular momentum up to the *Alfvén radius* which can slow down the star’s rotation sufficiently (Schatzman, 1962; Ray, 2012).

1.2 Observational data

Throughout the last decades, tremendous advances in observational astronomy allowed direct detections of such structures in great detail. The first evidence of the existence of protoplanetary disks was found by the infrared space telescope *IRAS* in the form of an excess emission at a wavelength of $12\ \mu\text{m}$ in the $\alpha - \text{Lyr}$ system (Vega) (Aumann et al., 1984) and soon also around several other systems (Aumann, 1985). The excess radiation was postulated to originate from the thermal emission of millimeter-sized particles in a extended region around these stars. The observations thus hinted towards the existence of remnants of the original collapsing cloud.

At roughly the same time direct imaging of the dust disk around $\beta - \text{Pic}$ was achieved (Smith & Terrile, 1984). The original observation is shown in Fig. 1.1. These dusty remnants of the earlier gas-rich protoplanetary disks are called *debris disks*. With the launch of the *Hubble Space Telescope* (HST) a powerful tool to observe star forming regions, such as the Orion nebula at sufficient angular resolution was available. Direct observations of protoplanetary disks were achieved in the years between 1993 and 1996 (O’dell et al., 1993; McCaughrean & O’dell, 1996). An example of an edge-on PPD imaged by the HST in the visible light spectrum is shown in Fig. 1.2. The observational signature is characterized by dust absorption in front of the emission nebula in the background. Dust absorption in the visible spectrum is dominated by small grains in the (sub-) micron range (Pollack et al., 1994). For small grains, the observational data thus leads to the conclusion that these disks are “puffed up” and that the grains are vertically well mixed.

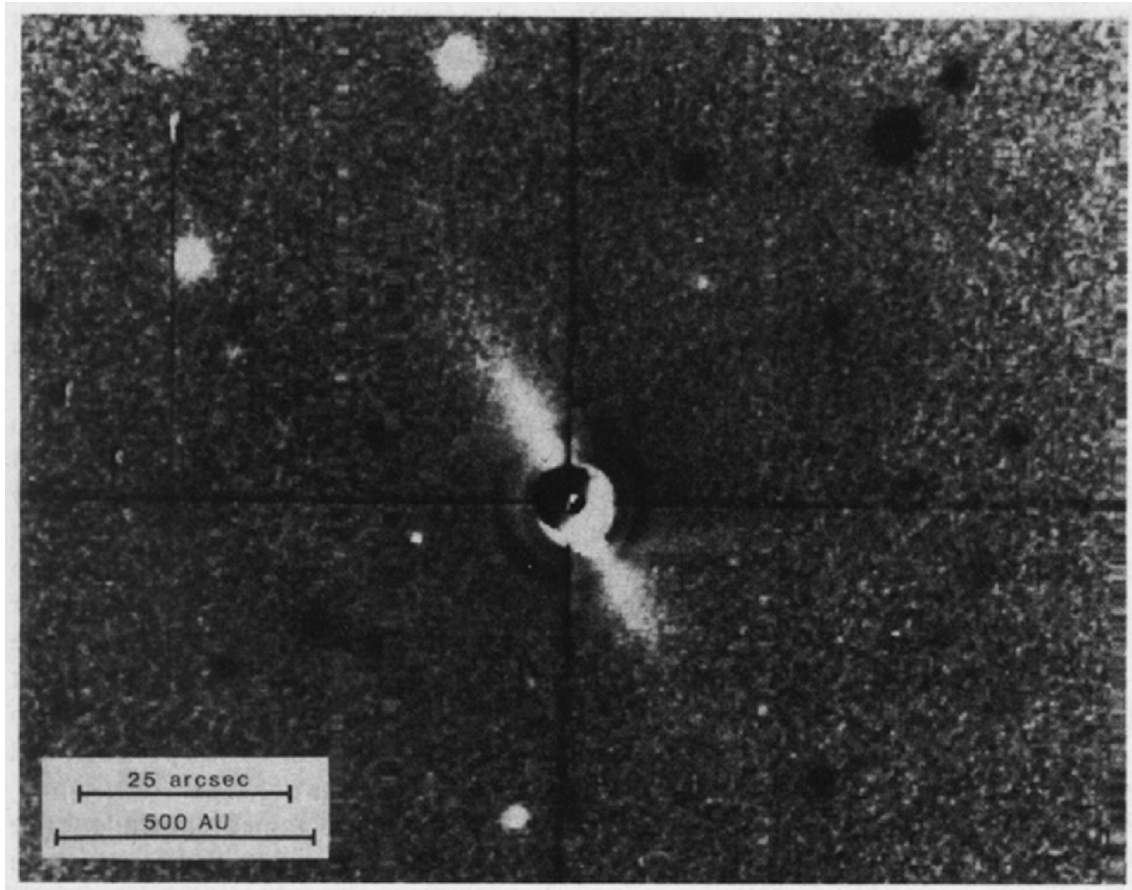


Figure 1.1: Observation of the debris disk around β -Pictoris from Smith & Terrile (1984).



Figure 1.2: HST observations of protoplanetary disks in the Orion nebula with the Wide-Field Planetary Camera 2 taken from McCaughrean & O'dell (1996). The left panel shows an emission line composite image consisting of OIII (blue), H α (green) and NII (red) radiation. In the right panel the continuum image at a wavelength of $\lambda = 547$ nm is displayed.

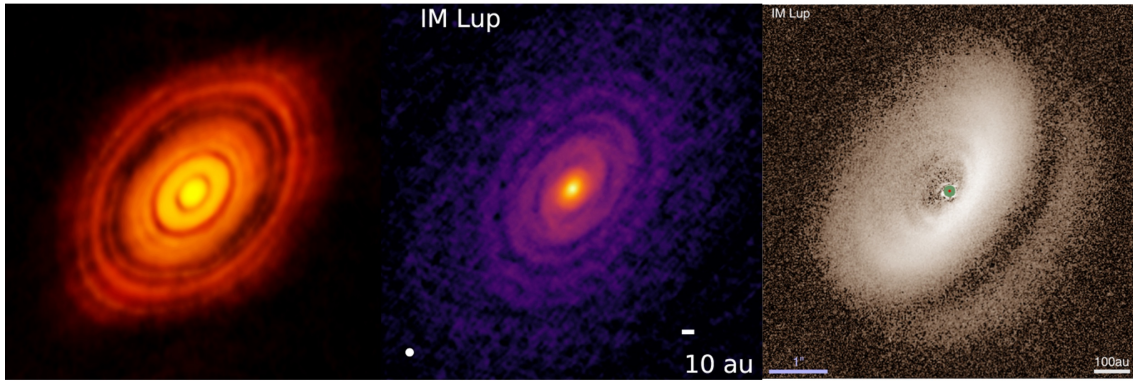


Figure 1.3: *Left panel:* ALMA continuum image of HL Tau showing detailed sub-structure including multiple gaps and rings. Source: ALMA (ESO/NAOJ/NRAO) (<https://www.eso.org/public/archives/images/large/eso1436a.jpg>)
Center panel: ALMA continuum image part of the DSHARP survey at a wavelength of $\lambda = 1.25$ mm of IM Lup taken from Huang et al. (2018b).
Right panel: SPHERE/IRDIS scattered light image in the H band ($\lambda \approx 1.6$ μm) of IM Lup taken from Avenhaus et al. (2018). The intensity is stretched logarithmically.

Since in the visible light and near infrared only the surface layers of PPDs are traced, sub-millimeter observations are a promising technique to probe the disk down to the mid plane. After the construction of the Atacama Large Millimeter / sub-millimeter Array (ALMA) tremendous progress in this area has been made. The interferometer allows high resolution observations down to 25 mas at wavelength of $\lambda = 870$ μm (ALMA Partnership et al., 2015). The first sub-millimeter observation at high angular resolution of a protoplanetary disk was performed on the disk around HL Tau, a T Tauri star at a distance of ≈ 140 pc (ALMA Partnership et al., 2015), displayed in Fig. 1.3. It was postulated that the numerous gaps might be a signpost of planets present in the disk due to the increase in eccentricity with radius and gap locations being compatible with several orbital resonances (ALMA Partnership et al., 2015).

In 2018 the The Disk Substructures at High Angular Resolution Project (DSHARP) (Andrews et al., 2018) 20 bright disks were observed with ALMA at a wavelength of $\lambda = 1.25$ mm, finding substructures, such as rings, gaps, spirals and asymmetries in the majority of the disks in the sample. ALMA is generally sensitive to thermal emission from mm-sized dust grains, which are expected to vertically settle towards the mid-plane, depending on the level of turbulence present in the disk (Goldreich & Ward, 1973; Dubrulle et al., 1995). Observations with ALMA hence dominantly probe the disk midplane. Using the VLT SPHERE instrument (Beuzit et al., 2019) in the visible and near-infrared spectrum, light scattered of small dust grains in the surface layers can be detected. Smaller grains are mostly well coupled to the gas and the vertical dust scale height is consequently large compared to mm-sized grains. A comparison of both types of observations in the context of IM Lup is shown in Fig. 1.3, where spiral structures are clearly visible in the detection with ALMA. In the scattered-light image the disk is

vertically much more extended, as expected, if small grains are suspended in the upper parts of the disk atmosphere.

Initially overlooked, the first confirmed planet was detected around the pulsar PSR 1257+12 by Wolszczan & Frail (1992) in the year 1992. Later in 1995, a Jupiter mass planet around the solar-type star 51 Pegasi was discovered by measuring variations in the radial velocity of the central star (Mayor & Queloz, 1995). To date, the staggering number of 4940 exoplanets were confirmed (Akeson et al., 2013), but a clear evidence of the observed substructures in protoplanetary disks being linked to embedded planets is still scarce. In one case direct imaging of a planetary companion with a mass of 5 to 9 Jupiter masses of PDS 70 embedded in a protoplanetary disk succeeded (Keppler et al., 2018, 2019).

Indirect detections by analyzing the gas kinematics by tracing line emission of CO-isotopologues were published, as for example for two planets in the HD 163296 system by Teague et al. (2018a). It can however not be excluded, whether these signatures cannot be reproduced by different physical mechanisms altering the gas velocities in the respective dust and gas gaps.

1.3 Theory of protoplanetary disk evolution

In the following sections an overview over disk dynamics in form of describing physical processes, governing the evolution of protoplanetary disks and the subsequent stages is presented, starting with a general picture of the evolution of PPDs and concluding with outflow phenomena such as photoevaporation and magnetically driven disk winds.

1.3.1 General evolution of disks

Young stellar objects (YSOs) are observed to evolve in different stages, usually divided into the following four classes. The initial collapse of the molecular core, from which both the central star and the protoplanetary disk form, occurs on the free-fall timescale which can be considered to last for 10^4 to 10^5 years. YSOs at this stage are basically completely obstructed by the surrounding optically thick gas and dust envelope, showing a *spectral energy distribution* (SED) of a blackbody radiator with the peak emission at mm wavelengths. At this stage these objects are usually referred to as Class 0 objects (Andre et al., 1993).

During its further evolution a disk starts to form and parts of the envelope accrete onto the pre-main-sequence (PMS) star at the center of the disk. Due to the partial dissolution of the optically thick envelope, the extinction is reduced and the SED displays emission in the near-infrared (NIR) of the heated dust in the environment around the star, which then corresponds to a Class I object Lada & Wilking (1984). During this stage of the evolution infalling gas from the envelope still becomes accreted and jets or outflows in general are common.

Once the envelope has been mostly accreted, the YSO is attributed to be in Class II, which still accretes material from the optically thick disk (Alcalá et al., 2017). At this stage a multitude of substructures in the dust continuum were observed, as e.g. in the DSHARP survey (Andrews et al., 2018), possibly indicating active planet formation processes.

After the gas and dust have entirely dissipated, accreted or assembled into planets, an

optically thin remnant of the initial disk remains, called a *debris disk* (Wyatt, 2008). These remnants are called Class III objects, as for example observed around the stars Fomalhaut, Vega and β -Pictoris (Holland et al., 1998; Smith & Terrile, 1984).

So-called *transition disks* (TDs) were found in a survey of 83 T Tauri star (TTS) in the Taurus / Aurigae star forming region (Strom et al., 1989). T Tauri stars are usually classified as PMS with masses lower than $2 M_{\odot}$, whereas Herbig Ae/Be stars are more massive. Classical T Tauri stars (cTTS) exhibit strong emission lines due to accretion shocks close to the star with excess radiation in the optical and UV (Edwards et al., 1994; Johnstone et al., 2014). Contrary to cTTS, weak line T Tauri stars (wTTS) are thought to have lost parts of their surrounding disks with negligible accretion flows (Johnstone et al., 2014). These objects were found to emit mostly in the mid- or far-infrared range (MIR, FIR) with a lack of NIR emission. This result hinted towards an inner hole or cavity free or mostly depleted of dust (Strom et al., 1989, 1993). The conclusion was that these transition disk would represent an evolved state of a PPD, where the dispersal of the disk has already started.

In a study of the objects DM Tau and GM Aur, inner cavity sizes of $r_c = 3 \text{ au}$ and $r_c = 24 \text{ au}$ were derived for the respective dust disks (Calvet et al., 2005a). Both disks are nevertheless still actively accreting and it was followed that the inner cavity should still contain some amount of gas, but only at most 0.02 lunar masses of dust (Calvet et al., 2005a).

Disks with a small inner dust disk remaining close to the star were classified as *pre-transitional disks* (Espaillat et al., 2014). From numerical studies it was furthermore postulated, that three to four giant planets would be necessary to reproduce the observed characteristics of TDs, with an additional depletion of the dust content in the cavity of 10^{-5} to 10^{-2} (Zhu et al., 2011). It became clear that the strong accretion rates of approximately $1 \times 10^{-8} M_{\odot} \text{ yr}^{-1}$ in TDs and a survival time scale of roughly 10^5 years could not be explained by accretion of a small part of the disk close to the star and that a mechanism transporting material from the outer edge of the cavity towards the star would be necessary Owen (2016).

Two types of TDs were identified, which are distinguished by a low mm-flux and a high mm-flux in the observations. Type I TDs would then corresponds to short-lived disks dispersing within 10^5 years, whereas Type II TDs would persist for longer time scales on the order of 10^6 years and it is debated whether disk winds could be responsible for the creation of TDs (Owen, 2016).

1.3.2 Disk gas structure & dynamics

Models of protoplanetary disks usually are formulated with the help of power laws. Based on the current distribution of mass in form of planets in our solar system, the lower bound of the primordial mass reservoir in the disk can be estimated. From this approach the Minimum Mass Solar Nebula model (MMSN) emerged (Weidenschilling, 1977; Hayashi, 1981). The mass of such a primordial disk would have been in the range of 0.07 to 0.1 solar masses and the surface density would scale as follows:

$$\Sigma_{\text{MMSN}}(r) = 1700 \left(\frac{r}{\text{au}} \right)^{-\frac{3}{2}} \text{ g cm}^{-2} \quad (1.1)$$

where Σ surface density computed by vertically integrating the volume density ρ in the disk:

$$\Sigma(r) = \int_{-\infty}^{\infty} \rho(r, z) dz. \quad (1.2)$$

In a simple a simple black-body disk being irradiated by stellar with a grazing angle ϕ onto its surface, the temperature scales with radius as Chiang & Goldreich (1997)

$$T(r) = \left(\frac{\phi}{2}\right)^{\frac{1}{4}} \left(\frac{R_*}{r}\right)^{\frac{1}{2}} T_* = \left(\frac{\phi L_*}{8\pi r^2 \sigma_{\text{SB}}}\right)^{1/4} \quad (1.3)$$

where R_* , T_* and L_* are the stellar radius, temperature and luminosity, respectively. The Stefan-Boltzmann constants is denoted by σ_{SB} . Throughout the following parts, the power law exponent of the surface density will be referenced with p , i.e. $\Sigma(r) \propto r^p$. Analogously, the temperature power law is expressed as $T(r) \propto r^q$. Considering the vertical structure of PPDs the density profile is a Gaussian with the scale height H assuming a local isothermal stratification:

$$\rho(z) = \frac{\Sigma_0}{\sqrt{2\pi}H} \exp\left(-\frac{z^2}{2H^2}\right) \quad (1.4)$$

This is only correct for "razor thin" disks, thus for disks with $H \ll r$. Without this approximation the profile takes the form (Nelson et al., 2013):

$$\rho(r, z) = \rho_{\text{mid}}(r_0) \left(\frac{r}{r_0}\right)^s \exp\left[\frac{1}{h^2} \left(\frac{r}{\sqrt{r^2 + z^2}} - 1\right)\right] \quad (1.5)$$

using the expression of the midplane density ρ_{mid} with the power law exponent $s = p - (3 + q)/2$.

$$\rho_{\text{mid}} = \frac{\Sigma_0}{\sqrt{2\pi}H} \quad (1.6)$$

where $h = H/r$ is the local aspect ratio. The gas scale height $H = c_s/\Omega$ can be expressed in terms of the local sound speed c_s and the Keplerian angular frequency $\Omega = \sqrt{GM_*/r^3}$ and is thus intrinsically linked to the temperature profile of the disk. With the isothermal sound speed:

$$c_s(r) = \sqrt{\frac{k_B T(r)}{\mu m_p}} \quad (1.7)$$

the gas scale height scales with radius as $H(r) \propto \frac{\sqrt{T(r)}}{\Omega_K} \propto r^{(3+q)/2}$. A disk with a temperature gradient of $q = -1$ would hence appear in a conical shape. Such a disk is often referred to as a "flat disk", although the disk is by no means flat in the literal sense. For values of $q < -1$ the disk is self-shadowing and for $q > -1$ the disk becomes flared. Using the simple black-body disk approximation described in Eq. 3.12, the temperature gradient would adopt the value off $q = -1/2$ which corresponds to an aspect ratio scaling of $h \propto r^{1/4}$. With these assumptions we would thus expect PPDs to be slightly flared, as for example in the case of IM Lup in Fig. 1.3.

Assuming an isothermal equation of state, the thermal pressure profile in the disk follows

$$P(r) = \rho(r)c_s^2(r) = \rho(r_0)c_s(r_0)^2 \left(\frac{r}{r_0}\right)^{p-\frac{3-q}{2}} \quad (1.8)$$

Considering typical values of $p = -1$ and $q = -1/2$ the pressure gradient exponent would be equal to $-\frac{11}{4}$. Protoplanetary disks in general thus have globally negative

pressure gradients unless a strong pressure bump that might be caused by e.g. planet-disk interaction or an inner cavity is present. A radial pressure gradient is equivalent to an additional force in the opposite direction and with this additional term the angular velocity Ω of the shear flow deviates from the Keplerian angular velocity Ω_K .

To compute the deviation from the Keplerian flow we start from the set of equations describing the motion of an isothermal, inviscid fluid neglecting magnetic interaction and self gravity:

$$\frac{\partial}{\partial t}\rho + \nabla \cdot (\rho\mathbf{v}) = 0 \quad (1.9)$$

$$\frac{\partial}{\partial t}\mathbf{v} + (\mathbf{v} \cdot \nabla)\mathbf{v} = -\frac{1}{\rho}\nabla P - \nabla\Phi \quad (1.10)$$

$$P = \rho c_s^2 \quad (1.11)$$

where Eq. 1.9 corresponds to the continuity equation, Eq. 1.10 to the *Euler equation* (or momentum equation) and the isothermal equation of state Eq. 1.11. Using the approach of (Nelson et al., 2013), the Euler equation in Eq. 1.10 adopts the form

$$r\Omega^2 = \frac{GM_*r}{(r^2 + z^2)^{\frac{3}{2}}} + \frac{1}{\rho}\frac{\partial P}{\partial r} \quad (1.12)$$

$$0 = \frac{GM_*z}{(r^2 + z^2)^{\frac{3}{2}}} + \frac{1}{\rho}\frac{\partial P}{\partial z} \quad (1.13)$$

assuming a steady-state and azimuthal axisymmetry and representing the radial and vertical force balance. Inserting Eq. 1.8 one obtains after some algebra the full form of the azimuthal angular velocity

$$\Omega(r, z) = \Omega_K \sqrt{(s + q) \left(\frac{H}{r}\right)^2 + (1 + q) - \frac{qr}{\sqrt{r^2 + z^2}}} \quad (1.14)$$

Using again the previous values of $s + p = -11/4$ and an disk aspect ratio of $H/r = 0.05$ the azimuthal gas motion at the disk midplane would be slightly sub-Keplerian, being about 0.3% smaller than Ω_K .

1.3.3 Magnetohydrodynamics

The dynamics of magnetic fields is ubiquitous in astrophysics, as e.g. the earth's magnetic field affecting the impact of solar winds, the solar magnetic field being responsible for ejection events and solar activity cycles. Magnetic fields furthermore can lower the star formation rate by opposing the gravitational collapse, although the effect might be less pronounced than assumed before (Krumholz & Federrath, 2019; Hennebelle & Inutsuka, 2019). Magnetic fields also pervade the universe on galactic scales (Parker, 1979) and their origin is thought to be small seed fields that subsequently becomes amplified by dynamo processes (Kulsrud & Zweibel, 2008).

Jets and outflows of young stellar objects are generally attributed to magnetohydrodynamic (MHD) interaction between material of the surrounding disk and the embedded magnetic field or the stellar magnetic field. These outflows can have significant impact on the dynamics of planet formation in the disk, on the reduction in star formation efficiency from natal cores through ejection of the envelope and on the turbulence in clusters or clouds (Frank et al., 2014).

To lay a foundation for the models in this thesis a summary of the key points of magnetohydrodynamics presented in chapter two of Mestel (2012) is given. The dynamics of the interaction between a charged distribution of matter the associated electromagnetic field is described by the Maxwell equations:

$$\nabla \cdot \mathbf{E} = 4\pi\rho_c \quad (1.15)$$

$$\nabla \cdot \mathbf{B} = 0 \quad (1.16)$$

$$\nabla \times \mathbf{E} = -\frac{1}{c}\partial_t\mathbf{B} \quad (1.17)$$

$$\nabla \times \mathbf{B} = \frac{4\pi}{c}\mathbf{J} + \frac{1}{c}\partial_t\mathbf{E}, \quad (1.18)$$

expressed in Gaussian units. The electric field is denoted by \mathbf{E} , the magnetic field by \mathbf{B} , the current density by \mathbf{J} and the charge density by ρ_c . The Lorentz transformation of the electric field to a frame moving with velocity \mathbf{v} can be written as $\mathbf{E}' = \gamma(\mathbf{E} + \mathbf{v}/c \times \mathbf{B})$, where $\gamma = 1/\sqrt{1 - v^2/c^2}$ is the relativistic Lorentz factor. In the following it is assumed that a approximately perfectly conducting fluid moves at nonrelativistic speeds. If this is the case, there exists a velocity where the electric field becomes negligible:

$$\mathbf{E} + \frac{\mathbf{v} \times \mathbf{B}}{c} \approx 0 \quad (1.19)$$

For nonrelativistic speed (i.e. $v \ll c$) one can neglect the displacement current $1/c \partial_t \mathbf{E}$ in the Ampère-Maxwell equation stated in Eq. 1.18. The justification for this simplification can be derived by dimensional analysis (following Spruit (2013)), taking L as a typical length scale, V as the velocity and $\tau = L/V$ as the characteristic velocity of the system. Inserting Eq. 1.19 in Eq. 1.18 one yields for the displacement current

$$\frac{1}{c}\partial_t\mathbf{E} \approx -\partial_t\frac{\mathbf{v} \times \mathbf{B}}{c^2} \propto \frac{V^2}{c^2}\frac{B}{L} \ll \frac{B}{L} \propto \nabla \times \mathbf{B}. \quad (1.20)$$

Since we assume the fluid to be in a nonrelativistic limit the quadratic term V^2/c^2 vanishes and the displacement current is negligible to the left hand side of Eq. 1.18. The relation between current and magnetic flux density thus reduces to the expression:

$$\nabla \times \mathbf{B} = \frac{4\pi}{c}\mathbf{J}. \quad (1.21)$$

With this approximation the Euler equation can be extended to describe fluids in the ideal MHD limit by simply adding the Lorentz force

$$\mathbf{F}_L = \rho_c \mathbf{E} + \frac{1}{c}\mathbf{J} \times \mathbf{B} \approx \frac{1}{c}\mathbf{J} \times \mathbf{B} \quad (1.22)$$

as a source term to the right hand side of Eq. 1.10:

$$\partial_t\mathbf{v} + (\mathbf{v} \cdot \nabla)\mathbf{v} = -\frac{\nabla P}{\rho} - \nabla\Phi + \frac{1}{c}\mathbf{J} \times \mathbf{B}. \quad (1.23)$$

Inserting the expression for the current \mathbf{J} from Eq. 1.21 and using the vector identity:

$$(\nabla \times \mathbf{B}) \times \mathbf{B} = -\frac{1}{2}\nabla B^2 + (\mathbf{B} \cdot \nabla)\mathbf{B} \quad (1.24)$$

the momentum equation takes the form:

$$\partial_t\mathbf{v} + (\mathbf{v} \cdot \nabla)\mathbf{v} = -\frac{1}{\rho}\left(\nabla P + \frac{B^2}{8\pi}\right) + \frac{1}{4\pi\rho}(\mathbf{B} \cdot \nabla)\mathbf{B} - \nabla\Phi. \quad (1.25)$$

To obtain the evolution of the magnetic field, the *induction equation* for ideal MHD is used which can be obtained by combining Eq. 1.19 and Eq. 1.17:

$$\partial_t \mathbf{B} - \nabla \times (\mathbf{v} \times \mathbf{B}) = 0 \quad (1.26)$$

In star forming regions and especially in protoplanetary disks the gas densities increase up to the point that the ionizing radiation and temperature are not sufficient to fully ionize the material. The limit of a perfect conductor is thus not justified anymore and the assumption of the vanishing electric field in Eq. 1.19 does not hold. For the sake of completeness the derivation of the additional terms in the induction equation representing the nonideal-MHD effects follows the concise description in Wardle (2007). Assuming multiple charged species denoted by j with mass m_j , charge $Z_j e$ and velocity \mathbf{v}_j , the sum of the contributions of the electric force, the magnetic force and the drag force caused by collision between the charged and neutral particles has to vanish:

$$Z_j e \mathbf{E} + Z_j e \frac{\mathbf{v}_j \times \mathbf{B}}{c} + m_j \rho \mathbf{v}_j \gamma_j. \quad (1.27)$$

The coefficient γ_j is given by $\gamma_j = \langle \sigma v \rangle_j / (m_j + m)$ with the collisional momentum transfer rate between neutral particles and species j $\langle \sigma v \rangle_j$ and the particle mass of the neutrals m (Wardle, 2007).

The current density of all species with density n_j then becomes

$$\mathbf{J} = \sum_j Z_j e n_j \mathbf{v}_j = \sigma_O \mathbf{E}_{\parallel} + \sigma_H \mathbf{b} \times \mathbf{E}_{\perp} + \sigma_P \mathbf{E}_{\perp}, \quad (1.28)$$

where the suffixes \parallel and \perp refer to the parallel and orthogonal components of the electric field with respect to the magnetic field direction, respectively. The symbols σ_O , σ_H and σ_P refer to the ohmic, Hall and Petersen conductivities which are given by (Wardle & Ng, 1999; Wardle, 2007)

$$\sigma_O = \frac{ec}{B} \sum_j n_j |Z_j| \beta_j \quad (1.29)$$

$$\sigma_H = \frac{ec}{B} \sum_j \frac{n_j Z_j}{1 + \beta_j^2} \quad (1.30)$$

$$\sigma_P = \frac{ec}{B} \sum_j \frac{n_j |Z_j| \beta_j}{1 + \beta_j^2}, \quad (1.31)$$

where β_j is the Hall parameter:

$$\beta_j = \frac{|Z_j| e B}{m_j c} \frac{1}{\gamma_j \rho}. \quad (1.32)$$

Finally, the induction equation can be extended with the nonideal terms to (Wardle, 2007):

$$\partial_t \mathbf{B} - \nabla \times (\mathbf{v} \times \mathbf{B}) + [\eta_{\text{ohm}} \nabla \times \mathbf{B} + \eta_{\text{hall}} (\nabla \times \mathbf{B}) \times \mathbf{b} + \eta_{\text{am}} (\nabla \times \mathbf{B})_{\perp}] = 0, \quad (1.33)$$

where the corresponding ohmic, Hall and ambipolar diffusivities can be formulated as

$$\eta_{\text{ohm}} = \frac{c^2}{4\pi\sigma_O}, \quad (1.34)$$

$$\eta_{\text{hall}} = \frac{c^2}{4\pi\sigma_{\perp}} \frac{\sigma_H}{\sigma_{\perp}}, \quad (1.35)$$

$$\eta_{\text{am}} = \frac{c^2}{4\pi\sigma_{\perp}} \frac{\sigma_P}{\sigma_{\perp}} - \eta_{\text{ohm}}, \quad (1.36)$$

with $\sigma_{\perp} = \sqrt{\sigma_{\text{H}}^2 + \sigma_{\text{P}}^2}$ (Wardle & Ng, 1999; Wardle, 2007). The expressions of the diffusivities can be simplified to $\eta_{\text{hall}} = \beta_e \eta_{\text{ohm}}$ and $\eta_{\text{am}} = \beta_i \beta_e \eta_{\text{ohm}}$ if only ions and electrons are assumed to be the charged species in the fluid (Wardle, 2007).

Inserting $\langle \sigma v \rangle_e$ for the electron-neutral collision frequency (Draine et al., 1983; Armitage, 2020) one obtains a simplified formulations of the ohmic diffusion coefficient (Armitage, 2020):

$$\eta_{\text{ohm}} = \frac{c^2 m_{\text{n}} m_{\text{e}} \langle \sigma v \rangle_e}{4\pi e^2 x_{\text{e}}} \approx \frac{234 T^{\frac{1}{2}} \text{ cm}^3}{x_{\text{e}} \text{ s}}, \quad (1.37)$$

that only depends on the local temperature and the ionization fraction x_{e} . Similarly the ambipolar diffusion coefficient becomes

$$\eta_{\text{am}} = \frac{B^2}{4\pi \langle \sigma v \rangle_e}. \quad (1.38)$$

1.3.4 Angular momentum transport & turbulence

In contrast to the age of the solar system and the earth, protoplanetary disks are observed to have a rather limited lifetime of a few millions years (Haisch et al., 2001; Mamajek et al., 2004; Ribas et al., 2015). A prominent idea is to explain the observed time scale by taking into account accretion processes in these disks. In the seminal work of Shakura & Sunyaev (1973) in the context of black holes, the foundation of the α -disk paradigm was laid down. The model assumes, that in an accretion disk neighboring concentric annuli interact by a friction force caused by viscous processes, leading to transport of angular momentum and thereby a conversion of gravitational energy to kinetic energy, as well as thermal energy, that dissipates in form of radiation. The radial inner annulus loses angular momentum due to the friction force whereas the outer one gains angular momentum. In general, the angular momentum flux in viscous disks would thus point outward. Looking at the evolution of a viscous disk of finite radial extent, the disk radius increases with time due to *viscous spreading* as a consequence of the outward-pointing angular momentum flux (Lynden-Bell & Pringle, 1974).

In order to estimate the impact of viscous processes in disks one can crudely estimate the viscous time scale t_{ν} as

$$t_{\nu} = \frac{r^2}{\nu} \quad (1.39)$$

where ν is the kinematic viscosity (Pringle, 1981). If only viscous effects on the molecular level are taken into account, the viscous time scale becomes exceedingly large. The molecular viscosity ν_{mol} based on kinetic theory of gases can be approximated as (Bird et al., 2002):

$$\nu_{\text{mol}} = \frac{1}{3} \bar{u} \lambda_{\text{mfp}} \quad (1.40)$$

where \bar{u} is the average magnitude of the particle velocities (Bird et al., 2002)

$$\bar{u} = \sqrt{\frac{8k_{\text{B}}T}{\pi m}}; m = \mu m_{\text{p}} \quad (1.41)$$

where μ is the mean molecular weight, and λ_{mfp} the mean free path of the particles:

$$\lambda_{\text{mfp}} \approx \frac{1}{\sigma_{\text{mol}} \rho} \quad (1.42)$$

with the collisional cross section $\sigma \approx \pi d_{\text{H}}^2$ and the gas number density ρ . If we assume $d_{\text{H}} \approx 0.1 \text{ nm}$ for the diameter of an hydrogen atom, a number density of $\rho \approx 8.8 \times 10^{12} \text{ cm}^{-3}$, corresponding to the density of the MMSN-model at the semi-major axis of Jupiter at 5.2 au and a temperature of $T = 123 \text{ K}$, we obtain a molecular viscosity of $\nu_{\text{mol}} \approx 1.94 \times 10^7 \text{ cm}^2/\text{s}$. Inserting the result of ν_{mol} in Eq. 1.39, the time scale becomes $t_{\nu} \approx 9.9 \times 10^{12} \text{ yr}$ which is significantly longer than the age of the observable universe. Molecular viscosity alone can thus not explain the limited lifetime of PPDs of several Myr.

In the context of α -disk models the viscosity is assumed to be an effective viscosity caused by underlying turbulent processes. It assumes the following form (Shakura & Sunyaev, 1973; Lynden-Bell & Pringle, 1974)

$$\nu = \alpha c_{\text{s}} H \quad (1.43)$$

where α is a dimensionless parameter describing the strength of turbulence. The main assumptions are that in turbulent processes the effective viscosity depends on the size l and the turnover velocity v_{edd} of the eddies $\nu \propto l v_{\text{edd}}$ (Pringle, 1981). In a viscous disk we can then approximate that turbulent eddies are limited in size by the disk thickness H and that the turbulence moves subsonically, which limits the maximum value of α to $\alpha \leq 1$ (Pringle, 1981). In early observations of PPDs α was estimated to be on the order of $\alpha \approx 0.01$ by measuring the accretion rates \dot{M}_{acc} of T Tauri stars which are typically $\dot{M}_{\text{acc}} \approx 1 \times 10^{-8} M_{\odot} \text{ yr}^{-1}$ (Hartmann et al., 1998). More recent results indicate significantly lower rates of turbulence corresponding to $10^{-4} \leq \alpha \leq 10^{-3}$ (Flaherty et al., 2015, 2017).

It is useful to obtain the evolution equation of the surface density and the radial velocity depending on the effective viscosity and the derivation follows the one of Frank et al. (2002). One might define a torque G acting between to radially adjacent annuli in the disk as

$$G = 2\pi r \nu \Sigma r^2 \frac{\partial \Omega_{\text{K}}}{\partial r}. \quad (1.44)$$

With this torque the vertically integrated variants of the continuity equation and the conservation of angular momentum become

$$r \frac{\partial \Sigma}{\partial t} + \frac{\partial}{\partial r} (r \Sigma v_r) = 0, \quad (1.45)$$

$$r \frac{\partial}{\partial t} (\Sigma r^2 \Omega_{\text{K}}) + \frac{\partial}{\partial r} (r \Sigma v_r r^2 \Omega_{\text{K}}) = \frac{1}{2\pi} \frac{\partial}{\partial r} G. \quad (1.46)$$

Combining the expression of the torque Eq. 1.44 with the conservation laws in Eq. 1.45 and Eq. 1.46, one yields the evolution of the surface density:

$$\frac{\partial}{\partial t} \Sigma = \frac{3}{r} \frac{\partial}{\partial r} \left[r^{\frac{1}{2}} \frac{\partial}{\partial r} \left(\nu \Sigma r^{\frac{1}{2}} \right) \right]. \quad (1.47)$$

In a similar manner the expression of the radial velocity follows:

$$v_r = -\frac{3}{\Sigma r^{\frac{1}{2}}} \frac{\partial}{\partial r} \left(\nu \Sigma r^{\frac{1}{2}} \right). \quad (1.48)$$

Assuming an approximately radially constant surface density profile and viscosity, the radial velocity can be written in a much simpler form:

$$v_r \approx -\frac{3}{2} \frac{\nu}{r}. \quad (1.49)$$

The question remains which physical mechanism causes the turbulence that is incorporated in the α -parameter.

A well known option is the magnetorotational instability (MRI), first theoretically formulated by Chandrasekhar (1960) and reintroduced into the astrophysical context of accretion disks by Balbus & Hawley (1991). The instability only requires a weak poloidal magnetic field, anchored in a sufficiently ionized, differentially rotating disk. If we imagine a magnetic field line as a flexible rubber band being connected to two gas parcels at the distinct radial locations r_a and r_b , the instability can be intuitively understood. As the Keplerian shearing motion wants to increase the direct distance between the two parcels, the rubber band and thus the magnetic field would counteract this tendency. The consequence of this force would be a slow down of the parcel at the location r_a and a speed up of the gas parcel at $r = r_b$. Due to this velocity change and the transport of angular momentum in positive radial direction, the new Keplerian orbit of parcel a would be situated further inward and the orbit of parcel b further outward, increasing the difference in Keplerian angular velocity. With this increased velocity difference the tension of the rubber band would increase further and amplify the whole procedure. This runaway process is clearly unstable and describes in a qualitative way the MRI.

Following the derivation given in Balbus & Hawley (1998), the stability criterion of a rotating flow threaded by a vertical magnetic field adheres to

$$k^2 v_A^2 > 2\Omega \frac{d\Omega}{d \ln r}, \quad (1.50)$$

where

$$v_A = \frac{B}{\sqrt{4\pi\rho_g}} \quad (1.51)$$

is the *Alfvén velocity*, representing the propagation velocity of transverse perturbations of the magnetic field, k the wave number, and Ω the angular frequency of the flow. In a Keplerian disk the maximum growth rate ω_{\max} and the fastest growing wave mode \mathbf{k}_{\max} become

$$|\omega_{\max}| = \frac{3}{4}\Omega_K \quad (1.52)$$

$$\mathbf{k}_{\max} = \frac{\sqrt{15}}{4} \frac{\Omega_K}{\mathbf{v}_A} \quad (1.53)$$

The MRI thus develops rapidly in a few local orbits, effectively only relying on a weak magnetic field and a well ionized, differentially rotating flow. Numerical simulations of the nonlinear evolution of the MRI were carried out in local shearing box simulations (Fromang & Papaloizou, 2007; Bai, 2011) and in a global framework (Dzyurkevich et al., 2010; Flock et al., 2011), yielding values for α on the order of 10^{-3} to $5 \cdot 10^{-3}$. Deep in the disk midplane the ionization rate by radiation of outside sources is weak and the ionization degree is hence low (Igea & Glassgold, 1999). Non-ideal MHD effects, such as Ohmic diffusion, prevent efficient operation of the MRI, creating a so-called ‘dead zone’ (Gammie, 1996; Dzyurkevich et al., 2013). Since the disk is expected to be mostly laminar in this region, accretion driven by magnetic fields would be constrained to the surface layers (Gammie, 1996).

An alternative to magnetically driven turbulence is the gravitational instability for sufficiently massive disks (Toomre, 1964), which in the nonlinear evolution causes a gravo-

turbulent state. This kind of turbulence strongly depends on shock heating, compression heating and cooling (Durisen et al., 2007). The condition for this instability depends on the *Toomre parameter* Q

$$Q = \frac{c_s \Omega_K}{\pi G \Sigma}, \quad (1.54)$$

which becomes approximatively unstable for $Q \leq 2$ (Kratte & Lodato, 2016). Gravitational instabilities can form spirals, clumps and might aid giant planet formation (Baehr et al., 2017). Different, purely hydrodynamical instabilities causing turbulence are the vertical shear instability (VSI) (Nelson et al., 2013), present in disks with short cooling times, the Rossby-wave instability (RWI) (Lovelace et al., 1999) which causes vortices in the vicinity of massive planets perturbing the disk, the global baroclinic instability (Klahr & Bodenheimer, 2003a) and the convective overstability (Klahr & Hubbard, 2014).

1.3.5 Dust dynamics

As introduced in Sec. 1.3.2, the gas in a protoplanetary disk typically revolves around the central star at slightly sub-Keplerian velocities due to the local, radially negative pressure gradient. In the ISM about one percent of the mass consists of dust grains of sizes below $1 \mu\text{m}$ and this dust-to-gas mass ratio is usually assumed to be the same in PPDs. Unlike the gaseous counterpart, dust can be approximated as a collisionless fluid with zero pressure. Without the additional force by the pressure gradient dust particles would move at Keplerian speeds. Embedded in the gas though, the grains are pushed out of the radial force equilibrium leading to radial dust drift. The rate and direction of this drift depends on the grain size and the underlying radial pressure gradient of the gas. This phenomenon has been discussed in the 70s by Whipple (1972) and Weidenschilling (1977) discussing the possible formation of dust rings as a consequence of a local, radial pressure bump.

It is customary to describe the degree of dust-gas coupling via a dimensionless stopping time, the *Stokes number* St :

$$St = \Omega_K t_s \quad (1.55)$$

with the stopping time t_s , which in turn can be expressed as (Whipple, 1972)

$$t_s = \frac{m_d \Delta v}{F_D}. \quad (1.56)$$

The stopping time depends thus on the dust grain mass $m_d = 4\pi/3\rho_{\text{mat}}a^3$, where ρ_{mat} is the dust material density and a the grain radius, the velocity difference between gas and dust Δv and the drag force F_D . It represents the time scale in which v_d decreases by a factor of e due to the dust-gas coupling (Weidenschilling, 1977). The drag force adopts different forms depending on the Reynold number $Re = 2apv/\nu$ of the flow. In the *Stokes regime* the mean free path of the gas λ_{mfp} is considered to be significantly smaller than the dust grain size a . The drag force then becomes

$$F_D = C_D \pi a^2 \rho \frac{v_d^2}{2}, \quad (1.57)$$

where C_D is the dimensionless drag coefficient (Whipple, 1972):

$$C_D = 24Re^{-1} \text{ for } Re < 1 \quad (1.58)$$

$$C_D = 24Re^{-0.6} \text{ for } 1 \leq Re \leq 800 \quad (1.59)$$

$$C_D = 0.44 \text{ for } Re > 800. \quad (1.60)$$

In the *Epstein regime* however, the mean free path λ_{mfp} is much larger than the dust grain size a . The drag force onto the grain then becomes independent of the Reynolds number of the flow (Weidenschilling, 1977):

$$F_D \approx \frac{4\pi}{3} \rho a^2 \Delta v \bar{u}. \quad (1.61)$$

Inserting Eq. 1.61 into Eq. 1.56 we yield the simple expression for the stopping time

$$t_s = \frac{\rho_{\text{mat}} a}{\rho \bar{u}}. \quad (1.62)$$

It is often stated, that the headwind caused by the velocity difference between dust and gas is directly responsible for the dust grains to spiral towards the star in a typical disk configuration. This is only half of the picture and Sec. 4.1 & Sec. 4.2 in (Weidenschilling, 1977) briefly summarize the key points:

- for $\text{St} \ll 1$ and thus small (typically sub- μm) grain sizes the particle stopping time is much smaller than the orbital period and dust grains hence approximately follow the movement of the gas with a negligible headwind. It is the lack of pressure support compared to the gas that leads to a force imbalance and the slow drift towards the gas pressure maximum, similar to dust settling towards the ground in a room when no significant air motion is present.
- for $\text{St} \gg 1$ the (roughly m-sized or more) bodies move basically independent from the gas flow at Keplerian velocities and consequently are subject to a headwind, which causes the bodies to lose angular momentum and spiral towards the gas pressure maximum.

An illustrative example of the dust drift velocities compared to the Stokes number is given in Fig. 1.4. The underlying model to compute the drift velocity depends on the radial pressure gradient and can be calculated as (Weidenschilling, 1977; Nakagawa et al., 1986; Birnstiel et al., 2012):

$$v_{\text{drift}} = -\frac{2\eta}{\text{St} + \text{St}^{-1}} + \frac{1}{1 + \text{St}^2} v_r, \quad (1.63)$$

$$\eta = -\frac{\partial P}{\partial r} \frac{1}{2\rho_g \Omega_K}, \quad (1.64)$$

where the second term in Eq. 1.63 stands for the drift velocity induced by the radial movement of the gas with velocity v_r , which can for example be inwardly directed in a typical α -disk model. In this case the approximate expression stated in Eq. 1.49 was used. The drift velocity is the highest if $\text{St} = 1$. For larger bodies the decoupling from the gas flow starts to dominate and the headwind becomes less effective. Below $\text{St} = 1$ the coupling between dust and gas becomes stronger and similarly prevent fast drift velocities. If the disk has some degree of (effective turbulent) viscosity, the accretion flow is able to entrain small particles, hence the plateaus towards smaller Stokes number for larger values of α in Fig. 1.4.

Since dust is prone to drift rapidly towards the pressure maximum, in unperturbed disks with a negative slope of the radial pressure distribution, some kind of process has to prevent the complete accretion of the dust reservoir available in the outer part of the disk. A planet, causing local pressure maxima, can effectively trap significant amounts

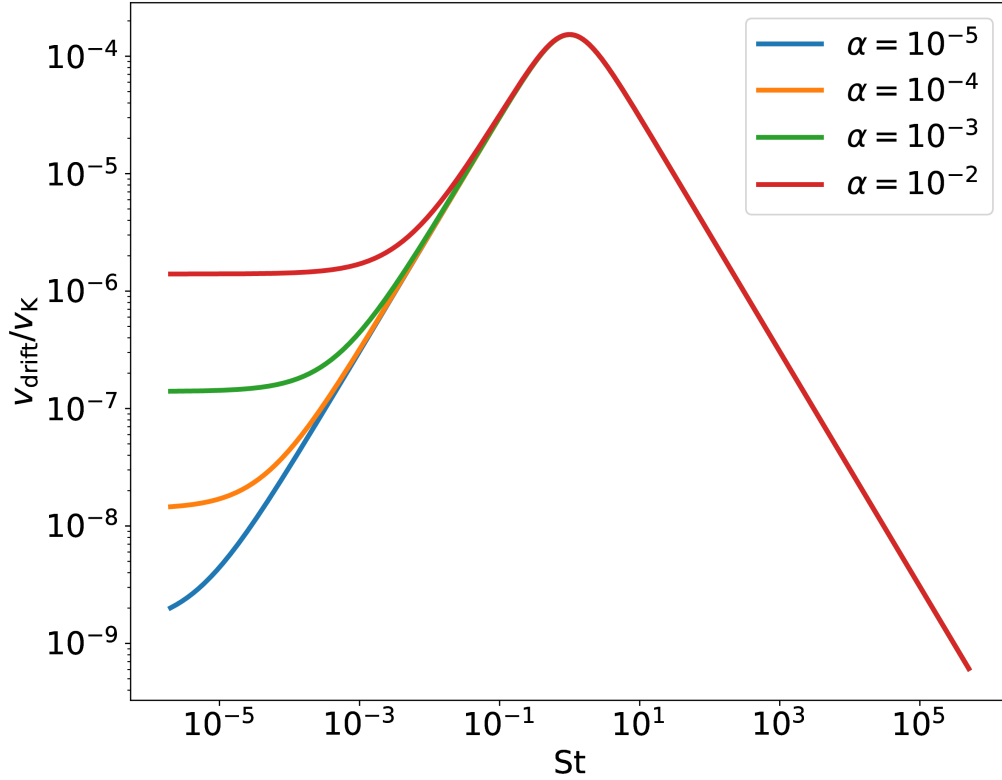


Figure 1.4: Dust drift time scale in units of the orbital time scale vs the dimensionless stopping time St for different value of the α -viscosity parameter.

of dust in ring-shaped structures (Pinilla et al., 2012).

The degree of turbulent mixing in these rings would then determine the width of these structures. Inferring the ring width from the observation can thus help to constrain the level of turbulence in these disks, excluding value of $\alpha < 10^{-4}$ for the DSHARP survey (Dullemond et al., 2018).

For dust-to-gas ratios approaching values close to unity, the backreaction or feedback of the dust onto the gas can cause complex behaviour, such as the *streaming instability*, causing localized dust concentrations that might be able to collapse into kilometer-sized planetesimals, overcoming the fragmentation barrier for much smaller sizes of pebbles (Youdin & Lithwick (2007a); Birnstiel et al. (2010); Schreiber & Klahr (2018)). By accreting pebbles onto these planetesimals, giant planet cores can form within the lifetime of the disk which then able to accrete the gas from their surroundings (Lambrechts & Johansen, 2012; Bitsch et al., 2015).

1.3.6 Planet-disk interaction

Planets embedded in disks are able to tremendously affect the dynamics of the system and might be responsible for substructures visible in sub-mm observations of nearby PPDs, as for example the numerous rings in HL Tau (ALMA Partnership et al., 2015) and the rings, gaps, spirals and crescent shaped asymmetries in the DSHARP survey

(Andrews et al., 2018). Assuming that effects of self gravity of the disk are negligible, the dynamics of a planet-disk system only depends on the mass ratio of the planet and the central star, often denoted by $q = M_p/M_*$, where M_p and M_* are the masses of the planet and the star, respectively.

The dynamics of the disk is perturbed by the additional potential of the planet ϕ_p which can be expressed as the following series expansion (Goldreich & Tremaine, 1980; Kley & Nelson, 2012)

$$\phi_p(r, \varphi, t) = -\frac{GM_p}{|\mathbf{r}_p - \mathbf{r}|} = \sum_{m=0}^{\infty} \phi_m(r) \cos\{m [\varphi - \varphi_p(t)]\}, \quad (1.65)$$

where \mathbf{r}_p is the planet position and $\varphi_p = \Omega_p t$ the azimuthal position angle of the planet and Ω_p the pattern speed. This approximation only holds for thin, isothermal, low mass disks combined with a low mass planet. Multiple types of resonances can be present in the system if the relative frequency of a specific mode m $\omega = m(\Omega(r) - \Omega_p)$ follows the relation in the limit of negligible pressure and self gravity effects (Goldreich & Tremaine, 1980; Kley & Nelson, 2012):

$$\omega = \begin{cases} 0 & \text{corotation resonance} \\ +\kappa & \text{inner Lindblad resonance} \\ -\kappa & \text{outer Lindblad resonance} \end{cases} \quad (1.66)$$

The epicyclic frequency κ is equal to Ω_K in Keplerian disks and describes the frequency with which a radially perturbed test particle would oscillate around its mean orbital radius r_p . The Lindblad resonances are situated at specific radial locations r_L depending on the azimuthal mode m (Kley & Nelson, 2012)

$$r_L = \left(\frac{m}{m \pm 1} \right)^{\frac{2}{3}} r_p. \quad (1.67)$$

With the consideration of pressure effects in the disk, the limit of the Lindblad resonances for $m \rightarrow \infty$ is $r_L = r_p \pm \frac{2}{3}H$, constraining the torque from the disk on the planet to a finite value (Goldreich & Tremaine, 1980; Kley & Nelson, 2012). Density perturbations arise from the location of the Lindblad resonances, which move away from the planet location and form spiral waves with the Keplerian shearing motion in the disk (Goldreich & Tremaine, 1979; Ward, 1997). These spiral arms in turn exert a gravitational pull, the differential Lindblad torque, on the planet which does not completely cancel out in typical disk configurations (Goldreich & Tremaine, 1979; Ward, 1986; Artymowicz, 1993; Ward, 1997). Since the azimuthal motion of the gas in the disk is slightly sub-Keplerian, the radial locations of the radially outer Lindblad resonances lie closer to the planet compared to the inner ones (Ward, 1997; Kley & Nelson, 2012). The outer spiral waves are trailing waves relative to the orbital motion of the planet and thus cause the negative torque, that outweighs the contribution of the torque by the inner, leading spiral waves. In general, the total Lindblad torque is thus expected to be negative and the planet would migrate inward, also called Type I migration (Ward, 1986). Typically, these migration rates seem to be rather high, up to two orders of magnitude higher than the viscous drift speed of the gas (Hourigan & Ward, 1984; Ward, 1997). The migration time scale would correspond to $\approx 2 \times 10^5$ yr for an earth sized planet at 5 au (Hayashi et al., 1985).

Another additional torque called the *corotation torque* on the planet arises through the motion of gas in the coorbital region (Goldreich & Tremaine, 1979). Due to the horseshoe motion of material in the coorbital region, angular momentum is exchanged between the gas and the planet at reversal of the gas motion close to the planet. Since the angular momentum exchange remains constrained within the coorbital region, unlike the Lindblad torque the corotation torque can saturate, which can be counteracted by the planet migration fast enough through the disk material or by turbulence replenishing the coorbital region (Ward, 1992; Paardekooper et al., 2011).

The angular momentum transfer by tidal interactions ultimately forces the material out of the coorbital region, depending on the diffusive action of the viscosity in the disk and the planet mass. If the tidal effects dominate over the viscous forces the problem becomes nonlinear, which happens for planet masses beyond $\approx 30 M_{\oplus}$ corresponding to a ‘super neptune’ in a disk with an aspect ratio of 0.05 (Korycansky & Papaloizou, 1996; Nelson et al., 2000). A criterion for the opening of a gap in the gas of a disk by a planet is given by (Crida et al., 2006):

$$\frac{3}{4} \frac{H}{R_H} + \frac{50\nu}{q r_p^2 \Omega_p} \lesssim 1, \quad (1.68)$$

with the Hill radius

$$R_H = r_p \left(\frac{M_p}{3M_*} \right)^{\frac{1}{3}} \quad (1.69)$$

is the radius of the Hill sphere, where the gravitational influence of the planet dominates over the one by the central star. Gap opening in the gas is thus more effective for higher planet masses and lower values of viscosity in the disk.

Type I migration is only applicable for low mass planets that are not able to open a gap with significant depth. Once the gap becomes deep enough, the material remaining in the coorbital region is insufficient in causing a corotational torque and the large gap shuts off the possibility of generating a torque at the Lindblad resonances by tidal interaction (Ward, 1997). The planet can still migrate on a viscous timescale $\tau_{\text{visc}} \propto r_p^2/\nu$ in this situation, which can be intuitively presented by the planet moving with the radial movement of the gap caused by viscous transfer of angular momentum (Lin & Papaloizou, 1986). This mechanism is known as Type II migration and is generally slower with a migration time scale of $\approx 10^4$ orbits at the initial position compared to Type I migration for jovian mass planets (Ward, 1997).

An additional type of mechanism, called *runaway migration* or *Type III migration* arises in massive disks and intermediate mass planets ranging from about Saturn to Jupiter masses (Masset & Papaloizou, 2003). As the sufficiently massive planet migrates, it depletes parts of the coorbital region of mass and the flow of gas through the coorbital region during the migration causes an additional corotational torque, that depends on the depletion of the coorbital region, which diverges if the depletion reaches the mass of the planet itself (Kley & Nelson, 2012). This type of migration is approximately dominant for disks with masses of more than 1% of the stellar mass and planet masses ranging from $30 M_{\oplus} \leq M_p \leq 300 M_{\oplus}$, achieving migration rates similar to the ones caused by the Type I mechanism (Masset & Papaloizou, 2003).

The direction of migration in all these processes is predominantly inward, but a combination of a more massive inner planet and a lighter outer planet can lead to outward migration, as discovered by Masset & Snellgrove (2001). In a massive disk with two

embedded planets of multiple Jupiter masses a combination of the Masset-Snellgrove effect and the runaway Type III migration can occur, leading to rapid outward migration jumps, temporarily almost doubling the semi-major axis of the planet within only several kyr (Rometsch et al., 2020).

As mentioned above spiral wakes originate from the region around the perturbing planet due to its tidal interaction with the disk. These spiral waves eventually produce shocks and transfer angular momentum by this process (Rafikov, 2002). Typically, multiple spiral arms with progressively diminishing amplitudes form and produce shocks at different radial locations (Bae & Zhu, 2018; Miranda & Rafikov, 2019b), which are able to open gaps in the gas by the resulting transfer of angular momentum (Dong et al., 2017; Bae et al., 2017). It is usually hypothesized that the substructures observed with ALMA as in the DSHARP sample can be caused by planets embedded in the disk at the respective gap locations, but hydrodynamical simulations including dust and gas revealed strikingly similar results compared to the observations with only one planet, as for example in the case of AS 209 (Zhang et al., 2018). Depending on the thermodynamics in the disk, the impact of the spiral shocks on secondary gap formation may be less pronounced which leads to an overestimation of the effect in locally isothermal simulations (Miranda & Rafikov, 2019a; Ziampras et al., 2020). Longer cooling time scales weaken the spiral arms (Ziampras et al., 2020) and the gap locations may significantly vary depending on the equation of state (Miranda & Rafikov, 2019a).

1.3.7 Disk winds

An alternative mechanism that could explain the limited lifetimes of protoplanetary disks of a few Myr could be *disk winds*. Outflows can be broadly categorized into the following types:

1. *Jets*: These narrow, usually double lobed outflows, first found around YSOs by Snell et al. (1980) are similar to their counterparts around black holes and Active Galactic Nuclei (AGNs). Outflows velocities of several hundreds of km s^{-1} are reached and mass loss rates ranging from $\approx 1 \times 10^{-8} M_{\odot} \text{ yr}^{-1}$ to $\approx 1 \times 10^{-5} M_{\odot} \text{ yr}^{-1}$ (Purser et al., 2016; Ray & Ferreira, 2021). The jet material is mostly neutral with an ionization degree of $\approx 1\%$ to 10% (Podio et al., 2009; Ray & Ferreira, 2021). The inner atomic part of the jet sweeps up ambient molecular gas and causes an ‘onion-shaped’ velocity structure, with the outer molecular flow being much slower ($1 \text{ km s}^{-1} - 30 \text{ km s}^{-1}$) (Frank et al., 2014).

The launching mechanism of jets is thought to be of magnetic nature, relying on magnetocentrifugal wind launching, described in the seminal work of Blandford & Payne (1982). Jet launching is confined to a small region close to the central star where the interaction between the stellar magnetic field and the magnetic field embedded in the disk becomes significant, known as the X-wind model (Shu et al., 1994).

2. *Broad magnetic winds*: The physics of broader magnetic disk winds being launched further outward from the surface of the protoplanetary disk is essentially similar to the jet launching mechanism. With these winds the emphasis lies more on winds with a larger opening angle, less collimation, slower wind speeds. Considering the Blandford-Payne (BP) launching mechanism (Blandford & Payne, 1982), the

wind extracts angular momentum and drives accretion flows in the underlying disk and provides thus an alternative way of disk mass depletion compared to the α -disk model. Wind mass loss rates are approximately on the order of $\dot{M}_{\text{wind}} = 1 \times 10^{-8} M_{\odot} \text{ yr}^{-1}$ to $1 \times 10^{-7} M_{\odot} \text{ yr}^{-1}$, with significant uncertainty due to the lack of data of magnetic field strengths in PPDs (Gressel et al., 2015; Bai, 2017a; Béthune et al., 2017; Rodenkirch et al., 2020). These winds can be considered to be similar to the molecular outflows associated with jets.

3. *Photoevaporation*: Besides magnetically driven outflows, photoevaporation is a purely thermal wind launching mechanism that is caused by high energy ionizing radiation from the central star (internal photoevaporation) or the external stellar environment (external photoevaporation), which can provide sufficient energy to heat up the outer layers of PPDs and thereby evaporate material quite efficiently. All types of photoevaporative winds would only act as sinks in the radial surface density distribution and would not lead to additional accretion flows, unlike their magnetic counterpart. Compared to the broad magnetic winds, photoevaporation could potentially exhibit similar mass loss rates and a resembling wind structure (Wang et al., 2019; Rodenkirch et al., 2020) which can be a challenge for categorizing observed outflows. Wind mass loss rates estimated for protoplanetary disks range from $\approx 1 \times 10^{-10} M_{\odot} \text{ yr}^{-1}$ for extreme ultraviolet (EUV) driven winds to $\approx 1 \times 10^{-8} M_{\odot} \text{ yr}^{-1}$ (Hollenbach et al., 1994) for X-ray and far ultraviolet (FUV) driven photoevaporation (Picogna et al., 2019, 2021; Ercolano et al., 2021; Gorti & Hollenbach, 2009).

Outflow phenomena such as jets and slower broad disk winds are quite common in YSOs, especially in the Class I phase where the object is still actively accreting significant amounts of gas and dust from the surrounding environment and the central star is mostly hidden due to the optically thick dust envelope, e.g. observations in the optical in Padgett et al. (1999). These kind of objects seem to necessitate an accretion disk for the existence of outflows (Ray & Ferreira, 2021). Examples of stars exhibiting narrow outflows in the form of jets with velocities of multiple hundreds of km s^{-1} are the Herbig-Haro star HH-30 (Burrows et al., 1996; Louvet et al., 2018) shown in the left panel of Fig. 1.5 and DG Tau (de Valon et al., 2020) in the right panel of Fig. 1.5. Such outflows are not only reserved for young Class I objects but can also be found in the later evolution of disks such as the Class II disk HD 163296 with an estimated age of 5 to 7 Myr (Montesinos et al., 2009) and a rich dust substructure including rings, gaps and a crescent shaped feature (Isella et al., 2018). CO-line observations indicate the presence of a molecular disk wind with an outflow velocity of $\approx 19 \text{ km s}^{-1}$ which is presumably not caused by material being dragged with a jet (Klaassen et al., 2013).

Photoevaporation

The idea of photoevaporation in the context of star formation regions and planet forming disks was put forward by Hollenbach et al. (1994) and Shu et al. (1993). An either external radiation field, e.g. from nearby O-type stars in the star forming region or ionizing radiation from the central pre-main sequence star can ionize parts of the disk and thereby cause a thermal expansion that results in a wind. The mechanism is similar to

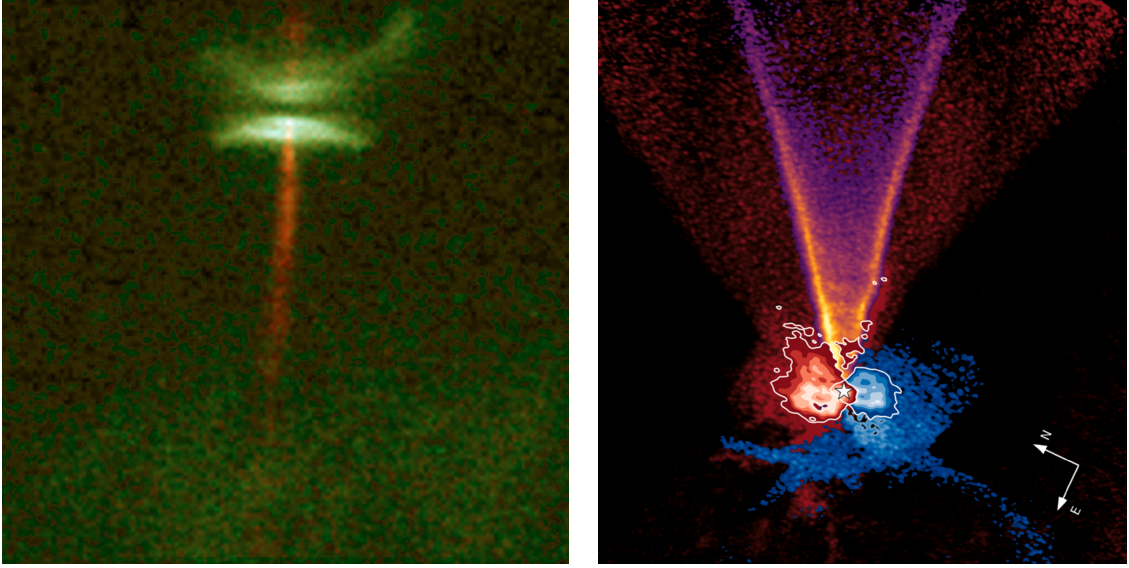


Figure 1.5: *Left panel:* Composite Image of the Herbig-Haro star HH-30 with the HST at $\lambda = 814 \text{ nm}$ (red) and $\lambda = 675 \text{ nm}$ (green). The jet moving at velocities of 100 km s^{-1} to 300 km s^{-1} is clearly visible in the longer wavelength filter as well as the scattered light of the flared disk with a radius of $\approx 250 \text{ au}$ in the shorter wavelength filter (Burrows et al., 1996). *Credit:* C. Burrows (STScI & ESA), the WFPC 2 Investigation Definition Team and NASA

Right panel: $^{12}\text{CO}(2-1)$ (red, blue and orange) and $^{13}\text{CO}(2-1)$ (inside contours) line observations of DG Tau taken from de Valon et al. (2020). The conical outflow reaches velocities up to 8 km s^{-1} and the ^{13}CO tracer probes the surface of the underlying disk.

the Parker solar wind where the critical surface at the sonic radius r_s is given by (Parker, 1958):

$$r_s = \frac{GM_*}{2c_s^2}, \quad (1.70)$$

with the local sound speed c_s and the mass of the central star M_* .

In the context of a protoplanetary disk, the equivalent characteristic radius is given by the gravitational radius r_g :

$$r_g = \frac{GM_*}{c_s^2}, \quad (1.71)$$

which is a factor of two larger than the sonic radius in the Parker wind model due to the different geometry of a straight disk surface (Shu et al., 1993). Assuming that the gas is in virial equilibrium, the kinetic energy K and the potential energy U fulfill the relation $T + 2U = 0$ which translates into the relation at the gravitation radius:

$$\frac{1}{2}r_g^2\Omega_K^2 + \frac{3}{2}\frac{k_B T}{\mu m_p} = \frac{2GM_*}{r_g}, \quad (1.72)$$

which allows the gas to escape with a terminal velocity of $\sqrt{2}c_s$ beyond r_g (Shu et al., 1993). In the early studies of Hollenbach et al. (1994); Shu et al. (1993) EUV-radiation was thought to be the driving factor of photoevaporative disk winds. The radiation would ionize and heat the upper layers of the disk to temperatures of $\approx 1 \times 10^4 \text{ K}$. Within the gravitation radius ($r_g \approx 9 \text{ au}$ for the solar system) the gas would still be bound, with a comparatively thick atmosphere due to the high temperature compared to the rest of

the disk. Secondary radiation of this ionized region would then drive the wind flow of the outer part of the disk. This model would only hold if the stellar wind would have mass loss rates lower than $2 \times 10^{-11} M_{\odot} \text{ yr}^{-1}$, preventing the bound atmosphere from being pushed out towards r_g (*weak wind case* in (Shu et al., 1993)) Wind rates of $\dot{M}_w \approx 1 \times 10^{-10} M_{\odot} \text{ yr}^{-1}$ were postulated and the lack of mass loss within 9 au would provide sufficient time for gas accretion of Jupiter and Saturn, which would explain the dichotomy between the gas and ice giants in our solar system (Shu et al., 1993).

Observations of star forming regions in M 16 and the Orion nebula M 42 revealed ‘cometary objects’, also called *proplyds* as an abbreviation for *PROtoPLANetarYDiskS*. These objects were discovered to be gaseous evaporation globules, where the outflow is caused by the strong UV radiation field of the surrounding massive stars (*external photoevaporation*) (Hester et al., 1996). The evaporation would be sufficient to truncate the disks in the region of M 42 within 1 Myr with a resulting remnant with a size of 1 au that would vanish rapidly due to viscous effects, rendering planet formation challenging (Johnstone et al., 1998).

N-body simulations including external UV-photoevaporation by Scally & Clarke (2001) showed that approximately half of the disks would not provide suitable environments for planet formation beyond a distance of 10 au from the central star, unless the disk would be rather massive with $M_{\text{disk}} > 0.4 M_{\odot}$, or if the planet formation process would be completed within 2 Myr. Tidal interactions between systems in local clusters might also be able to truncate disks significantly, although if both tidal interactions and external photoevaporation were significant, photoevaporation mostly dominates (Winter et al., 2018).

Internal photoevaporation by the central star however can cause an inner cavity in the in the disk when the accretion rate drops down to $\dot{M}_{\text{acc}} \approx 1 \times 10^{-10} M_{\odot} \text{ yr}^{-1}$ during the viscous disk evolution, equal to the photoevaporation rate between 5 to 10 au (Clarke et al., 2001). The wind then starves the inner part of the disk from material from the outer part and the inner disks accretes within a short time scale of $\approx 10^5$ years. The outer disk is then illuminated directly and disperses more rapidly. This two time scale behavior was coined the ‘UV switch’ (Clarke et al., 2001). Ionizing radiation following from accretion processes towards the star are generally not sufficient to explain the observed disk lifetimes (Matsuyama et al., 2003). T Tauri stars were found to provide a significant amount of ionizing radiation which increases during the evolution of the star, surpassing the effect of the UV-flux radiating from the accretion shock (Alexander et al., 2005). Hydrodynamic models of EUV-photoevaporation confirmed the fast dispersal of the outer disk within a time scale on the order of 10^5 yr (Alexander et al., 2006). It also became evident, that the gravitational radius r_g would not be a strict constraint of photoevaporative winds and that parts of the flow can originate from critical radii down to $r_{\text{cr}} \approx 0.15 r_g$ (Liffman, 2003; Adams et al., 2004; Font et al., 2004; Dullemond et al., 2007). Wind flows that cause inner cavities as in the UV-switch model were shown to encourage dust accumulation at the inner rim of the disk due to the local pressure bump, which would provide an alternative mechanism for creating substructures that are widely observed (Alexander & Armitage, 2007).

An anti-correlation between the X-ray luminosity L_X of T Tauri stars and the accretion rate \dot{M}_{acc} was observed by Preibisch et al. (2005). Since photoevaporation models indicate the formation of inner cavities, starving or at least modulating the accretion flow, the relation between L_X and \dot{M}_{acc} follows directly from the interaction of these winds

with the disk (Drake et al., 2009).

Including FUV- and X-ray radiation yields various different results in the literature and there is still a significant degree of uncertainty in the derived wind mass loss rates. In the model of Gorti & Hollenbach (2009) X-ray radiation doubles the wind mass loss rates compared to photoevaporation with FUV- and EUV-radiation only. The reason is that FUV-heating heavily relies on grain chemistry in the disk and X-rays reduce the positive charge in these particles. In consequence, the photoelectric heating by FUV-radiation is enhanced (Gorti & Hollenbach, 2009). The impact of X-rays was thus postulated to be only indirect and purely X-ray driven photoevaporation would be too weak.

In contrast to these results Owen et al. (2010) postulated that X-ray photoevaporation would be quite effective in removing mass from the disk reaching mass loss rates on the order of $1.4 \times 10^{-8} M_{\odot} \text{ yr}^{-1}$. In their model the wind is optically thin to the ionizing radiation and the temperature thus mostly only depends on the *ionization parameter* ζ (Tarter et al., 1969; Owen et al., 2012):

$$\zeta = \frac{4\pi F_X}{\rho_g} = \frac{L_X}{\rho_g R^2}, \quad (1.73)$$

where F_X is the X-ray flux of the star and L_X the X-ray luminosity. In Owen et al. (2010) the wind launching region extends over 1 au to 70 au. The improvement over previous models of X-ray photoevaporation was the computation of the temperature dependence on the ionization parameter with the full radiative transfer and ionization calculation, using a synthetic X-ray / EUV-spectrum (XEUV) of the star (Ercolano et al., 2009). The temperature recipe was then applied in 2D hydrodynamical simulations depending on the local ionization parameter, saving significant computational time and rendering the simulations feasible.

The mass loss rates of these XEUV-winds were found to scale linearly with the X-ray luminosity L_X of the central star and the results of Owen et al. (2011) corroborate the finding of Drake et al. (2009), confirming the anti-correlation of L_X and \dot{M}_{acc} . An important side-note is, that in the case of XEUV-photoevaporation the wind dynamics is basically only dependent on the X-ray physics and not on the underlying density at the wind launching front. The disk only provides the necessary material that is needed to drive the photoevaporative flow (Owen et al., 2012).

A process of rapid radiative clearing of PPDs was proposed in Owen et al. (2012), called *thermal sweeping*. In the later work of Haworth et al. (2016) it is described that this mechanism sets in if pressure maximum at the inner part of the disk is lower than the maximum possible pressure caused by the X-ray radiation. The rapid dispersal of the disk then proceeds on the local dynamical time scale and can potentially lead to a rapid growth of the inner cavity. It was however found, that this process is only active beyond 100 au in the most ideal cases, not explaining a rapid dispersal of the disk before a cavity of this size is reached (Haworth et al., 2016).

More recent models with parametrized XEUV-photoevaporation confirm the linear relation between L_X and the wind mass loss rate (Picogna et al., 2019; Picogna et al., 2021). These models furthermore state that photoevaporation in combination with viscous evolution of the disk is able to reproduce cavity sizes and accretion rates of half of the observed transition disk population.

Discrepancies arise when the results are compared to models with dynamical calculations of the gas temperature during the hydrodynamical simulation, as carried out by

e.g. Wang & Goodman (2017a) and Nakatani et al. (2018b). In Nakatani et al. (2018b) it is considered, that the effects of X-ray, EUV- and FUV-radiation the heating by X-ray radiation are not strong enough to drive significant photoevaporation flows. The mass loss rate was found to peak at metallicity Z between $0.1Z_{\odot} < Z < Z_{\odot}$, where Z_{\odot} is the solar metallicity. In the interval of $0.1Z_{\odot} \leq Z < 10Z_{\odot}$ a smaller value of Z implies weaker FUV-shielding by dust and a consequently higher wind rate. For lower metallicities in the range of $10^{-2}Z_{\odot} \leq Z < 10^{-1}Z_{\odot}$, the grain photoelectric heating by FUV-radiation is less efficient than the local cooling rate and the gas temperature thus decreases and so does the wind mass loss rate (Nakatani et al., 2018a).

Observational evidence of internal photoevaporation was first published by Pascucci & Sterzik (2009), who presented detections of the Ne II line in TW Hya, revealing an outflows with a blue-shift of 6 km s^{-1} which was attributed to a photoevaporative wind flow. It was later stated that, the outflow originates from a region within 10 au and that the observations were consistent with a photoevaporation model with a mass loss rate of $4 \times 10^{-9} M_{\odot} \text{ yr}^{-1}$ (Pascucci et al., 2011; Gorti et al., 2011). A radio jet and evidence for photoevaporation were observed around GM Aur (Macías et al., 2016). The mass loss rates are $3 M_{\odot} \text{ yr}^{-1}$ to $5 M_{\odot} \text{ yr}^{-1}$ and $1.3 \times 10^{-10} M_{\odot} \text{ yr}^{-1}$ for the jet and the broad outflow, respectively. It was postulated that EUV-photoevaporation would be responsible for the broad outflow component (Macías et al., 2016). In an observational study of 33 T Tauri stars with disks by Simon et al. (2016), the low velocity component (LVC) with its broad component (BC) and narrow component (NC) was compared with various models of disk winds. The BC was attributed to the base of magnetically driven winds, whereas the association of the NC with photoevaporation remained inconclusive. The high velocity component (HVC) was attributed to microjets in these sources.

In a similar study carried out by Fang et al. (2018), the HVC was found to be quite common with an occurrence of 72% of all full disks. When transition disks were considered, the occurrence rate dropped down to 13% which could be explained by the necessity of sufficient material close to the star to drive a jet. It was found in their study, that most of the mass loss that was deduced from the LVC originates from a region within a few au from the central star. This finding supports a magnetically driven disk wind since photoevaporation is expected to be weak close to the star as pointed out by the introduction of the critical and gravitational radius.

The theoretical study of Weber et al. (2020) compared previous observations with synthetic line profiles based on a magnetic wind, as well as a XEUV-photoevaporation model. The XEUV-wind was able to produce blue-shifted line profiles corresponding to a velocity range of 2 km s^{-1} to 5 km s^{-1} and a FWHM of 15 to 40 km s^{-1} . This NC of the LVC was consistent with the observations, but did not match the characteristics of the BC or the HVC. The MHD-wind however was able to reproduce all these components, while also causing a Keplerian double-peak pattern that is in conflict with most observations.

Magnetically driven winds

Magnetically driven winds are usually known as magnetocentrifugal winds in the context of the Blandford-Payne wind launching mechanism (Blandford & Payne, 1982). The main idea behind this concept is that the disk is threaded by a global, vertical magnetic field, which is inclined with respect to the disk surface. A simple sketch of the magnetic

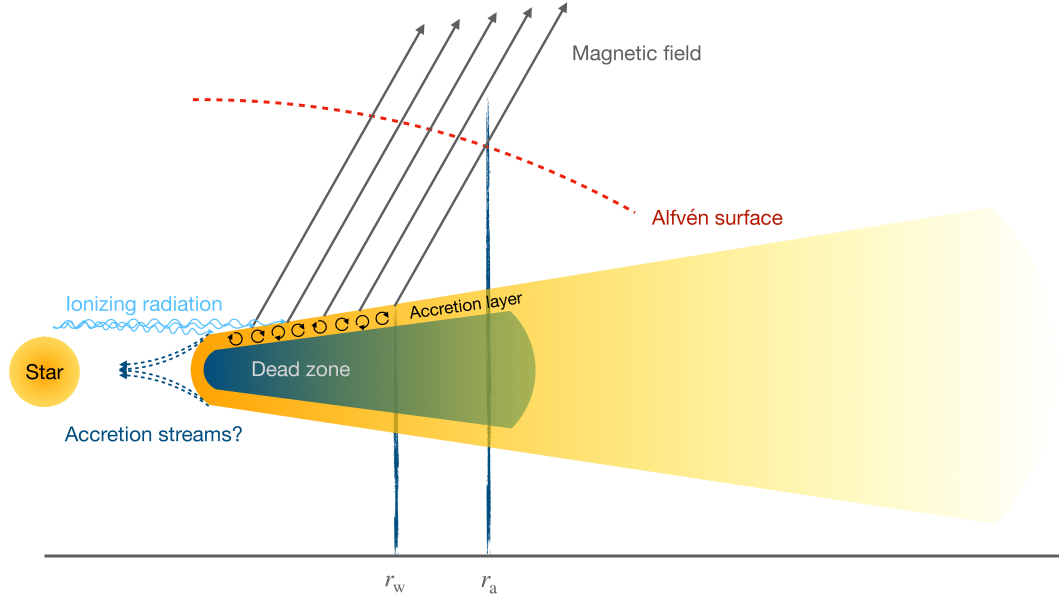


Figure 1.6: Sketch of a magneto-centrifugal disk wind. Within the Alfvén surface the magnetic pressure dominates over the thermal pressure and the magnetic field line can be considered as rigid rods that the gas follows. The foot point of the wind is denoted by r_w and the Alfvén point as r_a .

field lines anchored at the disk surface is given in Fig. 1.6. Assuming a mirror-symmetry with respect to the disk midplane, the magnetic field topology resembles the shape of an hourglass. In a rather simplified picture the gas can collapse more easily parallel to the magnetic field down to the accretion disk. The accretion flow tends to drag the field towards the star if the gas is sufficiently ionized and the hourglass shape would thus naturally form from the dynamics of the system.

For the purpose of describing the impact of the magnetic field on the gas dynamics, the definition of the so-called plasma beta is useful:

$$\beta = \frac{8\pi P}{B^2}, \quad (1.74)$$

which is simply the ratio of thermal over magnetic pressure. In the model of a magneto-centrifugal wind, the gas flows along the magnetic field lines, similar to beads on a rigid wire. For the magnetic field to be sufficiently stable with respect to the gas motion, so that the metaphor of rigid wires holds, the plasma beta needs to be small and the magnetic field has to be strong. Like beads on a rotating wire, the gas is then centrifugally accelerated starting from the foot point at the radial location r_w along the field until the gas velocity reaches the Alfvén velocity v_A at the Alfvén radius r_A .

The wind region is thereby separated by this Alfvén surface, as depicted in Fig. 1.6. Beyond the Alfvén surface the assumption of rigid magnetic field lines weakens and the field increasingly bends in the azimuthal direction, forming a spiral-shaped field structure (Spruit, 1996). Since the magnetic field can approximately be considered to corotate with the foot point at r_w , angular momentum is extracted from the wind launching surface to the Alfvén surface. The amount of angular momentum being transported is $j_w = \Omega_K (r_A^2 - r_w^2)$ and the whole mechanism can be compared to a lever arm, applying a torque onto the disk. Since angular momentum from the wind launching

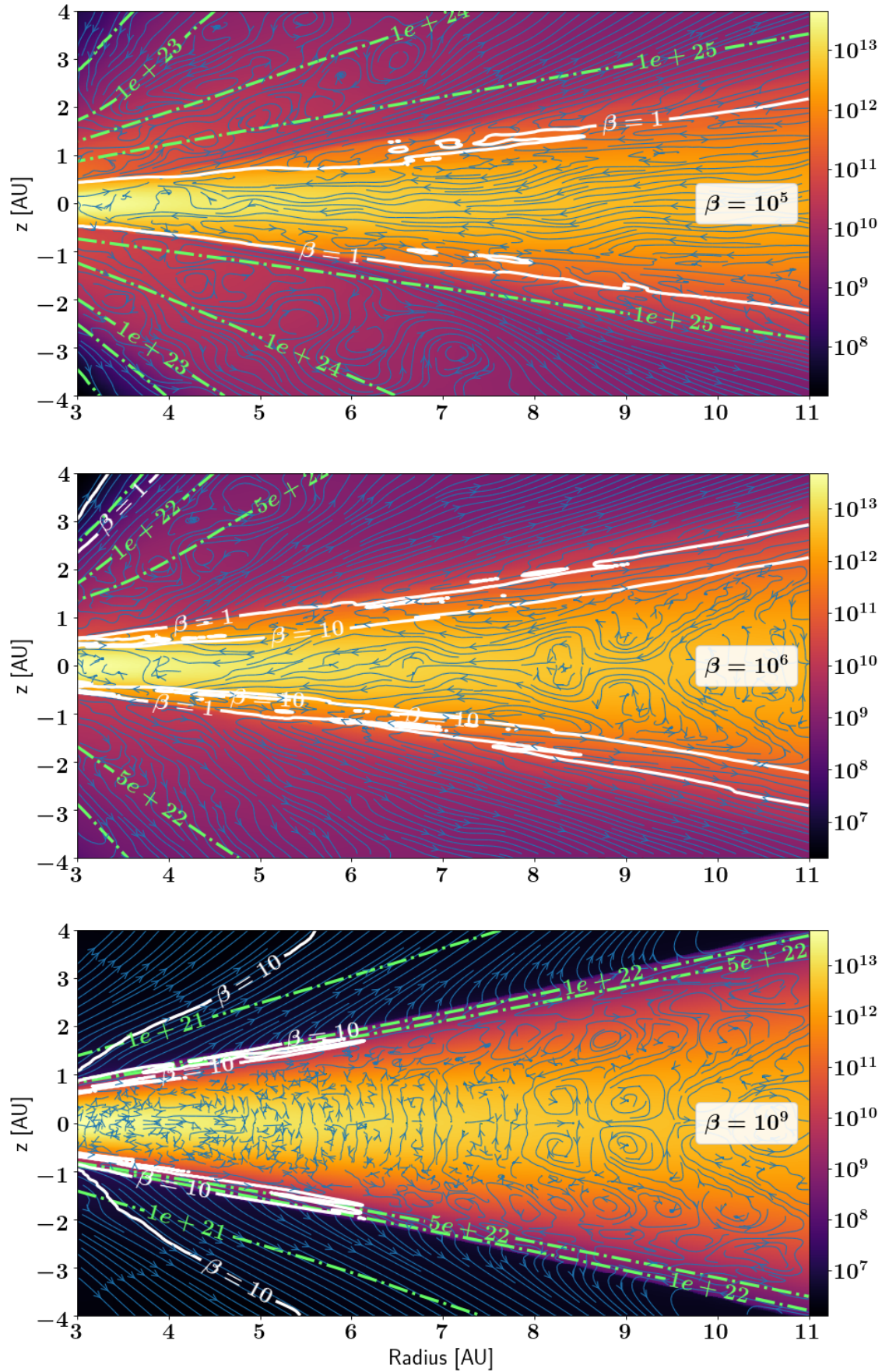


Figure 1.7: Example of a magnetically driven wind including XEUV-photoevaporation taken from Rodenkirch et al. (2020). The temperature prescription is based on the photoevaporation model of Picogna et al. (2019). The colorbar denotes the gas number density and the green dashed-dotted lines represent the radial column density in units of cm^{-2} .

location is carried away with the wind flow, the angular momentum deficit in the disk leads to an accretion flow. The accretion rate \dot{M}_{acc} can be directly linked to the wind mass loss rate \dot{M}_w when the *magnetic lever arm*

$$\lambda = \frac{r_A}{r_w} \quad (1.75)$$

is known. The relation between these quantities then becomes (Ferreira & Pelletier, 1995; Bai et al., 2016):

$$\xi_w = \frac{\frac{d\dot{M}_{w,c}}{d\ln(r)}}{\dot{M}_{\text{acc}}} = \frac{1}{2} \frac{1}{\lambda - 1}, \quad (1.76)$$

where $\dot{M}_{w,c}$ is the cumulative wind mass loss rate and ξ_w the *ejection index*. For cold magnetic winds the condition $\lambda \geq \frac{3}{2}$ is fulfilled and as a result of Eq. 1.76 the accretion rate is always at least equal to the wind mass loss rate, whereas for warmer magnetothermal winds smaller values for the magnetic lever arm are possible since the additional thermal pressure gradient assists the magnetic wind launching (Bai et al., 2016).

In the approximation of a cold, thin disk and negligible heating in the wind region, magnetocentrifugal wind launching is only possible if the magnetic field is inclined with an angle $\theta > \theta_{\text{crit}}$, where θ is the polar angle, starting from the rotation axis of the disk. The condition whether a wind flow is possible depends on the effective potential Φ_{eff} representing the ‘beads on a wire’ model (Spruit, 1996):

$$\Phi_{\text{eff}}(s) = -\frac{GM_*}{R(s)} - \frac{\Omega_K(r_w)^2}{2} r(s)^2, \quad (1.77)$$

where s is the distance travelled along the field line. The foot point of the wind flow r_w , as well as the magnetic field lines are assumed to rotate with the Keplerian angular frequency. Following the derivation given in Armitage (2020), the effective potential can be written in terms of s , r_w and θ :

$$\Phi_{\text{eff}}(s) = -\frac{GM_*}{\sqrt{r_w^2 + 2sr_w \sin \theta + s^2}} - \frac{\Omega_K(r_w)^2}{2} (r_w + s \sin \theta)^2. \quad (1.78)$$

Evaluating the second derivative at the launching point of the wind, one obtains after some algebra the wind launching condition for the polar inclination angle of the magnetic field (Armitage, 2020):

$$\left. \frac{\partial^2 \Phi_{\text{eff}}(s)}{\partial s^2} \right|_{s=0} = 1 - 4\sin^2(\theta) = 0, \quad (1.79)$$

from which directly follows, that the critical inclination angle of the magnetic field with respect to the rotation axis has to be $\theta_{\text{crit}} = 30^\circ$. For inclinations lower than this value the potential well prevents outflows without an additional driving force such as thermal pressure in the case of photoevaporative heating in the flow or a hot disk (Spruit, 1996). In a steady axisymmetric magnetically driven wind, four constants of motion define the flow, assuming a perfectly ionized fluid (ideal MHD). The equations in this form are taken from Bai et al. (2016) and a more detailed derivation can be found in Spruit (1996) and Lesur (2020). By considering the continuity equation one finds the constant

$$k = \frac{4\pi\rho v_p}{B_p}, \quad (1.80)$$

where v_p and B_p are the poloidal velocity and the poloidal magnetic flux density, respectively. The constant k represents the mass loading onto the individual field line (Lesur, 2020). The second and third constant of motion is the angular velocity of the magnetic field lines

$$\omega_B = \Omega_K - \frac{kB_\phi}{4\pi\rho_g r}, \quad (1.81)$$

assuming the wind base to rotate at the Keplerian angular frequency, and the specific angular momentum

$$l_B = \Omega_K r^2 - \frac{rB_\phi}{k}. \quad (1.82)$$

Finally, the conservation of energy leads to the Bernoulli constant \mathcal{B} , which can be written as follow, assuming an isothermal wind flow (Bai et al., 2016):

$$\mathcal{B} = \frac{v^2}{2} - \omega r v_\phi + c_s^2 \log(\rho_g / \rho_{g,0}) + \Phi_G, \quad (1.83)$$

with the gravitational potential $\Phi_G = \sqrt{GM_*/r}$.

In reality the dynamics of magnetically driven winds is much more involved and necessitates full-fledged MHD-simulations in multiple dimensions including nonideal MHD effects due to the partially low ionization fraction in protoplanetary disks. An issue with the traditional Blandford-Payne is that flux freezing down to the midplane of the disk prevents stationary solutions. The extraction of angular momentum by the magnetocentrifugal wind would cause accretion flows at the midplane but the almost vertical magnetic field at this location would effectively be dragged with the flow due to flux freezing in the ideal MHD approximation. As pointed out by Shu (1991), the increasing radial stresses would prevent magnetocentrifugal outflows. In the thin-disk limit steady-state wind models including ambipolar diffusion or Ohmic diffusion were calculated by Königl (1989), allowing a decoupling of the magnetic field and the gas in the disk, circumventing the flux freezing issue.

The models were extended to disks with finite vertical sizes and realistic conditions by Wardle & Königl (1993); Ferreira & Pelletier (1993) and Ferreira & Pelletier (1995). Later Casse & Keppens (2002) carried out the first global simulations of a magnetic jet launched from a resistive disk. Numerical models of winds with an initial plasma beta of $\beta = 1$ were presented by Zanni et al. (2007) and Tzeferacos et al. (2009) found the wind emerging from the simulations to be unsteady up to $\beta \approx 500$. Further studies focused on the distribution of the magnetic diffusivity and the symmetry of these outflows (Sheikhnezami et al., 2012; Fendt & Sheikhnezami, 2013).

It was found that alternatively to the magnetocentrifugal wind launching, winds could also effectively be driven by a vertical magnetic pressure gradient. This mechanism was called ‘magnetic tower flow’ (Lynden-Bell, 1996, 2003) where the toroidal magnetic field dominates in the wind launching region and the Alfvén surface consequently lies close to the disk surface. Accretion is therefore less effective in this framework. In the work of Stepanovs & Fendt (2014) and Stepanovs & Fendt (2016) the transition between magnetocentrifugal winds and outflows driven by magnetic pressure gradients was identified at $\beta \approx 100$.

Whereas these models focused more on jet-launching of YSOs or AGNs, local shearing box simulations of magnetic winds compatible with slower winds in protoplanetary disks were presented by Suzuki et al. (2010); Fromang et al. (2013); Bai & Stone (2013);

Bai (2013), pointing out the issue of different wind rates depending on the location of the vertical boundary condition in the box. Suzuki & Inutsuka (2009) stated that the wind would be launched from MRI turbulent layers at about two disk scale heights where the plasma beta reaches unity, assuming β to be 10^6 at the mid plane and that the wind flow would be able to create an inner hole in the disk (Suzuki et al., 2010). It was furthermore found that in local simulations the outflow rate may be sensitive to the applied resolution and that contrary to previous results the disk would remain largely unaffected by the wind dynamics (Fromang et al., 2013).

Global, non-ideal MHD simulations of magnetically driven winds in PPDs were carried out by Gressel et al. (2015) including Ohmic and ambipolar diffusion, concluding that ambipolar diffusion, dominating in the upper layers of the disk atmosphere, leads to more laminar wind flows and lower mass loss rates compared to simulations with Ohmic diffusion only.

Béthune et al. (2017) found asymmetric wind flows, non-accreting configurations and self-organizing structures such as rings. The results of Suriano et al. (2018) corroborate the ones by Béthune et al. (2017) in the way that rings emerge in ambipolar diffusion dominated disks by reconnection events. A combination of both photoevaporation and magnetically driven winds, also called magneto-thermal winds, were studied by Wang et al. (2019) and Rodenkirch et al. (2020) in the regime of magnetic pressure supported winds. With increasing magnetic field strengths photoevaporative winds smoothly transition into magnetic winds driven by the magnetic pressure gradient in the upper layers of the disk (Rodenkirch et al., 2020). In contrast to the results of Bai (2017b); Suriano et al. (2018); Wang et al. (2019) and Rodenkirch et al. (2020) simulations in Gressel et al. (2020) demonstrate magneto-centrifugal winds mainly driven by magnetic tension forces.

A combination of magnetically driven winds and XEUV-photoevaporation is displayed in Fig. 1.7, taken from Rodenkirch et al. (2020). In these simulations the photoevaporation model of Picogna et al. (2019) was used to compute the temperature of the ionized gas in the wind region. The magnetic field was initialized at different values of β , ranging from $\beta = 10^5$ to $\beta = 10^{10}$. The panels in Fig. 1.7 show the transition between a magnetically and a thermally driven wind. For $\beta = 10^5$ the wind flow is more turbulent and inside the disk a clear accretion flow is visible. Taking a closer look at the wind region, the magnetically driven wind density is too high to allow the XEUV-radiation to penetrate and heat the gas. For a weaker magnetic field the accretion flow subsides and the wind flow becomes more laminar. When the $\beta = 1$ surface moves above the critical column density of the photoevaporative heating, the wind can be considered to be thermally driven. In the panel with $\beta = 10^9$ the thermally driven wind has a significantly decreased density compared to the magnetically driven wind in the panels above.

Magnetically driven winds and photoevaporation can thus not completely separated and to determine clear distinction between both these wind types needs more detailed studies.

1.4 Motivation and aims of this thesis

As the title of the dissertation suggests, this work mainly consists of two topics: planet disk interaction and disk winds. Although these subjects seem to be quite independent, the implications of both mechanisms can lead to similar observational features. Planets can cause large cavities in the inner part of the protoplanetary disks (Rometsch et al., 2020) and so do disk winds. Rings in dust continuum observations could be explained by embedded planets, but magnetically driven winds were also proven to cause this kind of substructures (Riols & Lesur, 2018). Disk winds potentially have a tremendous impact on the gas and dust available in the protoplanetary disk and thereby could also influence planet formation significantly. It is thus of interest to find signatures of both winds and planet-disk interaction in order to constrain, if these phenomena are common and whether they are responsible for the structures in recent observational data. The substructures in the DSHARP survey (Andrews et al., 2018) are thought to be primarily connected to embedded planets and additional tracers would be valuable. Magnetically driven disk winds are often considered to be alternative mechanisms to explain the observed accretion rates in YSOs, as well as the ubiquitous outflow phenomena. The connection between dust dynamics, photoevaporation and magnetically driven winds is still largely unconstrained and needs further study. This work tries to shed light on some of these aspects.

In chapter 2 we start with a case study of the prominent HD 163296 system and compare the dust continuum observations of the disk with hydrodynamical models, assuming that the observed substructures are caused by planet-disk interaction. The FARGO3D code (Benítez-Llambay & Masset, 2016; Benítez-Llambay et al., 2019) will be used to simulate multiple dust species coupled to the gas dynamically, modeled by a pressureless fluid approach. Synthetic ALMA observations created from radiative transfer images will be directly compared to the original observation, especially with respect to the crescent-shaped feature in one of the large gaps of HD 163296. The aim is to determine whether this feature could help to connect such substructures to embedded planets. Rings and gaps in gas and dust, that emerge in the simulation, will be compared to the observed fitted values. Furthermore, the dust mass in the asymmetry and its dependence on the physical parameters of the system will be analyzed.

Chapter 3 focuses on dust dynamics in magnetically and thermally driven disk winds. Since both types of winds could be present in observed systems, it could be of interest if dust can be entrained in these outflows and if the dust content in the wind would be sufficient to be observed. We will furthermore aim to determine whether dust in photoevaporative and magnetically driven winds could help to distinguish both wind types from each other. The FARGO3D code will again be used in an axisymmetric 2.5D configuration, including magnetic fields with nonideal MHD effects, such as Ohmic diffusion and ambipolar diffusion. Dust will be dynamically included in the form of pressureless fluids, allowing a self consistent model of dust entrainment in disk winds. Synthetic radiative transfer images using RADMC-3D (Dullemond et al., 2012a) will be created in order to discuss the observational signatures of dust entrainment.

In chapter 4 the numerical framework used in chapter 3 will be extended to model both photoevaporation and MHD-winds in transition disks with large inner cavities.

The aim is to quantify, whether accretion flows form inside of the gap in the gas and whether the accretion rates are compatible with recent surveys of accreting T Tauri stars and if photoevaporation could quench these accretion streams by blowing away a sufficient amount of gas that flows into the cavity before the inner boundary would be reached.

Finally, in chapter 5 key results of this thesis will be summarized and further directions for future projects and improvements of the models presented here will be given.

Dust dynamics in planet-disk interaction

This chapter is based on the paper Rodenkirch et al. (2021) published in *Astronomy & Astrophysics* in 2021. I carried out all of the simulations, the data analysis and and I created all the plots presented here. The co-authors provided valuable comments that improved the manuscript. For the data reduction, the python tool `simdata`¹ developed by Thomas Rometsch and me was used.

2.1 Motivation

The advent of high angular resolution millimeter continuum observations with the Atacama Large Millimeter and Submillimeter Array (ALMA) has made it possible to gain insights into the substructures of protoplanetary disks. The striking results of the first highly resolved observation of the protoplanetary disk HL Tau unveiled a rich variety of concentric rings in the dust continuum (ALMA Partnership et al., 2015). An extensive survey with the goal to image detailed structures in 20 disks was performed with the DSHARP campaign (Andrews et al., 2018) at an unprecedented resolution. Rings and gaps seem to be ubiquitous in these disks and appear independently of the stellar luminosity (Huang et al., 2018a). A subset of the observations display nonaxisymmetric structures such as spirals and crescent-shaped features.

Currently, a matter of debate is whether these structures are signposts of embedded planets (Zhang et al., 2018). Planet-disk interaction has been a central topic in discussing the dynamics of protoplanetary disks, first with analytic studies of resonances and spiral density waves (Goldreich & Tremaine, 1979, 1980) or planetary migration (Lin & Papaloizou, 1986).

As shown by numerical, two-fluid simulations by Paardekooper & Mellema (2004) a planet of 0.1 Jupiter masses (M_{jup}) is sufficient to open a gap in the dust. Even lower masses down to 0.05 M_{jup} can lead to gap formation if mainly mm-sized dust particles are present (Paardekooper & Mellema, 2006). Dust structures created by planet-disk interaction are generally more diverse than their counterpart in the gas (Fouchet et al., 2007; Maddison et al., 2007). For massive planets of 5 M_{jup} and cm-sized grains, Fouchet et al. (2010) found azimuthally asymmetric dust trapping in the context of 3D SPH sim-

¹Source: <https://github.com/rometsch/simdata>

ulations. Embedded dust grains are prone to drifting towards pressure maxima in the disk (Whipple, 1972). Thus, perturbations caused by a sufficiently massive planet can efficiently trap up to meter-sized bodies on the outer edge of the gap, form a ring structure, and may aid planetesimal formation (Ayliffe et al., 2012).

Dong et al. (2015) found that multiple planets hold clues to explaining large cavities at near-infrared and millimeter wavelengths, as observed in transition disks (Strom et al., 1989; Calvet et al., 2005b; Hughes et al., 2009). In a system with two planets, dust trapped in the leading and trailing Lagrange points (L4 & L5) can be a transient feature, depending on the outer planet (Picogna & Kley, 2015). In the context of low-viscosity disks, multiple rings and gaps emerge with a single planet via shocks of the primary and secondary spiral arm (Zhu et al., 2014; Bae et al., 2017).

Torques caused by the gravitational interaction between planets and the disk lead to migration (Kley & Nelson (2012) for a review) which, in turn, affects the observable dust substructures, for example changes in the ring intensity or asymmetric triple ring structures depending on the migration rate and direction (Meru et al., 2019; Weber et al., 2019a). Migration is sensitive to the underlying disk physics and can be chaotic in very low viscosity disks (McNally et al., 2019). In general, protoplanetary disks seem to be only weakly turbulent, indicating regimes of α on the order of 10^{-4} to 10^{-3} (Flaherty et al., 2015, 2017; Dullemond et al., 2018), using the turbulent α viscosity parametrization from Shakura & Sunyaev (1973). When referring to low viscosity in disks, the magnitude of the effective α viscosity is what is referred to, driving angular momentum transport and thus accretion due the underlying turbulent processes. Therefore, a low effective viscosity can be linked to weak turbulence.

Spiral waves in the gas, excited by a planet, are mostly hidden in the dust dynamics, favoring gaps and rings (Dipierro et al., 2015). The gravitational instability (Toomre, 1964) in sufficiently massive disks can however trigger spiral waves trapping large particles (Rice et al., 2004, 2006). These waves are in principle also observable in scattered light observations (Pohl et al., 2015).

Nonaxisymmetric features, such as vortices, can be created by the Rossby wave instability (Lovelace et al., 1999; Li et al., 2000) enabling dust trapping (Baruteau & Zhu, 2016). Observationally these might be visible as "blobs" or crescent-shaped features as seen in IRS 48 van der Marel et al. (2013) or HD 135344B Cazzoletti et al. (2018). Alternatively, hydrodynamic instabilities, such as the baroclinic instability (Klahr & Bodenheimer, 2003b) or the vertical shear instability, are able to form vortices (Manger & Klahr, 2018). As discussed in the previous chapter 1, the MRI can most likely not operate in the deeper parts of the protoplanetary disk, whereas in the outer parts, high-energy photons may ionize the gas sufficiently to activate the MRI. The transition between the dead zone and the MRI-active region, and thus the change in turbulent viscosity, can also create ring structures (Flock et al., 2015).

With all these possible substructure formation mechanisms at hand, it is of interest to identify markers of planets embedded in protoplanetary disks. A popular and well-studied disk is the one around the Herbig Ae star HD 163296 at a distance of 101 pc (Gaia Collaboration et al., 2018). The appearance in the 1.25 mm continuum emission of the disk is dominated by two, already beforehand observed rings at a radial distance of 67 au and 100 au relative to the central star, respectively (Isella et al., 2016, 2018). An additional faint ring has been detected at 159 au. An intriguing feature is the crescent-shaped asymmetry within the inner gap located at 48 au (Huang et al., 2018a).

The feature itself is situated at a radial distance of 55 au, that is, with an offset of 7 au from the gap center (Isella et al., 2018). An image of the original observation is shown in Fig. 2.17.

The origin of such a structure is unknown, however, a preliminary model was presented

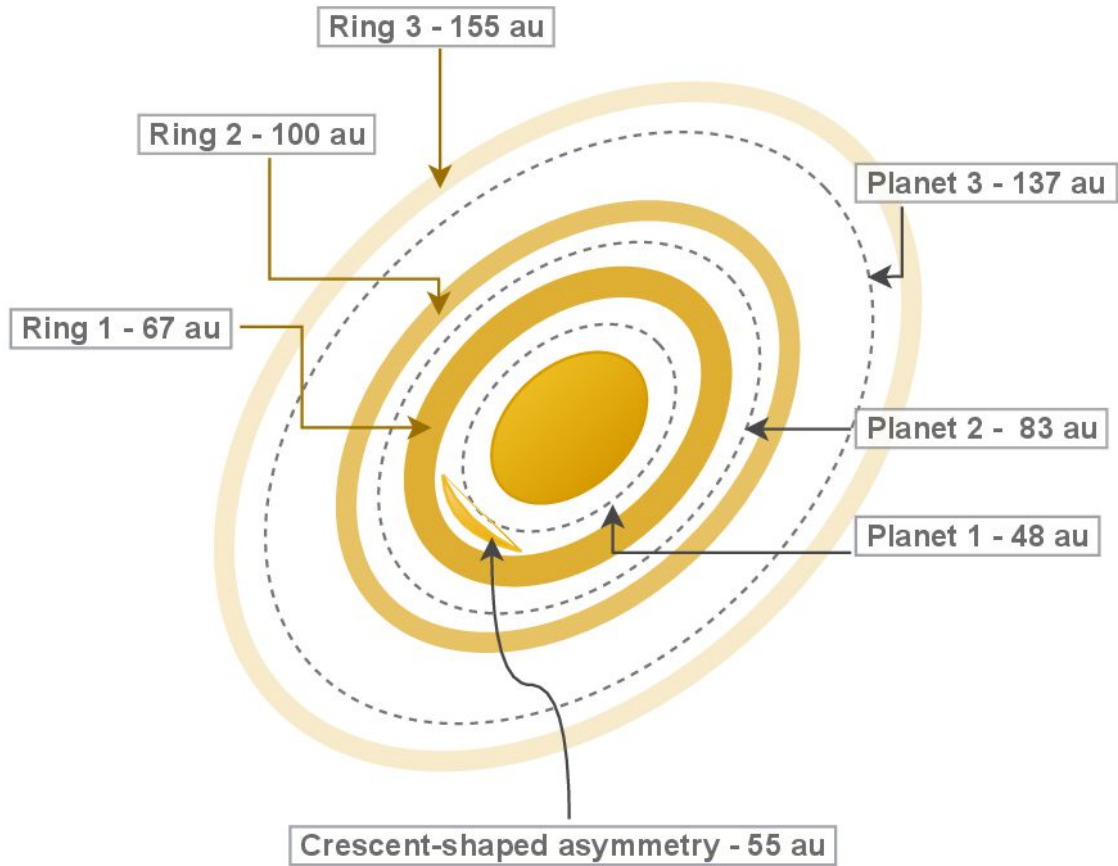


Figure 2.1: Sketch of the observed dust substructure of the HD 163296 system. The colored rings and the crescent-shaped feature mimic the dust whereas the grey dashed lines indicate the semi-major axes of the modeled planetary system. The labels introduced in this figure will be used throughout the text.

in Zhang et al. (2018), based on planet-disk interaction. In these models, asymmetries in the co-orbital region are common if the viscosity is low.

Prior to the publication of the results from the DSHARP campaign, the HD 163296 disk was modeled by Liu et al. (2018). Their models incorporated 2D two-fluid hydrodynamical simulations with three planets in their respective positions matching the observed gaps. Thanks to synthetic images using radiative transfer calculations, it was possible to match the observed density profile with 0.46, 0.46, and 0.58 Jupiter masses for the three planets and a radially increasing turbulent viscosity parametrization.

In the suite of simulations by Zhang et al. (2018) using hydrodynamical models with Lagrangian particles the proposed mass fits are 0.71, 2.18, and 0.14 Jupiter masses for an α -viscosity of 10^{-3} . In their lower viscosity models of $\alpha = 10^{-4}$ masses of 0.35, 1.07, and 0.07 Jupiter masses were fitted.

Further observational constraints of the hypothetical two outer planets were provided by kinematical detections by Teague et al. (2018b). Their model predicts masses of 1 and 1.3 Jupiter masses for these planets. Pinte et al. (2020) argue that velocity "kinks" observed in the CO observations with ALMA are evidence of nine planets in the DSHARP sample, including two planets in the HD 163296 disk at 86 au and 260 au. The signal-to-noise ratio is not sufficient to probe the inner gap at 48 au.

We want to further explore the possibility of reproducing the observed structures by planet-disk interaction with a focus on the crescent-shaped asymmetry in the dust emission. This asymmetric feature has been present in the works discussed above but it has not yet been subject to more detailed analysis. Given the motivation of the crescent-shaped feature in the observation of HD 163296, we aim to constrain the visibility of such an agglomeration of dust caused by planet-disk interaction and its dependence on the physical parameters of the system, such as planet mass, turbulent viscosity, and dust size. Similarly to the study by Zhang et al. (2018), we employ two-dimensional hydrodynamical models with a fluid formulation of dust.

Section 3.2 introduces the physical model and code setup as well as the post processing pipeline to predict observable features. In Sect. 3.3, we present the main results of our study. Section 3.4 compares these findings with previous works and addresses limitations of the model. In Sect. 3.5, we summarize the main results and give our concluding remarks.

2.2 Model

All hydrodynamical models presented in this work were performed with the FARGO3D multi-fluid code (Benítez-Llambay & Masset, 2016; Benítez-Llambay et al., 2019) and making use of an orbital advection algorithm (Masset, 2000). The code is based on the public version of FARGO3D with the addition of allowing a constant dust size throughout the simulation and a spatially variable viscosity.

2.2.1 Basic equations

The FARGO3D code solves the conservation of mass (Eqs. [3.1] and [3.4]) and conservation of momentum (Eqs. [3.2] and [3.5]) for gas and dust in our model setups:

$$\partial_t \Sigma_g + \nabla \cdot (\Sigma_g \mathbf{v}_g) = 0, \quad (2.1)$$

$$\Sigma_g [\partial_t \mathbf{v}_g + (\mathbf{v}_g \cdot \nabla) \mathbf{v}_g] = -\nabla P + \nabla \cdot \Pi - \Sigma_g \nabla \Phi - \sum_i \Sigma_i \mathbf{f}_i, \quad (2.2)$$

$$\partial_t \Sigma_{d,i} + \nabla \cdot (\Sigma_{d,i} \mathbf{v}_{d,i} + \mathbf{j}_i) = 0, \quad (2.3)$$

$$\Sigma_{d,i} [\partial_t \mathbf{v}_{d,i} + (\mathbf{v}_{d,i} \cdot \nabla) \mathbf{v}_{d,i}] = -\Sigma_{d,i} \nabla \Phi + \Sigma_{d,i} \mathbf{f}_i. \quad (2.4)$$

Here, Σ_g denotes the gas surface density, $\Sigma_{d,i}$ the corresponding dust species, $P = \Sigma_g c_s^2$ the gas pressure which is linked to the density by a locally isothermal equation of state with the sound speed c_s , Φ the gravitational potential of the star and planets, \mathbf{f}_i the interaction forces between gas and dust and \mathbf{v}_g and $\mathbf{v}_{d,i}$ the gas and dust velocities respectively.

The viscosity stress tensor is given by

$$\Pi = \rho\nu \left[\nabla\mathbf{v} + (\nabla\mathbf{v})^T - \frac{2}{3}(\nabla\cdot\mathbf{v})\mathbf{I} \right], \quad (2.5)$$

where \mathbf{I} is the unit tensor.

Dust feedback is included by the term $\sum_i \Sigma_i f_i$ in Eq. 3.2.

FARGO3D does not implement a Riemann-solver to compute the solution of the equations stated above, but uses a mixture of finite difference and finite volume method to obtain a solution of the hydrodynamical problem. The code furthermore solves the equations in two distinct steps, called the ‘source step’ and the ‘transport step’ using an *operator splitting* technique Stone & Norman (1992). Following the description in Benítez-Llambay & Masset (2016) the problem is usually expressed in partial differential equations of the form

$$\frac{\partial Q}{\partial t} + \nabla \cdot (Q\mathbf{v}) = S(Q, \mathbf{v}, t), \quad (2.6)$$

with some quantity Q , a flow velocity \mathbf{v} and a source term S . In the operator splitting approach, an intermediate solution Q_{inter} at $t + \Delta t_{\text{inter}}$ is obtained at first as the source step, and afterwards the transport step is executed based on the intermediate solution:

$$\frac{\partial Q}{\partial t} = S(Q, \mathbf{v}, t) \quad (2.7)$$

$$\frac{\partial Q}{\partial t} + \nabla \cdot (Q\mathbf{v}) = 0. \quad (2.8)$$

For the transport step the intermediate solution $Q(t + \Delta t_{\text{inter}})$ would be used. This structure provides an easily extensible framework and the implementation of the turbulent mixing and diffusion of dust grains by using the dust diffusion described in Weber et al. (2019a) is just an additional source step in the code. The corresponding dust diffusion flux j_i used in the model here can be written as:

$$j_i = -D_i (\Sigma_g + \Sigma_{d,i}) \nabla \left(\frac{\Sigma_{d,i}}{\Sigma_g + \Sigma_{d,i}} \right), \quad (2.9)$$

with the diffusion constant D_i being proportional to the turbulent viscosity ν (Youdin & Lithwick, 2007b):

$$D_i = \nu \frac{1 + \text{St}_i^2}{(1 + \text{St}_i^2)^2}. \quad (2.10)$$

The Stokes number St_i of dust species i is proportional to the stopping time t_{stop} and depends on the integrated surface density as follows:

$$\text{St}_i = t_{\text{stop}} \Omega_K = \frac{\pi a_i \rho_d}{2 \Sigma_g}, \quad (2.11)$$

where Ω_K is the Keplerian angular frequency, a_i the dust grain size, and ρ_d the material density of the grains. The gas-dust interaction is modeled using the Epstein drag law, which is expected to be valid if the particle size is smaller than the mean-free path of surrounding gas molecules. Here, the drag force is proportional to the relative velocities between the corresponding fluids (Whipple, 1972). The drag force f_i can be expressed as

$$f_i = -\frac{\Omega_K}{\text{St}_i} (\mathbf{v}_{d,i} - \mathbf{v}_g). \quad (2.12)$$

2.2.2 Disk model

In the disk model, the planet-disk interaction is implemented as an additional smoothed potential term (Plummer-potential) for each planet which takes the form (Weber et al., 2019b)

$$\Phi = -\frac{GM_*}{r} - \sum_i \left\{ \frac{GM_{p,i}}{[|\mathbf{r} - \mathbf{r}_{p,i}|^2 + bH(\mathbf{r}_{p,i})^2]^{\frac{1}{2}}} - \frac{GM_{p,i}}{r_{p,i}^2} r \cos\phi \right\}, \quad (2.13)$$

where the sum is taken over all respective planet masses and locations $M_{p,i}$ and $\mathbf{r}_{p,i}$. The last term counteracts the shift of center of mass due to the non-zero companion masses (Weber et al., 2019b). The smoothing length is set to bH with $b = 0.6$, where $H(r) = c_s(r)/\Omega_K(r)$ is the pressure scale height at the radial distance r . The specific factor acts as a correction for 3D effects in the 2D simulation (Müller et al., 2012).

Three planets are modeled in the simulations. The two outer ones are set to the locations indicated by Teague et al. (2018b). The inner planet is put at the corresponding gap location while the mass is varied in the different runs. In the fiducial models, the planet locations and masses are $r_p = \{48, 83, 137\}$ au, $M_{p0} = \{0.53, 0.29, 0.53\} M_{\text{jup}}$, respectively. From this point on we refer to the three planets as planet 1, planet 2, and planet 3. The same notation is used for the apparent ring structures, namely, ring 1: the observed or modeled ring at 67 au; and ring 2 at 100 au (see Fig. 2.1).

We chose to lower the mass of planet 2 compared to the one predicted in Teague et al. (2018b) since it allows a sufficiently massive ring 2 while not significantly disturbing the crescent-shaped asymmetry by its repeated gravitational interaction.

For the fiducial model, the corresponding parameter variations were set, with the planet mass, M_p , adjusted to its final value, M_{p0} , at the beginning of the simulation. The mass growth time scale, however, is known to have an impact on the formation of disk structures, such as vortices (Hammer et al., 2019; Hallam & Paardekooper, 2020). We therefore investigate the robustness of the results by testing different planet growth time scales:

$$M_p(t) = \frac{1}{2} \left[1 - \cos \left(\pi \frac{t}{T_G} \right) \right] M_{p0}. \quad (2.14)$$

T_G refers to the planet growth time scale ranging from $10T_0$ to $500T_0$ with T_0 denoting the orbital period at $r_0 = 48$ au. By using this simplified growth prescription, we do not directly model the accretion of gas onto the planets and, thus, we do not artificially remove any mass from the simulation domain. Furthermore, for all models, the displacement of the center of mass by the influence of the planets is taken into account as an additional indirect term added to the potential. The semi-major axes of the planets are kept fixed throughout the whole simulation.

The initial surface density profile is assumed to be a power law with an exponential cutoff:

$$\Sigma_{g/d} = \Sigma_{g/d,0} \left(\frac{r}{r_0} \right)^{-p} \exp \left[- \left(\frac{r}{r_0} \right)^s \right], \quad (2.15)$$

with $r_0 = 48$ au and the initial gas and dust surface densities $\Sigma_{g,0}$ and $\Sigma_{d,0}$. Similarly to the models of Liu et al. (2018), we chose a surface density slope of $p = 0.8$. For the dust, a sharper cutoff of $s = 2$ was chosen as compared to the gas cutoff of $s = 1$. In all simulation runs, an initial dust-to-gas ratio of $(\sum_i \Sigma_{d,i}) / \Sigma_g = 0.01$ is assumed.

We approximate the disk thermodynamics with a locally isothermal equation of state.

The model is parametrized through locally isothermal sound speed:

$$c_s = \frac{H(r_0)}{r_0} \left(\frac{r}{r_0} \right)^{\frac{1}{4}} \Omega_K r. \quad (2.16)$$

This corresponds to a flared disk with flaring index 0.25. The aspect ratio H/r at r_0 is set to a value of 0.05. Assuming a mean molecular weight of $\mu = 2.353$ the mid plane temperature profile can be written in the following way

$$T_{\text{mid}}(r) = \sqrt{\frac{\mu m_p}{k_B}} c_s \approx 25 \left(\frac{r}{r_0} \right)^{-\frac{1}{2}} \text{K}, \quad (2.17)$$

with the proton mass m_p . The temperature at 48 au matches the findings of Dullemond et al. (2019).

We assume a radially smoothly increasing turbulent viscosity profile, motivated by Eq. 4 in the work of Liu et al. (2018) and similar dead zone parameterizations presented in Pinilla et al. (2016) and Miranda et al. (2016):

$$\alpha(r) = \alpha_{\text{min}} \left\{ 1 - \frac{1}{2} \left(1 - \frac{\alpha_{\text{max}}}{\alpha_{\text{min}}} \right) \left[1 - \tanh \left(-\frac{r-R}{\sigma r_0} \right) \right] \right\}, \quad (2.18)$$

where the parameters R and σ are set to 144 au and 1.25, respectively. Similarly to the values in Liu et al. (2018), the parameter R refers to the mid-point of the transition in α , whereas σ defines the slope.

2.2.3 Boundary conditions

The radial velocities in the ghost cells are set according to anti-symmetric boundary conditions. On a staggered mesh this corresponds to $v_r(r_{\text{ghost}}) = -v_r(r_{\text{act}})$, where r_{ghost} is the ghost cell and r_{act} the equivalent mirrored cell on the active hydro mesh near the boundary. The value at the staggered boundary itself is set to zero. The azimuthal velocities are set to the initial Keplerian profile in the ghost zone.

The surface density is extrapolated according to the density gradient exponent p . Additionally, wave damping is applied within 15% of the respective boundary radius. In this region, the density is exponentially relaxed towards the initial values within 0.3 local orbital time scales. The procedure follows the wave damping boundary conditions used in de Val-Borro et al. (2006).

We tested the robustness of the wave damping with respect to the chosen inner boundary condition. No significant wave reflections are detected for both a symmetric and anti-symmetric inner boundary condition. The relative difference between these two approaches is on the order of 10^{-5} compared to the reflected perturbations of $\approx 10^{-2}$ without wave damping.

2.2.4 Code setup and parameters

Various ranges of individual disk parameters were considered for constraining the impact onto dust features in the simulations. Table 3.1 gives an overview over the performed simulations and their parameter choices.

For most of the runs, a resolution of 560 radial and 895 azimuthal cells was chosen where the grid is logarithmically spaced in radial direction. Compared to the local disk

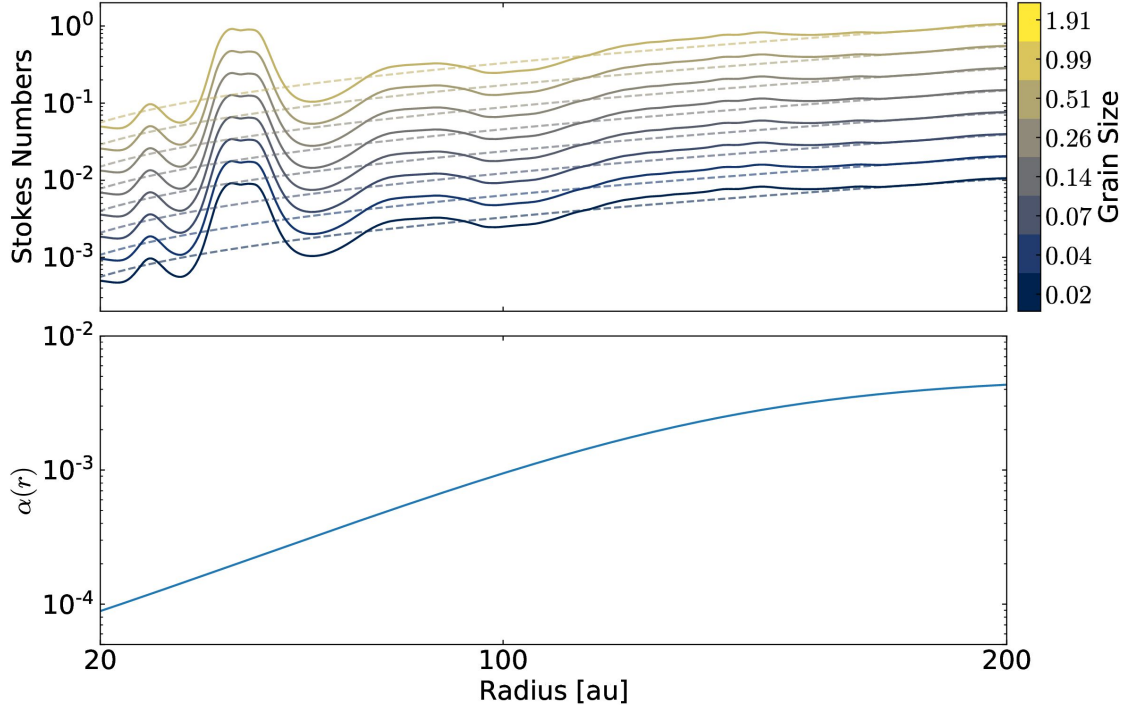


Figure 2.2: *Upper panel:* Azimuthally averaged values of the Stokes number St of model fid. The dashed lines indicate the initial values and the solid lines represent the state after $500 T_0$.

Lower panel: Prescribed α viscosity. The blue line visualizes the radially increasing α viscosity set in the model.

scale height, a ratio of roughly 7 cells per scale height is achieved in each direction; the models with the suffix `_dres` were run with a resolution of 14 cells per scale height. The low-resolution runs are subject to a larger numerical diffusion compared to the high resolution models. Although these runs can be used for mass estimates of the crescent-shaped feature, the results should be taken with caution concerning the dust substructure lifetime. Whenever this difference becomes significant we default to the high-resolution runs. Further details are given in appendix 2.4. For all simulations the mass of the central star is set to $1.9 M_\odot$. The parameters α_{\min} and α_{\max} are set to 10^{-5} and $5 \cdot 10^{-3}$ which results in a value of $\alpha(r_0) \approx 2 \cdot 10^{-4}$ at the location of $r_0 = 48$ au. The radial profile of $\alpha(r)$ is shown in the lower panel of Fig. 2.2.

The dust is sampled by eight separate fluids with Stokes numbers spaced logarithmically ranging from $2.5 \cdot 10^{-3}$ to $2.5 \cdot 10^{-1}$ at $r_0 = 48$ au. In the code, the equivalent grain size at r_0 is applied to the whole domain and is kept constant throughout the whole simulation. With an initial value of $\Sigma_{g,0} = 37.4 \text{ g/cm}^2$ the minimum and maximum grain sizes are $a_{\min} = 0.19 \text{ mm}$ and $a_{\max} = 19 \text{ mm}$. No dust size evolution is modeled here. It should be noted that these state the initial values of St and changes with time depending on the gas surface density, as shown in the upper panel of Fig. 2.2. The most prominent change of an increase of about one order of magnitude in St occurs at the gap carved by planet 1 after 500 orbits.

The majority of models neglect dust feedback to the motion of the gas. Each dust species can thus be scaled in density individually without violating the validity of the

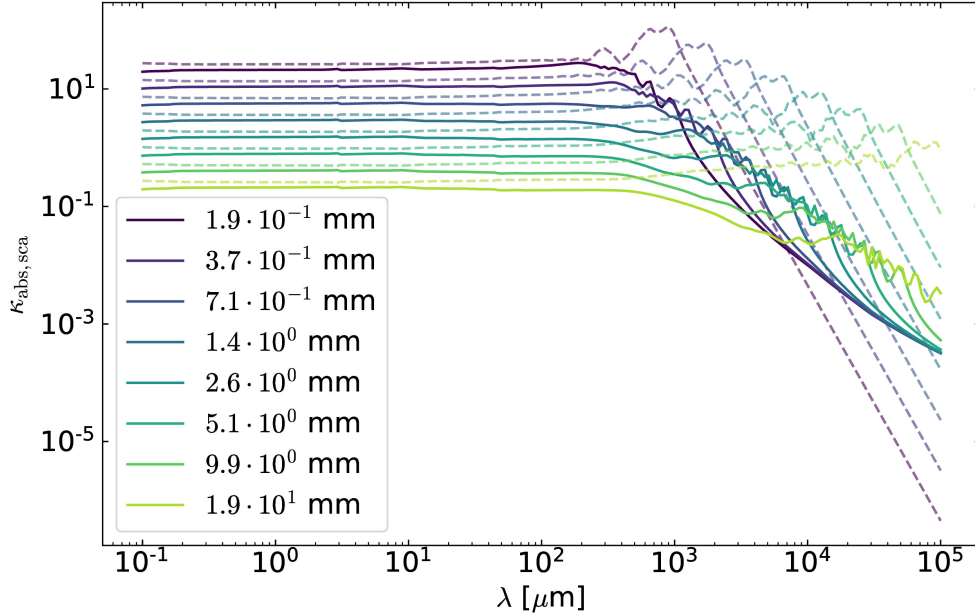


Figure 2.3: Dust opacities computed from the DSHARP opacities (Birnstiel et al., 2018). Shown are the absorption opacity coefficients κ_{abs} (*straight lines*) and the scattering opacities κ_{sca} (*dashed lines*) for all simulated dust species.

dynamical features.

Per default, the simulations are executed until $1000 T_0$. Simulation runs with a nonzero growth time scale T_G and the model `fid_dres` are run until $2000 T_0$. After ≈ 900 orbits, the gas and dust structure converges. The crescent-shaped asymmetry builds up to a stable niveau after less than 100 orbits. We refer to Sect. 3.3 for more details.

2.2.5 Radiative transfer model and post-processing

To compare the results of the hydrodynamical simulations with the observational data synthetic images are produced with RADMC-3D (Dullemond et al., 2012b) and the CASA package (McMullin et al., 2007). The results of the hydrodynamical simulations have to be extended to three dimensional dust density models which then serve as input for the radiative transfer calculations with RADMC-3D.

Using the given Stokes numbers of the hydro model, the respective dust sizes are computed via Eq. 3.6. The number density size distribution of the dust grains follows the MRN distribution $n(a) \propto a^{-3.5}$ (Mathis et al., 1977), where a is the grain size.

Dust settling towards the mid-plane is considered following the diffusion model of Dubrulle et al. (1995):

$$H_d = \sqrt{\frac{\alpha}{\alpha + \text{St}}} H. \quad (2.19)$$

Here, we assume a Schmidt number on the order of unity. The grid resolution for the radiative transfer is identical to the hydrodynamical mesh. In the polar direction, the grid is expanded by 32 cells which are equally spaced up to $z_{\text{lim}} = \pi/2 \pm 0.3$. The vertical disk density profile is assumed to be isothermal and the conversion from the

Simulation	H/r	$M_{\text{pl1}} [M_{\text{jup}}]$	$M_{\text{pl2}} [M_{\text{jup}}]$	e	N_r	N_ϕ	$r_{\text{cut}} [\text{au}]$	α	T_G
fid	0.05	0.53	0.29		560	895		$2 \cdot 10^{-4}$	0
fid_dres	0.05	0.53	0.29		1120	1790		$2 \cdot 10^{-4}$	
hr4	0.04								
hr45	0.045								
hr55	0.055								
hr6	0.06								
taper10									10
taper50									50
taper100									100
taper500									500
p1m1		0.11							
p1m2		0.19							
p1m3		0.27							
p1m4		0.36							
p1m5		0.44							
p1m1fb		0.11							
p1m2fb		0.19							
p1m3fb		0.27							
p1m4fb		0.36							
p1m5fb		0.44							
p1m6fb									
p1m6fb_dres					1120	1790			
p2m1			0.16						
p2m2			0.22						
p2m3			0.28						
p2m4			0.35						
p2m5			0.41						
p2m6			0.47						
ecc1				0.02					
ecc2				0.04					
ecc3				0.06					
ecc4				0.08					
ecc5				0.10					
cut1							150		
cut2							175		
cut3							200		
cut4							225		
cut5							250		
alpha1								$1 \cdot 10^{-5}$	
alpha1_dres					1120	1790		$1 \cdot 10^{-5}$	
alpha2								$1 \cdot 10^{-4}$	
alpha3								$5 \cdot 10^{-4}$	
alpha3_dres					1120	1790		$5 \cdot 10^{-4}$	
alpha4								$1 \cdot 10^{-3}$	
alpha4_dres					1120	1790		$1 \cdot 10^{-3}$	
alpha5								$2 \cdot 10^{-3}$	
alpha6								$3 \cdot 10^{-3}$	
alpha6_dres					1120	1790		$3 \cdot 10^{-3}$	

Table 2.1: Relevant simulation runs and their respective numerical parameters. Blank spaces assume an identical parameter as the fiducial model fid. The simulation labels starting with hr denote models with a variation in aspect ratio. The models starting with p include a change in the mass of planet 1 or 2 depending on the following digit. A suffix of fb describes models with dust feedback activated. All models use a radially varying alpha viscosity model with $\alpha = 2 \cdot 10^{-4}$ except the simulations denoted by alpha1 to alpha6 where a radially constant value of α was chosen.

surface density to the local volume density is calculated as follows:

$$\rho_{\text{cell}} = \frac{\Sigma}{\sqrt{2\pi}H_d} \cdot \text{erf}^{-1}\left(\frac{z_{\text{lim}}}{\sqrt{2}H_d}\right) \cdot \frac{\pi}{2}H_d \frac{\left[\text{erf}\left(\frac{z_+}{\sqrt{2}H_d}\right) - \text{erf}\left(\frac{z_-}{\sqrt{2}H_d}\right)\right]}{z_+ - z_-}. \quad (2.20)$$

The error function term is a correction for the limited domain extend in the vertical direction that would otherwise lead to an underestimation of the total dust mass. Similarly, the second correction term accounts for the finite vertical resolution, especially important for thin dust layers with strong settling towards the mid-plane. The coordinates z_+ and z_- denote the cell interface locations in polar direction along the numerical grid.

For each grain size bin and a wavelength of 1.3 mm, the corresponding dust opacities were taken from the `dsharp_opac` package, which provides the opacities presented in Birnstiel et al. (2018). These opacities are based on a mixture of water ice, silicate, troilite, and refractory organic material. Numerical values of the absorption and scattering opacities κ_{abs} and κ_{sca} for all simulated dust species are plotted in Fig. 2.3. The grains are assumed to be spherically shaped and to have no porosity. In the RADMC-3D model, the central star is assumed to have a mass of 1.9 solar masses with an effective temperature of 9333 K which results in a luminosity of $2.62 \cdot 10^{34}$ erg/s. The system is assumed to be at a distance of 101 pc. For the dust temperature calculation a number of $n_{\text{phot}} = 10^8$ photon packages and for the image reconstruction $n_{\text{phot_scat}} = 10^7$ photon packages were used. The thermal Monte-Carlo method is based on the recipe of Bjorkman & Wood (2001). We include isotropic scattering in the radiative transfer calculation. A comparison between the prescribed gas temperatures and the computed dust temperatures is given in Appendix 2.5.

For simulating the detectability of the various features present in the model we use the task `simalma` from the CASA-5.6.1 software. A combination of the antenna configurations `alma.cycle4.8` and `alma.cycle4.5` was chosen. The simulated observation time for configuration 8 is two hours whereas the more compact configuration is integrated over a reduced time with a factor of 0.22 corresponding 0.44 hours.

We employed the same cleaning procedure as made available in Isella et al. (2018) to reduce the artificial features from the incomplete UV coverage and to allow a comparison to the observation. The procedure involves the CASA task `tclean` with a robust parameter of -0.5 and manual masking of the disk geometry. Consistent with the radiative transfer model, the observed wavelength is simulated to be at 1.3 mm, corresponding to ALMA band 6.

2.3 Results

In the following parts the outcome of the simulation runs listed in Table 3.1 will be presented and analyzed. First, the variety of substructures emerging from the interaction of gas, dust, and the three planets will be described. Afterwards parameter dependence and observability will be addressed.

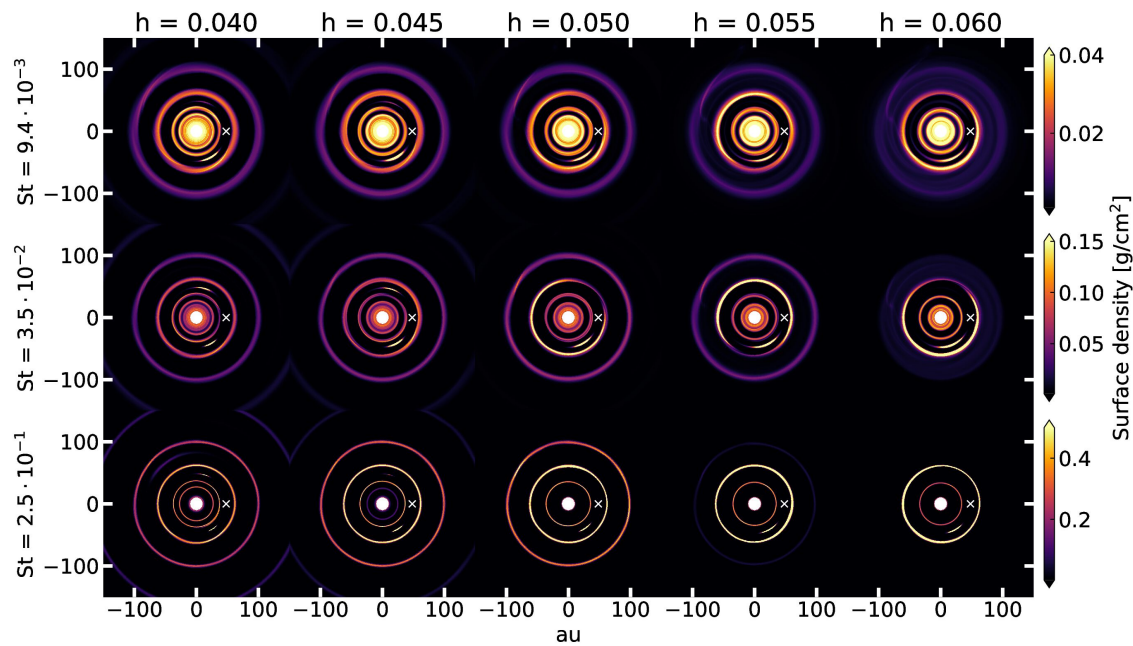


Figure 2.4: Shown are dust surface density maps for a subset of three fluids with varying values of the aspect ratio $h = H/r$ at 500 orbits at 48 au. Crescent-shaped asymmetries are visible for all aspect ratios. Large values of h weaken dust accumulation in the co-orbital regions of the planets. The white crosses mark the position of planet 1.

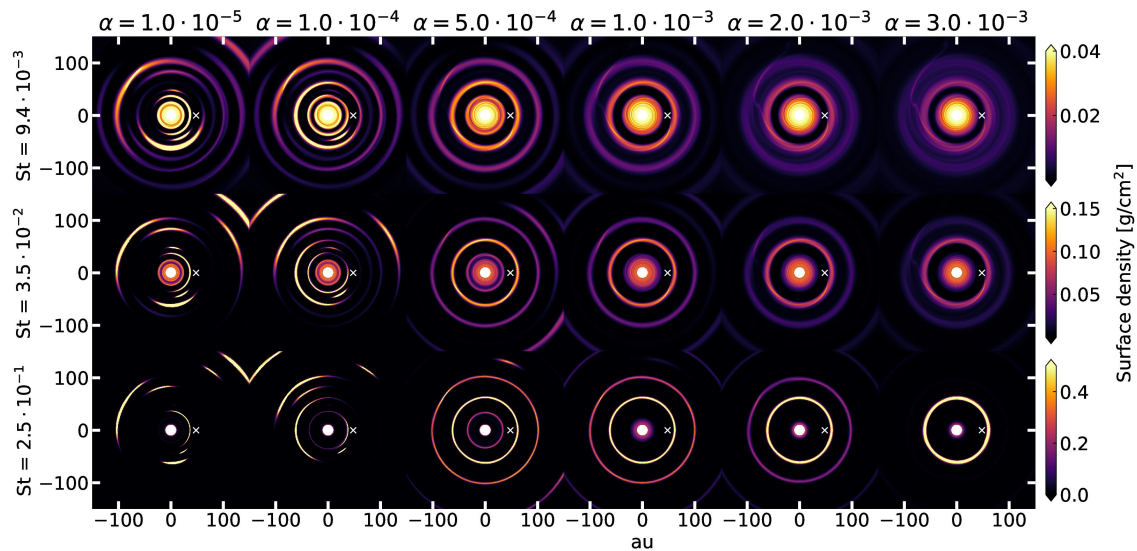


Figure 2.5: Dust surface density maps for different values of a radially constant α -viscosity after 500 orbits at 48 au. For $\alpha \leq 10^{-4}$ strong asymmetries are present. ring 2 weakens or vanishes for large viscosities. The white crosses mark the position of planet 1.

2.3.1 Dust substructure overview

A variety of dust substructures emerges from the planet-disk system during its dynamical evolution. Figures 2.4 and 2.5 show the dust surface density structure for a selected parameter space of aspect ratio and the turbulent viscosity, characterized by α . In the following analysis of the crescent-shaped asymmetries, simulation snapshots after 500 orbits at 48 au are compared with each other since their evolution is comparable for all resolutions. Most prominently multiple rings form in most cases. As expected, fluids with larger Stokes numbers St and thus larger grain sizes exhibit thinner rings and more concentrated substructures. Especially, nonaxisymmetric features can be seen mostly for $a \geq 2.6$ mm or $St > 10^{-2}$. For smaller dust sizes, the dust is better coupled to the gas and resembles its structure more closely.

Additionally, if a crescent-shaped asymmetry is present, it is situated in the gap caused by the innermost planet at 48 au for the majority of the parameter space. Further asymmetries appear if the α -viscosity is radially constant with values of $\alpha \leq 1 \cdot 10^{-3}$ or for low values of the aspect ratio h . Dust is preferably trapped in the Lagrange point L5. In Fig. 2.4, rings and asymmetries become weaker with increasing aspect ratio. A crescent-shaped feature at the L5 position is present for all aspect ratios whereas a second similar asymmetry at the L4 point appears for values of $H/r < 0.05$. The crescent weakens for smaller grain sizes. Also the second prominent ring beyond planet 2 at 83 au clearly weakens for larger aspect ratios. In the case of a combination of the largest grain sizes and H/r , the ring completely vanishes.

To highlight the importance of the turbulent α viscosity parameter, a subset of results with radially constant values of α are shown in Fig. 2.5. Not surprisingly, larger values of alpha generally lead to a more diffuse and symmetric distribution of dust. Below $\alpha = 5 \cdot 10^{-4}$ no concentric rings form due to vortices in the gas. Crescent-shaped features in both Lagrange points of the innermost planet are visible in the very low viscosity case of $\alpha = 10^{-5}$. A sufficiently large viscosity on the other hand also leads to the disappearance of the second ring in the limit of larger grains and Stokes numbers, similarly to the large aspect ratio in Fig. 2.4. The collection of these results also stresses the problem of a radially constant α viscosity with respect to the observed HD 163296 system. To reproduce a nonaxisymmetric feature in the vicinity of the inner planet and a smooth ring-shaped outer structure, a radially increasing value of α would be the natural choice. This is also consistent with an embedded dead zone at the inner part of the disk and a more active outer disk region with a higher degree of ionization (Miranda et al., 2016; Pinilla et al., 2016). We thus chose a radially increasing α viscosity for all remaining simulation runs.

Models with a variation in the dust cutoff radius only show little changes in the resulting dust structures. Only this subset of the possible parameter space already exposes the degeneracy of the emerging substructures with respect to the chosen disk models.

2.3.2 Rings

Before quantifying the nonaxisymmetric feature in the model, we want to compare properties of the ring structures with previous works and observations. The general procedure is to azimuthally average the dust density maps after 1000 orbits at 48 au and to invoke a Gaussian fitting of the dust rings, comparable to Dullemond et al. (2018). Since the ring structure is approximately converged after 900 orbits, the following pro-

Const.	$\Sigma_{g,0}$ (48 au) [$\frac{g}{cm^2}$]	$\Sigma_{g,0}$ (1 au) [$\frac{g}{cm^2}$]	a_{min} [mm]	a_{max} [mm]	κ_{min} [$\frac{cm^2}{g}$]	κ_{max} [$\frac{cm^2}{g}$]
a	19.7	436.8	0.191	19.1	1.32	0.11
ϵ_{dg}	1.5	33.1	0.014	1.44	0.41	1.94

Table 2.2: Results for both the high and low mass model as derived from the optical depth fitting of ring 1 in Sect. 2.3.2. Both the initial gas surface densities $\Sigma_{g,0}$ at 1 and 48 au are listed. Depending on the gas density a different dust grain size distribution with the minimum and maximum size of a_{min} and a_{max} was chosen. Their respective opacity values are listed under κ_{min} and κ_{max} .

a [mm]	St	w_{ring1} [au]	w_{ring2} [au]	r_{ring1} [au]	r_{ring2} [au]
0.2	$2.5 \cdot 10^{-3}$	4.09 ± 0.09	10.5 ± 0.17	62.26 ± 0.09	100.18 ± 0.16
0.4	$4.9 \cdot 10^{-3}$	3.13 ± 0.08	7.10 ± 0.09	62.05 ± 0.08	99.90 ± 0.09
0.7	$9.4 \cdot 10^{-3}$	2.27 ± 0.07	4.80 ± 0.04	61.90 ± 0.07	99.25 ± 0.04
1.4	$1.8 \cdot 10^{-2}$	1.68 ± 0.05	3.34 ± 0.01	61.86 ± 0.05	98.87 ± 0.01
2.6	$3.5 \cdot 10^{-2}$	1.28 ± 0.04	2.37 ± 0.01	61.89 ± 0.04	98.69 ± 0.01
5.1	$6.8 \cdot 10^{-2}$	1.00 ± 0.03	1.76 ± 0.01	61.92 ± 0.03	98.67 ± 0.01
9.9	$1.3 \cdot 10^{-1}$	0.80 ± 0.03	1.33 ± 0.01	61.93 ± 0.03	98.67 ± 0.01
19.1	$2.5 \cdot 10^{-1}$	0.64 ± 0.02	1.01 ± 0.01	61.94 ± 0.02	98.66 ± 0.01

Table 2.3: Gaussian fit results of the simulated dust rings for all Stokes numbers, St. Ring widths are denoted by $w_{ring1,2}$ whereas the ring position is labeled $r_{ring1,2}$.

a [mm]	St	M_{ring1} [M_{earth}]	M_{ring2} [M_{earth}]
0.2	$2.5 \cdot 10^{-3}$	2.1	1.9
0.4	$4.9 \cdot 10^{-3}$	2.9	2.9
0.7	$9.4 \cdot 10^{-3}$	4.0	4.7
1.4	$1.8 \cdot 10^{-2}$	5.5	8.0
2.6	$3.5 \cdot 10^{-2}$	7.9	12.3
5.1	$6.8 \cdot 10^{-2}$	11.5	17.0
9.9	$1.3 \cdot 10^{-1}$	17.3	22.2
19.1	$2.5 \cdot 10^{-1}$	28.0	26.9
sum (high mass model)		79.3	95.9
sum (low mass model)		13.1	15.8

Table 2.4: Gaussian fit results of the simulated dust rings for all Stokes numbers, St, similar to Tab. 2.3.2. Given is the amount of dust trapped in the rings for each individual dust species and the total dust mass for each respective ring.

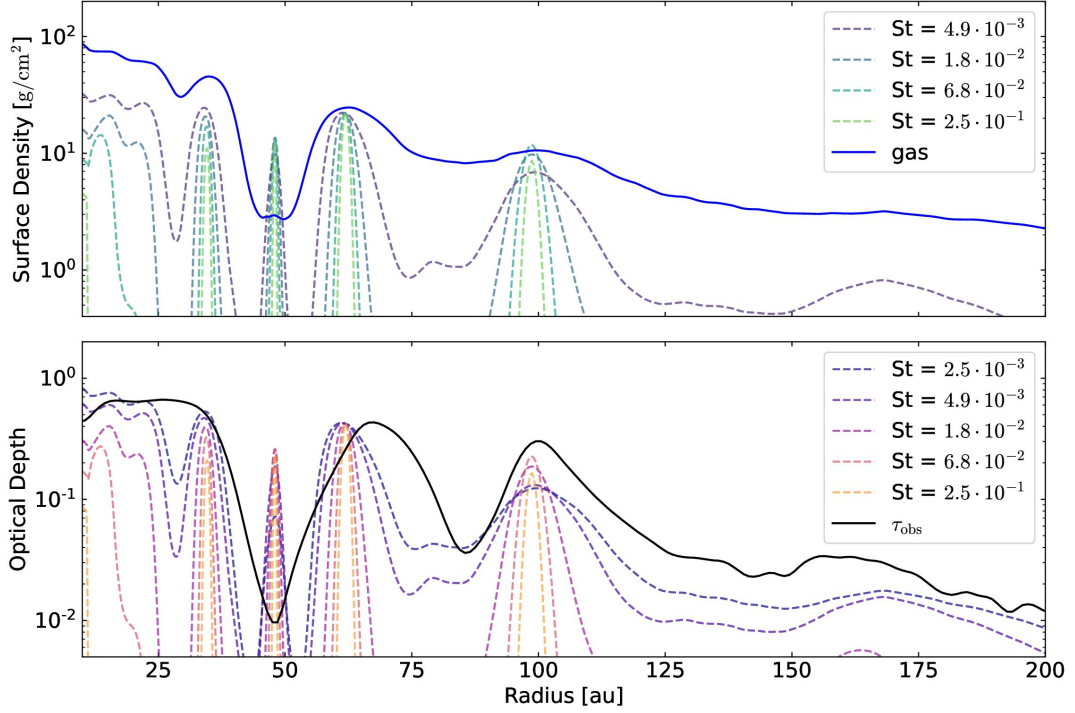


Figure 2.6: *Upper panel:* Azimuthally averaged dust and gas surface densities of model `fid_dres` after 1000 orbits at 48 au. Dust density profiles are normalized to the gas peak value at the location of ring 1.

Lower panel: Azimuthally averaged optical depths of model `mid` after 1000 orbits at 48 au compared to the observed optical depth τ_{obs} . Simulated optical depths are normalized to τ_{obs} at the location of ring 1.

cedure is based on the snapshots at 1000 orbits.

Figure 2.6 shows the results of the high resolution fiducial model `fid_dres` as an example of the radial surface density structure. The increased resolution was chosen since the lower resolution models may overestimate the ring width and the trapped dust mass due to numerical diffusion (Appendix 2.4). In the upper panel, the dust species is rescaled to gas density peak of ring 1. The dust rings are clearly thinner than the gaseous envelope and the ring width decreases with increasing dust grain sizes due to the stronger drift.

With the corresponding opacities κ_i a rough estimate of the resulting optical depth can be computed by $\tau_{\text{sim}} = \kappa_i \Sigma_i$, where i denotes the dust species index. The results of this estimate are displayed in the lower panel of Fig. 2.6. All optical depths are rescaled to the values at the position of ring 1 from the profile τ_{obs} derived in Huang et al. (2018a). The profile provided in their work excludes contributions from the prominent nonaxisymmetric structures. Several properties become apparent. Ring 1 is wider than in the simulated profile and the peak location of ring 1 is located further outward with respect to the simulated one. Furthermore, the peak value of the optical depth of ring 2 from smaller grains and Stokes numbers is lower in the simulations compared to the estimated value from the observation. A partial explanation of these differences could be that the actual dust-to-gas ratio could become larger than in the models so that dust feedback shifts the ring further outward and spreads the ring, as shown in Weber et al.

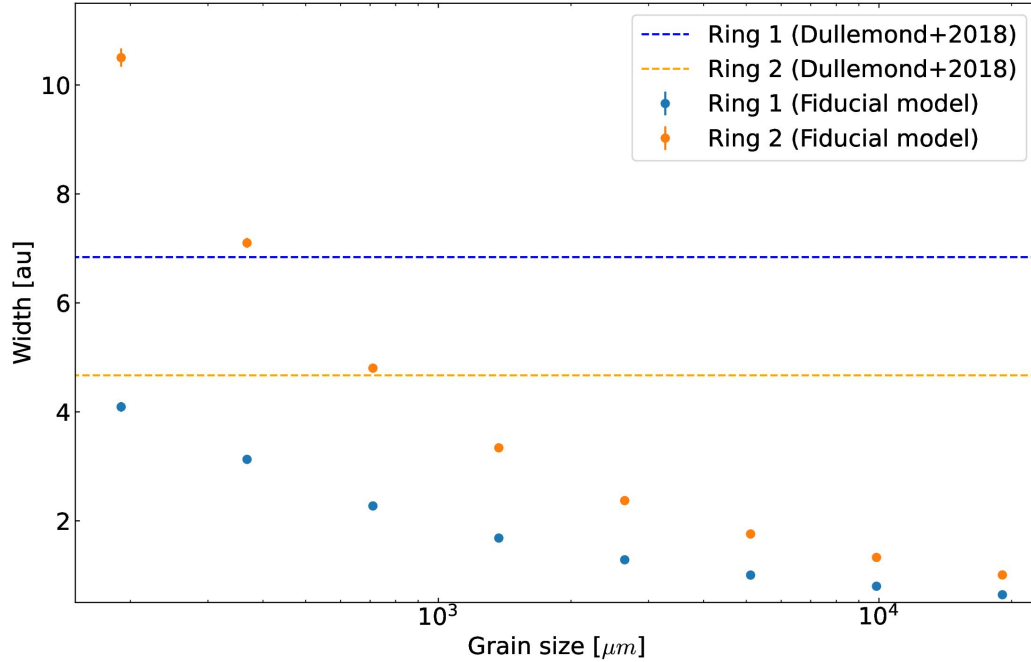


Figure 2.7: Ring widths of model `fid_dres` after 1000 orbits at 48 au. Simulated values are compared to the inferred ring widths of Dullemond et al. (2018), displayed as the horizontal dashed lines.

(2018) and Kanagawa et al. (2018). Here, the dust-to-gas ratio is not sufficient to cause a significant effect in the models including dust feedback.

One conclusion drawn by Dullemond et al. (2018) was that the optical depth observed in the DSHARP survey is remarkably close to unity and that the rings were optically thin. Later Liu (2019) and Zhu et al. (2019) argued that dust scattering could account for this phenomenon and that the actual optical depth could be larger. In the case of HD 163296 the mass hidden in ring 1 could be thus larger than expected.

For ring fitting we use a Gaussian:

$$\Sigma_{\text{fit}}(r) = A \exp\left(-\frac{(r - r_0)^2}{2w}\right) \quad (2.21)$$

with the peak value A , the ring location r_0 and the ring width w . In Fig. 2.7, the fitted ring widths from model `fid` are plotted and compared to the observed values in Dullemond et al. (2018). Grain sizes of the high mass model are used. The width of ring 2 is matched close to a grain size of 1 mm. On the other hand, the width of ring 1 is not reached with the parameters chosen in our models. It should be noted that the gas ring width is about 8 au, just slightly larger than the observed value of about 7 au. Smaller Stokes numbers could in principle reproduce these findings. The equivalent model `p1m6fb_dres` including dust feedback shows no significant differences.

2.3.3 Surface density estimation

With ring 1 being the most prominent substructure in the observed system, its estimated lower bound for the surface density would be a reasonable choice for rescaling the simulated dust density maps. Furthermore, the crescent-shaped feature of interest

is located closely to ring 1. To estimate a minimum mass of trapped dust in this feature an appropriate normalization of the density with respect to ring 1 would be a natural choice.

There are two possible methods in achieving a simple normalization. First, we rescale the sum of all azimuthally averaged dust densities so that the combined optical depth at the location of ring 1 equals the observed value. To maintain the validity of the dynamics of the system, the Stokes number corresponding to the grain size of a fluid has to be unmodified by this process. The immediate consequence is then a change in the dust-to-gas ratio if the densities are rescaled, since a change in the gas surface density with a constant grain size would modify the Stokes number (see Eq. 3.6). With a change in the dust-to-gas ratio, the dust dynamics only remain comparable if no dust feedback is considered.

The second choice would be to maintain an initial dust-to-gas ratio of 0.01 and to change the dust grain size and the gas surface density. A modification of the grain size affects in turn the dust opacities and thus the optical depth. Consequently, the process of generating τ_{sim} , rescaling it to τ_{obs} and inferring the corrected dust surface densities has to be iterated until convergence is achieved. Keeping the dust-to-gas ratio constant is important for the model runs with dust feedback enabled.

Table 2.3.2 provides relevant results from these two approaches which will be denoted by the high and low mass model in the following parts. With the unchanged grain sizes the dust-to-gas ratio diminishes to $\approx 2.4 \cdot 10^{-3}$. For the iterative approach with the dust-to-gas ratio unchanged, the grain size distribution shifts towards smaller grains with a maximum size $a_{\text{max}} \approx 1.44$ mm and a minimum size $a_{\text{min}} = 0.014$ mm.

Results of the Gaussian fits onto the dust rings of the fiducial model are listed in Table 2.3.2 for all simulated dust species. The inferred ring widths are decreasing with increasing grain sizes and Stokes numbers. The peak maxima shift towards the star for larger grain sizes since the dust drift becomes more dominant in this regime. The total dust mass of all species is computed for both the low and high mass model. Dullemond et al. (2018) found masses of $56 M_{\text{earth}}$ and $43.6 M_{\text{earth}}$ for ring 1 and ring 2 respectively assuming 1 mm grains with the same opacities values as used in the model presented here. The results of both the low and high mass model encompass the values of Dullemond et al. (2018).

The high mass model will be the preferred choice in the following diagrams and analysis since the opacity is dominated by smaller grain sizes compared to the low mass model. The choice is motivated by the broad ring structures apparent in the observations.

2.3.4 Secondary planet mass

In the models p2m1 - p2m6, the mass of the secondary planet at 83 au is varied to verify its impact on the ring structure. The results of Teague et al. (2018b) indicate a planet mass of $1 M_{\text{jup}}$ within an error margin of 50%.

In our model runs, we chose a mass of $0.29 M_{\text{jup}}$ for planet 2 since a larger mass causes a stronger dissipation of the crescent-shaped asymmetry. Lower masses significantly decreased the dust content in ring 2 and thus the fiducial planet mass value was chosen as the sweet spot between a strong ring contrast and an maximized asymmetric dust accumulation. In Fig. 2.8 a parameter study of the planet 2 mass influence is shown, involving the models p2m1 to p2m6. The nonaxisymmetric feature at the L5 point is

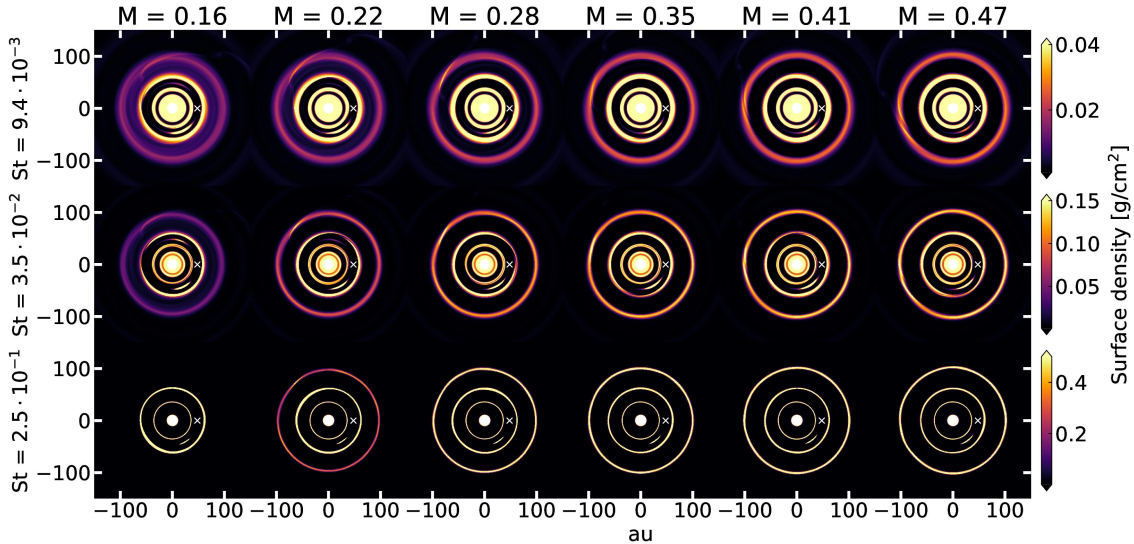


Figure 2.8: Dust surface density maps for a subset of three fluids with varying values of the planet 2 mass in M_{jup} at 500 orbits at r_0 . The white crosses mark the position of planet 1.

sensitive to the mass of planet 2. In general, the passing of the planet acts as a perturber, inhibiting an effective dust trap in L5. The effect is visible in Fig. 2.8 for smaller grain sizes. Lower planet masses weaken the dust trapping in ring 2. We identify the balance between effective trapping in ring 2 and optimal dust trapping in the crescent-shaped feature to be on the order of $\approx 0.25M_{\text{jup}}$, thus the choice of the fiducial model parameter.

2.3.5 Asymmetries

Of particular interest is the crescent-shaped asymmetry in the vicinity of ring 1 in HD 163296. Such a feature arises naturally in planet-disk interaction models including dust in the form of dust trapping in a Lagrange point of the gap carving planet. In this case planet 1 is responsible for dust trapping in the trailing L5 point which is also visible in Figs. 2.4 and 2.5 for a significant subset of the parameter space. An equivalent result was presented in Isella et al. (2018). In the following subsections, we aim to perform a more extensive analysis of this feature to constrain physical properties of the dynamical system.

Structure & dust feedback

In Fig. 2.9, in the left panels dust surface density maps are shown in polar coordinates for four different dust fluids of model `fid_dres`. The region is focused around the co-orbital region of planet 1. Clearly, dust is concentrated in the trailing Lagrange point L5 of the Jupiter mass planet at 48 au. Several trends become apparent: not surprisingly, dust grains are trapped more efficiently for larger grain sizes and Stokes numbers due to the stronger drift. Furthermore, the shape is more elongated for smaller Stokes numbers.

We consider whether the dynamics of this feature change with the consideration of a dust back-reaction onto the gas. An example of the impact from dust feedback (model

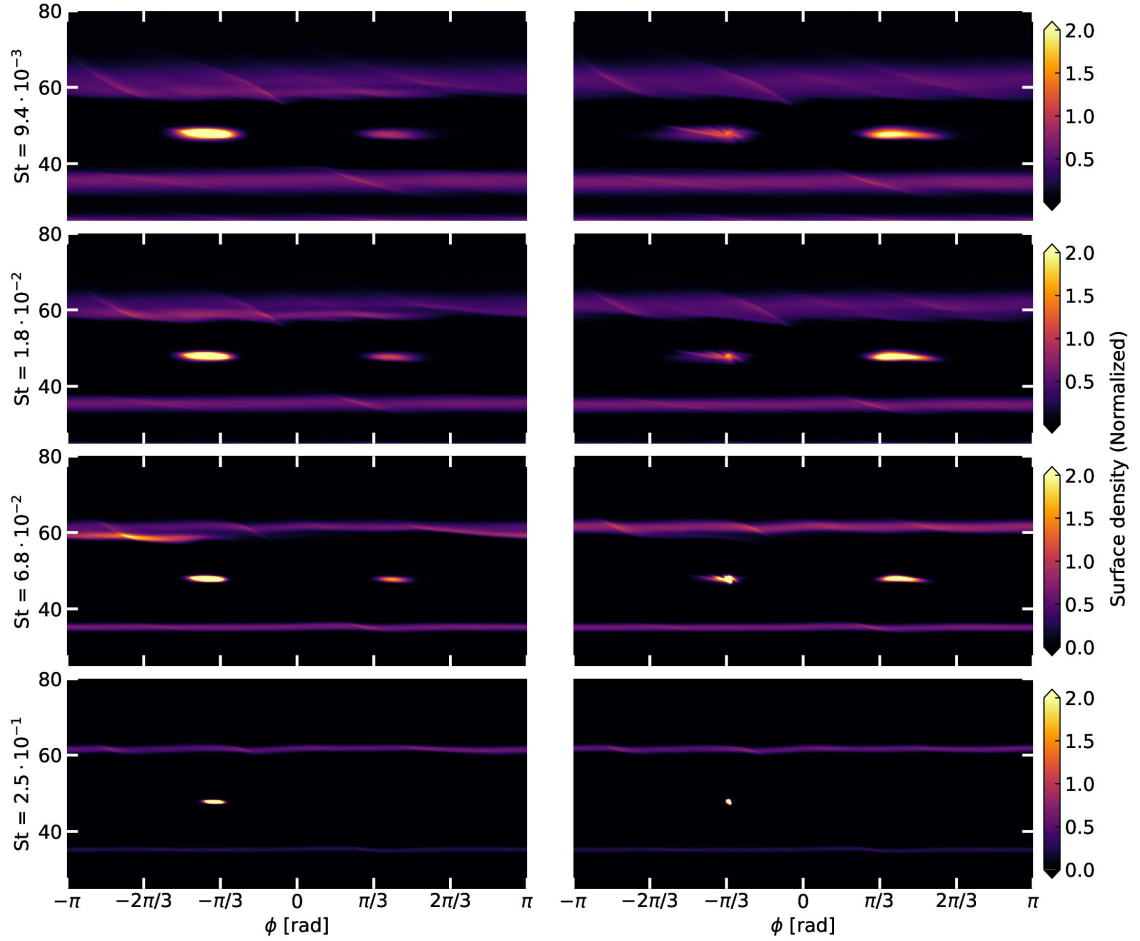


Figure 2.9: Dust surface density maps in polar coordinates for model `fid_dres` without dust feedback (left hand side) and `p1m6fb_dres` with dust feedback after 500 orbits at 48 au for four different initial Stokes numbers and dust sizes. A dust agglomeration around the location of the trailing Lagrange point L5 is present for all Stokes numbers. Unlike the nonfeedback case, the right panels show that dust is trapped more efficiently in the leading Lagrange point L4 for smaller Stokes numbers. For $St \lesssim 6.8 \cdot 10^{-2}$, the L4 feature is more pronounced than the dust over density around L5. Dust feedback leads to an instability at the L5 point and fragments the asymmetric feature. Dust densities are normalized to the peak value of ring 1.

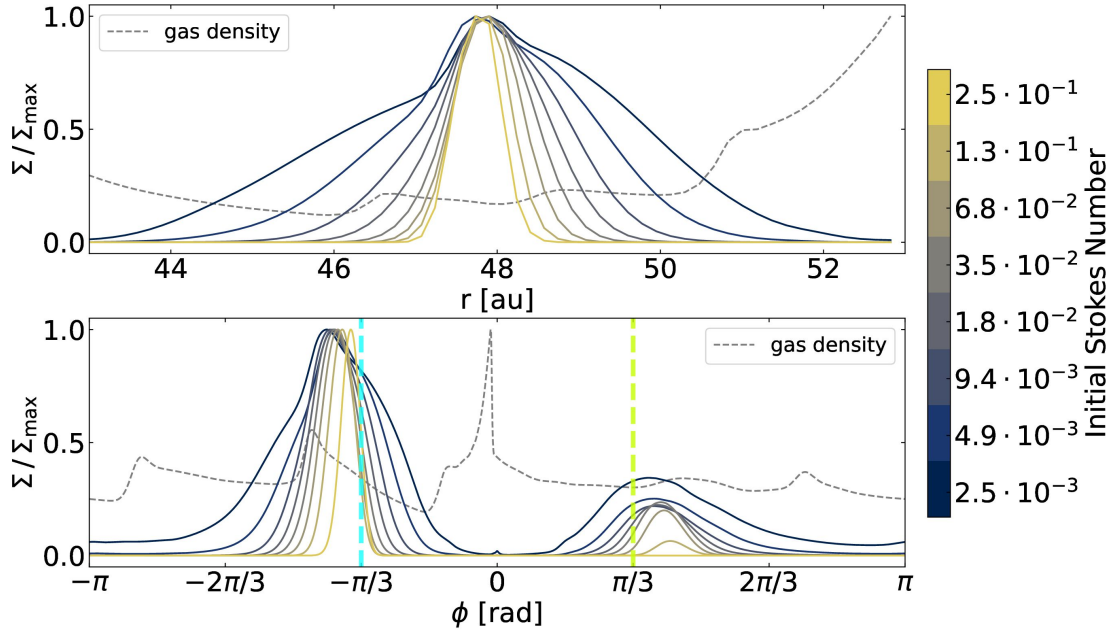


Figure 2.10: Radial and azimuthal cut through the maximum of the crescent-shaped asymmetry around L5 of the fiducial model `fid_dres` after 500 orbits at 48 au. The color map indicates the different initial Stokes numbers of the dust fluids. The dashed lines represent the gas density. The surface densities are normalized to their respective maximum value in the co-orbital region of planet 1. The light-blue and light-green vertical lines indicate the Lagrange points L5 and L4, respectively.

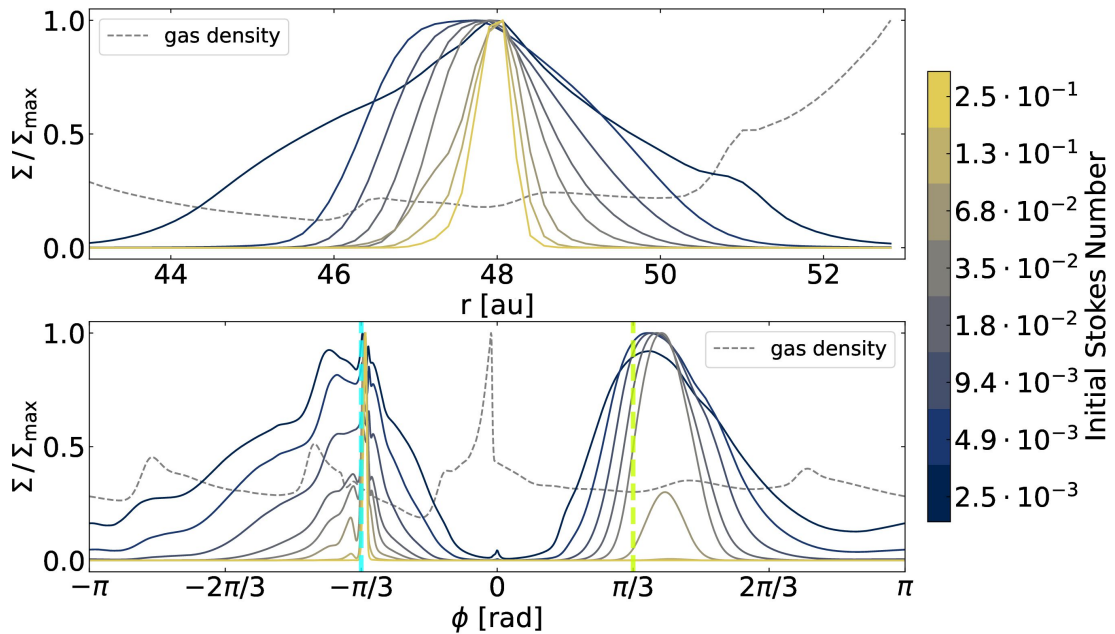


Figure 2.11: Radial and azimuthal cut through the maximum density value in the co-orbital region of the model `p1m6fb_dres` with dust feedback after 500 orbits at 48 au. The light-blue and light-green vertical lines indicate the Lagrange points L5 and L4 respectively. Depending on the location of the feature the density cuts are normalized to the peak value in the region of L4 or L5. Smaller dust with $St \lesssim 6.8 \cdot 10^{-2}$ is preferably concentrated in L4.

p1m1fb_dres) is given in Fig. 2.9 on the right hand side, with the same parameters as in model fid_dres. The crescent-shaped feature exhibits different structures compared to model fid_dres at the location of L5. The dust back-reaction onto the gas triggers and instability leading to fragmentation of the dust feature. Unlike the fiducial model, the additional crescent in the leading Lagrange point L4 of planet 1 is more pronounced than the L5 feature for smaller grain sizes and Stokes numbers. In the explored parameter space, dust is significantly trapped for small aspect ratios or very low values of $\alpha < 10^{-4}$ without the modeling of dust feedback. With the fiducial set of parameters the L4 feature slowly dissipates after more than a 1000 orbits.

A closer look on the radial and azimuthal extent of these dust shapes is provided in Fig. 2.10 for all simulated dust fluids. The surface densities of the crescent-shaped asymmetry are normalized to its maximum value. The radial and azimuthal width increases with decreasing values of the Stokes number. In the lower panel the density peak at the trailing L5 dominates the leading peak at L4 for all dust species. For smaller Stokes numbers and grain sizes the density maximum moves away from the planet location similar to the peak shift of the concentric dust rings described in Sect. 2.3.2.

In Fig. 2.11 we display the results of model p1m6fb_dres. In contrast to the nonfeedback case, the density peak at L4 becomes significant for $St \leq 6.8 \cdot 10^{-2}$. In the vicinity of the L5 point two density peaks appear due to the fragmentation by dust feedback. The azimuthal gas density profile reveals the momentary location of the spiral wakes caused by the planets as well as the gas accumulation around planet 1 itself at $\phi = 0$.

Dynamical stability

In principle, the crescent-shaped features in the co-orbital region are subject to diffusive processes such as dust diffusion due to turbulent mixing or gravitational interaction with the planetary system (for example eccentric orbits). The dust trapping mechanism has to counteract these disruptive forces for the feature to be dynamically stable.

Figure 2.12 corroborates this line of argument. The stability of the L5 feature is sensitive to the local value of the α viscosity. Given a value of $\alpha = 10^{-5}$, the feature remains stable throughout almost the entirety of the simulation whereas $\alpha = 10^{-3}$ shortens the existence down to about 300 dynamical time scales. For larger viscosities, no discernible feature develops and the co-orbital region simply empties its dust content from the initial condition.

Studying the results of the models p1m1 to p1m5 we find that below about 0.2 to 0.25 Jupiter masses for planet 1 no stable feature forms since the gravitational interaction is not sufficient to enforce dust trapping in the Lagrange points. Qualitatively, the feature life time is thus very sensitive to the given physical parameters. It should be noted that the absolute value in dynamical time scales could be underestimated due to the numerical diffusion present in the lower resolution runs. This additional diffusive effect prevents a stable trapping region around L4 and L5. Further details are provided in appendix 2.4. Therefore, in Fig. 2.12, we plotted results with 14 cells per scale height.

Dust mass

A substantial amount of dust can be trapped in the feature at L5. The total mass ranges from roughly $1 M_{\text{earth}}$ for the low mass model to $10 - 15 M_{\text{earth}}$ for the high mass model. An overview of the relevant parameters and their impact on the trapped dust mass is

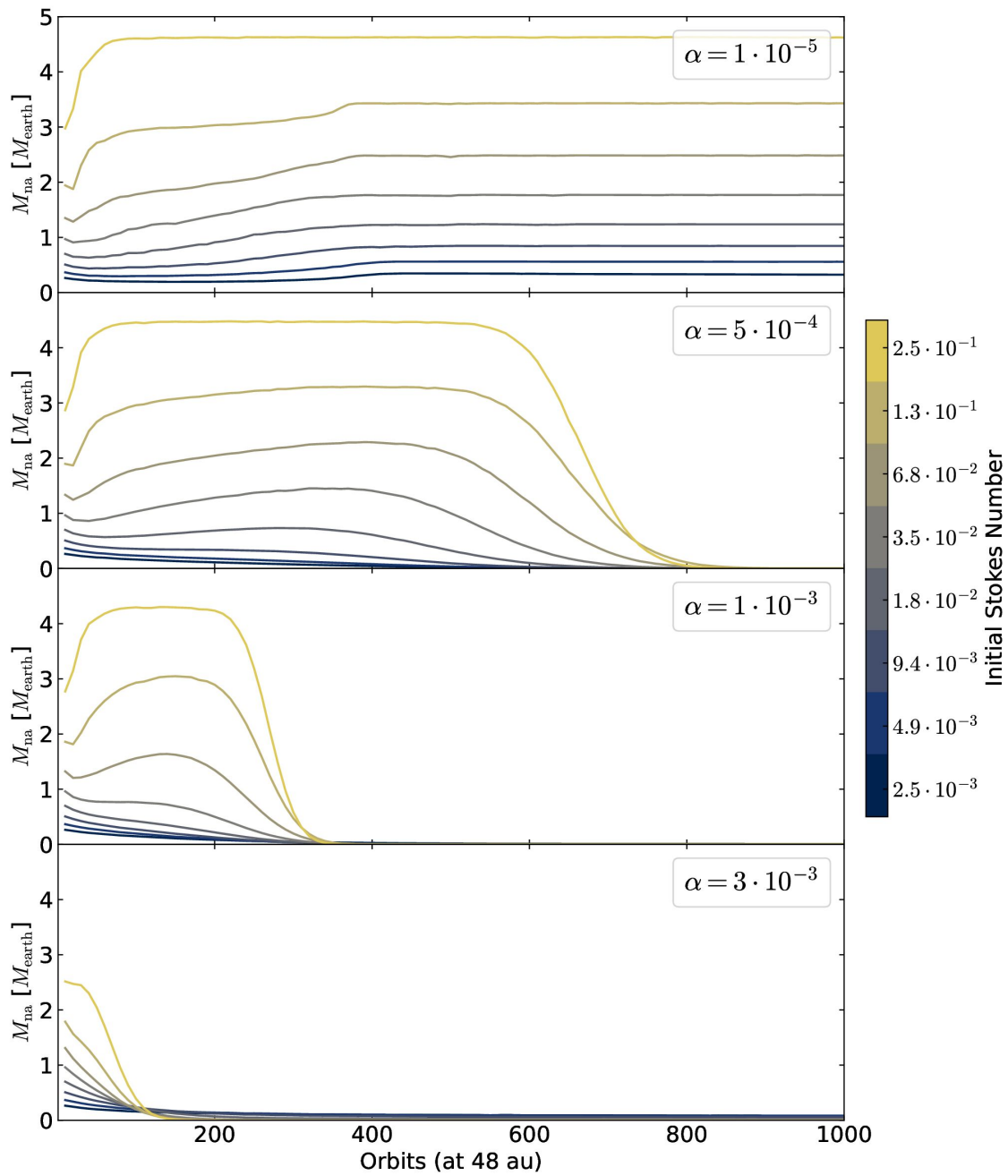


Figure 2.12: Development of the trapped dust mass in the L5 region for different α viscosities over time with a resolution of 14 cells per scale height. Dust masses M_{na} in the nonaxisymmetric feature denoted are integrated down to a cut-off value of $10^{-2} \Sigma_{\text{max}}$ and normalized to the high mass model stated in Table 2.3.2.

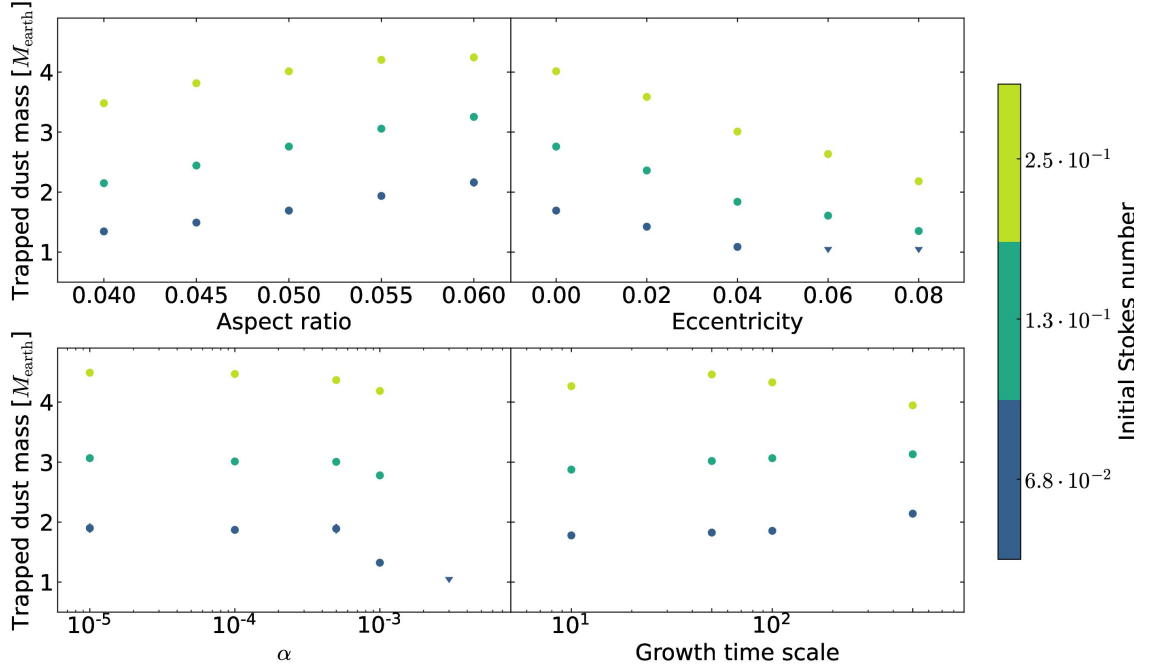


Figure 2.13: Trapped dust masses in earth masses in the L5 feature for the largest three initial Stokes numbers. The mass values are averaged over the approximately constant mass time frame starting from $100 T_0$. Dust masses are normalized according to the high mass model stated in Table 2.3.2. Missing data points are equivalent to a nonexistence of a stable crescent-shaped asymmetry in the co-orbital region around 48 au.

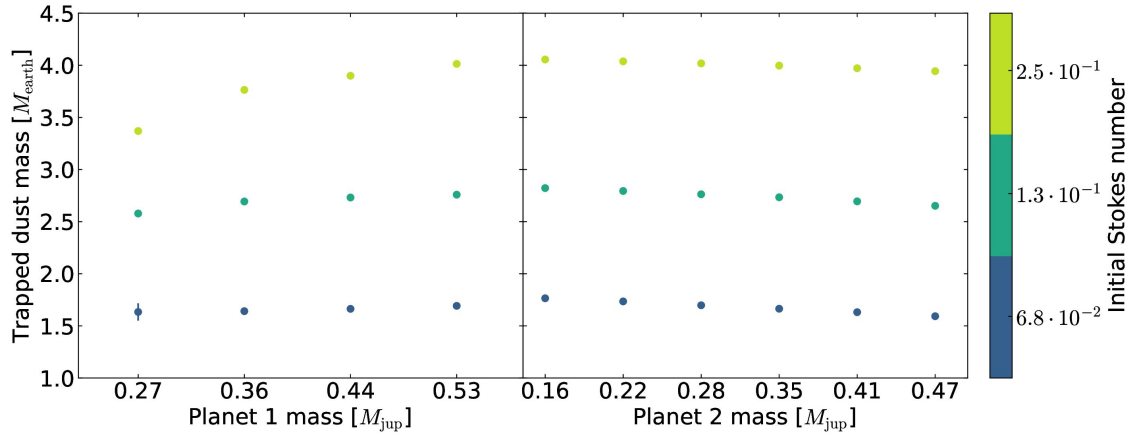


Figure 2.14: Trapped dust masses in earth masses in the L5 feature for the largest three initial Stokes numbers depending on the masses of planet 1 and planet 2, similar to Fig. 2.13.

given in Fig. 2.13 and Fig. 2.14. Generally, if a sufficiently stable crescent-shaped asymmetry develops, the order of magnitude of the trapped dust mass is comparable for all parameters. Here, we only consider the three largest dust species since smaller grains are prone to be weakly trapped.

Only the low-resolution simulations are compared to each other in this parameter study. The mass of the crescent-shaped feature was averaged over 200 orbits starting from $100 T_0$ when convergence is reached. Looking at the aspect ratio dependence, we

find that an increase in H/r also leads to a higher dust mass of the L5 feature. A more massive planet also causes an increase in the trapped dust mass. The lighter the planet, the less stable the agglomeration of dust becomes. As mentioned above, for less than about 0.2 to $0.25 M_{\text{jup}}$ no stable feature forms at L5. Considering the influence of the α viscosity parameter a local value of $\alpha \geq 10^{-3}$ causes a significant loss of dust mass. For $\alpha \geq 2 \cdot 10^{-3}$ no feature develops. Simulation results with a radially constant value of α are used here

Finally, the introduction of an eccentric planetary orbit leads to an almost linear decrease of the trapped dust mass with respect to the eccentricity value. For values ≥ 0.06 no feature forms for dust Stokes numbers of $6.8 \cdot 10^{-2}$ and below.

An increase in the mass of planet 2 has a small influence on the trapped dust mass. The continuous gravitational interaction perturbs the crescent-shaped asymmetry decreases the amount of mass trapped in the feature. The difference between $0.16 M_{\text{jup}}$ and $0.47 M_{\text{jup}}$ however accounts to roughly 5% of trapped dust mass.

Growth time scale

The growth time scale of the planet mass can have a significant impact on the formation of vortices (Hammer et al., 2017, 2019; Hallam & Paardekooper, 2020). Therefore, simulation runs including longer growth time scales with values of $T_G = 10, 50, 100$ and 500 orbits were performed. Qualitatively, the results are mostly unaffected by the choice of T_G . In Fig. 2.13 the masses only deviate about 10 % from the fiducial model. With the longest growth time scale of 500 orbits smaller grains are trapped more efficiently whereas the mass contained in the largest grains decreases slightly. Deviations from the fiducial model for these long growth time scales could also be caused by a loss of dust content and local redistribution of grain sizes due to dust drift in the simulation domain.

Figure 2.15 reveals the temporal evolution of the dust content in the asymmetry around the L5 point for all four growth time scales. For all runs grains smaller than ≈ 1 mm become depleted after more than 1000 orbits of evolution. After initial jumps in dust mass all simulations reach a stable stationary state considering millimeter grain sizes and above.

The formation of vortices is sensitive to the planet growth time scale since the vortex smooths out the gap edge and reduces the steepness of the corresponding edge slope which in turn weakens the Rossby wave instability (Hammer et al., 2017). This effect is important for longer planet growth time scales and leads to weaker, elongated vortices. In the context of dust trapping in the Lagrange points however, the process takes place in the co-orbital region and the amount of mass concentrating in the asymmetries is determined by the initial dust content available within this region (Montesinos et al., 2020). Since the dust trapping here is related to the horseshoe motion in the co-orbital region, it is a different mechanism and the evolution of the gap edge does not seem to have a major influence on the dynamical origin of the asymmetric features.

2.3.6 Synthetic images

The main question remains: whether dust trapping in the L5 point in the models presented could explain the observed feature in HD 163296. We apply the procedure described in Sect. 3.2.5 and thus extend the surface density maps to three dimensional

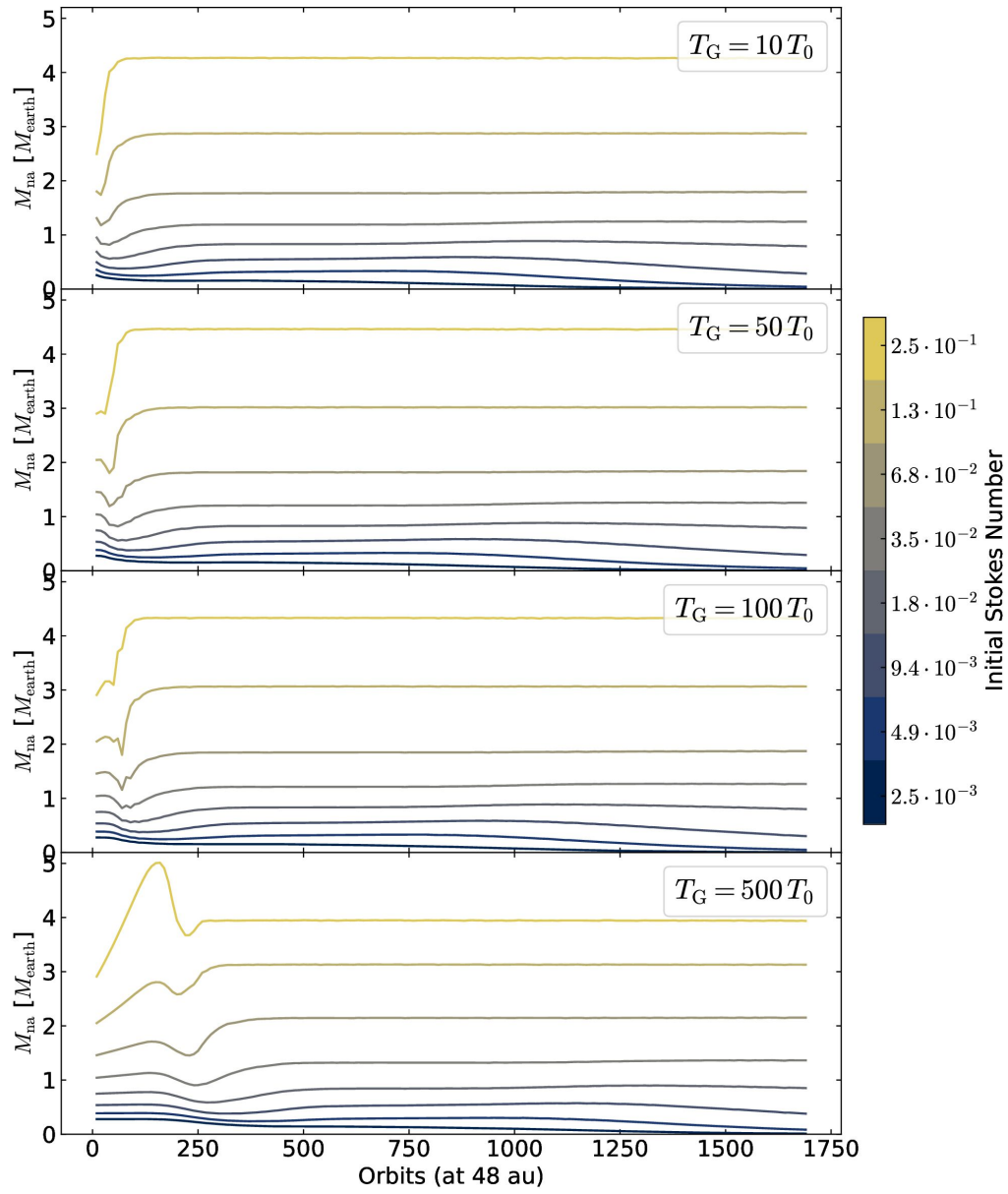


Figure 2.15: Evolution of the trapped dust mass M_{na} in the asymmetry around the L5 point for different planet growth time scales T_G .

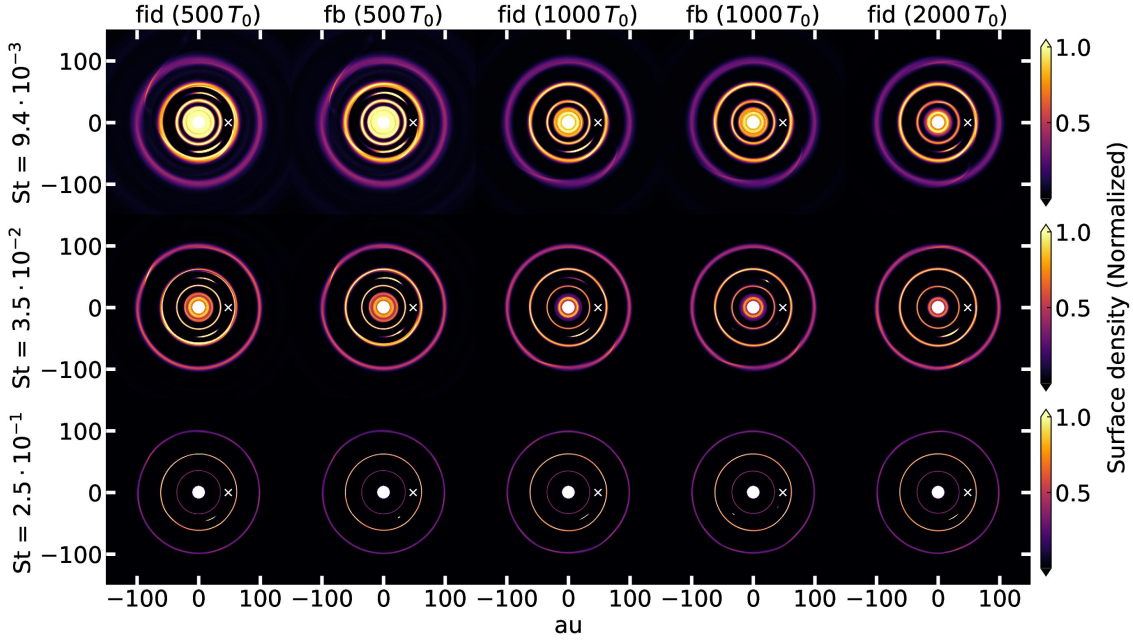


Figure 2.16: Comparison of the dust surface density map for three different dust sizes of the models `fid_dres` (fiducial) and `p1m6fb_dres` (feedback) at different simulation times. The surface densities are normalized to the peak value at ring 1.

grids, then we perform dust radiative transfer calculations RADMC-3D and simulate the observation with ALMA by using the CASA package accordingly. Snapshots of the density maps for these synthetic images are shown in Fig. 2.16. Both the high-resolution fiducial model `fid_dres` and the dust feedback model `p1m6fb_dres` are used.

The resulting dust density grid crucially depends on the vertical dust scale height H_d and thus the dust settling prescription (see Eq. 2.19). With the assumption of constant grain sizes throughout the disk the local Stokes number is used for the calculation of H_d . The grain sizes distribution is the same as the one in the simulation runs. Depending on the low or high mass model, the grain sizes and opacities and densities were adjusted accordingly. We chose to leave α as a free parameter for the vertical dust settling recipe which will be denoted as α_z . In Fig. 2.17 synthetic images from various snapshots of the simulation are compared to the observation. The images qualitatively reproduce the observed features. The key difference with respect to the crescent-shaped feature is the more elongated shape compared to the fiducial model. Furthermore, the models produce a radially symmetrically located feature whereas the observed one is situated closer to ring 1. After 500 and 1000 orbits at 48 au the feature at L4 is still visible due to the slow dissipation at the L4 point. In the image computed from the snapshot at 2000 orbits of the simulation `fid_dres`, only the L5 feature appears, as also seen in Fig. 2.16. As already discussed in Sect. 2.3.5 and Fig. 2.9 a significant amount of dust agglomerates in the L4 region for smaller grain sizes and Stokes numbers. This effect is clearly visible in the synthetic image of `p1m6fb_dres` at 500 orbits with dust feedback enabled in Fig. 2.17. No such feature is present in the observation. The fragmentation of the crescent-shaped asymmetry around L5 becomes more apparent in the later stages of the simulation. After 1000 orbits dust is concentrated in clumps of small azimuthal extent. These features are substantially different from the observation. Since the high mass

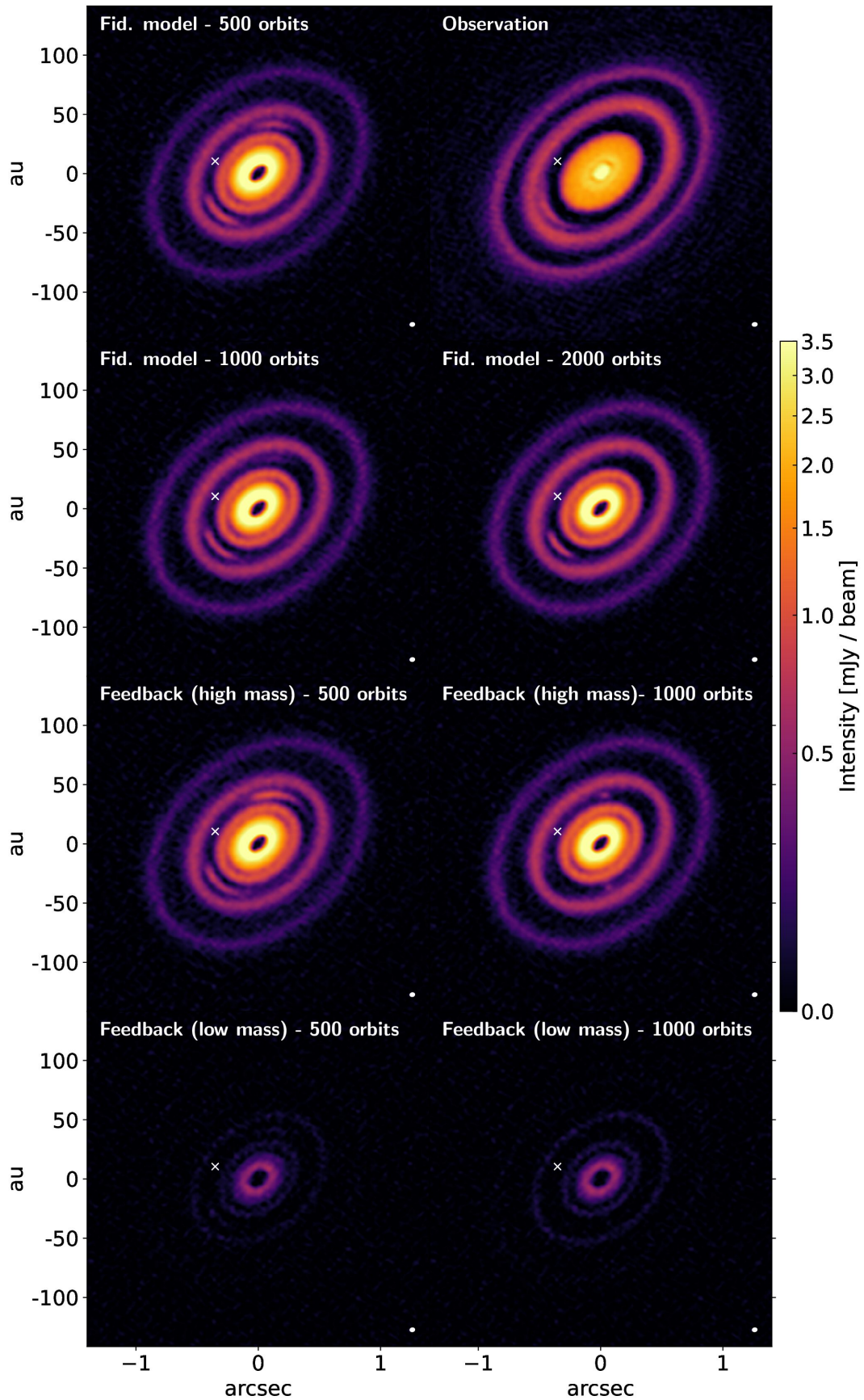


Figure 2.17: Comparison of the synthetic images based on the models `fid_dres` (first and second column), `p1m6fb_dres` (third and fourth column) with the observation taken from Andrews et al. (2018); Isella et al. (2018). The ellipsis at the lower right of each panel visualizes the synthesized beam. The beam size is 49.7×41.4 mas for the synthetic images. The rms noise reaches $\approx 50 \mu\text{as}$. The synthetic images are projected with an inclination of 46.7° and a position angle of 133.33° .

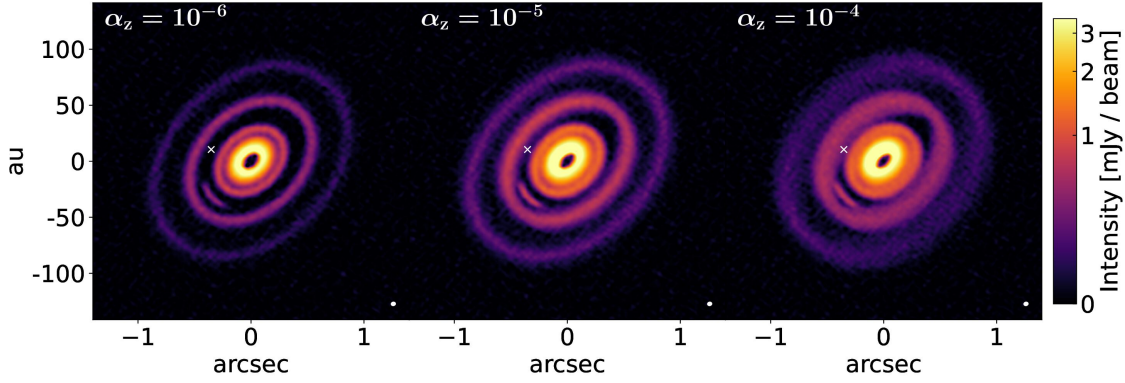


Figure 2.18: Comparison of the synthetic images based on the model `fid_dres` after 2000 orbits at 48 au with respect to the vertical dust mixing parametrized by α_z .

model assumes a lower dust-to-gas ratio, the synthetic images created from the high-mass model and the respective grain size distribution only serve as a comparison of the visibility of such features in the co-orbital region. Additionally, synthetic observations based on the low mass model are shown in Fig. 2.17. As expected, the larger values of the opacity for the grains with the maximum Stokes numbers compared to the high mass model leads to much narrower rings and substructures. The high mass model is thus more suitable for the HD 163296 system.

Focusing on ring 2, the intensity is slightly lower compared to the observations. This result is consistent with Fig. 2.6, where the optical depth of ring 2 does not reach the derived values of Huang et al. (2018a) for smaller grains. In looking at the inner part of the disk within the gap at 48 au, the simulated images show a secondary gap caused by planet 1 that is not present or visible in the observed structure. Furthermore, the influence of vertical mixing of dust grains can be investigated with the three synthetic images in Fig. 2.18 of the nonfeedback model. The model run with an increased dust scale height ($\alpha_z = 10^{-4}$) displays a more diffuse intensity map and a slight decrease in intensity perpendicular to the axis of inclination. A difference in ring thickness depending on the azimuthal location is not visible in the observed system. For the weakest vertical mixing ($\alpha_z = 10^{-6}$) the dust substructures appear completely flat. Ring 2 is much fainter than the observed intensity and ring 1 appears significantly thinner. The model with $\alpha_z = 10^{-5}$ comes closer to the observed ring thickness while having a mostly azimuthally constant ring structure.

Assuming dust trapping in the L5 point of the observation, we can propose potential coordinates for a yet undetected planet. Comparing the results of model `fid_dres` with the ALMA image, the planet offset relative to the disk center is $\delta RA \approx -0.352$ arcsec and $\delta DEC \approx 0.104$ arcsec. This corresponds to the coordinates $RA=17h56m21.2563s$, $DEC=-21d57m22.3795s$. In Fig. 2.19, simulated ALMA observations are shown for planet mass growth time scales ranging from $T_G = 10 T_0$ to $500 T_0$. Ring 2 becomes less massive for longer planet growth time scales since dust drift depletes the outer regions before the planets reach a sufficiently high mass for efficient trapping.

The inner disk structure including the crescent-shaped asymmetry remains unaffected by the choice of parameters.

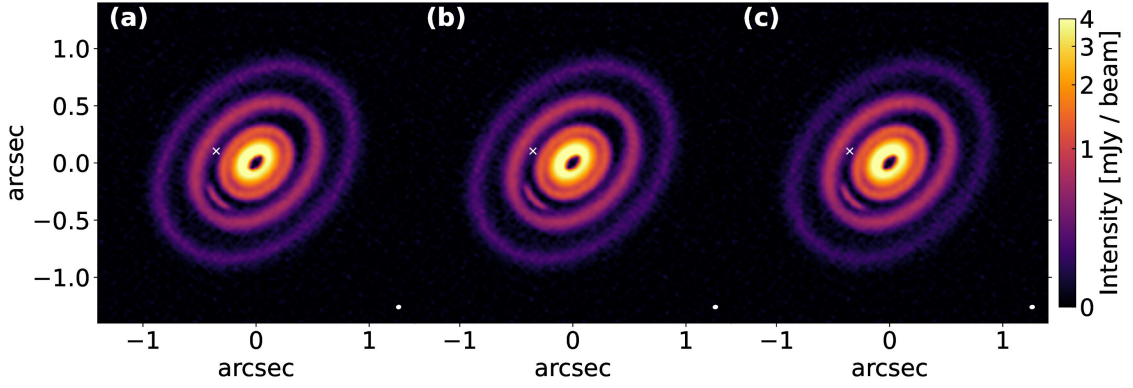


Figure 2.19: Comparison of the synthetic images of different planet growth time scales (a): $T_G = 10 T_0$, (b): $T_G = 100 T_0$, (c): $T_G = 500 T_0$. The snapshots are taken after 2000 orbits at 48 au.

2.4 Resolution study

In the model `fid_dres`, the resolution is doubled to 1120×1790 cells in radial and azimuthal direction respectively compared to model `fid`. Figure 2.20 indicates that an increased resolution leads to a more stable asymmetry in the Lagrange point L5. No decline in mass can be observed in the simulated time frame (1000 orbits at 48 au). The feature in the low-resolution model `fid`, however, depletes rapidly after 600 orbits.

Since the dust trapped in this feature is sensitive to diffusive and disruptive effects, such as viscosity, eccentricity and the passing of the outer planet, the accelerated dispersal may be attributed to numerical diffusion.

Quantifying the absolute value of the numerical diffusion is complex, however the order of magnitude can be estimated by a simple comparison of the high resolution run `alpha3_dres` with $\alpha = 5 \cdot 10^{-4}$ and the fiducial model. As shown in Fig. 2.12, the feature lifetime is approximately comparable to the one of the lower resolution run `fid` with a local $\alpha = 2 \cdot 10^{-4}$. Therefore, the effect of the numerical diffusion in the low resolution model should be approximately equivalent to $\alpha \approx 5 \cdot 10^{-4}$. Since FARGO3D is second-order accurate in space and the error of the dust module has been found to be proportional to a power law with an exponent of -2.2 as a function of the number of grid cells (Benítez-Llambay et al., 2019), the numerical diffusion is expected to be equivalent to $\alpha \approx 1 \cdot 10^{-4}$ in the model `fid_dres`. The resolution is thus sufficient to describe the effect of prescribed local viscosity of $\alpha = 2 \cdot 10^{-4}$.

Nevertheless, the absolute values of the amount of trapped dust mass in the stable phase is not significantly affected by the low resolution effect and lower resolution models are thus acceptable to quantify these values.

2.5 Dust temperatures

In Fig. 2.21 dust temperatures from the radiative transfer calculation of the fiducial model and the prescribed gas temperatures are shown. While gas temperature gradient is smaller than the one for the dust, the temperatures and the slope of both match well at the location of planet 1, the primary region of interest where the crescent-shaped asymmetry forms. For the large grain sizes studied in this paper, a gray body approxi-

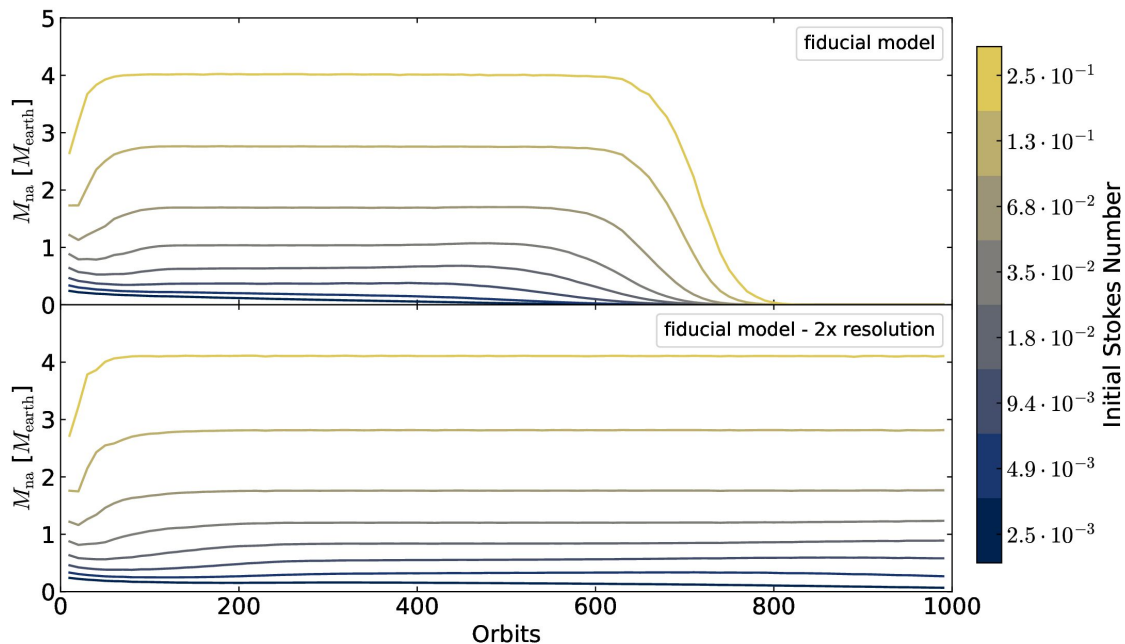


Figure 2.20: Development of the trapped dust mass in the L5 region of the simulations fid and fid_dres over time. In the lower panel, the grid resolution is doubled in both the radial and azimuthal direction. The dispersal of the features are prolonged in the high resolution setup.

mation for the temperature is approximately valid. We thus see no significant increase in temperature comparing the grain sizes to each other.

2.6 Discussion

In the following, we compare our results with previous works on the HD 163296 system and equivalent simulations as well as the limits and caveats of the models presented here.

2.6.1 Comparison to previous works

Upon studying the observed gap widths, Isella et al. (2016) postulated a range of $0.5 M_{\text{jup}}$ to $2 M_{\text{jup}}$ for planet 1 at 48 au, $0.05 M_{\text{jup}}$ to $0.3 M_{\text{jup}}$ for planet 2 at 83 au, and $0.15 M_{\text{jup}}$ to $0.5 M_{\text{jup}}$ for planet 3 at 137 au. With more detailed hydrodynamical models by Liu et al. (2018) using a multi-fluid dust approach the planet masses were constrained to $0.46 M_{\text{jup}}$, $0.46 M_{\text{jup}}$ and $0.58 M_{\text{jup}}$ for the three planets respectively. At this point no asymmetries were observationally resolved.

Among the publication of the DSHARP survey Zhang et al. (2018) performed an extensive parameter study with hydrodynamical planet-disk interaction simulations using a Lagrangian particle dust formalism. Their results indicate planet masses of $0.35 M_{\text{jup}}$, $1.07 M_{\text{jup}}$ and $0.07 M_{\text{jup}}$ if a radially constant α viscosity of 10^{-4} is assumed. The predicted masses of $1 M_{\text{jup}}$ and $1.3 M_{\text{jup}}$ by Teague et al. (2018b) for the two outer planets exceed the hydrodynamical results. However, with the uncertainties of about 50% the planet masses used in the models can be consistent with the kinematical detections.

Our models indicate that for fiducial model parameters, for example an aspect ratio of

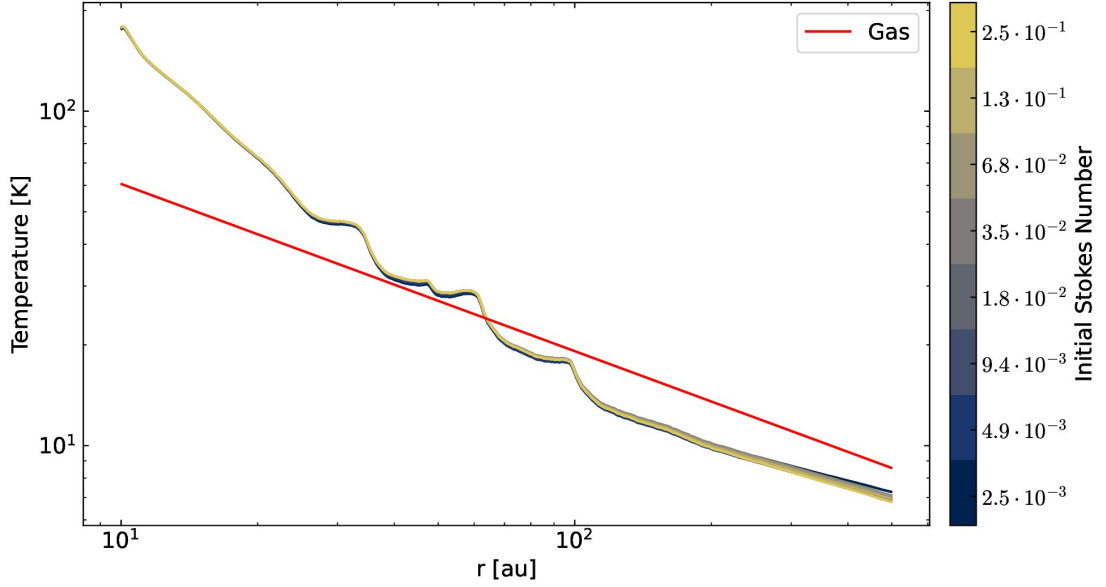


Figure 2.21: Comparison of prescribed gas temperature in the hydrodynamical simulation and the dust temperatures of the thermal Monte-Carlo calculation at the disk mid plane for all grain sizes.

0.05 and a radially increasing α viscosity similar to Liu et al. (2018), a minimum mass of $\approx 0.25 M_{\text{jup}}$ for planet 1 is necessary to produce a stable dust trap in the trailing Lagrange point L5. For higher masses, the amount of dust trapped in the crescent-shaped asymmetry can be slightly decreased (see 2.3.4).

The initial gas surface density at 48 au of $\Sigma_{g,0} = 19.7 \text{g/cm}^2$ for the high mass model assuming a local dust-to-gas mass ratio of $\approx 2.4 \cdot 10^{-3}$ is close to the findings of Zhang et al. (2018) with $\Sigma_{g,0} = 3 - 30 \text{g/cm}^2$. Isella et al. (2016) used a value of $\Sigma_{g,0} = 10 \text{g/cm}^2$. Given the proximity of the crescent-shaped asymmetry and ring 1 in the observations, it is a natural choice to normalize the dust density to the values derived from the optical depth comparison.

Marzari & Scholl (1998) found that if planetesimals are small enough to be affected by the gas drag, the stability of the L4 point is reduced and the density distribution of L4 and L5 becomes asymmetric. A similar effect was observed in the gas by Masset (2002) if viscosity is included. In this case, compared to the gas drag affecting the dust, the viscous gas drag acts as the effect causing the asymmetric gas distribution. Similar results in the context of hydrodynamical simulations, including gas and dust, were found by Lyra et al. (2009). Recently, Montesinos et al. (2020) presented hydrodynamical simulations that include multi-species particle dust and explore the stability of the L4 and L5 in the presence of a massive planet with at least one Jupiter mass. Their findings basically agree with the results presented in this paper without the effect of dust feedback. They state, that L5 captures a larger amount of dust compared to the L4 point. They argue that colder disks allow for more efficient dust trapping in these Lagrange points, lower viscosity leads to a more symmetric distribution of dust in L4 and L5 and dust entering the co-orbital region from the outer part of the disks seems to not significantly contribute to the mass of the clumps in L4 and L5.

Interestingly, the Trojans populating L4 and L5 around Jupiter seem to be more numer-

ous around the L4 point (Yoshida & Nakamura, 2005). In our models this effect only appears if dust feedback plays a significant role in this region.

2.6.2 Model assumptions

Dust opacities are highly sensitive to the relevant material composition and spatial structure. Estimating the surface densities from the optical depth is thus subject to a significant uncertainty. This is amplified by the choice of the dust size distribution and dust size limits. However, the features of interest, such as the crescent-shaped feature and ring 1, match the observations reasonably well with the high mass model, setting $a_{\min} = 0.19$ mm and $a_{\max} = 19$ mm with the MRN size distribution.

The lifetime of the crescent-shaped asymmetry in L5 depends on diffusive processes, such as the turbulent viscosity and mixing of dust grains. In the resolution study (see appendix 2.4) the resulting life time seems not to be limited within the simulated time frame. In lower resolution studies investigated in this paper the numeric diffusion artificially truncates the feature's life time. Even by employing highly resolved simulations, the age estimation of the crescent-shaped feature and, thus, approximately the planet itself would be difficult with the degenerate parameter space. Eccentricity and viscosity both shorten the time scale of dispersal significantly. More detailed studies and observations are necessary to constrain dynamical age of the substructures which need to be performed at higher spacial resolution.

In the observation presented in Isella et al. (2018), the crescent-shaped asymmetry is located at $r = 55$ au instead of $r = 48$ au. No combination of parameters in our models are able to reproduce this effect. An eccentric planet would be an intuitive choice but only leads to a disruption of the crescent-shaped feature. Dust feedback can lead to an unstable feature, ultimately leading to small clumps. In the earlier stages, dust feedback promotes dust trapping in the L4 point. No such effect is seen in the observations. Another explanation of the positioning of the crescent-shaped asymmetry could be planet migration. Depending on the migration direction and speed, the locations of the rings and features in the co-rotation region can be asymmetrically shifted in radial direction (Meru et al., 2019; Pérez et al., 2019; Weber et al., 2019a). Additionally, sudden migration jumps in a system of multiple planets can temporarily create trailing asymmetries with respect to the migrating planet as shown in Rometsch et al. (2020).

It should be noted that dust coagulation and fragmentation is not considered here. More sophisticated models including these effects as shown in Drażkowska et al. (2019) could be used in this case but are computationally demanding.

Ring 2 is slightly fainter in our models compared to the observations. The amount of dust that can be trapped in ring 2 depends on planet 3 since it truncates the dust flow from the outer part of the disk. One hypothesis might be that planet 3 formed later than planet 2 and thus allowed a larger amount of dust to be accumulated in the second ring. As shown in Fig. 2.5 it is furthermore possible to confine the range of permissible values of α by the disappearance of ring 2 for large viscosities ($\alpha > 2 \cdot 10^{-3}$) and low viscosities ($\alpha < 5 \cdot 10^{-4}$) due to vortex activity.

The synthetic images in Fig. 2.17 display an additional gap in the inner dust disk. This secondary is caused by the interaction with the spiral wakes originating from planet 1. The effect is mostly visible for large Stokes numbers and dust sizes as well as high planet masses. However, it is necessary to have a close-to-Jupiter-mass planet is nec-

essary to trap the needed amount of dust in the L5 point to be comparable to the observations. The results of Miranda & Rafikov (2019b) indicate that radiative effects are important, even at large distances of the central star, since locally isothermal models over-pronounce the effect of the spiral wakes and secondary gaps. The same effect was shown to be important for the inner gas disk of HD 163296 in the work of Ziampras et al. (2020). It can be expected that the additional secondary ring in the inner disk disappears when radiative effects are taken into account. Nevertheless, the inner dust disk is not the main aspect of our work and the locally isothermal approach can be considered to be sufficient for modeling the crescent-shaped feature.

The planet growth time scale has only a minor impact on the overall dust substructure emerging in the simulations. Differences are likely caused by the change in dust content and local dust size distribution due to dust drift. Longer growth time scales lead to a lower intensity of ring 2 due to the lack of material that has already drifted inwards before being trapped by the outer planets. The dynamical structure, in particular, the shape and location of the crescent-shaped asymmetry, is basically unaffected within the explored parameter space of growth time scales. The synthetic images that are based on the low-mass model show narrower rings and differ significantly from the observations. Therefore, the high-mass model is favored in this study.

2.7 Conclusion

In this work, we present a parameter study of the crescent-shaped feature of the protoplanetary disk around HD 163296 using multi-fluid hydrodynamical simulations with the FARGO3D code. The model includes eight dust fluids with initial Stokes numbers ranging from $St = 2.5 \cdot 10^{-3}$ to $St = 2.5 \cdot 10^{-1}$ and grain sizes of $a_{\min} = 0.19 \text{ mm}$ and $a_{\max} = 19 \text{ mm}$ for the high-mass model. Additionally, synthetic ALMA observations based on radiative transfer models of the hydrodynamical outputs are presented. Comparing the model with the observation, the results are a qualitative match.

We show that the observation of the crescent-shaped feature puts an important constraint on the disk and planet parameters – always under the assumption that the feature is truly caused by dust accumulation in the planet’s trailing Lagrange point L5. Most importantly, it constrains the level of viscosity and planetary mass. The main findings can be summarized as follows:

1. The observed crescent-shaped asymmetry in the observation (Isella et al., 2018) can be reproduced with a roughly half Jupiter-mass planet in the respective gap location at 48 au. Dust is effectively trapped in the trailing Lagrange point L5. In the case of negligible dust feedback, the L4 point is not sufficiently populated to be observable. The peak of the asymmetric dust density distribution shifts towards the planet location for larger Stokes numbers and grain sizes.
2. Rescaling the dust densities to the observed optical depth of ring 1 at 67 au dust masses of 10 to 15 earth masses can be trapped in a crescent shaped feature located at the L5 point. The trapped dust mass is relatively insensitive to the choice of viscosity, aspect ratio, planet mass, and eccentricity as well as the planet growth timescale.

3. Including the dust back reaction onto the gas can lead to dust trapping, preferably at the leading Lagrange point L4 for initial Stoke numbers of $St \leq 6.8 \cdot 10^{-2}$ as well as, at later stages, to the fragmentation of the crescent-shaped asymmetry near the L5 point.
4. Diffusive and disruptive effects counter the stability of the dust trap in L5. Values of $\alpha \geq 2 \cdot 10^{-3}$ prevent the formation of an asymmetric and stable feature. Introducing eccentricity leads to the same result. The shifted location of the observed crescent-shaped feature at 55 au is not justified by an eccentric planet carving the corresponding gap in the given parameter space.
5. If the L5 feature is caused by an embedded planet, the models allow an estimation of the azimuthal planet position in the gap. The planet offset relative to the disk center is $\delta RA \approx -0.352$ arcsec and $\delta DEC \approx 0.104$ arcsec which corresponds to the coordinates RA=17h56m21.2563s, DEC=-21d57m22.3795s.

We can thus conclude that a combination of $\approx 0.53 M_{\text{jup}}$ and $\approx 0.26 M_{\text{jup}}$ for the inner planets in combination with a MRN dust size distribution with $a_{\text{min}} = 0.19$ mm and $a_{\text{max}} = 19$ mm as well as a local value of $\alpha = 2 \cdot 10^{-4}$ can reproduce the observed crescent-shaped asymmetry and ring structures sufficiently well. The dust-to-gas ratio in the models may be overestimated since none of the features emerging in the simulations that include feedback, for example two crescent-shaped asymmetries and fragmentation, are present in the observation. Additional high-resolution studies are necessary to constrain the parameter space further, also in regard to the long-term stability of the feature.

Dust entrainment in magnetically and thermally driven disk winds

This chapter is based on the paper Rodenkirch & Dullemond (2022), published in *Astronomy & Astrophysics* in 2022. I conducted all of the simulations, analyzed the results, wrote the text and created all figures. In the same manner as in chapter 2 the python tool `simdata` developed by Thomas Rometsch and me was used to load the simulation outputs.

In the following, the mechanism of dust entrainment in disk winds and the detectability by scattered light observations will be investigated. Magnetically driven disk winds serve as a suitable candidate as the primary acceleration mechanism of small dust grains due to their larger wind mass loss rates and wider range of operation at small disk radii.

3.1 Motivation

The vertical transport of dust grains within protoplanetary disks strongly depends on the turbulent motion of the gas in the respective regions. Besides turbulence driven by the MRI alternative mechanisms that can also operate in the weakly ionized parts of the disk. In the presence of short gas cooling times the vertical shear instability (VSI) causes vertical oscillations which are able to transport small dust grains towards the upper layers of the disk (Stoll & Kley, 2014, 2016; Flock et al., 2020; Blanco et al., 2021). Vortices triggered by the VSI in combination with the Rossby wave instability (Lovelace et al., 1999) may act as long-lived dust traps (Manger & Klahr, 2018; Pfeil & Klahr, 2021).

Since recent observation hint towards small viscosity and thus small values of α on the order of 10^{-4} to 10^{-3} (Flaherty et al., 2015, 2017), the effect of disk winds might be a possible explanation for the limited disk lifetimes of a few million years (Mamajek et al., 2004). In the context of photoevaporation, ionizing radiation either from the central star or the from the stellar environment heats the surface layers of the disk and drives winds due to the thermal pressure gradient. Depending on the dominant type of radiation, the wind mass loss rates are on the order of $10^{-10} M_{\odot} \text{ yr}^{-1}$ with EUV radiation (Hollenbach et al., 1994; Font et al., 2004), and $10^{-8} M_{\odot} \text{ yr}^{-1}$ to $10^{-7} M_{\odot} \text{ yr}^{-1}$ with FUV radiation (Adams et al., 2004; Gorti & Hollenbach, 2009) and X-ray radiation (Ercolano et al., 2009; Owen et al., 2010, 2012; Picogna et al., 2019; Ercolano et al., 2021; Picogna et al., 2021).

An alternative way to produce strong disk winds are magnetically driven winds. In

the presence of a global magnetic field the differential shearing motion of the disk generates a magnetic pressure gradient, accelerating matter and thereby driving the outflow. In the strong field limit the gas follows the magnetic field lines and is magnetocentrifugally accelerated, as described in Blandford & Payne (1982). Contrary to photoevaporation, magnetically driven winds extract angular momentum from the disk and drive accretion. The accretion flow has to pass by the mostly vertically aligned magnetic field in the disk which only allows stationary solutions if the coupling between gas and magnetic field is weak, thus if significant diffusive non-ideal MHD effects are present (Wardle & Koenigl, 1993; Ferreira & Pelletier, 1993; Ferreira & Pelletier, 1995).

Dust entrainment in protoplanetary disk winds has been mostly examined in photoevaporative winds. Low gas densities in the wind limit the maximum grain size to a few μm . For EUV-photoevaporation Owen et al. (2011) determined a grain size limit of $\approx 2.2\mu\text{m}$. Hutchison et al. (2016b) performed small scale smoothed particle hydrodynamics simulations of a dusty EUV-driven wind and formulated an analytical expression for the maximum entrainable dust grain size. They conclude that typically the limiting size is less than $4\mu\text{m}$ for typical T Tauri stars and they also argue that dust settling may lower this limit further. Franz et al. (2020) simulated dust entrainment in post-processed XEUV-wind flows of Picogna et al. (2019) and found a larger maximum dust size of $11\mu\text{m}$. Dust entrainment in magnetically driven winds was tested by vertical 1D models in the work of Miyake et al. (2016), concluding that grains in the range of $25\mu\text{m}$ to $45\mu\text{m}$ can float up to 4 gas scale heights above the disk mid plane. Gicalone et al. (2019) used a semi-analytical MHD-wind description to compute the dust transport and report a maximum dust size of $1\mu\text{m}$. Considering the effect of radiation pressure, sub-micron dust grains can be blown away from the disk and support clearing out remaining dust (Owen & Kollmeier, 2019).

In this paper we present fully dynamic, multi-fluid, global, azimuthally symmetric, non-ideal MHD simulations of protoplanetary disk winds including XEUV-heating to model photoevaporative flows. We aim to study dust entrainment in magnetically and thermally driven disk winds in a dynamic fashion that also considers the vertical dust distribution due to turbulent diffusion of dust grains. We thus extend the previous study in Rodenkirch et al. (2020) by including dust as a pressureless fluid. We furthermore post-process the dust density maps to examine observational signatures of such dusty winds.

In Sec. 3.2 we describe the theoretical and computational concepts of the model. The results are presented in Sec. 3.3 and Sec. 3.4 discusses limitations of the model as well as the comparison to other studies. Finally, in Sec. 3.5 we give concluding remarks.

3.2 Model

The simulations are carried out with the FARGO3D code Benitez-Llambay & Masset (2016); Benitez-Llambay et al. (2019) in a 2.5D axisymmetric setup using a spherical mesh with the coordinates (R, θ, φ) . Throughout this work the cylindrical radius will be referred to as r , whereas the spherical radius will be denoted as $R = \sqrt{r^2 + z^2}$.

Label	β_0	α	X-ray heating	r_c	ϵ_{ion}	Resolution	Simulation time
b5c2	10^5	10^{-4}	✓	2	10^3	500 x 276	2000 orbits
b4c2	10^4	10^{-4}	✓	2	10^3	500 x 276	2000 orbits
b4c2np	10^4	10^{-4}	✗	2	10^3	500 x 276	1000 orbits
b4c2a3	10^4	10^{-3}	✓	2	10^3	500 x 276	1000 orbits
b4c2eps2	10^4	10^{-3}	✓	2	10^2	500 x 276	1000 orbits
phc2	[n/a]	10^{-4}	✓	2	10^3	500 x 276	2000 orbits
phc10	[n/a]	10^{-4}	✓	10	10^3	500 x 276	2000 orbits

Table 3.1: Simulations and key parameters. The numerical resolution is given in number of cells in radial and polar direction. The simulation time is measured in units of orbits at the inner radius r_{in} .

3.2.1 Basic equations

In this model, the FARGO3D code solves the following set of equations

$$\partial_t \rho_g + \nabla \cdot (\rho_g \mathbf{v}_g) = 0, \quad (3.1)$$

$$\rho_g (\partial_t \mathbf{v}_g + \mathbf{v}_g \cdot \nabla \mathbf{v}_g) = -\nabla P + \nabla \cdot \mathbf{\Pi} - \rho_g \nabla \Phi \quad (3.2)$$

$$+ \frac{1}{4\pi} (\nabla \times \mathbf{B}) \times \mathbf{B}, \quad (3.3)$$

$$\partial_t \rho_{d,i} + \nabla \cdot (\rho_{d,i} \mathbf{v}_{d,i} + \mathbf{j}_i) = 0, \quad (3.4)$$

$$\rho_{d,i} [\partial_t \mathbf{v}_{d,i} + (\mathbf{v}_{d,i} \cdot \nabla) \mathbf{v}_{d,i}] = -\rho_{d,i} \nabla \Phi + \sum_i \rho_i f_i, \quad (3.5)$$

where Eqs. 3.1 and 3.4 describe the mass conservation of gas and dust with ρ_g and $\rho_{d,i}$ being the gas and dust density, respectively. The suffix i denotes the corresponding dust species. Eqs. 3.2 and 3.5 represent the momentum equations of gas and dust. Note that we do not consider the dust backreaction onto the gas in Eq. 3.2 since the dust-to-gas mass ratio is assumed to be low. The symbol P refers to the thermal gas pressure, \mathbf{B} the magnetic flux density vector, \mathbf{v} the velocity vectors, $\Phi = -\frac{GM_*}{R}$ the gravitational potential and f_i the drag forces between dust and gas.

To mimic the vertical transport in the disk that could be driven by the activity of the VSI, turbulent mixing of dust grains caused by the underlying turbulent viscosity in the gas is considered by using the diffusion flux \mathbf{j}_i , equivalent to the models described in chapter 2. The key difference here, is that the expression for the Stokes number using the integrated surface density of the gas and a locally isothermal equation of state is not applicable in the case of heated winds. We thus express the dimensionless Stokes number in terms of the stopping time t_s and the thermal velocity of the gas as follows:

$$\text{St} = \Omega_K t_s = \Omega_K \frac{\rho_{\text{mat}} a_i}{\rho_g v_{\text{th}}}, \quad (3.6)$$

with the Keplerian angular frequency $\Omega_K = \sqrt{GM_*/r^3}$, the material density of the dust grain ρ_{mat} and the mean thermal velocity of the gas:

$$v_{\text{th}} = \sqrt{\frac{8k_B T_g}{\mu m_p \pi}}. \quad (3.7)$$

The Boltzmann constant is expressed as k_B , the gas temperature as T , the mean molecular weight as μ and the proton mass as m_p . With increasing gas temperatures the

Stokes number is hence becoming smaller and dust grains are expected to couple more strongly to the gas motion. The energy equation can be stated as

$$\frac{\partial e}{\partial t} + \nabla \cdot (e\mathbf{v}) = -P \nabla \cdot \mathbf{v} \quad (3.8)$$

The adiabatic equation of state is given by

$$P = (\gamma - 1)e \quad (3.9)$$

where $\gamma = 5/3$ is the adiabatic index. The induction equation including ohmic and ambipolar diffusion reads as follows (Béthune et al., 2017):

$$\frac{\partial \mathbf{B}}{\partial t} - \nabla \times \left(\mathbf{v} \times \mathbf{B} - \frac{4\pi}{c} \eta_{\text{ohm}} \cdot \mathbf{J} + \eta_{\text{am}} \cdot \mathbf{J} \times \mathbf{b} \times \mathbf{b} \right) = 0 \quad (3.10)$$

where $\mathbf{b} = \mathbf{B}/|\mathbf{B}|$ the normalized magnetic field vector, \mathbf{J} the electric current density vector, η_{ohm} the ohmic diffusion coefficient and η_{am} the ambipolar diffusion coefficient.

3.2.2 Disk model

Initial conditions of the gas in the disk

The vertically integrated surface density profile $\Sigma(r)$ is assumed to be a power law $\Sigma(r) = \Sigma_0 r^{-p}$ and the volumetric gas density takes the form

$$\rho_g(r, z) = \frac{\Sigma_0}{\sqrt{2\pi}H} \exp \left[\frac{1}{h^2} \left(\frac{r}{\sqrt{r^2 + z^2}} - 1 \right) \right] \quad (3.11)$$

where $h = H/r$ is the local aspect ratio and $H = c_s/\Omega_K$ the gas scale height with the local isothermal sound speed $c_s = \sqrt{k_B T(r)/(\mu m_p)}$.

In a simple a simple blackbody disk being irradiated by stellar light with a grazing angle ϕ onto its surface, the temperature scales with radius as (Chiang & Goldreich, 1997)

$$T_g(r) = \left(\frac{\phi}{2} \right)^{\frac{1}{4}} \left(\frac{R_*}{r} \right)^{\frac{1}{2}} T_* = \left(\frac{\phi L_*}{8\pi r^2 \sigma_{\text{SB}}} \right)^{1/4} \quad (3.12)$$

where R_* , T_* and L_* are the stellar radius, temperature and luminosity, respectively. The Stefan-Boltzmann constant is denoted by σ_{SB} . Thus we assume a radial power law profile for the temperature with $T(r) = T_0 r^{-q}$ and the gas scale height scales with radius as $H(r) \propto \sqrt{T(r)} \propto r^{(3-q)/2}$.

Within a certain cutoff radius r_c we set the density to zero with a sharp transition and we thus mimic a disk with an inner cavity of size r_c . The sharp transition quickly softens and relaxes to the shape of a smooth inner rim during the simulation run after a few orbits. The cavity in the model is applied for both gas and dust.

The initial values of the azimuthal gas velocity are slightly sub-Keplerian (Nelson et al., 2013):

$$v_\phi(r, z) = \Omega_K r \sqrt{h^2(p+q) + (q+1) - \frac{qr}{\sqrt{r^2 + z^2}}} \quad (3.13)$$

We assume no initial velocities in the radial and polar direction, i.e. $v_r = v_\theta = 0$.

Coronal Gas Structure

The hydrostatically stable coronal gas structure with density $\rho_c(R)$ and pressure $P_c(R)$ serves as a density floor throughout the simulation and prevents excessively low initial densities which prevents numerical instabilities. One of the main factors for these issues is the Alfvén velocity v_A , since $v_A \propto 1/\sqrt{\rho_g}$ becomes large and thereby severely limits the simulation time step. We use the same prescription as used in the previous models in Rodenkirch et al. (2020) based on Sheikhezami et al. (2012).

The density is set to

$$\rho_c(R) = \rho_{c0}(r_i) \left(\frac{r_i}{R}\right)^{\frac{1}{\gamma-1}} \quad (3.14)$$

where r_i is the radius at the inner boundary of the simulation domain and γ the adiabatic index. The corresponding pressure profile is given by:

$$P_c(R) = \rho_{c0}(r_i) \frac{\gamma-1}{\gamma} \frac{GM_\odot}{r_i} \left(\frac{r_i}{R}\right)^{\frac{\gamma}{\gamma-1}} \quad (3.15)$$

The density at the inner boundary $\rho_{c0}(r_i)$ is related to the disk's density at the mid plane and r_i with the density contrast $\delta = \rho_{c0}(r_i) / \left[\Sigma(r_i) / \left(\sqrt{2\pi}H\right)\right]$. Depending on Σ_0 we set the density contrast to values ranging from $\delta = 10^{-7}$ to $5 \cdot 10^{-7}$. In absence of X-ray / EUV heating the gas temperature is directly set to the coronal temperature.

Dust structure

Vertical dust settling towards the mid plane becomes more effective in the upper layers of the disk and the overall vertical thickness of the dust layer is over-estimated in models of a dust scale height uniquely depending on mid plane values as in Dubrulle et al. (1995) (Dullemond & Dominik, 2004). We therefore use the following vertical dust distribution

$$\rho_d(r, z) = \epsilon_{dg} \rho(r, z) \left\{ \frac{\text{St}(r, z=0)}{\alpha} \left[\exp\left(\frac{z^2}{2H^2}\right) - 1 \right] - \frac{z^2}{2H^2} \right\} \quad (3.16)$$

given in Fromang & Nelson (2009). The dust-to-gas mass ratio of the dust fluids is denoted by ϵ_{dg} and the dimensionless diffusion coefficient follows the α -viscosity prescription $\nu = \alpha c_s H$ (Shakura & Sunyaev, 1973) with the kinematic viscosity ν . We assume a constant value for the Schmidt number $\text{Sc} = 1$.

The initial azimuthal velocities are set to $v_{d,\phi} = \Omega_K \sqrt{r^2 + z^2}$. Similar to the gas the initial radial and polar velocities of the dust fluids are set to zero.

Ionization rate

In all of the following models X-ray radiation is considered including both a radial and scattered component. The parametrization is based on the prescription of Igea & Glassgold (1999) and Bai & Goodman (2009):

$$\begin{aligned} \zeta_X = & \zeta_{X,\text{sca}} \left[\exp\left(-\frac{\Sigma_{\text{top}}}{\Sigma_1}\right)^{0.65} + \exp\left(-\frac{\Sigma_{\text{bot}}}{\Sigma_1}\right)^{0.65} \right] \left(\frac{R}{\text{au}}\right)^{-2} \\ & + \zeta_{X,\text{rad}} \exp\left(\frac{\Sigma_{\text{rad}}}{\Sigma_2}\right)^{0.4} \left(\frac{R}{\text{au}}\right)^{-2} \end{aligned} \quad (3.17)$$

Both coefficients are multiplied by a factor of 20 compared to the cited values to model a fiducial X-ray luminosity of $L_X = 2 \times 10^{30} \text{ erg s}^{-1}$ and are set to $\zeta_{X,\text{rad}} = 1.2 \times 10^{-10} \text{ s}^{-1}$ and $\zeta_{X,\text{sca}} = 2 \times 10^{-14} \text{ s}^{-1}$. The critical column densities account to $\Sigma_1 = 7 \times 10^{23} \text{ cm}^{-2}$ and $\Sigma_2 = 1.5 \times 10^{21} \text{ cm}^{-2}$.

Additionally, cosmic rays are modeled by the parametrization of Umebayashi & Nakano (2009) where a characteristic column density of 96 g cm^{-2} was chosen. The symbols Σ_{bot} and Σ_{top} refer to the column densities integrated along the polar direction, starting from the lower boundary (suffix *bot*) and the upper boundary (suffix *top*). The radial column densities Σ_{rad} are computed starting from the radial inner boundary.

$$\zeta_{\text{cr}} = 5 \times 10^{-18} \text{ s}^{-1} \exp\left(-\frac{\Sigma_{\text{top}}}{\Sigma_{\text{cr}}}\right) \left[1 + \left(\frac{\Sigma_{\text{top}}}{\Sigma_{\text{cr}}}\right)^{3/4}\right]^{-4/3} \quad (3.18)$$

$$+ \exp\left(-\frac{\Sigma_{\text{bot}}}{\Sigma_{\text{cr}}}\right) \left[1 + \left(\frac{\Sigma_{\text{bot}}}{\Sigma_{\text{cr}}}\right)^{3/4}\right]^{-4/3}$$

To account for short-lived radio nuclides in the disk, an ionization rate of $\zeta_{\text{nuc}} = 7 \times 10^{-19} \text{ s}^{-1}$ caused by the ^{26}Al isotope (Umebayashi & Nakano, 2009) acts as an ionization rate floor value. The resulting total ionization rate then simply sums up to $\zeta = \zeta_X + \zeta_{\text{cr}} + \zeta_{\text{nuc}}$.

Ionization fraction

The coupling of the magnetic field to the underlying gaseous medium is intricately linked to the ionization chemistry of the disk. Not only the different gas species in the atmosphere but also the grain size, structure and abundance play an important role in the ionization balance, since grains are able to adsorb free electrons from the environment onto their surface (Ilgner & Nelson (2006)).

A widely used and simplified model was introduced by Oppenheimer & Dalgarno (1974), consisting of kinetic reactions including a light molecular species and a heavy ion species. In the limit of negligible effects of the heavy ion species the ionization fraction x_e can be analytically approximated as:

$$x_e = \sqrt{\frac{\zeta}{\tilde{\alpha}n}}, \quad (3.19)$$

where ζ is the total ionization rate, $\tilde{\alpha}$ the dissociative recombination rate coefficient and n the neutral number density of the molecular species (Oppenheimer & Dalgarno, 1974; Ilgner & Nelson, 2006). Incorporating the effects of dust or additional volatile species in the reaction scheme renders an analytical solution impossible and would result in a computationally challenging problem in the context of magneto-hydrodynamical simulations. A semi-analytical solution for fractal dust aggregates was elaborated by Okuzumi (2009). The main assumption here is an approximatively Gaussian charge distribution in the dust grains. This approximation is reasonably well fulfilled if the dust aggregate consists of at least 400 monomers (Dzyurkevich et al., 2013). In this approach, the ionization equilibrium is described by the following equations (Okuzumi, 2009):

$$\frac{1}{1 + \Gamma} - \left[\frac{s_i u_i}{s_e u_e} \exp(\Gamma) + \frac{1}{\Theta} \frac{\Gamma g(\Gamma)}{\sqrt{1 + 2g(\Gamma)} - 1} \right] = 0 \quad (3.20)$$

with the parameter Θ :

$$\Theta = \frac{\zeta n_g e^2}{s_i u_i \bar{\sigma} \bar{a} n_d^2 k_B T} \quad (3.21)$$

The function $g(\Gamma)$ is evaluated as:

$$g(\Gamma) = \frac{2\tilde{\alpha}\zeta n_g}{s_i u_i s_e u_e (\bar{\sigma} n_d)^2} \frac{\exp(\Gamma)}{1 + \Gamma} \quad (3.22)$$

After solving Eq. 3.20 numerically for Γ with a simple Newton-Raphson scheme, finally the ion and electron densities n_i and n_e can be calculated:

$$n_i = \frac{\zeta n_g}{s_i u_i \bar{\sigma} n_d} \frac{\sqrt{1 + 2g(\Gamma)} - 1}{(1 + \Gamma)g(\Gamma)} \quad (3.23)$$

$$n_e = \frac{\zeta n_g}{s_e u_e \bar{\sigma} n_d} \frac{\sqrt{1 + 2g(\Gamma)} - 1}{\exp(-\Gamma)g(\Gamma)} \quad (3.24)$$

The sticking coefficients s_i and s_e are set to 1 and 0.3 respectively, as described in Okuzumi (2009). The thermal ion and electron velocities $u_{i,e}$ follow:

$$u_{i,e} = \sqrt{\frac{8k_B T}{\pi m_{i,e}}} \quad (3.25)$$

where m_e describes the electron mass and the ion mass is set to $m_i = 24 m_p$, corresponding to magnesium.

With the assumption of fractal dust aggregate with a dimension of $D = 2$, the dust aggregate size becomes $\tilde{a} = a_0 N^{1/2}$ with the number of monomers N of size a_0 . Similarly, the geometric cross section $\bar{\sigma}$ of these aggregates can be expressed as $\bar{\sigma} \approx \pi a_0^2 N$. The dust number density n_d can be calculated as $n_d = \epsilon_{\text{ion}} n_g / (\frac{4\pi}{3} a_0^3 N)$ with the dust-to-gas ratio ϵ_{ion} used in the ionization model.

In the limit of a vanishing dust-to-gas mass ratio the ionization fraction x_e approaches

$$x_e = \frac{n_e}{n_g} = \sqrt{\frac{\zeta}{\tilde{\alpha} n}}, \quad (3.26)$$

where ζ is the total ionization rate, $\tilde{\alpha} = 3 \times 10^{-6} \text{ cm}^3 \text{ s}^{-1} / \sqrt{T}$ the dissociative recombination rate coefficient and n the neutral number density of the molecular species (Oppenheimer & Dalgarno, 1974; Ilgner & Nelson, 2006).

In Fig. 3.1 the results of the implementation are shown. The parameters are the same as the ones of the fiducial model in Okuzumi (2009). In the limit of a large number of monomers in the dust aggregate Γ approaches ≈ 2.8 , equal to the result of Okuzumi (2009). The ion and electron ionization fraction in the right panel of Fig. 3.1 are consistent with the fiducial model. As expected, both ionization fractions adopt the same value in the limit of $N \rightarrow \infty$.

In the same manner as described in Bai (2017b) we increase the ionization fraction in the wind region as a proxy for the effect of FUV-radiation:

$$x_{\text{fuv}} = 2 \cdot 10^{-5} \exp \left[- \left(\frac{\Sigma_{\text{rad}}}{\Sigma_{\text{fuv}}} \right)^4 + \frac{0.3 \Sigma_{\text{fuv}}}{\Sigma_{\text{rad}} + 0.03 \Sigma_{\text{fuv}}} \right]. \quad (3.27)$$

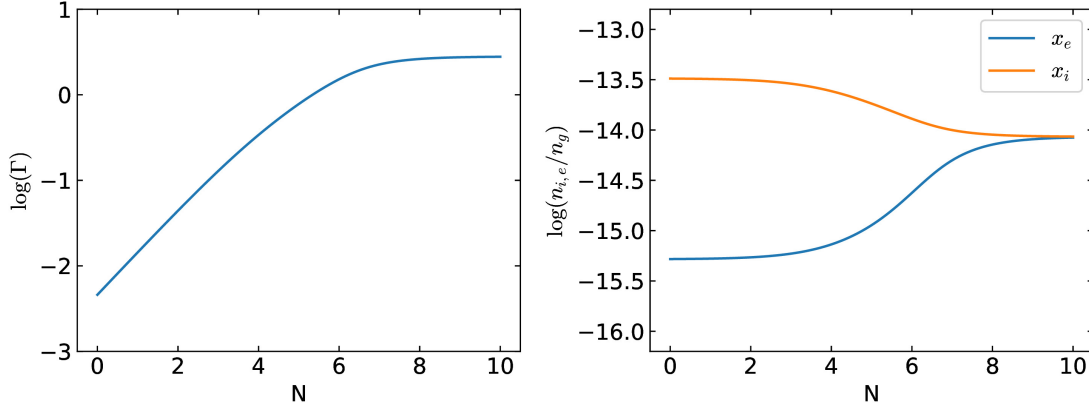


Figure 3.1: Numerical test results of the ionization model based on Okuzumi (2009). The left panel shows the logarithm of the parameter Γ versus the logarithm of the number of monomers N in the dust aggragate and the right panel displays the results of the electron and ion fraction x_e, x_i versus the logarithm of the number of monomers N .

Magnetic field profile

The magnetic field is set such that the initial plasma beta β at the mid plane is independent of the radius r . The poloidal field is initialized from the vector potential A_ϕ

$$A_\phi(r, \theta) = \sqrt{\frac{8\pi P}{\beta}} \left(\frac{r}{r_0}\right)^{\frac{2p+q+1}{4}} \left[1 + m \cdot \tan(\theta)^{-2}\right]^{-\frac{1}{\sigma_0^5}} \quad (3.28)$$

described in Bai (2017b) and exhibits an outward-bent, hourglass shape depending on the parameter m where $m = 0$ would correspond to a completely vertical field. In order to avoid excessively small time steps in the low density regions close to the rotation axis we limit the local Alfvén velocity $v_A = B / \sqrt{4\pi\rho_g}$ to $18v_K(r_0)$ by increasing the density in the cell accordingly, similar to Riols & Lesur (2018). This procedure does not affect the bulk of the wind flow. The radial power law exponent of the vector potential assures that the value of the plasma beta is independent of the radius at the initial state of the simulation.

Non-ideal MHD coefficients

Using the electron fraction x_e the local ohmic diffusion coefficient η_{ohm} can be written as (Blaes & Balbus, 1994):

$$\eta_{\text{ohm}} = \frac{c^2 m_n m_e \langle \sigma v \rangle_e}{4\pi e^2 x_e} \approx \frac{234 T^{\frac{1}{2}} \text{ cm}^3}{x_e \text{ s}}, \quad (3.29)$$

where m_n and m_e are the neutral and electron mass respectively. The electron-neutral collision frequency was set to $\langle \sigma v \rangle_e = 8.28 \cdot 10^{-10} T^{-1/2} \text{ cm}^3 \text{ s}^{-1}$ (Draine et al., 1983). The ambipolar diffusion coefficient η_{am} becomes:

$$\eta_{\text{am}} = \frac{B^2}{4\pi \langle \sigma v \rangle_i n_g^2 x_i}. \quad (3.30)$$

The ion-neutral collision rate is set to $\langle \sigma v \rangle_i = 1.9 \cdot 10^{-9} \text{ cm}^3 \text{ s}^{-1}$ (Draine et al., 1983). Since large diffusivities severely limited the simulation time step a super time stepping

scheme was implemented and more details are given in Sec. 3.2.3. We furthermore limit the magnetic Reynolds number for ambipolar diffusion $Rm = c_s H / \eta_{\text{am}}$ to $Rm \geq 0.05$, similar to Gressel et al. (2015), confirming that this approximation does not significantly alter the simulation outcome.

3.2.3 Super time stepping

In a diffusion-dominated parabolic problem the time step used to advance the solution has to fulfill the stability criterion:

$$\Delta t < \frac{\Delta x^2}{D}, \quad (3.31)$$

where Δx is the grid cell size and D the diffusion coefficient. The CFL-condition for solving explicit hyperbolic PDEs numerically only linearly depends on the grid cell size:

$$\Delta t = C \frac{\Delta x}{u}. \quad (3.32)$$

C is the dimensionless Courant number and u a characteristic flow velocity. Compared to the CFL-condition the diffusion-limited time step scales quadratically with the grid cell sizes and thus slows down the computation significantly if the diffusion coefficient becomes comparatively large.

In the context of simulations of magnetically driven winds large diffusivities appear in weakly-ionized region of the disk where η_{ohm} and / or η_{am} lead to significant diffusive effects. A relatively cost efficient method to increase the time step without losing stability is the Super Time-Stepping technique (STS) for parabolic or mixed advection-diffusion problems. Introduced by Alexiades et al. (1996), the first-order method divides one explicit super step ΔT in multiple sub-steps $\tau_1, \tau_2, \dots, \tau_N$. The algorithm ensures stability while maximizing $\Delta T = \sum_i^N \tau_i$. The optimized length of each sub-step is based on Chebyshev polynomials:

$$\tau_j = \Delta t_{\text{exp}} \left[(\nu - 1) \cos \left(\frac{2j - 1}{N} \frac{\pi}{2} \right) + \nu + 1 \right], \quad (3.33)$$

where Δt_{exp} is the explicit time step constrained by Eq. 3.31. The sum of all sub-steps then gives:

$$\Delta T = \Delta t_{\text{exp}} \frac{N}{2\sqrt{\nu}} \left[\frac{(1 + \sqrt{\nu})^{2N} - (1 - \sqrt{\nu})^{2N}}{(1 + \sqrt{\nu})^{2N} + (1 - \sqrt{\nu})^{2N}} \right]. \quad (3.34)$$

The parameter ν adopts values between 0 and 1. In the limit of $\nu \rightarrow 0$ the method is N times faster than the explicit integration. Lower values of ν however can lead to oscillations and eventually to an unstable solution. Limiting the number of sub-steps N to a maximum of 12 seems to be a good trade off between accuracy and performance Simon et al. (2013).

In FARGO3D the magnetic field is updated with the method of characteristics and constrained transport (MOCCT) Hawley & Stone (1995) whereby the constrained transport method described in Evans & Hawley (1988) is used Benitez-Llambay & Masset (2016). In this method the evolution of the magnetic field is determined by computing the electromotive forces (EMFs) Benitez-Llambay & Masset (2016):

$$\mathcal{E} = \mathbf{v} \times \mathbf{B} \quad (3.35)$$

Two implementations of the super time stepping technique will be compared in the following analysis. The first option is to incorporate STS with an operator splitting approach, introduced in Sec. 2.2.1 in chapter 2. In this approach the magnetic field is updated only considering the non-ideal MHD terms, i.e. ohmic and ambipolar diffusion. Taking this updated magnetic field as an input for the subsequent steps in FARGO3D, an operator splitting technique is employed.

A different method is computing the contribution to the total EMFs of each sub-step j with duration τ_j . Instead of updating the magnetic field during the STS step and the result is added to the EMFs, weighted by a factor of $\tau_j/\Delta T$. The magnetic field updates at every sub-step are only applied on a temporary buffer field. The main B-field is then updated with the total EMFs, containing contributions from non-ideal terms and the ordinary MHD dynamics.

In order to test the correctness of the implementation, a decaying standing Alfvén wave test for ambipolar diffusion as described in Choi et al. (2009) Sec. 4.2 is used. The time dependence of the first normal mode is given by Choi et al. (2009):

$$h(t) = h_0 \sin(\omega_R t) e^{\omega_I t} \quad (3.36)$$

with $\omega = \omega_R + i\omega_I$. The terms ω_R and ω_I are the real and imaginary parts of the angular frequency of the Alfvén wave. The dispersion relation is given by Choi et al. (2009):

$$\omega^2 + i \frac{c_A^2 k^2}{\langle \sigma v \rangle_i n_i} \omega + c_A^2 k^2 \quad (3.37)$$

where k is the real wavenumber and c_A the characteristic Alfvén speed.

In the test according to Choi et al. (2009) the magnetic field is set to $\mathbf{B} = B_0 \hat{x}$ with $B_0 = 1$. The density is uniformly set to 1. The wave is initialized in the \hat{x} direction with an initial velocity of:

$$v_y = v_0 c_A \sin(kx) \quad (3.38)$$

The amplitude of the perturbation is set to $v_0 = 0.1$, the characteristic Alfvén velocity to $1/\sqrt{2}$, the ion density to $\rho_i = 0.1$ and the wavenumber to $k = 2\pi/L$ where $L = 1$ is the domain size. The collision rate coefficient $\langle \sigma v \rangle_i$ is varied from 100 to 1000. Instead of an oblique wave test, the simulations are run in a one-dimensional configuration. With this set of parameters, results can be compared to the ones obtained by Choi et al. (2009).

In Fig. 3.2 and Fig. 3.3 the test results are shown. The numerical results fit the analytical solution well. Especially visible in Fig. 3.2, the operator splitting approach is less accurate compared to the weighted EMF method. Stability was found to be fulfilled up to five sub-steps. An additional loss of accuracy is to be expected when operator splitting is used and an overall loss of accuracy in comparison to the solution without STS is also anticipated since this approach is only first-order accurate. It should be noted that a deviation from the analytical solution in Fig 3.3 is also visible in the equivalent plot in Choi et al. (2009).

Heating and cooling

We employ the same temperature prescription as described in Rodenkirch et al. (2020) based on Picogna et al. (2019) to mimic the outflow due to photoevaporation in the simulation runs modeling a warm (magneto-) photoevaporative wind. According to

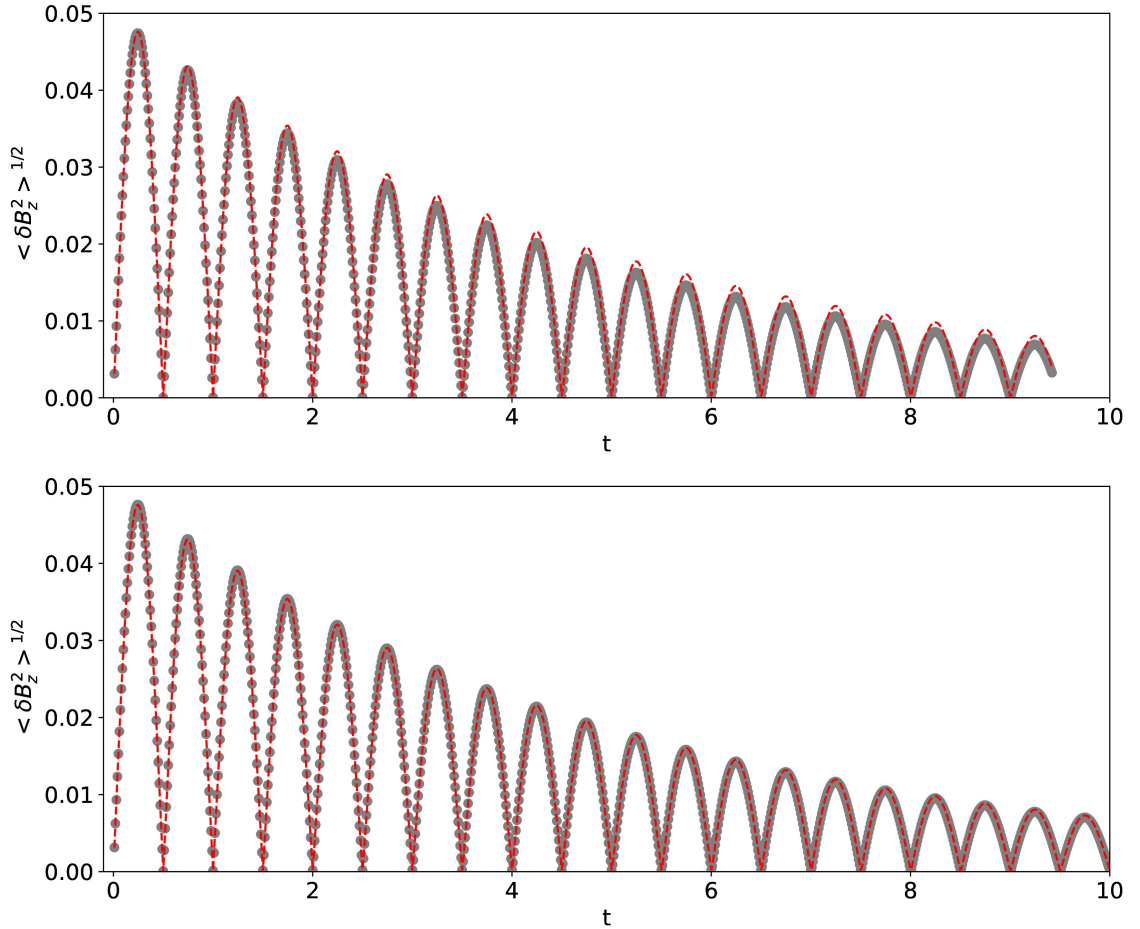


Figure 3.2: Decaying Alfvén wave test for $\langle \sigma v \rangle_i = 1000$. The top panel shows the r.m.s. magnetic field component with the operator splitting approach. The results in the bottom panel were created with the weighted EMF method. Dots correspond to the simulation results whereas the dashed line is the analytical solution.

their model, X-ray / EUV-heating is significant up to radial column densities of $\Sigma_{r,\text{crit}} = 2.5 \times 10^{22} \text{ cm}^{-2}$. In these regions the temperatures T_{photo} are updated to the values given by Eq. 1 in Picogna et al. (2019). For the computation of the temperatures the local ionization parameter ζ as to be calculated (Tarter et al., 1969; Owen et al., 2012):

$$\zeta = \frac{L_X}{\rho_g R^2}. \quad (3.39)$$

The corresponding temperature curves are plotted in Fig. 3.4, depending on the radially integrated column number density. Beyond the critical column density $\Sigma_{r,\text{crit}}$ the temperature is cooled to the original gas temperature $T_0 = T_g$.

In the case of the cold magnetic wind model b4c2np (see Table 3.1), the temperature in the corona is only slightly increased by 20 % compared to the bulk temperature in the disk. We use a simple β -cooling recipe in the whole simulation domain to exponentially damp the temperatures to T_0 on a time scale β_{cool}

$$T(t^n + \Delta t) = T(t^n) + (T(t^n) - T_0) \exp\left(\frac{\Delta t}{\beta_{\text{cool}}}\right) \quad (3.40)$$

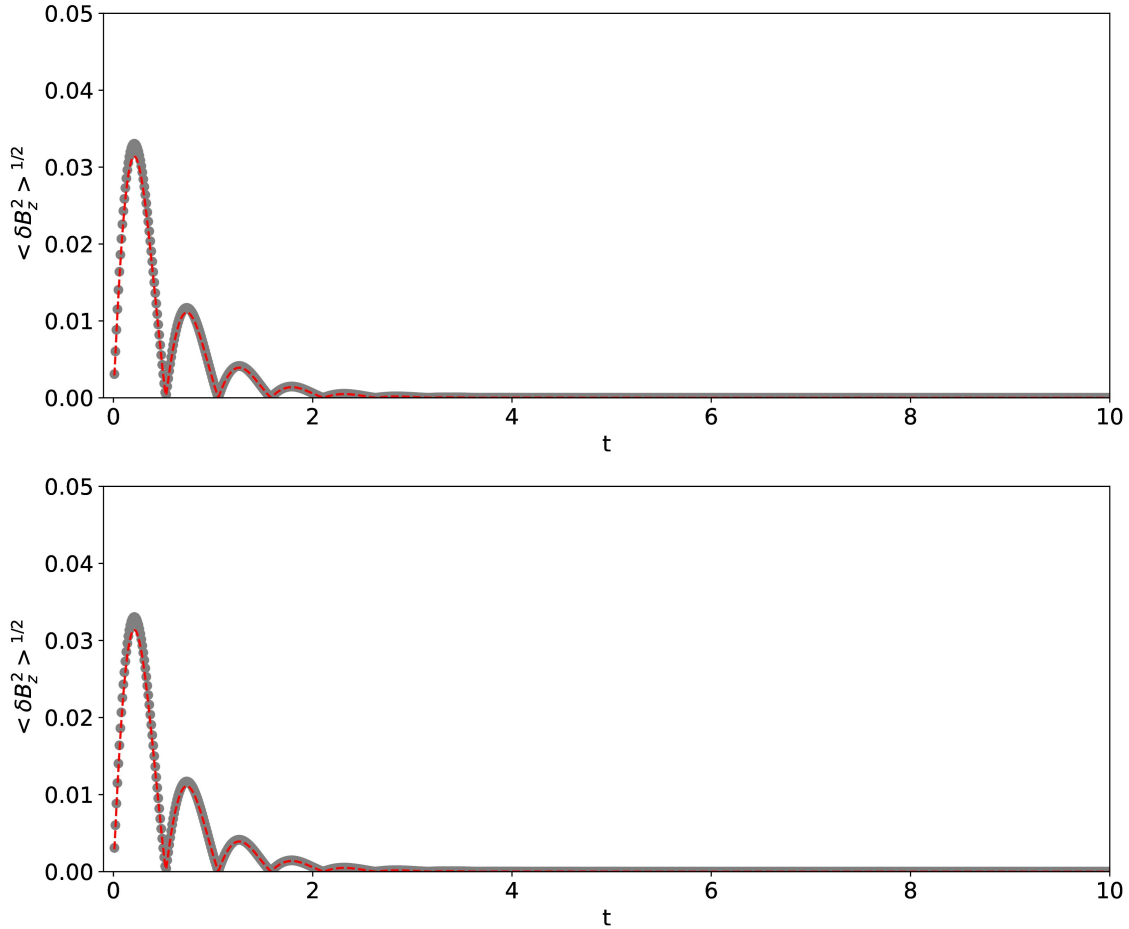


Figure 3.3: Decaying Alfvén wave test for $\langle \sigma v \rangle_i = 100$. The top panel shows the r.m.s. magnetic field component with the operator splitting approach. The results in the bottom panel were created with the weighted EMF method.

3.2.4 Boundary conditions

We employ simple symmetric boundary conditions for most of the variables and boundaries where the values of the active cells are copied to the ghost cells. At the inner radial boundary the radial velocity follows an outflow boundary condition where $v_r = 0$ in the ghost zone if $v_r > 0$ in the active cell. In the contrary case v_r is copied to the ghost cell. The same procedure is applied to the outer radial boundary with the opposite sign. With this formulation mass influx from outside of the domain is avoided.

At the θ_{\min} and θ_{\max} boundaries v_ϕ , v_θ , B_ϕ , B_θ and the EMF in radial direction change sign in the ghost zone to mimic a polar boundary. In MHD-disk models the radial inner boundary condition can lead to spurious effects in the simulation domain. The same applies to the outer radial boundary where, if ill defined, artificial collimation affects the flow (Ustyugova et al., 1999). To avoid these difficulties we add a zone with additional artificial ohmic diffusion, so that the coupling between the gas and the magnetic field is weak enough that spurious effects are damped and the simulation domain remains largely unaffected. A similar approach was used at the inner boundary in Cui & Bai (2021) to stabilize the inner region of the domain.

Dimensionless values of the artificial ohmic resistivity are $\eta_{\text{ohm,in}} = 2 \times 10^{-4}$ and $\eta_{\text{ohm,out}} =$

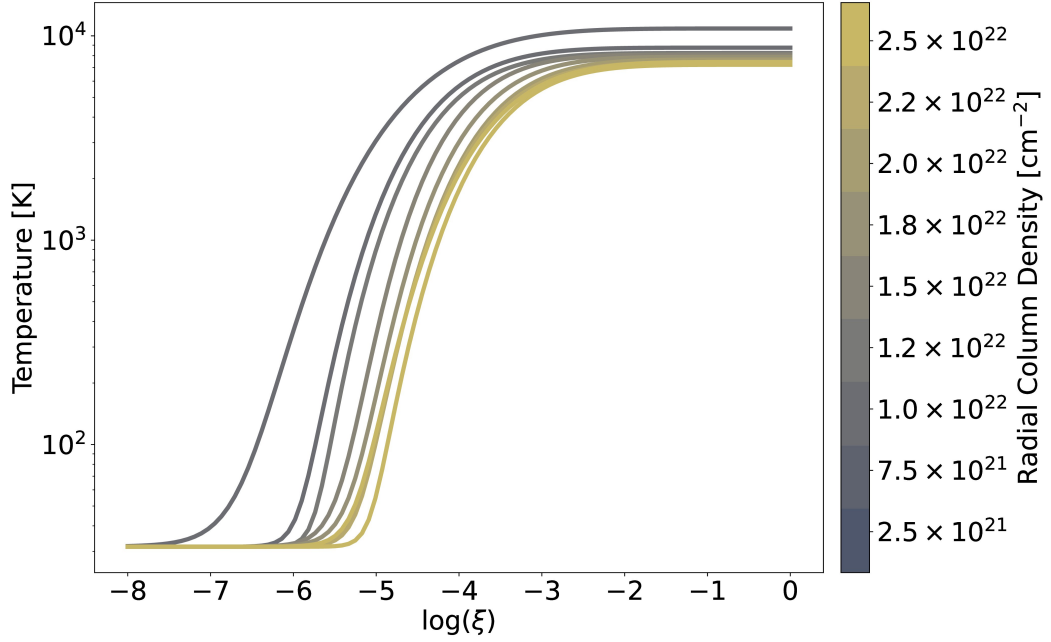


Figure 3.4: Photoevaporation temperature curves depending on the radially integrated column number density and the local ionization parameter ξ .

1×10^1 at the inner and outer damping zone, respectively. The extent of the damping zones is 10% of the inner and outer radius. With the choice of these values we find that the simulation domain and the time step are largely unaffected by the boundary conditions. Adding an inner cavity with greatly reduced amount of gas and dust furthermore ensures negligible impact of the inner boundary condition on the wind flow.

3.2.5 Radiative transfer model and post-processing

We post-process the dust density outputs with the radiative transfer code RADMC-3D (Dullemond et al., 2012a). In order to obtain three dimensional dust density distributions the axisymmetric simulation outputs are extended in the azimuthal direction by repeating the densities in 300 cells in ϕ . For the thermal Monte-Carlo step and the image reconstruction with scattered light $n_{\text{phot}} = 10^6$ and $n_{\text{phot_scat}} = 10^8$ photon packages are used, respectively.

Every synthetic observation is created with only one dust species since the limited number of fluid would lead to artificial discrete step-like features in the image. The dust opacities are computed with `optool` (Dominik et al., 2021) and are similar to the DIANA opacities (Woitke et al., 2016) with a material mixture of 87 % pyroxene, 13 % carbon (by mass) but with an increased porosity of 64 % to be consistent with a dust material density of $\rho_{\text{mat}} = 1 \text{ g/cm}^3$ in the simulations. Concerning the dust grain sizes, we compute the opacities for $a_1 = 0.1 \mu\text{m}$, $a_2 = 1 \mu\text{m}$ and $a_3 = 10 \mu\text{m}$ corresponding to the dust sizes in the simulations. The corresponding opacities are plotted in Fig. 3.5. Anisotropic scattering effects are included by using the Henyey-Greenstein phase function approximation (Henyey & Greenstein, 1941). A classical T Tauri star (CTT) is assumed with a

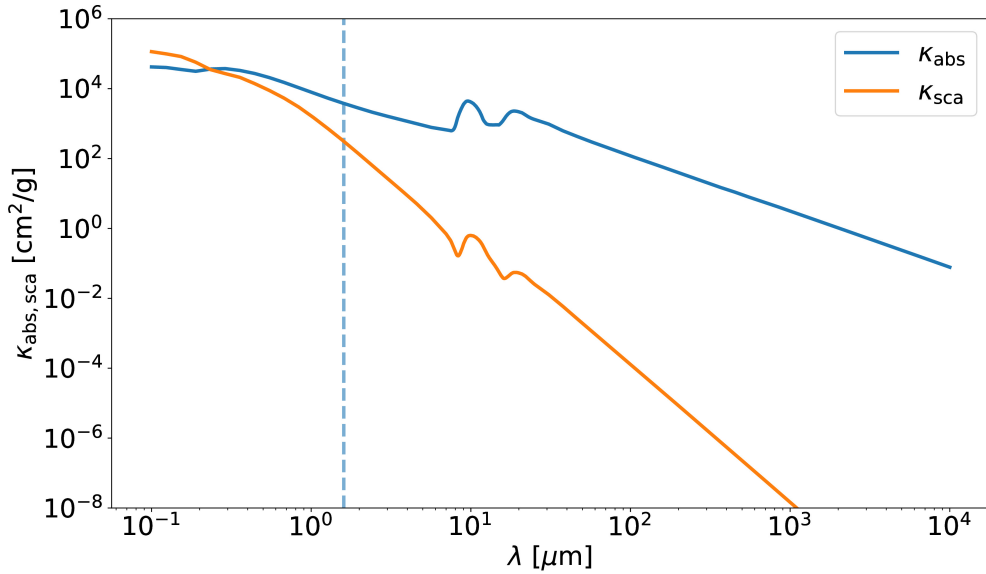


Figure 3.5: Absorption and scattering opacity coefficients κ_{abs} and κ_{sca} for a grain size of $a = 0.1 \mu\text{m}$ similar to the DIANA opacities, created with `optool` (Dominik et al., 2021). The vertical dashed line marks the H-band at $\lambda = 1.6 \mu\text{m}$.

temperature of $T_* = 4000 \text{ K}$ and a radial extent of $R_* = 2.55 R_\odot$ at a distance of 150 pc which is in the range of typical properties of observed CTTs (Alcalá et al., 2021). The resulting images are convolved with a gaussian beam size of 75 mas to account for typical observational resolution limits using VLT / SPHERE (Beuzit et al., 2019; Avenhaus et al., 2018).

3.3 Results

Sec. 3.3.1 describes the relevant parameters and simulation runs. In the following subsections we present the simulation results starting with a description of the wind flow structure emerging from the disk in Sec. 3.3.2 and continue with the dust dynamics in Sec. 3.3.3. The effectiveness of dust entrainment and the outflow angle of the grains is addressed in Sec. 3.3.4, Sec. 3.3.5 and Sec. 3.3.6. Finally, in Sec. 3.3.9 we compare synthetic observations computed from the simulation output with existing observations.

3.3.1 Parameters & normalization

Tab. 3.1 summarizes the key parameters of the different simulation runs presented in this study. The first part of the label describes whether a magnetic wind (e.g. b4 with $\beta = 10^4$) or a photoevaporative wind without magnetic fields was modeled (with label ph). Subsequently, the letter ‘c’ refers to the cavity location (e.g. c2 for a cavity at 2 au). The sub-labels np, a3 and eps2 refer to ‘no photoevaporation’, $\alpha = 10^{-3}$ and $\epsilon_{\text{ion}} = 10^{-2}$, respectively.

In the code all quantities are treated in dimensionless units that are scaled as follows:

$$v_0 = r_0 \Omega_K(r_0) \quad (3.41)$$

$$\rho_0 = M_\odot / r_0^3 \quad (3.42)$$

$$P_0 = \rho_0 v_0^2 \quad (3.43)$$

where the length unit is set to $r_0 = 5.2$ au. The initial density profile is scaled to reach a surface density of $\Sigma = 200$ g/cm² at $r = 1$ au and decreases radially with power law slope of $p = 1$. The central star mass is set to $0.7 M_\odot$ and the disk follows a moderate aspect ratio of $H/r_0 = 0.055 (r/r_0)^{1/4}$ which corresponds to a flared disk with a temperature slope of $q = 1/2$. These parameters correspond to a stellar luminosity of $L_* = 1.5 L_\odot$ with the assumption of a grazing angle of $\phi = 0.02$. The luminosity is in line with the stellar parameters of $T_* = 4000$ K and $R_* = 2.55 R_\odot$ mentioned in Sec. 3.2.5.

A temperature floor of $T_{\min} = 10$ K and a cooling time scale of $\beta_{\text{cool}} = 10^{-4}$ is applied. The fiducial value of the inner cavity size is chosen to be $r_c = 2$ au. Further parameters are the adiabatic index of $\gamma = 5/3$ and the mean molecular weight $\mu = 1.37125$.

In Sec. 3.2.2 the model necessitates an assumption of the dust content in the disk. In this work the ionization model is parametrized with a static value of the dust-to-gas ratio $\epsilon_{\text{ion}} = 10^{-3}$ and a monomer size of $a_0 = 5$ μm that constitute aggregates with 400 particles, resulting in a grain size of 100 μm . Increasing the dust-to-gas ratio by one order of magnitude does not alter the ionization fraction profile by a great amount, as described in Sec. 3.3.8. In order to simplify the model, the dynamically simulated dust fluids are not coupled to the ionization model and the relative insensitivity to the chosen parameters in the midplane supports this approximation.

All simulation runs are carried out with three dust species of the sized $a = 0.1$ μm , 1 μm and 10 μm , intended to represent the three cases of full entrainment, slow decoupling, and fast decoupling from the gas in the wind. The material density of the grains is set to $\rho_{\text{mat}} = 1$ g/cm³.

The computational grid adopts a spherical symmetry and contains 500 logarithmically spaced cells in radial direction whereas 276 cells are used in the polar (θ) direction. In order to increase the vertical resolution closer to the disk mid plane, the polar cells are arranged in a stretched grid, with a cell size at the polar boundaries that is twice as larger compared to the mid plane. With this approach a resolution of 7 cells per H in polar direction at $r = r_0, z = 0$.

3.3.2 Gas flow structure

Fig. 3.6 visualizes the gas wind flow for the simulation runs phc2, b5c2 and b4c2. The latter two include magnetic fields whereas the former only includes the photoevaporation recipe. Comparing both magnetic winds in Fig. 3.6 the magnetic field structure consists mostly of straight field lines for $\beta = 10^4$, whereas the weaker field shown in the central panel exposes a more irregular field structure towards the inner region of the disk. For this field strength and configuration the wind is in the transition between a thermally dominated and a magnetically dominated wind. Note that these are simulation snapshots and not averaged wind flows.

In terms of wind total mass loss rates all of these three runs display similar results, as shown in Fig. 3.7. Generally, the wind converges to a steady-state flow after a time scale

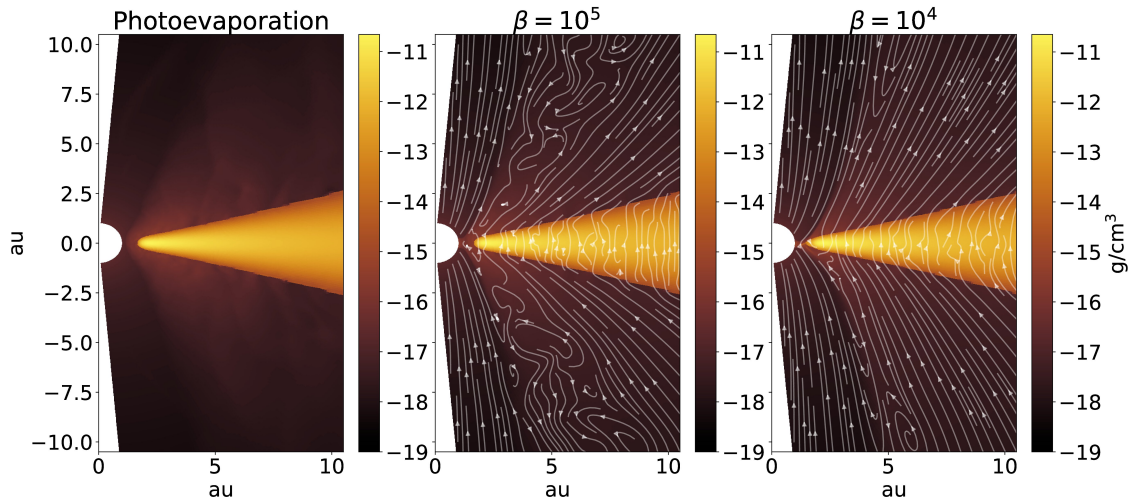


Figure 3.6: Shown are gas density maps of the simulations phc2, b5c2 and b4c2 after 500 orbits at 1 au. Magnetic field lines are represented by the white lines in the corresponding panels.

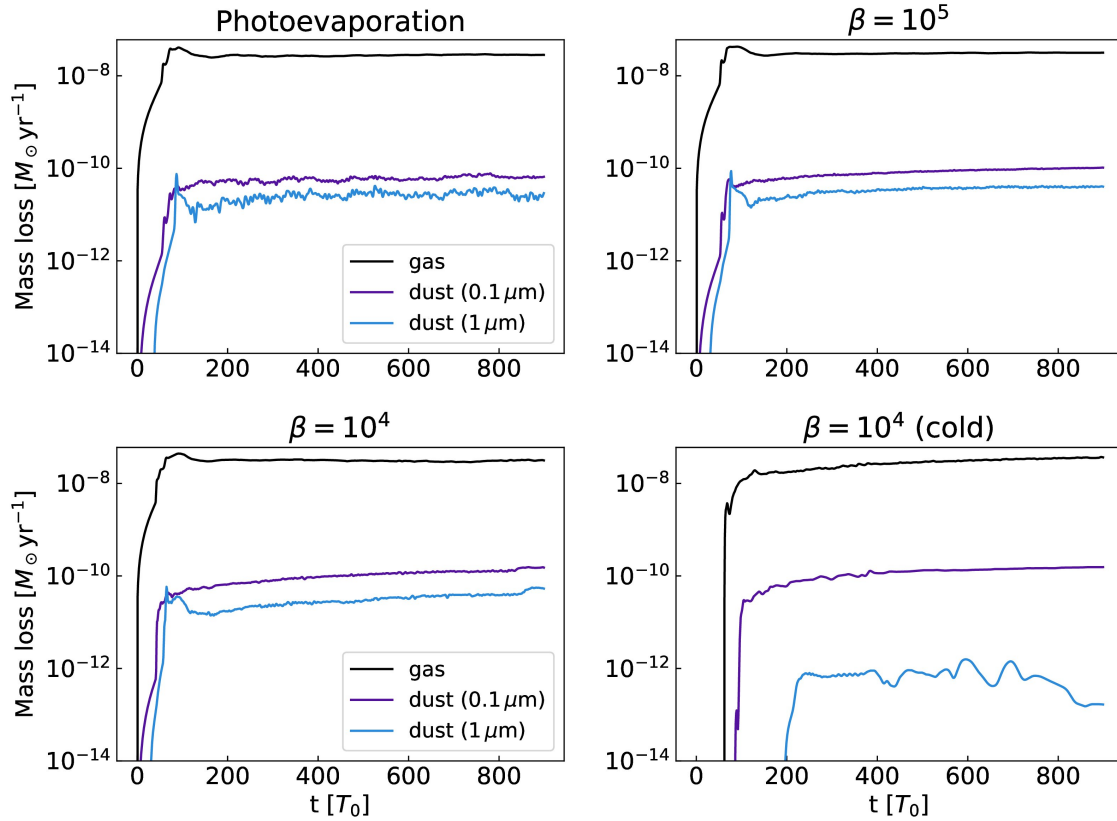


Figure 3.7: Total wind mass loss rates of gas and dust for the simulation runs phc2, b5c2, b4c2 and b4c2np. Results from 10 μm grains are excluded due to the negligible outflow and the lack of entrainment in the wind for all runs shown above.

about 200 orbits at 1 au and the simulation time chosen for these runs is thus sufficient to explore relevant wind dynamics in the inner region.

The sharp cutoff of the disk at $r = 2$ au quickly relaxes towards a stable equilibrium after a few orbits. The choice of the initial shape of the inner rim is thus not relevant for the wind flow. We observe accretion of gas through the inner cavity when a magnetic field is present. This effect, which can be best observed in the right panel of Fig. 3.6, is more pronounced for larger magnetic field strengths and is caused by wind-driven accretion.

The photoevaporation gas mass loss rates reach $\approx 2.83 \times 10^{-8} M_{\odot} \text{ yr}^{-1}$, in good agreement with Picogna et al. (2019). The mass loss rates in the simulation runs b5c2 and b4c2 are $\approx 3.13 \times 10^{-8} M_{\odot} \text{ yr}^{-1}$ and $\approx 3.03 \times 10^{-8} M_{\odot} \text{ yr}^{-1}$, respectively. In the case of a purely magnetically driven wind without any heating by ionizing radiation of model b4c2np the wind mass loss rates are similar with a value of $3.19 \times 10^{-8} M_{\odot} \text{ yr}^{-1}$. The mass loss rates are computed at 95 % of the outer radial simulation boundary. The region within five gas scale heights of the disk is excluded from the mass loss rate to avoid the corruption of the results from circulation within the disk.

3.3.3 Dust flow structure

In Fig. 3.8 the dust flows are shown for the grain sizes $0.1 \mu\text{m}$, $1 \mu\text{m}$ and $10 \mu\text{m}$. Generally, $10 \mu\text{m}$ sized grains are hardly entrained with the wind flow since the drag force is too weak to counteract the gravitational pull. $0.1 \mu\text{m}$ grains are well coupled to the gas flow and can be considered as tracers of the wind. Throughout the analysis we will refer to the flow angle or inclination angle, meaning the angle enclosed between the dust flow direction and this disk mid plane axis at $z = 0$. The inclinations θ_d of the dust flows is smaller for the thermally driven wind shown on the left hand side compared to the magnetically driven wind on the right hand side. The magnetic field is well coupled to the gas in the wind region where the ionization fraction $x_{e,i}$ surpasses 10^{-4} and the field topology forces the wind flow to be more inclined compared to the thermally driven wind.

The same phenomenon also appears for $1 \mu\text{m}$ grains shown in the second row of Fig. 3.8. Due to the weaker coupling and the lack of pressure support the dust flow is less inclined with respect to the gaseous wind compared to smaller grains. The dust flow exhibits wave-like patterns in the case of $\beta = 10^5$ and becomes more stable for larger magnetic field strengths. These wave structures coincide with the irregular magnetic field patterns displayed in Fig. 3.6. We furthermore point out that the dust flow consisting of $1 \mu\text{m}$ grains is efficiently launched in the inner part of the disk, whereas beyond several au the wind significantly weakens. The dusty wind cannot be sustained in the lower density regions further out and up in the disk since the Stokes number significantly increases.

An example of a dust flow in a cold magnetically driven wind is given in Fig. 3.9 for an initial $\beta = 10^4$. The inclination with respect to the mid plane is smaller compared to the warm magnetothermal or photoevaporative winds. Grains with a size of $1 \mu\text{m}$ are entrained at a rather shallow inclination angle and similar to the warm winds, dust entrainment is negligible considering $10 \mu\text{m}$ dust particles. While material in the winds including photoevaporation is ejected with a velocity of $\approx 15 \text{ km s}^{-1}$ the outflow velocity of the cold magnetic wind in b4c2np only reaches values of $\approx 5 \text{ km s}^{-1}$. The

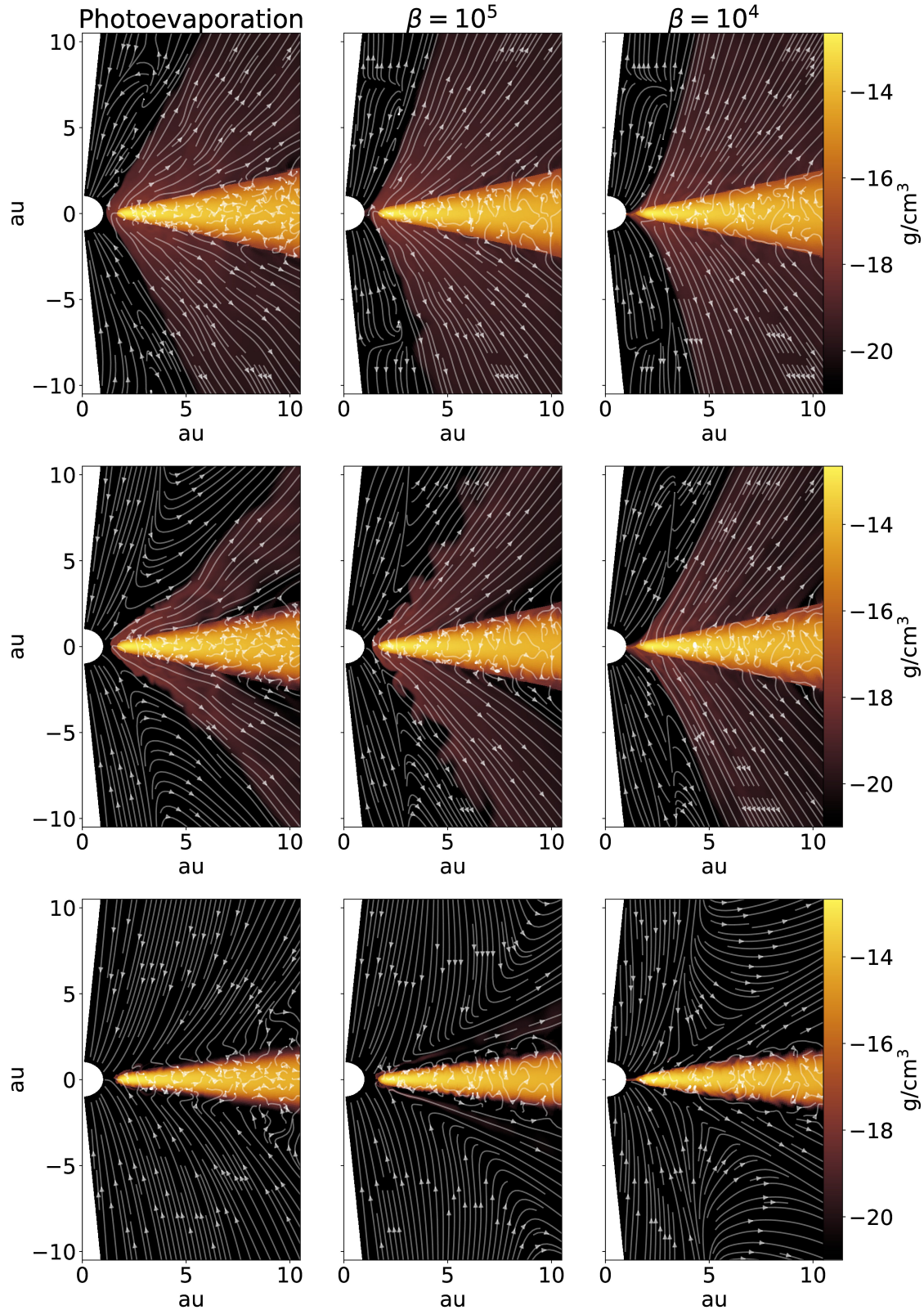


Figure 3.8: The panels show the dust density maps for the simulations phc2, b5c2 and b4c2 after 500 orbits at 1 au. Dust velocity streamlines are annotated by the white arrowed lines. The upper, center and lower three panels visualize the flow of grains with size $0.1 \mu\text{m}$, $1 \mu\text{m}$ and $10 \mu\text{m}$, respectively.

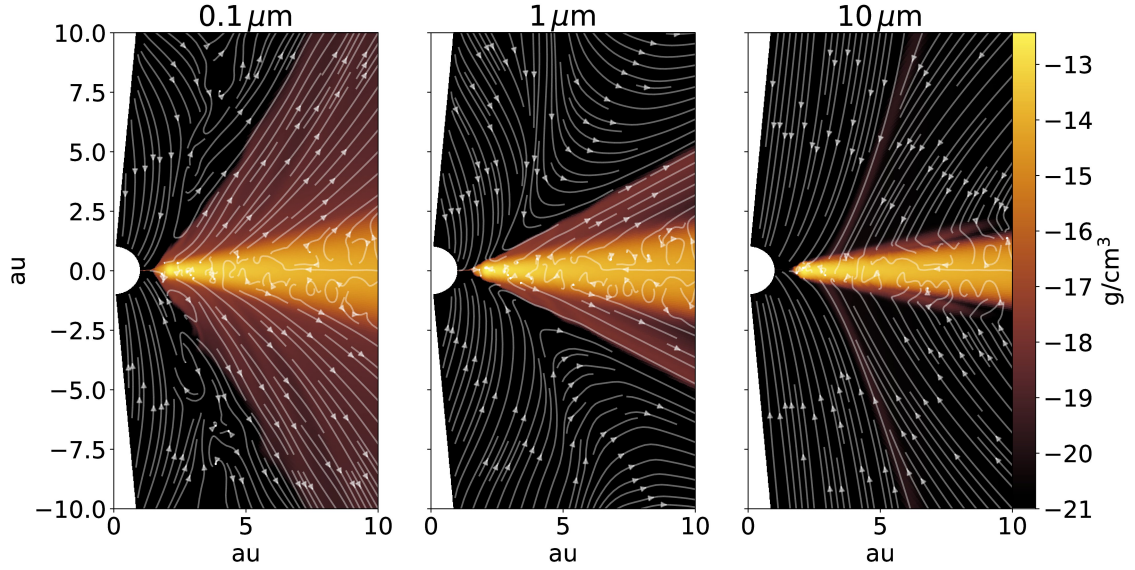


Figure 3.9: Dust density maps for the simulation b4c2np after 500 orbits at 1 au. Dust velocity streamlines are annotated by the white arrowed lines.

decreased wind speed causes a smaller drag force between gas and thus lowers the dust entrainment efficiency. Given that the mass loss rate is approximately equal to the one of the heated winds, the gas and dust densities in the wind region are significantly higher.

In Fig. 3.10 the cumulative mass loss rate depending on the cylindrical radius of the foot point of the wind is shown. The wind streamlines are traced backwards from the cells close to the outer radial boundary and the foot point is registered when the streamlines crosses the surface at 5 gas pressure scale heights. Only streamlines with foot point $r_f \geq 3$ au are considered since the wind flow structure and the limited resolution do not in every case ensure a successful construction of traceable streamlines close to the inner cavity. The mass loss rates are obtained from a velocity and density field averaged over 50 orbits at 1 au starting from 600 orbits.

Warm magnetic winds lead to more dust entrainment and a stronger magnetic field increases the dust mass loss rate significantly. The dashed lines in Fig. 3.10 mark the radius within from within 99 % of the mass loss occurs which illustrate less efficient dust entrainment for larger grains further out in the disk. Numerical values are 32.3 au, 34.5 au, 43 au and 88.8 au for the simulations phc2, b5c2, b4c2, b4c2a3 and $0.1 \mu\text{m}$ grains, respectively. Analogously, the limits for $1 \mu\text{m}$ grains are 14.6 au, 12.7 au, 14.6 au and 44.3 au. The general trend is that the dust grains are preferably entrained starting from the inner regions of the disk. The limiting radius decreases with increasing dust size and hence we expect a much larger ejection region of dust for the smallest grain size. Considering the results of the simulation b4c2a3 with an increased viscosity of one order of magnitude ($\alpha = 10^{-3}$) the limiting radius lies significantly further outward. Increased turbulent diffusion effectively transports dust grains towards the wind launching front at larger radii.

Going back to Fig. 3.7 the mass loss rate for the two relevant dust species stabilizes over a few hundred orbits in the case of a thermal wind. In the case of magnetically driven winds however, dust mass loss rates reach a quasi-steady state but are slowly increasing

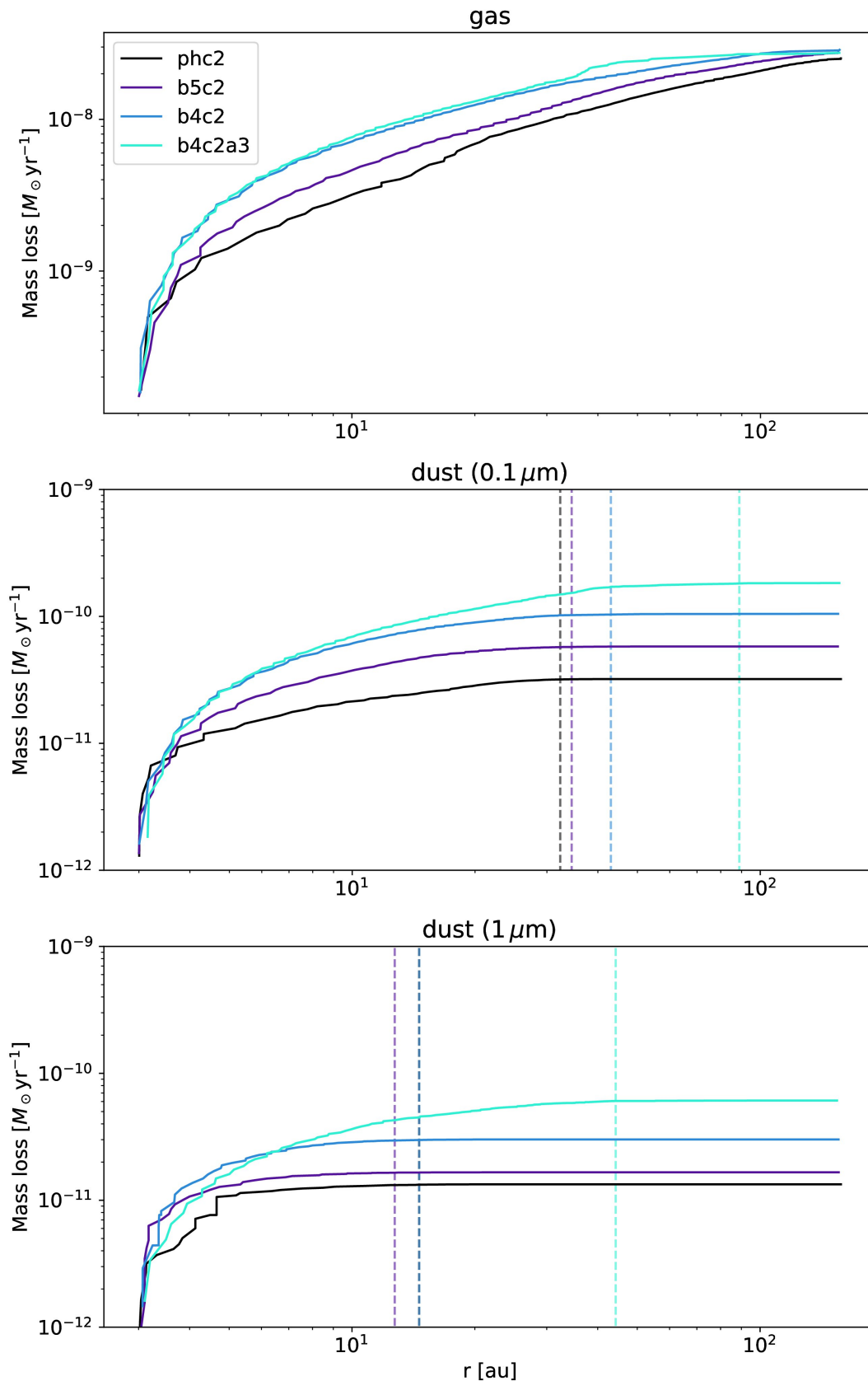


Figure 3.10: Cumulative mass loss rates of gas and dust for the simulation runs phc2, b5c2, b4c2 and b4c2a3 starting from 3 au. The cylindrical radius or foot point of the loss is obtained by tracing backwards the corresponding streamline from the outer radial boundary down to 5 scale heights above the disk mid plane. The flow field is averaged over 50 orbits at 1 au starting at 600 orbits. The vertical dashed lines mark the limit of the region where 99 % of the mass loss occurred.

throughout the simulation. In the presence of a cold magnetic wind, the mass loss rates of larger micron-sized dust grains are lower compared to the ionized winds since the flow angle is rather shallow and the entrainment efficiency suffers from the decreased wind speed.

3.3.4 Maximum grain size and flow angle

In order to quantify the maximum entrained grain size and the entrainment angle, we choose the approach to numerically integrate streamlines of various dust species based on the gas velocity field from the simulations. The following system of equation is solved numerically with the given velocity field of the corresponding simulation output:

$$\frac{\partial v_{d,r}}{\partial t} = \frac{v_{d,\phi}^2}{r} - \frac{GM_*}{(r^2 + z^2)^{\frac{3}{2}}} r - \frac{v_{d,r} - v_{g,r}}{t_s} \quad (3.44)$$

$$\frac{\partial v_{d,z}}{\partial t} = -\frac{GM_*}{(r^2 + z^2)^{\frac{3}{2}}} z - \frac{v_{d,z} - v_{g,z}}{t_s} \quad (3.45)$$

$$\frac{\partial v_{d,\phi}}{\partial t} = -\frac{v_{d,\phi} - v_{g,\phi}}{t_s} \quad (3.46)$$

The numerical integration was carried out with the VODE solver Brown et al. (1989). We verified that the streamlines are comparable to the ones in the dust velocity field output from the simulation. No significant deviations were visible.

The results are shown in Fig. 3.11 for 20 logarithmically distributed grain sizes ranging from 0.1 μm to 10 μm . The resulting trajectories match the corresponding dust streamlines from the actual simulation. As the starting point we chose $r = 8 \text{ au}$, $z = 2.5 \text{ au}$ which is situated well above the wind launching front. As expected from the simulation outputs 10 μm grains fall back towards the disk surface in the case of winds including photoevaporation (models phc2, b5c2 and b4c2). Generally, grains are lifted more efficiently in the case of warm, magnetic winds. Grains larger than $\approx 3 \mu\text{m}$ to $4 \mu\text{m}$ are lifted further but eventually fall back onto the disk at larger radii in the presence of a thermal wind.

For warm, magnetically driven winds, the limiting grain size shifts towards $\approx 6 \mu\text{m}$. In a cold, magnetic wind the picture changes and only sub-micron dust grains are lifted far from the disk surface and particles larger than 1 μm fall back onto the disk or are not entrained at all. The decreased wind speed is responsible for the lower dust entrainment efficiency as mentioned in Sec. 3.3.3.

Since the dust flow inclination angle is strongly dependent on the grain size, we quantify the inclination by fitting linear functions to the dust trajectories presented in Fig. 3.11. We only consider the final 25 % part of the cylindrical radius of the trajectory for the fits. The corresponding slopes and inclination angles based on the simulations phc2, b5c2, b4c2 and b4c2np are plotted in Fig. 3.12. For small grains and warm winds the difference in the inclination angle is rather small. The inclination of the flow of 1 μm grains ranges from roughly 67° to 69° . Considering 3 μm grains however, the inclination angle is 36.1° assuming a thermal wind compared magnetic winds with 44.4° and 46.5° for $\beta = 10^5$ and $\beta = 10^4$, respectively. Generally, the inclination angle is larger for warm, magnetic winds, especially considering micron sized grains.

A significant difference in inclination is however observed in a cold magnetic wind.

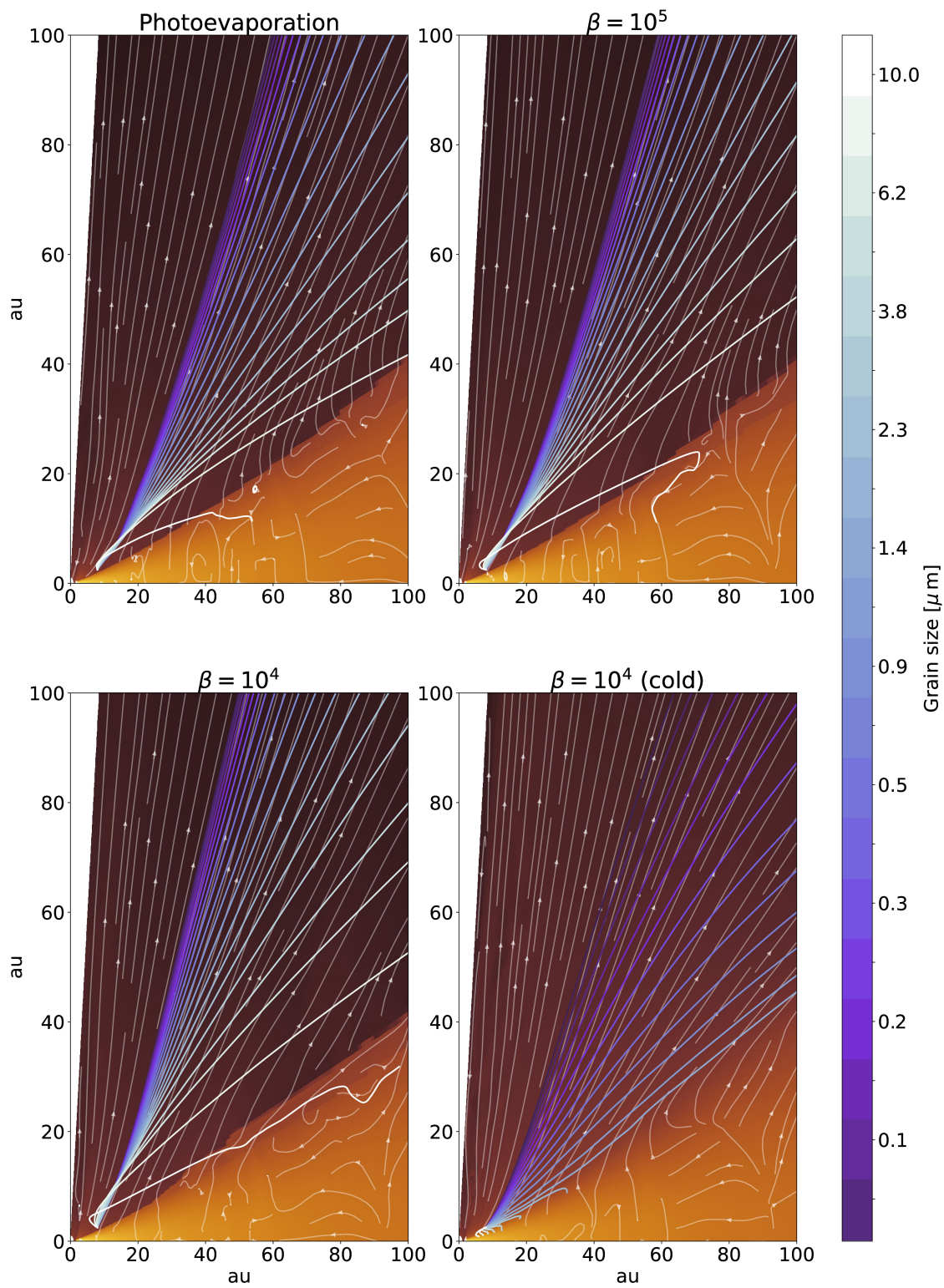


Figure 3.11: Numerically integrated dust trajectories for snapshots after $500 T_0$ of the simulation runs phc2, b5c2 and b4c2. The orange color map represents the gas density and the thin arrowed white lines denote the gas velocity streamlines. The thicker colored lines visualize the dust trajectories for grain sizes ranging from 0.1 μm to 10 μm .

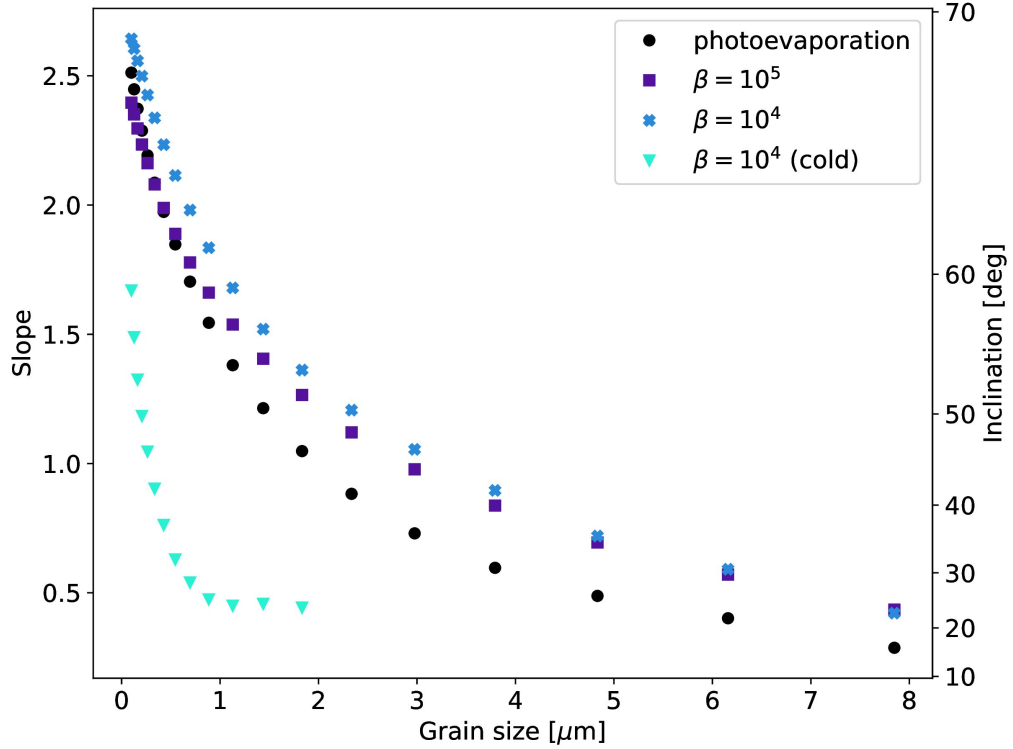


Figure 3.12: Asymptotic dust flow inclination depending on the grain size for the simulation runs phc2, b5c2, b4c2 and b4c2np.

While $0.1 \mu\text{m}$ -sized dust grains are entrained by an angle of 59.1° , the inclination drops down rapidly to roughly 25° for micron-sized grains, as expected.

3.3.5 Wind launching surface

Since the dust entrainment efficiency seems to be dependent on the dust reservoir at the location of the foot point of the wind, we therefore provide a more detailed analysis of the radial dependencies of the dust entrainment efficiency in this sub-section.

We only focus on winds including photoevaporation where the wind launching surface is marked by a sharp transition in the gas density. Fig. 3.13 and Fig. 3.14 visualize vertical slices of normalized gas and dust densities as well as the respective Stokes number profile. As expected, in Fig. 3.13 the dust scale height of $10 \mu\text{m}$ sized grains narrows with increasing radius as the Stokes number within the bulk of the disk increases due to the negative radial density slope. The kink at roughly 4.5 gas scale heights represents the wind launching surface. Clearly, the dust scale height is too small to lift a considerable amount of grains to the launching surface, especially at larger radii.

A comparison between the different dust species at 5 au is given in Fig. 3.14. The trend of larger dust scale heights with smaller Stokes numbers is readily visible. Weaker wind flows by several orders of magnitude appear for $1 \mu\text{m}$ sized grains compared to $0.1 \mu\text{m}$ particles. Only the vertical distribution of the smallest $0.1 \mu\text{m}$ grains that are well coupled to the gas appear to correspond the gas density distribution.

In the following, we aim to examine the dust entrainment efficiency depending on the radial location in the disk. We therefore trace various quantities, such as dust-to-gas ratio, Stokes number, temperature and gas number density along the wind launching

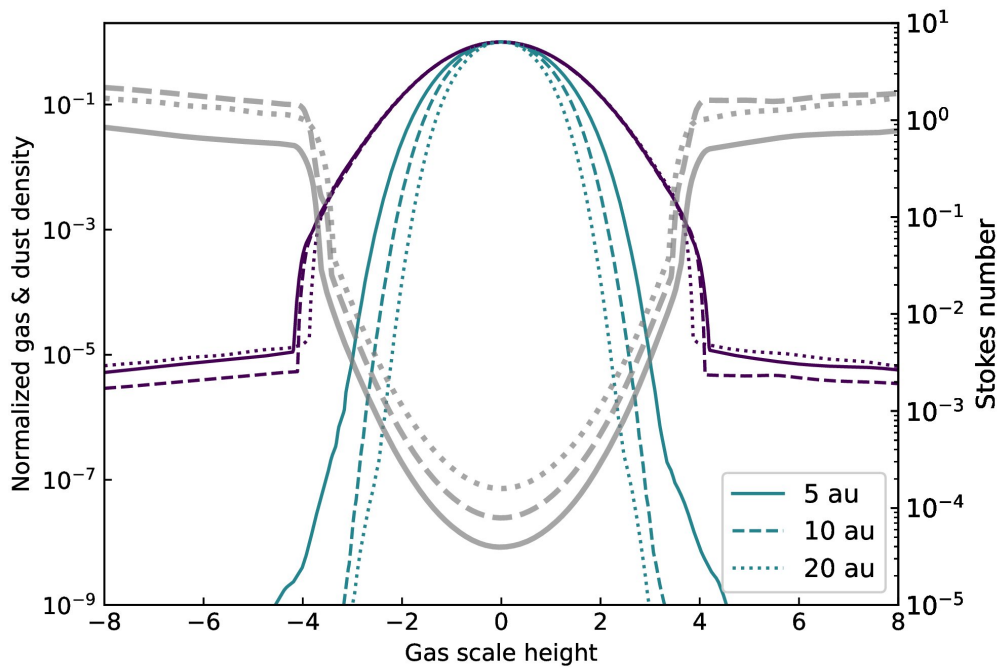


Figure 3.13: Normalized vertical density slices of the phc2 at different radial locations in the disk. The violet lines represent the normalized gas density while the turquoise lines display the dust density of $10\ \mu\text{m}$ grains. The grey lines denote the respective Stokes number profile.

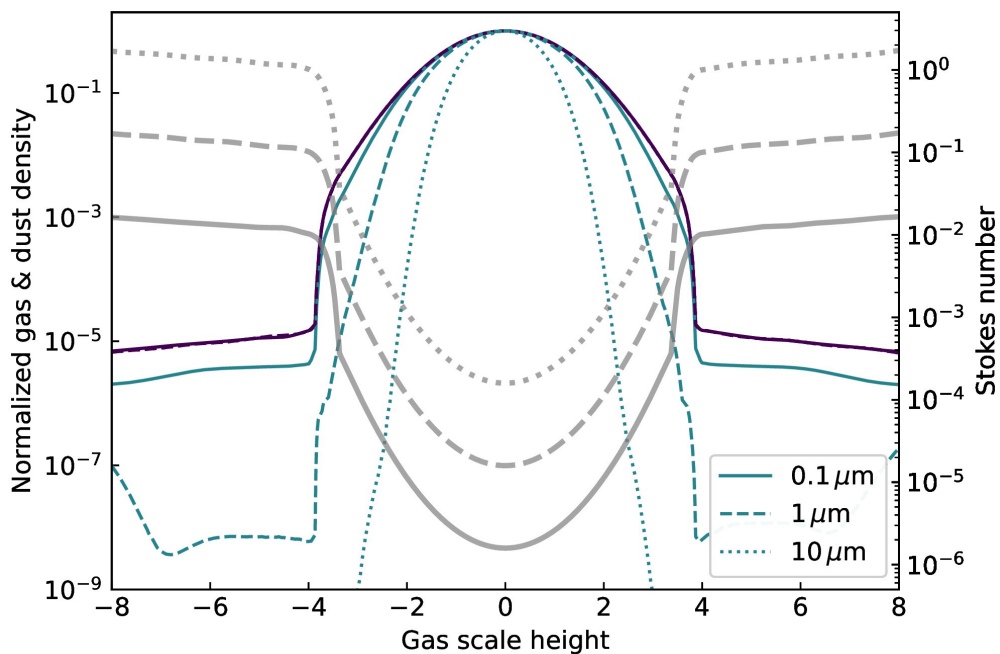


Figure 3.14: Normalized vertical density slices and Stokes number profiles of the phc2 similar to Fig. 3.13 for the grain sizes $0.1\ \mu\text{m}$ (straight lines), $1\ \mu\text{m}$ (dashed lines), $10\ \mu\text{m}$ (dotted lines) at 5 au.

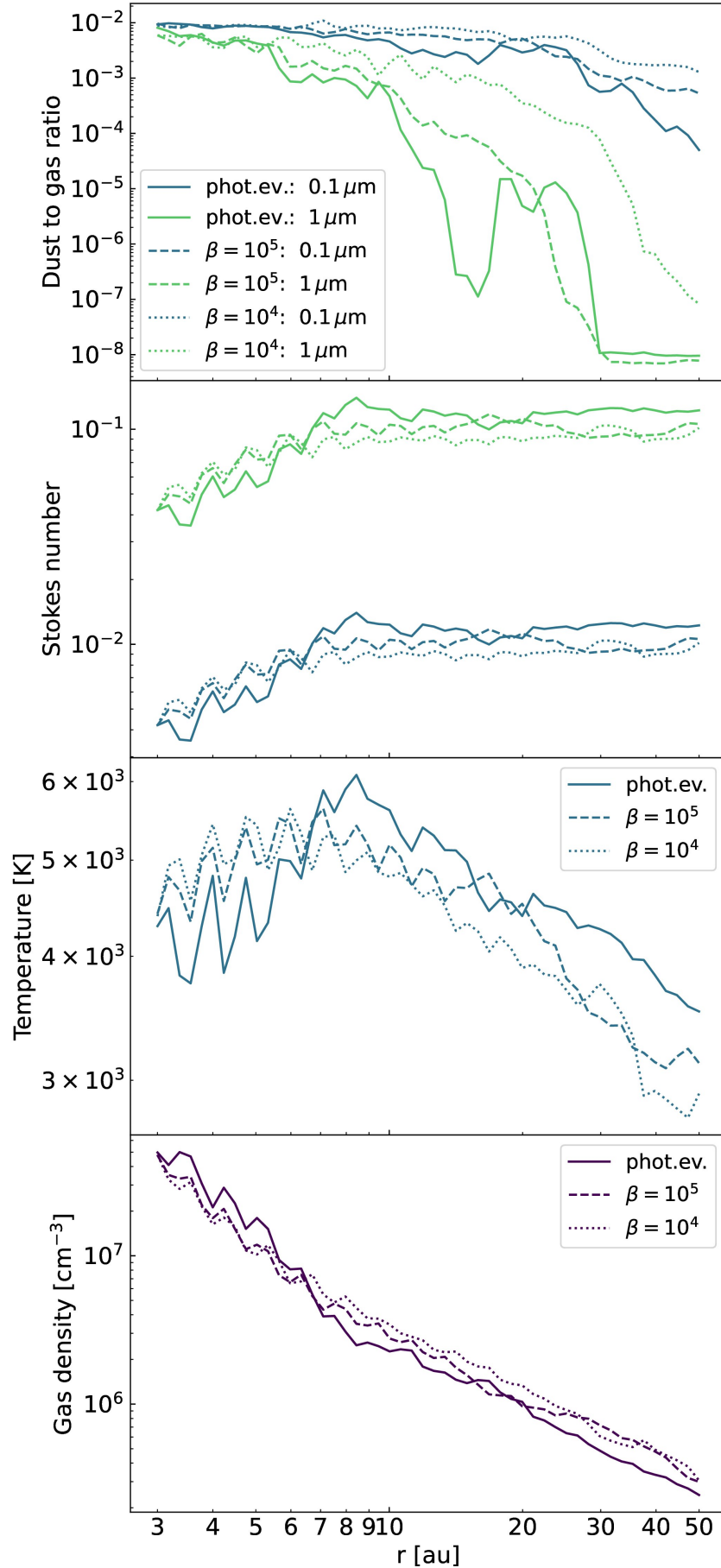


Figure 3.15: Physical quantities at the wind launching surface of the simulation runs phc2 (straight lines), b5c2 (dashed lines) and b4c2 (dotted lines). In the top two panels the blue lines represent 0.1 μm -sized grains, whereas the green lines denote 1 μm -sized grains.

surface. Numerically we define this surface to be located about 0.3 gas scale heights above the kink in the vertical gas density profile in order to decrease the impact of fluctuations close to the surface of the disk. The kink location is determined by numerically evaluating local extrema in the second derivative of the vertical gas density profile which we find to be a robust method to find the launching surface.

The corresponding quantities at these positions are displayed in Fig. 3.15 where thermally and magnetically driven winds with $0.1 \mu\text{m}$ and $1 \mu\text{m}$ sized grains are taken into account. Clearly, the dust entrainment efficiency, defined by the dust to gas ratio close to the wind launching front shown in the upper most panel of Fig. 3.15, decreases significantly with increasing radius. At the inner part of the flow close to the cavity at 2 au, $0.1 \mu\text{m}$ sized grains are basically perfectly entrained with the wind for both photoevaporative and magnetically driven outflows since the initial dust-to-gas ratio is $\epsilon_{\text{dg}} = 10^{-2}$. In the outer part of the disk the dust-to-gas ratio in the wind decreased by one to two orders of magnitude. For $1 \mu\text{m}$ sized grains the effect is more pronounced with a decline of six orders of magnitude. It becomes apparent that generally the magnetically driven wind with $\beta = 10^4$, represented by the dotted lines, leads to a higher dust-to-gas ratio in the wind flow compared to weaker field strengths or a purely thermally driven wind. One could argue that dust entrainment becomes less effective at larger radii because of the more diluted gas in the wind and thereby larger Stokes numbers. This is however not the case as shown in the second panel of Fig. 3.15. In the inner part of the disk up to ≈ 8 au to 9 au the Stokes number close to the launching surface increases until it stagnates and remains constant at the outer part of the disk. The decrease in dust entrainment efficiency can thus not be attributed to a weaker coupling between gas and dust in these regions. The gas density in the wind close to the launching surface indeed decreases with radius as shown in the bottom panel of Fig. 3.15. On the other hand, the gas temperature heated by the ionizing radiation from the central star in turn also decreases with radius. The peak in temperature is reached at ≈ 8 au to 9 au, agreeing with the stagnation point of the Stokes number profile. By linear fitting the quantities at the wind launching surface in logarithmic space we determine the power law slopes. Beyond 8 au the thermal velocity v_{th} decreases $\propto r^{-0.13}$ whereas the gas density profile follows the power law $\propto r^{-1.41}$. Looking at the definition of the Stokes number in Eq. 3.6 we expect an approximately constant relation $\text{St} \propto \Omega_{\text{K}} / (\rho_{\text{g}} \cdot v_{\text{th}}) \propto r^{0.04}$ with a Keplerian angular frequency following $\Omega_{\text{K}} \propto r^{-1.5}$.

3.3.6 Gas and dust streamlines

In Fig. 3.16 velocities, Stokes number and Alfvén Mach number are plotted for a representative streamline starting at $r = 8$ au. Since the flow is close to a steady state we can consider the streamline as a proxy for the actual trajectory of a dust and gas parcel moving in the wind. The radial velocities in the left-most panel are almost constant with the cylindrical radius whereas the vertical velocities in z-direction significantly increase up to values on the order of 15 km s^{-1} . The models including magnetic effects generally lead to slightly faster wind flows increasing with the magnetic field strength. Depending on the dust grain size the velocity can be significantly less compared to the gas velocity, differing by roughly 5 km s^{-1} . Dust velocities are also consistently faster in the magnetic wind case. Looking at the Stokes numbers of the two smallest dust species, the values up to unity are reached for micron-sized grains far from the disk. The right-

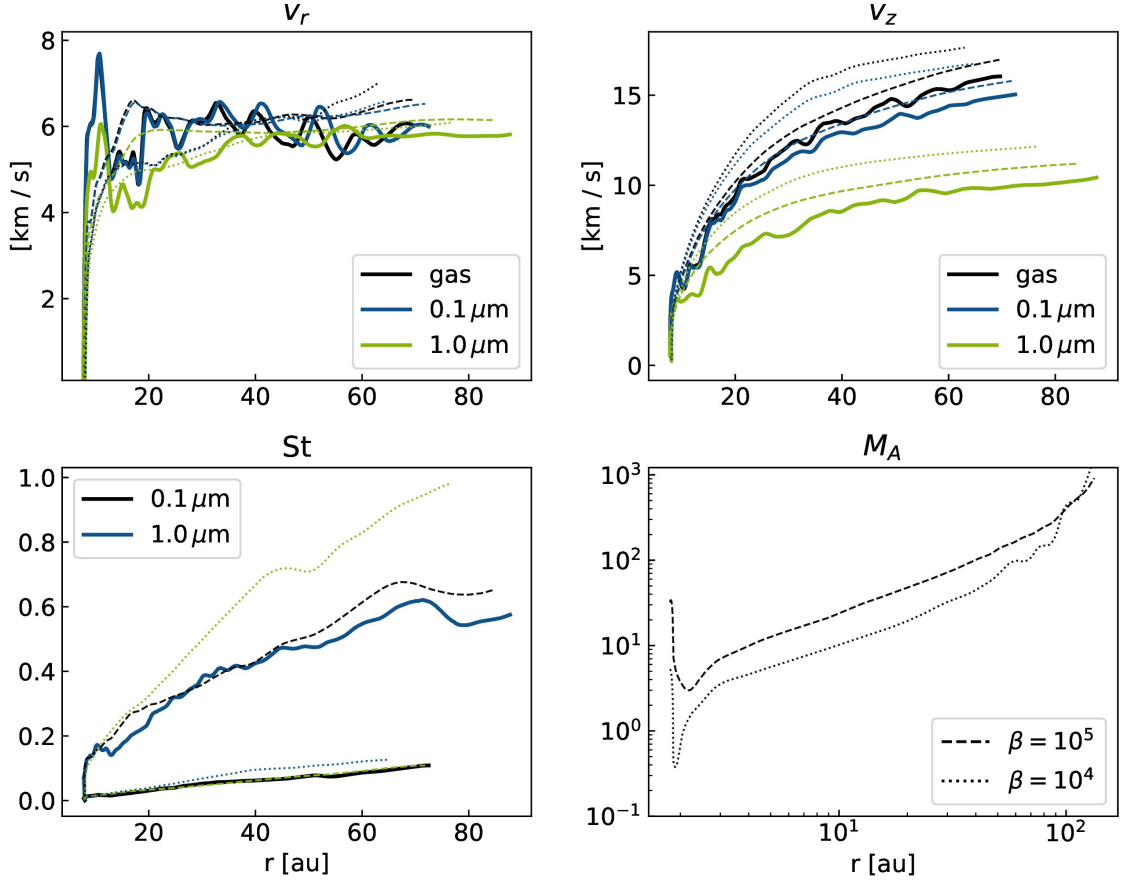


Figure 3.16: Streamlines starting from $r = 8 \text{ au}, z = 2.5 \text{ au}$. Shown are poloidal velocities of gas and dust along the streamline (*left two panels*) and the respective Stokes numbers St as well as the Alfvén Mach number M_A (*right two panels*).

most panel demonstrates that the wind is only sub-alfvénic for a small part close to the wind launching front. Even in the simulation run b4c2 with an initial $\beta = 10^4$ the wind quickly reaches super-alfvénic speeds which in consequence represents a small magnetic lever arm. This picture is in line with recent models of magneto-thermal winds such as Gressel et al. (2015); Bai (2017a); Rodenkirch et al. (2020).

3.3.7 Dust temperature estimate

The relatively high temperatures in the ionized wind models heat the dust grains that are entrained in the gas flow. We will show in the following that dust particles do not reach the dust sublimation threshold and would thus remain solid along their trajectories. The expression of the heating rate per unit surface q_d is described in Gombosi et al. (1986), taking into account both contact and friction heating. We follow the approach of Stammler & Dullemond (2014) in this regard and evaluate the subsequent expressions:

$$q_d = \rho_g C_{H,d} (T_{\text{rec}} - T_d) |v_g - v_d| \quad (3.47)$$

where the heat transfer coefficient $C_{H,d}$ is expressed as

$$C_{H,d} = \frac{\gamma + 1}{\gamma - 1} \frac{k_B}{8\mu m_p s^2} \left[\frac{s}{\sqrt{\pi}} \exp(-s^2) + \left(\frac{1}{2} + s^2 \right) \text{erf}(s) \right] \quad (3.48)$$

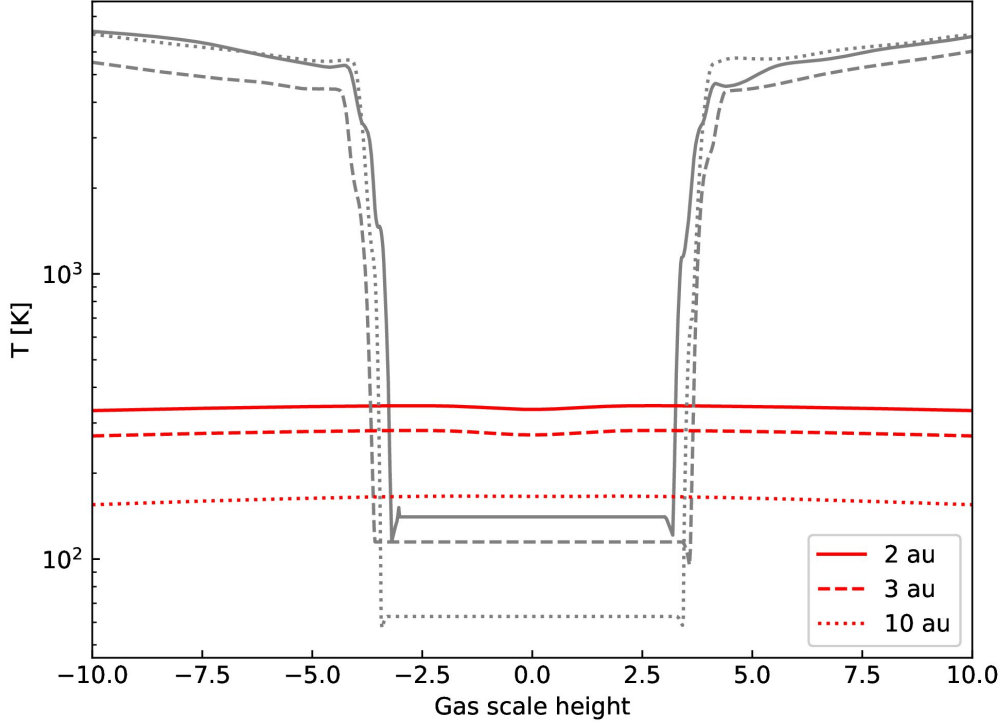


Figure 3.17: Vertical slices of gas and dust temperatures at different radial location in the disk and wind region of the photoevaporation simulation phc2. The grey lines represent the gas temperatures whereas the red lines display the equilibrium dust temperatures of the $0.1 \mu\text{m}$ grains.

with the error function erf and the normalized difference between dust and gas velocities:

$$s = \frac{|v_g - v_d|}{\sqrt{2k_B T_g / (\mu m_p)}} \quad (3.49)$$

The recovery temperature T_{rec} is given by the expression (Gombosi et al., 1986):

$$T_{\text{rec}} = \frac{T_g}{\gamma - 1} \left[2\gamma + 2(\gamma - 1)s^2 - \frac{\gamma - 1}{\frac{1}{2} + s^2 + \frac{s}{\sqrt{\pi}} \exp(-s^2) \text{erf}^{-1}(s)} \right] \quad (3.50)$$

The dust equilibrium temperature is then finally computed by solving

$$q_d + \frac{R_*}{r^2} \epsilon_d \sigma_{\text{SB}} T_*^4 - 4\sigma_{\text{SB}} T_d^4 = 0 \quad (3.51)$$

with the thermal cooling efficiency factor

$$\epsilon_d = \frac{\kappa_P(T_*)}{\kappa_P(T_d)} \quad (3.52)$$

using the Planck mean opacity κ_P with the corresponding temperature. Fig. 3.17 provides the solutions of the equilibrium dust temperatures in comparison with the gas temperatures in a photoevaporative flow including $0.1 \mu\text{m}$ grains. We assume a sun-like star in the computation and find maximum dust temperatures of $T_d \approx 345 \text{ K}$ at a radial distance of $r = 2 \text{ au}$. Due to the thin gas in the wind region the ambient heating has

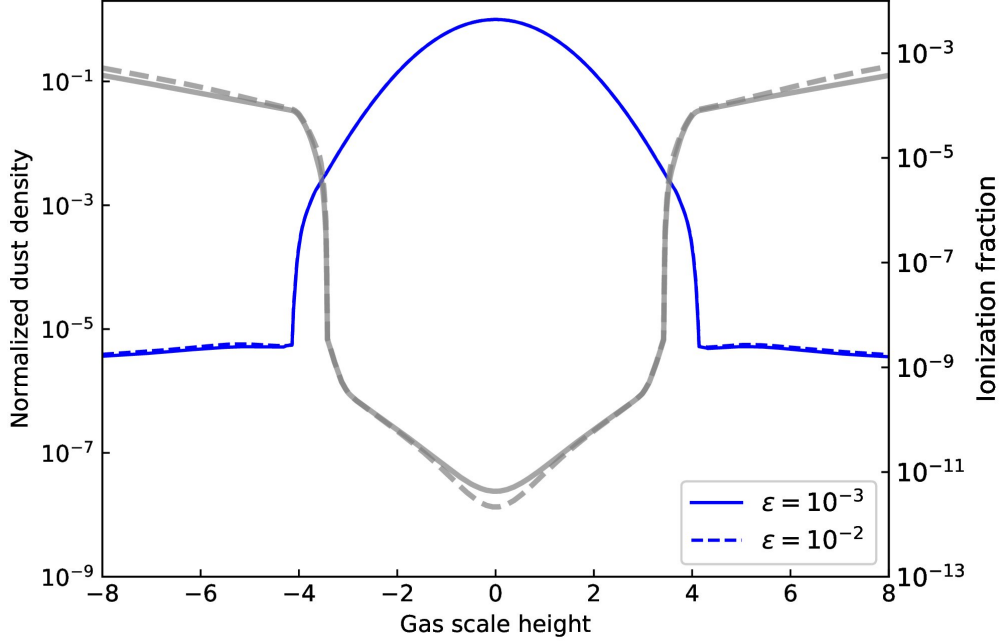


Figure 3.18: Normalized dust density (*blue lines*) and ionization fraction (*grey lines*) in the simulations b4c2 and b4c2eps2 with a dust-to-gas ratio of $\epsilon = 10^{-3}$ and $\epsilon = 10^{-2}$, respectively. The snapshot is taken after 1000 orbits at 1 au.

an almost negligible impact on the dust temperature. Without the flux of the central star the dust grains would reach $T_d \approx 40\text{K}$ only being heated by the ionized gas. In the wind flows presented here dust temperatures are clearly below the dust sublimation threshold which would be $\approx 980\text{K}$ assuming pyroxene as the grain material embedded in a thin medium of the density $\rho_g = 1 \times 10^{-16}\text{g/cm}^3$ (Pollack et al., 1994).

3.3.8 Ionization fraction

Since the ionization fraction depends on the dust-to-gas ratio ϵ_{ion} in the disk a comparison between $\epsilon_{\text{ion}} = 10^{-3}$ and $\epsilon_{\text{ion}} = 10^{-2}$ of the simulation runs b4c2 and b4c2eps2 is shown in Fig. 3.18. The ionization is relatively insensitive to the increased dust-to-gas ratio and only decreases by a small amount in the weakly ionized disk mid plane. In the dust density slice the effects are negligible.

3.3.9 Synthetic observations

Given that the wind flow is rather thin and dust is not perfectly entrained for larger grain sizes and distances from the central star, the observability of such dusty winds deserves a closer look. As a first simple estimate we compute the radial optical depth depending on the polar angle θ . The results are displayed in Fig. 3.19 for three dust species ranging from $0.1\mu\text{m}$ to $10\mu\text{m}$ in the H-band. The optical depth $\tau_{\text{obs},i}$ of dust species i is calculated by

$$\tau_{\text{obs},i} = \int_{r_{\text{min}}}^{r_{\text{max}}} \kappa_{\text{sca},i} \rho_{\text{d},i} \quad (3.53)$$

with the scattering opacity $\kappa_{\text{sca},i}$. The inner and outer radial boundaries are denoted by r_{min} and r_{max} , respectively. In Fig. 3.19 the bulk of the disk appears to be optically thick

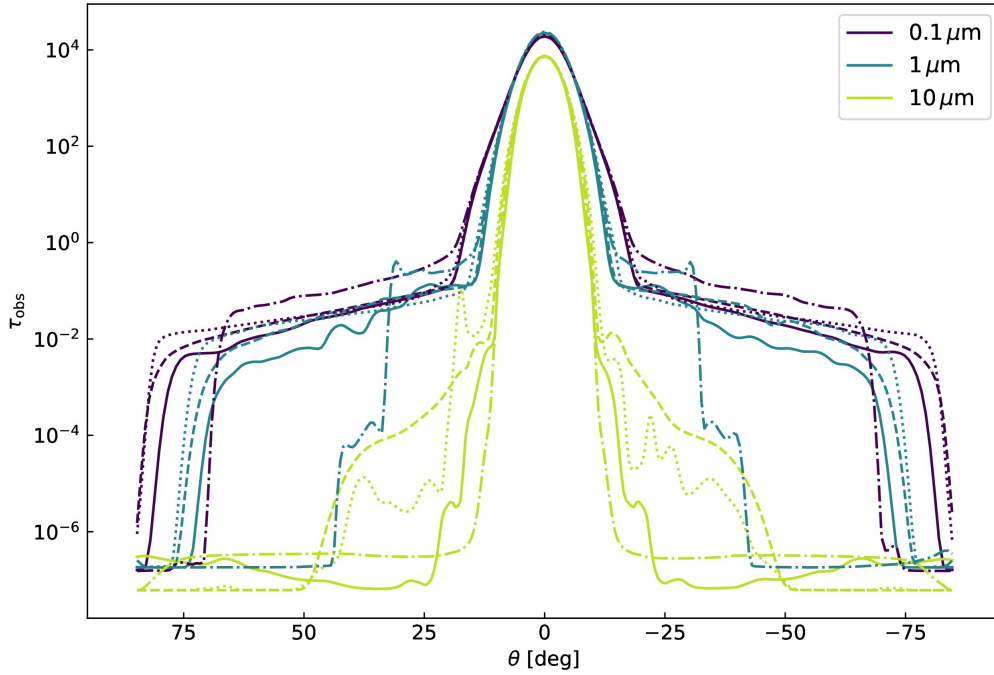


Figure 3.19: H-band radial optical depth τ_{obs} originating from the central star depending on the polar angle for three dust species with sizes $0.1 \mu\text{m}$, $1 \mu\text{m}$ and $10 \mu\text{m}$ indicated by the color scheme. The continuous lines refer to the photoevaporation simulation phc2, the dashed lines to the magnetic wind b5c2 with $\beta = 10^5$ and the dotted lines to the run b4c2 with $\beta = 10^4$.

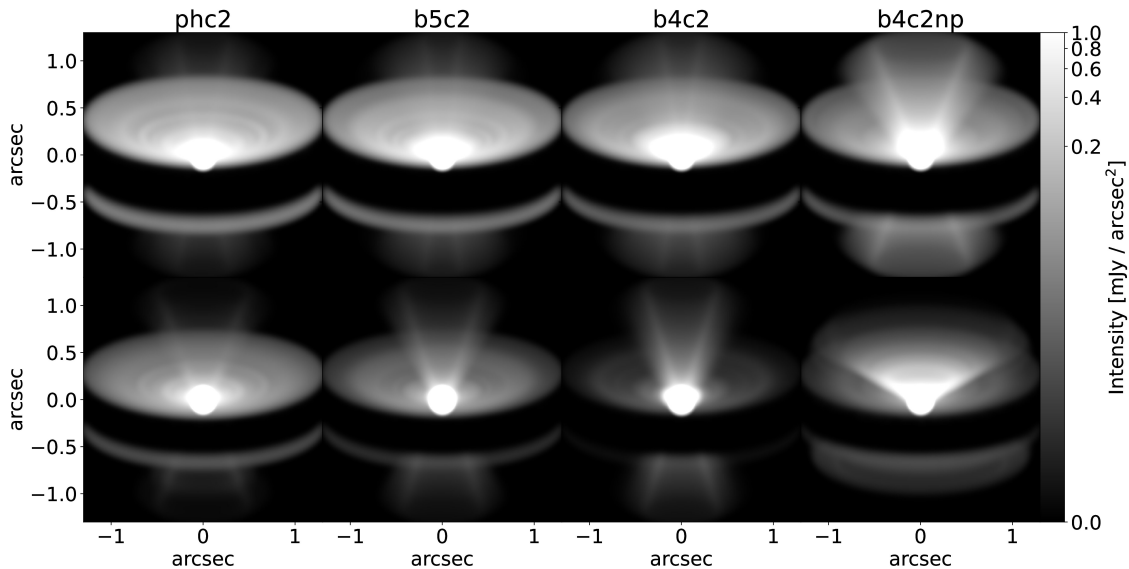


Figure 3.20: Radiative transfer images of simulation runs with photoevaporation (*left most column*), $\beta = 10^5$ (*center left column*), $\beta = 10^4$ (*center right column*) and a cold magnetic wind with $\beta = 10^4$ (*right most column*). The upper panels are based on dust grains with $a = 0.1 \mu\text{m}$ whereas the lower panels demonstrate synthetic images of the flow with $a = 1 \mu\text{m}$. The object is modeled at a distance of 150 pc with a solar type star at an inclination of 70° .

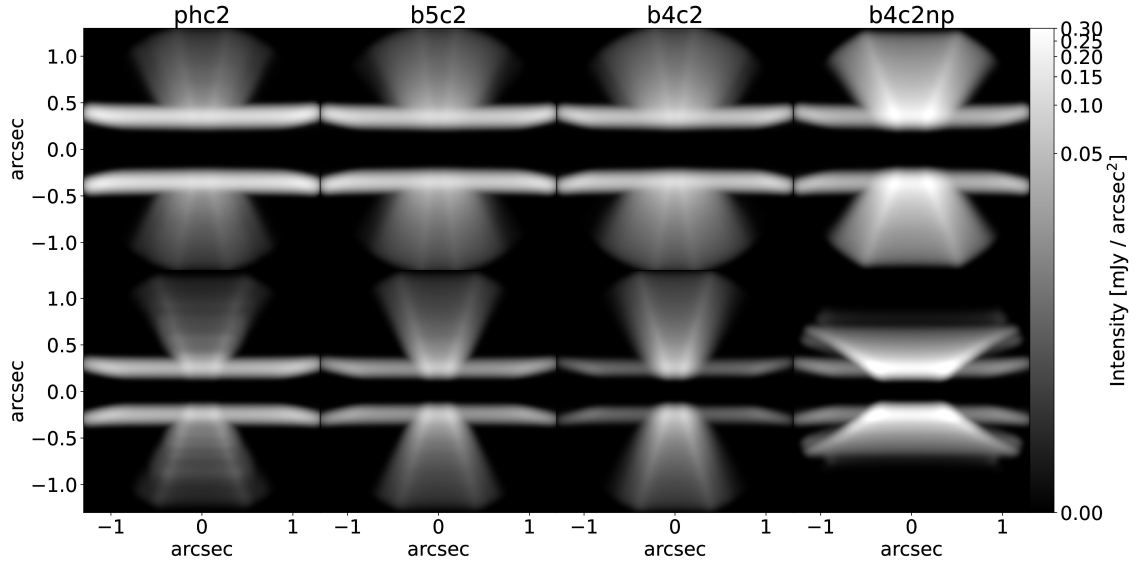


Figure 3.21: Radiative transfer images of the same simulation runs as in Fig. 3.20 but with an edge-on view at an inclination of 90° .

for all dust species in the H-band. The wind itself however is optically thin throughout the whole flow and its optical depth reaches values of $\tau_{\text{obs}} \approx 10^{-1}$ in the direction of the wind base. Naturally, the optical depth decreases with larger viewing angles due to the thinner dust and gas density in these regions.

For $1\ \mu\text{m}$ -sized grains the optical depth is comparable to the one for $0.1\ \mu\text{m}$ grains but tapers off at a flatter angle of 70° due to the less inclined dust flow. Finally, the larger $10\ \mu\text{m}$ grains are almost irrelevant since dust entrainment is negligible and the densities are therefore approaching the dust density floor value. In Fig. 3.20 and Fig. 3.21 synthetic observations are shown with inclination angles of 70° and 90° , respectively. In comparison to the disk brightness the wind structure can be clearly identified as an hourglass-shaped signature. Smaller $0.1\ \mu\text{m}$ grains are confined to a narrower cone with diffuse emission towards the outer regions. A rather sharp transition between the region devoid of dust close to the rotation axis and the inner most part of the dusty wind is visible.

The wind is not completely illuminated by the stellar light because of the decreasing dust content towards the outer regions of the disk. Comparing the results with the scattered light emission of $1\ \mu\text{m}$ grains, the large dust particles lead to a conical shape with a wider opening angle. This feature is expected from Fig. 3.12 where the increased grain size leads to weaker gas-dust coupling and therefore causes a dust flow with a smaller inclination. In addition, larger grains are entrained less efficiently in the outer regions of the disk compared to smaller grains, due to the stronger dust settling towards the disk mid plane. In combination with the larger opening angle of the flow we therefore detect a less diffuse, conical shape with a sharp transition in brightness towards the outer regions of the disk.

It is also visible that magnetic winds with stronger fields confine the dust flow more towards the rotation axis and exhibit a larger inclination angle of the dust flow. The cold MHD-wind model exhibits a brighter wind region compared to the models including photoevaporation. As expected, the opening angle of the $0.1\ \mu\text{m}$ wind flow is larger

compared to the warm wind models and resembles the emission of $1\ \mu\text{m}$ if photoevaporative heating is included. In the cold wind model $1\ \mu\text{m}$ -sized grains are entrained in a shallow angle and could be identified as a disk with a larger aspect ratio than the thermodynamics would otherwise allow in the system. At a viewing angle of 70° the backside of the disk almost shadows the dusty wind, making it difficult to identify such a dusty outflow on the basis of a low resolution or a low signal-to-noise ratio. Generally, we find the brightness contrast between wind and disk to be less in the case of $1\ \mu\text{m}$ grains if the viewing angle is 70° . In the edge-on view shown in Fig. 3.21 the wind signature brightness is comparable to the disk brightness for both grain sizes.

The synthetic observations were produced with the opacities for $a = 0.1\ \mu\text{m}$ for both grain sizes. In future projects a more detailed study with realistic opacities and more variation in grain size should be carried out.

3.4 Discussion

In the following we will discuss limitations of our wind model and compare the key results with other works in the literature. An advantage of the fluid description over a Lagrangian, particle formulation of dust grains in the simulations is the ability to resolve low density regions if a large density contrast between midplane and corona / wind is present, which is the case in the disk-wind system shown here. The disadvantage is the lack of proper modeling of a dust grain size distribution. A single-size dust population is unlikely due to dust growth and fragmentation. The synthetic observations thus only serve as a hint towards the detectability of dusty winds and the expected shape of the flow assuming the corresponding predominant dust size. Including multiple dust fluids in the synthetic observations would lead to misleading structures in the emission because of the rather sharp transition between the inner dust free cone and the wind region.

Deducing the maximum dust grain size from the wind flow angle seems to be rather difficult since the underlying parameter space is degenerate. On the one hand, the opening angle of the dusty wind increases with the grain size. On the other hand, the same effect occurs with colder magnetically driven winds. A distinction could be made by probing the wind speed, which is smaller in the cold wind case, albeit being a specific example.

If the wind is optically thin for the ionizing radiation of the central star, the difference between photoevaporative winds and warm magnetically driven winds is minor. In future works, the parameter space could be extended by varying the luminosity of the central star and by using a more sophisticated photoevaporation model as presented in Ercolano et al. (2021); Picogna et al. (2021).

Within the simulated time frame we do not observe any significant asymmetry between the upper and lower wind. Such asymmetric flows were observed in simulations by Béthune et al. (2017), Suriano et al. (2018) and Riols & Lesur (2018). Ring formation by magnetically driven winds does not occur in our simulation runs compared to Suriano et al. (2018) and Riols & Lesur (2018) where ambipolar diffusion is prescribed to be the dominant non-ideal MHD effect. In their work however, larger field strength in the regime of $\beta = 10^3$ were probed. Riols & Lesur (2018) also observed ring formation for $\beta = 10^4$ and included fluid dust focusing on the dust dynamics in the mid plane.

Given that the same photoevaporation recipe is used in this paper as the one in Franz

et al. (2020) our results are compatible in this regime. They conclude a maximum entrainable grain size of $11\ \mu\text{m}$. As shown in Fig. 3.11 our photoevaporative models allow a short-term lifting of $10\ \mu\text{m}$ dust grains which eventually fall back onto the disk. In the complete dust fluid picture the small dust grain scale height prevents any dust entrainment starting from the wind launching front. More recently, Franz et al. (2021) studied the observability of dust entrainment in photoevaporative winds based on their models in Franz et al. (2020). They conclude that the wind signature in scattered light is too faint to be observed with SPHERE IRDIS, but might be detectable with the JWST NIRCcam under optical conditions. In their synthetic observations a similar ‘chimney’-shaped wind emission is visible compared to our photoevaporative models.

Giacalone et al. (2019) found a positive correlation between gas temperature and maximum dust grain size in their semi-analytical magneto-centrifugal wind model which corresponds best to our cold magnetically driven wind model b4c2np. Our results corroborate their findings of a maximum entrainable dust size in the sub-micron regime in a cold wind around a typical T Tauri star. Our models including photoevaporation furthermore agree with Hutchison et al. (2016a) where the maximum grain size was determined to be $< 10\ \mu\text{m}$ depending on the disk radius for a typical T Tauri star. They additionally argue that dust settling most certainly limits this maximum size further which we confirm in our models, where the diminishing dust entrainment efficiency can be attributed to the dust settling towards the mid plane.

In recent scattered light observations of RY Tau (Garufi et al., 2019) a broad dusty outflow obstructing the underlying disk was detected. Both lobes are inclined by roughly 45° . The presence of a jet in this system advocates a magnetic wind launching mechanism that causes the features observed in the near-infrared. We do not observe an optically thick wind that would be able to completely obstruct the disk, since the dust densities are too low, especially in the models including photoevaporation. A possibility might hence be a slow, cold, magnetic wind at higher field strengths. The large opening angle in the observation would suggest a wind flow containing dust grains of the size of several μm if photoevaporation would be the significant wind mechanism. If a cold magnetically driven wind was the dominant factor, smaller sub-micron grains would be the solution compatible with our models.

In this work we neglected the effect of radiation pressure that may be able to blow out small dust grains. Franz et al. (2020) argued that a photoevaporative wind can entrain grains of sizes roughly 20 times larger compared to a compatible radiation pressure model from Owen & Kollmeier (2019). Since we use similar parameters for the photoevaporation model, the effect of radiation pressure should not significantly affect the dust dynamics in the studied parameter space.

In the photoevaporation models the gaseous part of the wind reaches temperatures of up to $10^4\ \text{K}$. We additionally verified that the dust temperature stays below the dust sublimation temperature.

3.5 Conclusion

We presented a suite of fully dynamic, global, multi-fluid simulations that model dust entrainment in photoevaporative as well as magnetically driven disk wind using the FARGO3D code. We demonstrated that both types of winds are able to efficiently transport dust in the wind flow and addressed the observability of such dusty winds with

the help of the RADMC-3D radiative transfer code. In the following we summarize the main results:

- The maximum entrainable dust grain size a_{\max} both depends on the type of the wind launching mechanism and the turbulent diffusivity of the disk. Whereas magnetic winds including XEUV-photoevaporation only show minor differences in a_{\max} , ranging from $3 \mu\text{m}$ to $6 \mu\text{m}$, cold magnetically driven winds at comparable field strengths only entrain sub-micron sized grains efficiently.
- With increasing radius the dust to gas ratio in the wind drops rapidly, mainly due to the smaller dust scale height in comparison to the gas scale height. Dust grains are unable to reach the wind launching surface in the outer regions of the disk and the dust content in the wind starting from these locations hence decreases. In the case of warm, ionized winds the Stokes number stays approximately constant with radius beyond 8 au. Generally, magnetically driven winds including photoevaporation are slightly more efficient in entraining dust compared to pure photoevaporative flows.
- The dust flow angle θ_d decreases with increasing grain size to the weaker coupling between gas and dust. In warm, ionized winds the flow angle reaches values of $67^\circ \leq \theta_d \leq 69^\circ$ for $a = 1 \mu\text{m}$ sized grains. At a grain size of $a = 3 \mu\text{m}$ a photoevaporative dust flow provides $\theta_d \approx 36^\circ$ whereas a warm magnetic wind leads to a steeper dust flow with $\theta_d \approx 45^\circ$. In a cold magnetic wind the flow angle is significantly smaller, being $\theta_d \approx 59^\circ$ for $a = 0.1 \mu\text{m}$ and $\theta_d \approx 25^\circ$ for micron-sized grains.
- Radiative transfer images in the H-band suggest a rather weak, optically thin emission for photoevaporative winds. A more pronounced, conical shape is visible considering $1 \mu\text{m}$ grains. The larger dust flow angle θ_d leads to a narrower emission region in the case of warm, ionized magnetic winds. Cold magnetic winds appear with a significantly larger opening angle with comparable grain sizes. The emission region of the wind appears brighter and more easily detectable due to the increased dust density of the slower magnetic wind.

Our results presented in this paper might help to constrain the magnetic field strength as well as the dominating wind mechanism if such dust signatures will be detected in future observations. The dust grain size could be determined via the inclination angle of the flow. Although the parameter space is degenerate, probing the wind speeds might help to differentiate between thermally and cold magnetically driven winds

Accretion phenomena in transition disks

4.1 Motivation

Since classical T Tauri (cTTs) stars show medial accretion rates of $\approx 1 \times 10^{-8} M_{\odot} \text{ yr}^{-1}$ (Hartmann et al., 1998), the physical mechanism at the origin of these flows has been of particular interest in the last decades. The most prominent explanation of this phenomenon has been the α -disk model (Shakura & Sunyaev, 1973; Pringle, 1981), where the effective viscosity caused by underlying turbulent motion is the driving factor of angular momentum transport and accretion, which would apply a value of $\alpha \approx 10^{-2}$ for an accretion rate of $1 \times 10^{-8} M_{\odot} \text{ yr}^{-1}$. Since there is evidence that PPDs are not necessarily strongly turbulent, as shown by Flaherty et al. (2015, 2017), the observed accretion rates could rely on an alternative way that drives accretion. Magnetically driven winds are a popular explanation since they cause mass loss both in form of a wind and accretion, as for example in the case of magnetocentrifugal winds (Blandford & Payne, 1982).

As mentioned earlier, in the presence of a magnetic field, the MRI is also a viable option for a cause of accretion, but non-ideal MHD effects, basically decoupling the magnetic field from the gas, that are active in the dead zone within the disk might diminish the efficiency of the MRI severely (Gammie, 1996). Layered accretion can still occur since the upper atmosphere of the disk is sufficiently ionized. The accretion however was found to be mostly concentrated into short bursts, incompatible with the observations (Jones et al., 2012)

The accretion rates \dot{M}_{acc} are theoretically expected to scale linearly with the disk mass if viscous accretion would be responsible for these flows (Hartmann et al., 1998; Manara et al., 2016). This can be intuitively understood by using the viscous time scale t_{visc} at the location of the outer edge of the PPD. Assuming that the disk would be accreted on the order of this time scale, the accretion rate follows as (Jones et al., 2012; Manara et al., 2016)

$$\dot{M}_{\text{acc}} \propto \frac{M_{\text{disk}}}{t_{\text{visc}}(r_{\text{out}})}. \quad (4.1)$$

In the observations the accretion rate can be deduced by estimating the accretion luminosity L_{acc} from strong emission lines due to the accretion shock close to the star, which

follow the relation (Hartmann et al., 1998; Manara et al., 2016)

$$\dot{M}_{\text{acc}} = \left(1 - \frac{R_*}{R_m}\right)^{-1} \frac{L_{\text{acc}} R_*}{GM_*}, \quad (4.2)$$

where R_* is the stellar radius, R_m the magnetospheric radius and M_* the stellar mass. Observationally, a correlation between the accretion rate and the stellar mass with a power law exponent of roughly 1.8 has been found (Muzerolle et al., 2003; Natta et al., 2004) which can be self consistently explained in the context of the common cloud collapse and viscous accretion, recovering the same relation (Dullemond et al., 2006).

Of special interest are the accretion rates observed in transition disks (TDs). Although these objects present large cavities in the inner part of the disk, strong accretion rates are measured nevertheless. In a study performed by Manara et al. (2014) 22 TDs were examined with respect to the presence of outflows and accretion phenomena. The observations were carried out with the help of the X-SHOOTER instrument at the VLT, allowing broad band spectroscopy from UV- to NIR-radiation (Vernet et al., 2011). About 80% of the sources were found to accrete at rates similar to cTTs and also revealed a LVC component signal indicating wind activity. No clear correlation between the inner radius of the dust disk r_c , marking the outer edge of the cavity, and \dot{M}_{acc} was found. The accretion rates were situated in a range between $\approx 1 \times 10^{-10} M_{\odot} \text{ yr}^{-1}$ to $1 \times 10^{-8} M_{\odot} \text{ yr}^{-1}$ up to a cavity size of $r_c \approx 70 \text{ au}$ (Manara et al., 2014).

In a follow up survey using UV-excess radiation as a tracer of the accretion rate onto the star, 66 sources were observed in the Lupus star forming region and a correlation between accretion rate and dust mass of the disks with a power law exponent of 0.7 ± 0.2 was found. This profile is shallower than expected from viscous theory but does not statistically exclude a linear scaling relation (Manara et al., 2016). This correlation could not be confirmed in CO-line emission, being used as a proxy for the gas content of the disk. It was postulated that CO-observations could not be applicable here since the CO could be absorbed into more complex molecules (Manara et al., 2016).

The findings of a similar survey in the Chameleon I star forming region by Mulders et al. (2017) corroborate the result of Manara et al. (2016), stating a power law exponent of 0.8 ± 0.2 . In both studies, MHD-winds were mentioned as a possible alternative mechanism to explain discrepancies between the observations and viscous accretion theory of PPDs. The statistical significance of the correlations in Manara et al. (2016) and Mulders et al. (2017) is however not high enough to exclude a linear relationship between \dot{M}_{acc} and M_{disk} and a need for quantitative results for wind driven accretion in transition disks was mentioned.

A simplified model of the cavital region in a transition disk subject to a wind driven flow was presented by Wang & Goodman (2017b), finding that the accretion velocities would be close to the local sound speed and that surface densities deduced from the observations could be reproduced if a small fraction of the gas column would be accreted.

Given the lack of full MHD-wind models of accretion in transition disks, this chapter attempts to perform such a study. In the previous chapter 3, we focused more on the wind region itself and the observability of dust entrainment. The inner cavity employed in these simulations rather served the purpose of isolating the inner disk from spurious boundary effects, than to provide a testbed for accretion inside cavities of transition disks.

These simulations can however be easily extended for larger cavities, leaving more space to examine the accretion flow. The resulting issues of such a setup in form of the initial magnetic field configuration and the high Alfvén velocities in the low-dense regions limited by the numerical floor density will be addressed in Sec. 4.2. Numerical results and the scaling relation between accretion rate and disk mass will be presented in Sec. 4.3. Comparisons between these results and previous studies as well as potential caveats will be discussed in Sec. 4.4. Concluding remarks summarizing the main points will be given in Sec. 4.5.

4.2 Numerical model & parameters

The disk wind model described in chapter 3 was modified to allow a detailed study of possible accretion flows in the inner cavity caused by the magnetic disk wind. For this purpose the radial density cutoff to mimic the cavity was put further outward for these simulations. Enlarging the cavity allows for an accretion flow that remains more independent from the effects of the inner radial boundary as well as inner rim of the disk. The radial location of the inner rim was therefore set to $r_c = 10$ au and $r_c = 50$ au. A significant numerical challenge is the treatment of the corona for a cold MHD-wind which is given in Sec. 3.2.2 in chapter 3.

In the previous simulations with a smaller cavity the corona was quickly blown away by the wind and the inner depleted region was not the focus of the study. In this context however, the model of a cold wind necessitates a background gas of roughly equal temperature compared to the wind since the cooling recipe does not differentiate between the wind and the background gas.

In the simulation domain a gas sphere with a temperature of ≈ 300 K is hydrodynamically unstable under the influence of the gravitational potential of the central star and the collapse of this background gas causes a strong flow towards the midplane region in the cavity. This flow quenches potential accretion flows and prevents realistic modeling of the region. One solution would be a completely adiabatic simulation with a hot corona that would be hydrodynamically stable. The wind however is most likely optically thin and the adiabatic approximation would be unrealistic.

The second solution which was chosen in this study is to lower the background density such that the effect of the collapsing flow in the ‘empty’ regions are negligible. The density contrast $\delta = \rho_{c0}(r_i) / [\Sigma(r_i) / (\sqrt{2\pi}H)]$ was lowered by two orders of magnitude to $\delta = 5 \cdot 10^{-9}$ compared to $\delta = 5 \cdot 10^{-7}$ in the previous study. With this decrease the Alfvén velocity $v_A \propto 1/\sqrt{\rho}$ generally increases and limits the time step of the simulation further. The choice of the density contrast was found to be a suitable trade-off between simulation run time and limiting the effect of the background gas. All simulation runs with varying parameters are listed in Tab. 4.1.

4.3 Results

4.3.1 Magnetic field profile

A remaining problem is the magnetic field profile in the cavity, as well as the transition between the embedded field in the disk and the one in the background gas. It is not clear how the magnetic field strength is distributed radially and which configuration

Label	β_0	α	Heating	Σ_0 [g/cm ²]	r_{out} [au]	r_c	Resolution	Simulation time
b4c10	10 ⁴	10 ⁻⁴	✓	200	50	10	500 x 240	570 orbits
b4c10lf	10 ⁴	10 ⁻⁴	✓	200	50	10	500 x 240	630 orbits
b5c10	10 ⁵	10 ⁻⁴	✓	200	50	10	500 x 240	830 orbits
b4c50	10 ⁴	10 ⁻⁴	✓	200	200	50	500 x 240	1110 orbits
b3c50np	5 · 10 ³	10 ⁻⁴	✗	200	200	50	500 x 240	1150 orbits
b4c50np	10 ⁴	10 ⁻⁴	✗	200	200	50	500 x 240	1680 orbits
b5c50np	10 ⁵	10 ⁻⁴	✗	200	200	50	500 x 240	3100 orbits
b10c10np	10 ¹⁰	10 ⁻⁴	✗	200	50	50	500 x 240	2200 orbits
b4c50npm2	10 ⁴	10 ⁻⁴	✗	400	200	50	500 x 240	1000 orbits
b4c50npm4	10 ⁴	10 ⁻⁴	✗	800	200	50	500 x 240	1000 orbits
b4c50npm6	10 ⁴	10 ⁻⁴	✗	1200	200	50	500 x 240	1000 orbits
b4c50npm8	10 ⁴	10 ⁻⁴	✗	1600	200	50	500 x 240	1000 orbits

Table 4.1: Simulations and key parameters. The numerical resolution is given in number of cells in radial and polar direction. The simulation time is measured in units of orbits at the inner radius r_{in} at 1 au.

is most suitable to examine the possibility of accretion flows in transition disks. If the vector potential is initialized in the same way as in the previous wind simulation suite in chapter 3 and ignoring the dependence on the polar angle θ for the moment we obtain:

$$A_\phi(r, \theta) = \sqrt{\frac{8\pi P}{\beta}} \left(\frac{r}{r_0}\right)^{\frac{2p+q+1}{4}}. \quad (4.3)$$

With the assumption of an axisymmetric vector potential, the polar component of the magnetic field in the midplane at $\theta = \pi/2$ or $z = 0$ results in:

$$B_\theta(r, \theta = 0) = (\nabla \times \mathbf{A})|_\theta = \frac{1}{r} \frac{\partial}{\partial r} (rA_\phi) \propto \frac{p}{2} - \frac{3-q}{4}, \quad (4.4)$$

with the previously in chapter 1 Sec. 1.3.2 introduced surface density slope p and the temperature slope q . By taking the square we arrive at the same power law as in Eq. 1.8 and the ratio of thermal and magnetic pressure, the plasma beta β , thus remains constant with radius.

This relation only holds for regions within the disk and β significantly drops at the location of the inner cavity. Considering the density contrast of approximately nine orders of magnitude, β decreases by a similar amount and the magnetic field hence dominates in the cavity.

To study the influence of this choice, another approach would be to lower the magnetic field strength in the cavity. Here, an exponential cutoff was chosen:

$$A_\phi(r, \theta) = \sqrt{\frac{8\pi P}{\beta \{1 + \exp[-a(r-b)]\}}} \left(\frac{r}{r_0}\right)^{\frac{2p+q+1}{4}}, \quad (4.5)$$

where a and b are the steepness and the location of the cutoff, respectively. The radial distribution of the plasma beta for both the simulation run b4c10np and b4c10np1f is visualized in Fig. 4.1. By choice, β is constant within the disk region for both runs. In the strong field case (b4c10np) the plasma parameter initially drops down to $\beta = 10^{-5}$ whereas in the low-strength field configuration on the right hand side in Fig. 4.1 β is larger by several orders of magnitude, as expected.

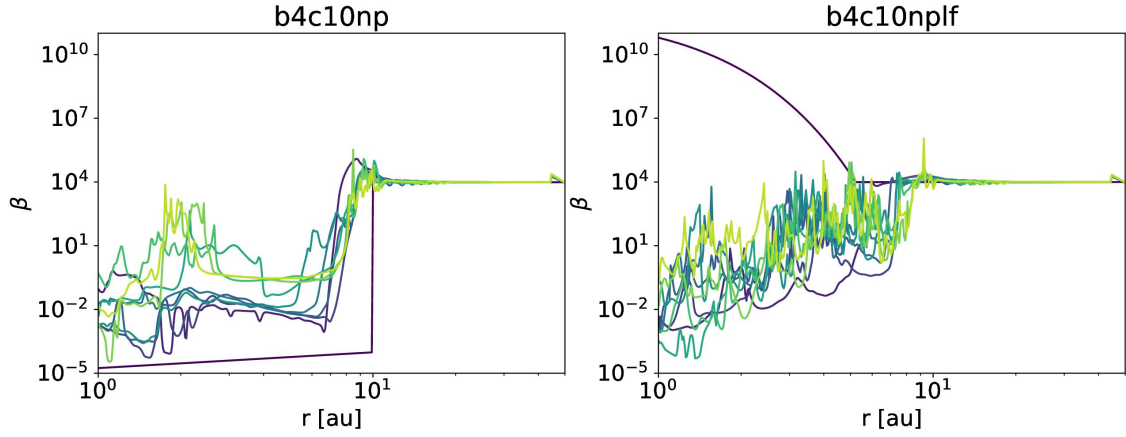


Figure 4.1: Comparison of the plasma parameter β for the first 100 orbits at 1 au in steps of 10 orbits for the simulation runs b4c10np (*left*) and b4c10np1f (*right*). On the left hand side prescription for a radially constant β within the disk region was extended into the cavity. On the right hand side the magnetic field strength was exponentially cut off in the gap.

During the first 100 orbits with reference to the inner boundary at 1 au both simulation runs equilibrate towards similar radial distributions of β . Significant differences in the overall evolution of the primitive variables become apparent in Fig. 4.3. The plots represent the state of the simulation after 10 orbits at 1 au. While the magnetic field is in a force free configuration in both the lower and upper hemisphere far from the midplane, the magnetic tension forces in the midplane straighten the field lines to a vertical orientation for the run b4c10np.

This development can be quantified by computing the effective radial velocity of the magnetic field advection v_B which reads as follows (Bai & Stone, 2017):

$$v_B = \frac{E_\phi}{B_z} = \frac{\partial_t A_\phi}{B_z} = \frac{v_r B_z - v_z B_r}{B_z}. \quad (4.6)$$

The results for the 10 first orbits at 1 au of the run b4c10np are plotted in Fig. 4.2. Within the cavity the initial curvature of the magnetic field is relaxed and transitions towards the aforementioned straight field shape, which consequently manifests as a positive advection velocity v_B . This process proceeds and completes after a few orbits until the advection of the field lines changes direction towards the central star.

The visualized excerpt of the simulation domain in Fig. 4.3 also reveals the beginning of the magnetic wind build-up. A narrow overdensity appears in the low-density cavity. This phenomenon is not caused by gas accretion from the inner rim of the disk towards the star but by the background gas falling vertically towards the midplane. The toroidal magnetic field ‘winds up’ and increases in strength due to the shearing motion between the azimuthally stationary corona and the disk rotating at approximately Keplerian speeds. The buildup is most pronounced at the inner rim where the ionization fraction is higher since the ionizing radiation directly illuminates the corresponding parts without being blocked by the disk material.

In the low-field configuration of the run b4c10np1f the gas becomes more unstable compared to b4c10np. Strong magnetic pressure gradients at the inner rim location of the disk drive gas flows into the cavity and towards the star since no considerable resistance is present in the low-density low-field region. The weak magnetic field orients

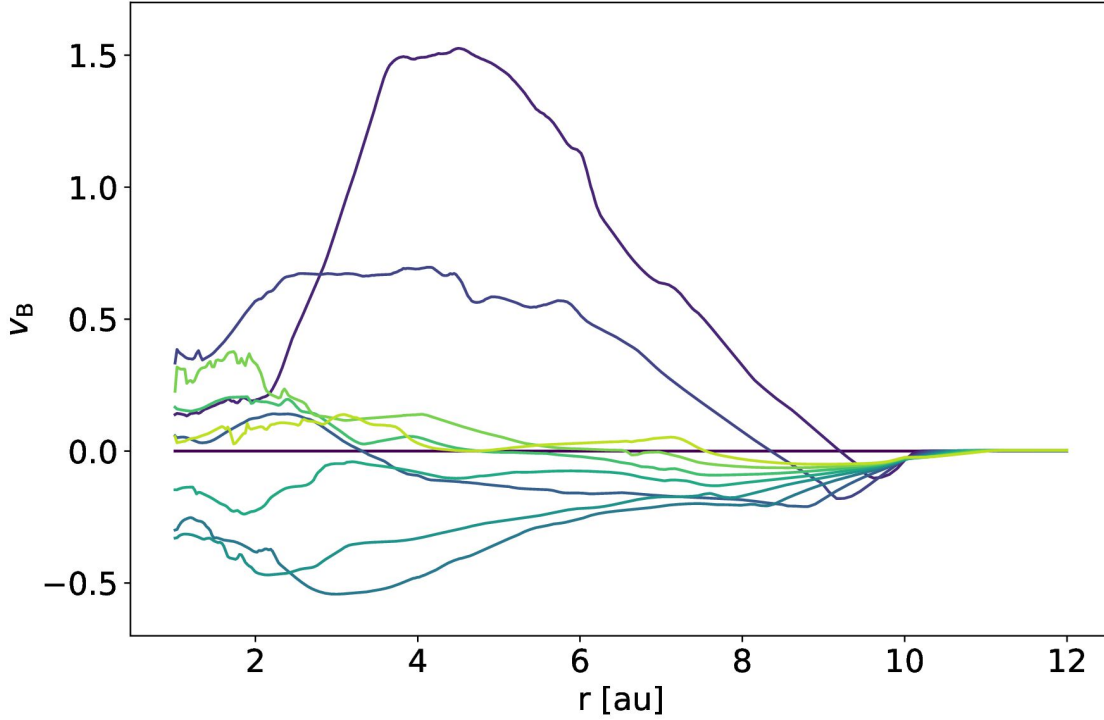


Figure 4.2: Comparison of the density distribution (*left*) and the toroidal magnetic field strength *right* after 10 orbits at 1 au for the simulation runs b4c10np (*top*) and b4c10np1f (*bottom*). The velocity v_B is expressed in dimensionless code units.

itself along the gas flow directions and becomes almost radial in the gap. A low-density atmosphere accumulates in the cavity, being vertically limited by the infalling background gas. The toroidal magnetic field structure becomes more complex compared to the one of the strong-field run and increases within a region of $r \approx 5$ au. This initially rather unstable magnetic field configuration is less suitable for analyzing accretion flows emerging from the disk-wind interaction that is expected to set in when the wind is fully developed.

4.3.2 Gas dynamics

A variety of complex behavior emerges from the simulated system during its evolution. First, we focus on the run b4c10np with a density cutoff at 10 au without photoevaporation effects, as shown in Fig. 4.4. Time scales will be expressed relative to the orbital time scale T_0 at inner boundary of the simulation at 1 au.

After a view orbits a narrow band of overdense gas forms within the gap, as discussed above and shown in Fig. 4.3. The band is basically a shock front caused by the infalling background gas. Once the simulation reaches a few orbits at the location of the inner rim of the disk a radial accretion stream forms and replaces the shock front. This is the case in the left panel of Fig. 4.4, where the inner rim of the disk has passed ≈ 3 orbits. Close to the inner boundary of the simulation gas and thereby magnetic flux start to accumulate and an additional wind starts to emerge, visible as two narrow vertical bands in the left panel of Fig. 4.4. It is not entirely clear if this effect is artificial or physical. The choice of location of the inner boundary presumably affects this part of the simulation

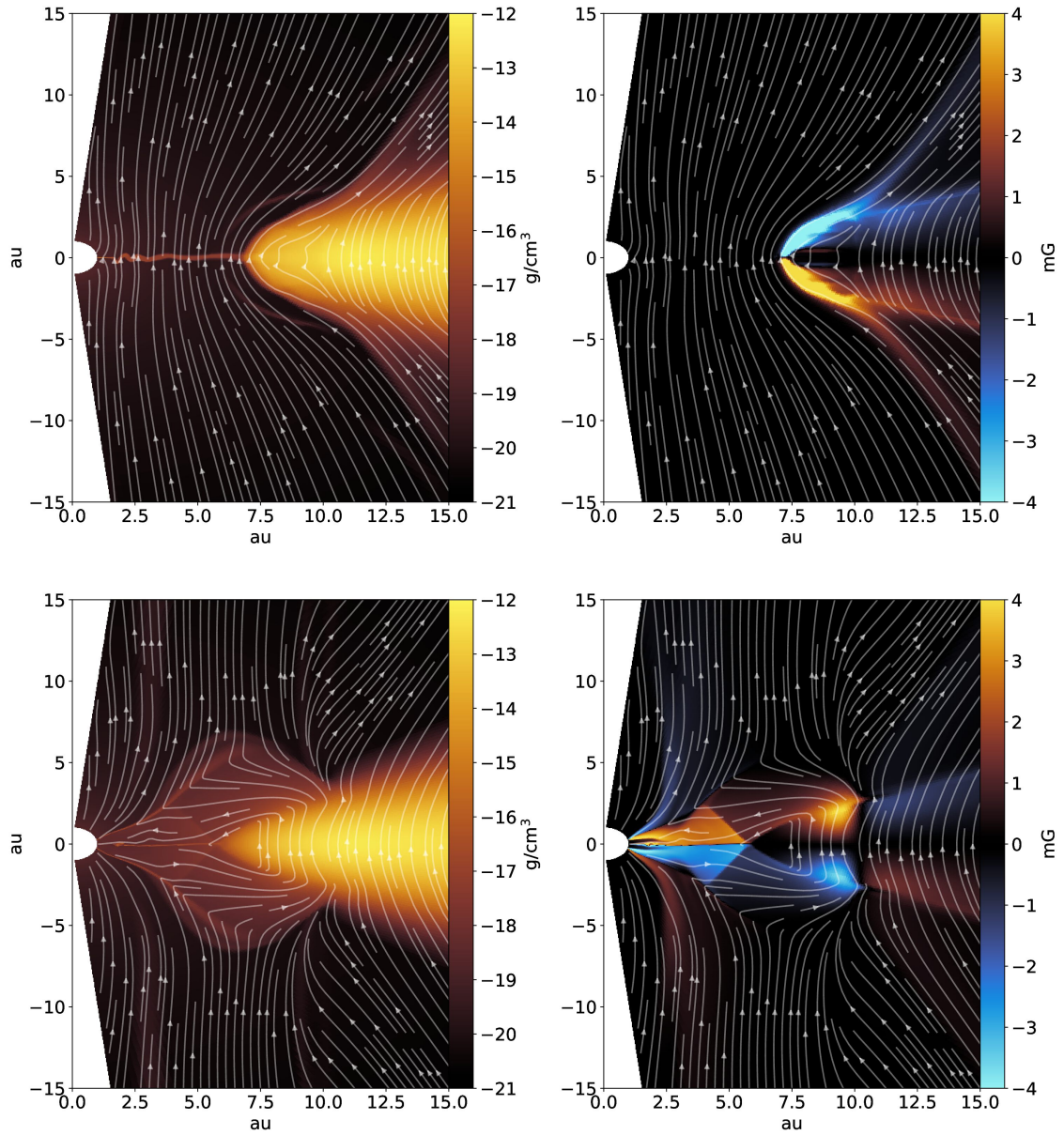


Figure 4.3: Comparison of the density distribution (*left*) and the toroidal magnetic field strength *right* after 10 orbits at 1 au for the simulation runs b4c10np (*top*) and b4c10np1f (*bottom*). The white-arrowed streamlines represent the magnetic field lines.

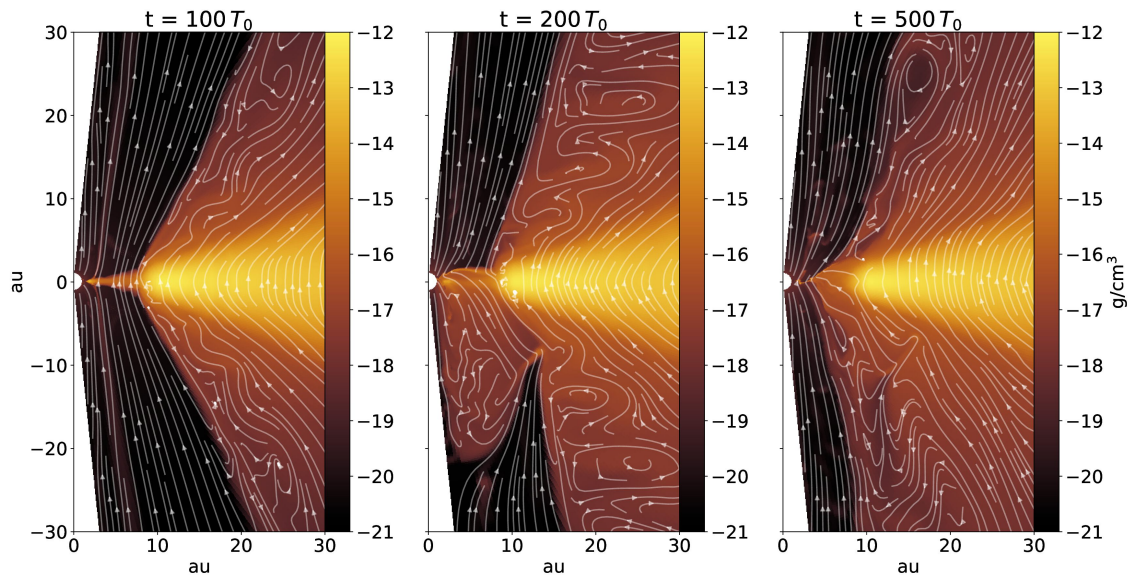


Figure 4.4: Density maps of the wind-accretion system taken from the simulation b4c10np after an evolution of $t = 100 T_0$, $200 T_0$ and $500 T_0$, where T_0 is orbital time scale at 1 au. The white arrowed lines represent the magnetic field lines.

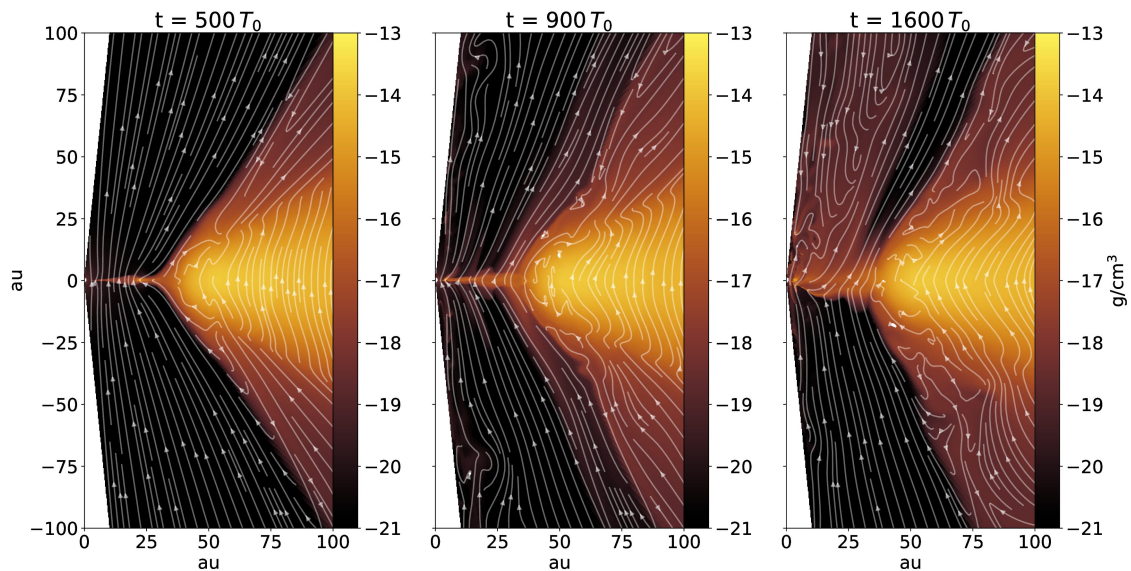


Figure 4.5: Density maps of the wind-accretion system taken from the simulation b4c50np after an evolution of $t = 500 T_0$, $900 T_0$ and $1600 T_0$, similar to Fig. 4.4.

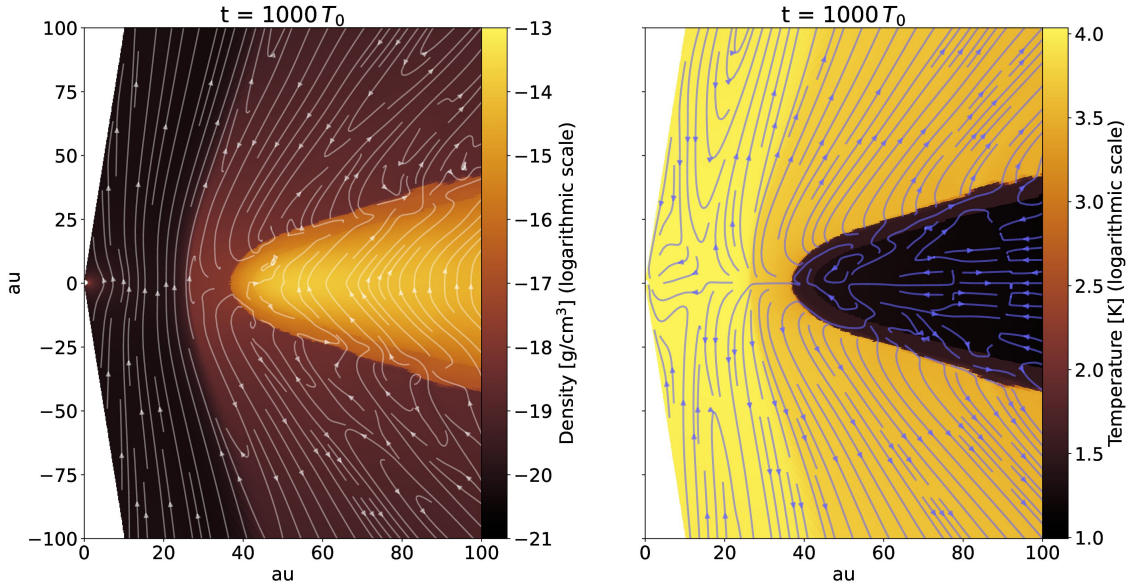


Figure 4.6: Density and temperature map taken from the simulation b4c50np at $t = 1000 T_0$ including photoevaporation and a cavity at $r_c = 50$ au. In the left panel the white arrowed lines represent the magnetic field lines whereas on the right hand side the blue lines trace the streamlines of the velocity field of the snapshot.

since accretion through the boundary is challenging to model accurately and accretion most likely stops due to the decoupling between the gas and the magnetic field by the Ohmic diffusion buffer. The phenomenon however does not have a significant on the accretion flow at larger radii.

At later times, the center and right panel of Fig. 4.4 show a lopsided wind starting from within the cavity which eventually evolves into a more irregular outflow involving both sides. A possible cause for the behavior could be the increasingly larger amount of magnetic flux present in the cavity that launches the wind in the same manner like the disk itself.

To analyze whether the dynamics are affected by the proximity of the inner simulation boundary to the inner rim of the disk, the density maps of the run b4c50np with a larger cavity of 50 au are displayed in Fig. 4.5. The location of the inner simulation boundary was chosen to be 1 au. The phenomenology stays roughly the same compared to b4c10np. The accretion flow enters the cavity, stabilizes and causes a narrow wind close to the inner boundary. Eventually, a one-sided wind forms, similar to the simulation runs with a cavity at 10 au. The mechanism thus seems to be rather insensitive to the distance of the inner rim of the disk to the simulation boundary.

A snapshot of a simulation run including photoevaporation and a cavity at $r_c = 50$ au is shown in Fig. 4.6. No accretion flow is visible as all of the inflowing matter evaporates due to the heating of the ionizing radiation. The temperature map displayed on the right hand side in Fig. 4.6 reveals, that the wind flow emerging from inner rim of the disk reaches temperatures of multiple thousands of Kelvin, which are typical values for XEUV-driven photoevaporation. In order to test, whether it can be excluded that a wrong configuration of the initial conditions of the disk could be responsible for the accretion flows, three snapshots of the simulation run b10c10np with $\beta = 10^{10}$ and $r_c = 10$ au are presented in Fig. 4.7. Although the cut in the gas density at the inner boundary of the

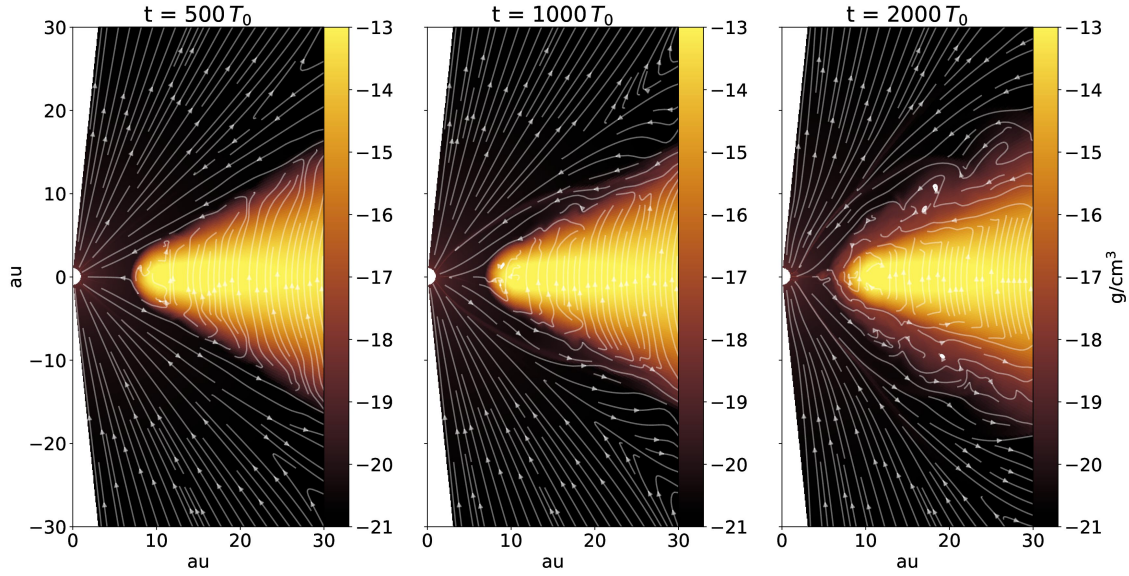


Figure 4.7: Density map taken from the simulation b10c10np with $\beta = 10^{10}$ and a cavity at $r_c = 10$ au. The white arrowed lines annotate the magnetic field lines.

disk at $r = r_c$ is basically a step function, no long term effects of this initial condition are visible in the evolution of the disk. The inner rim quickly smooths out and no accretion flow develops since the magnetic field six orders of magnitude weaker compared to the fiducial model.

Furthermore, no photoevaporation effects were included that could stability the inner part. Besides slightly more diffuse outer layers of the transition disk, the system remains comparatively stable. It can thus be excluded that the initial conditions would be responsible for the accretion phenomena observed in the results presented in this section.

4.3.3 Accretion rates

The primary focus of this study is the determination of the accretion rates due to magnetic wind effects in transition disks. For this purpose the actual accretion rate \dot{M}_{acc}^s was measured in the simulations by evaluating

$$\dot{M}_{\text{acc}}^s(r) = -2\pi r \int_{-z_0}^{z_0} \rho(r, z) v_r(r, z) dz, \quad (4.7)$$

where z_0 is the vertical limit of the part of the accretion stream.

Accretion flows already form in the early stages of the simulation without any significant wind effects in the vicinity of the stream, as visible in Fig. 4.4 and Fig. 4.5. The question is which physical mechanism causes the accretion and therefore a rough estimate of the accretion rate as a consequence of magnetic stresses can be made, starting from the conservation of angular momentum.

The basis for the calculation is the momentum equation stated in chapter 1 in Eq. 1.25. Expressing the momentum equation in a conservative form, multiplying the azimuthal component with r to obtain the evolution of angular momentum and neglecting thermal

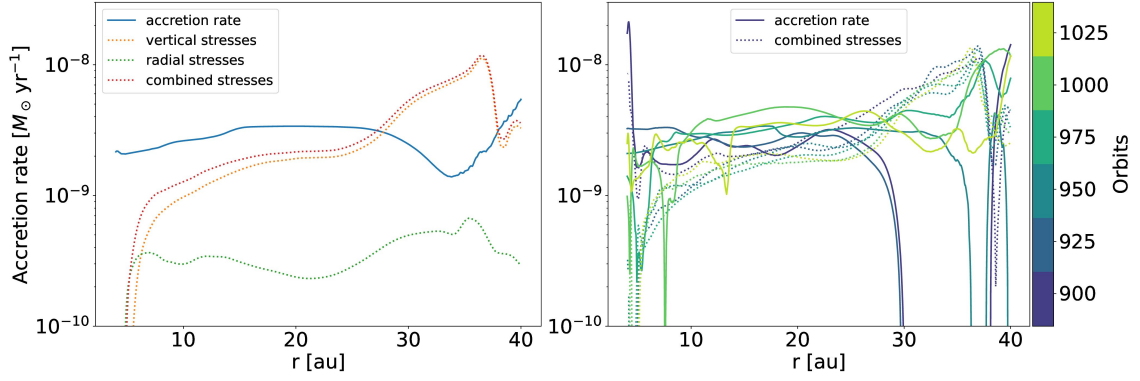


Figure 4.8: *Left panel:* Accretion rate in solar masses per year and stresses versus radius of the simulation run b4c50np with a cavity of 50 au. The simulation outputs were averaged over a time span of $\Delta t = 150 T_0$ starting from $t = 900 T_0$. The blue line represents the direct accretion rate $\dot{M}_{\text{acc}}^{\text{s}}$ and the dotted line the accretion rate $\dot{M}_{\text{acc}}^{\text{t}}$ computed by the Maxwell stresses. These results were split up by both the vertical and radial contributions of the Maxwell stress.

Right panel: Accretion rate $\dot{M}_{\text{acc}}^{\text{s}}$ (solid lines) and the accretion rate computed by the Maxwell stresses $\dot{M}_{\text{acc}}^{\text{t}}$ (dotted lines) varying in time. The time unit represents orbits at 1 au.

pressure effects yields (Balbus & Hawley, 1998):

$$\frac{\partial}{\partial t} (\rho r v_\phi) + \nabla \cdot \left[\rho r v_\phi \mathbf{v} - \frac{B_\phi \mathbf{B}_p}{4\pi} + \frac{B_p^2}{8\pi} \hat{\mathbf{e}}_\phi \right] = 0, \quad (4.8)$$

where \mathbf{B}_p is the poloidal magnetic field component (no azimuthal part) and $\hat{\mathbf{e}}_\phi$ is the azimuthal unit vector. Assuming azimuthal symmetry, the divergence of the last term representing the poloidal magnetic pressure vanishes. If we furthermore consider a steady-state solution and vertically integrate the result similar to Eq. 4.7 we obtain:

$$\int_{-z_0}^{z_0} \left[\frac{1}{r} \frac{\partial}{\partial r} r^2 \left(\rho v_\phi v_r - \frac{B_\phi B_r}{4\pi} \right) + \frac{\partial}{\partial z} \left(r \rho v_\phi v_z - r \frac{B_\phi B_z}{4\pi} \right) \right] dz = 0. \quad (4.9)$$

y The vertical integration of the gas density results in the surface density Σ and both magnetic terms can be denoted as the radial and vertical Maxwell-stress tensor $T_{\phi r}$ and $T_{\phi z}$, respectively:

$$T_{\phi r} = \frac{B_\phi B_r}{4\pi}, \quad (4.10)$$

$$T_{\phi z} = \frac{B_\phi B_z}{4\pi}. \quad (4.11)$$

The vertically integrated radial Maxwell-stress will be expressed as $\bar{T}_{\phi r}$. Substituting $\dot{M}_{\text{acc}} = -2\pi r \Sigma v_r$ as well as applying the previous simplifications yields:

$$-\frac{1}{2\pi} \frac{\partial}{\partial r} (r v_K \dot{M}_{\text{acc}}^{\text{t}}) + \frac{\partial}{\partial r} (r^2 \bar{T}_{\phi r}) + r T_{\phi z} \Big|_{-z_0}^{z_0} = 0, \quad (4.12)$$

with the local Keplerian velocity $v_K = \sqrt{\frac{GM_*}{r}}$.

Under the assumption of a radially constant accretion rate the left most term can be

simplified further by evaluating the derivative, which finally leads to the identical result for the ‘theoretical’ accretion rate $\dot{M}_{\text{acc}}^{\text{t}}$ as the one in Bai (2017b):

$$\dot{M}_{\text{acc}}^{\text{t}} = \frac{4\pi}{v_{\text{K}}} \left[\frac{\partial}{\partial r} (r^2 \bar{T}_{\phi r}) + r T_{\phi z} \Big|_{-z_0}^{z_0} \right]. \quad (4.13)$$

Equipped with these diagnostics, the physical nature of the accretion flow can be examined in more detail. Results for the accretion rates are displayed in Fig. 4.8. The accretion rate of the simulation run b4c50np with a cavity at 50 au and a cold magnetic wind reveals a radially almost constant accretion rate on the order of $\dot{M}_{\text{acc}}^{\text{s}} \approx 3 \times 10^{-9} M_{\odot} \text{ yr}^{-1}$ at $r = 20$ au.

The accretion rate resulting from the computation of the Maxwell stresses however is smaller by approximately a factor of two at this radial location. These accretion rates do not completely match the measured rates of the flow but are of comparable order of magnitudes. The panel on the right hand side of Fig. 4.8 demonstrates that the accretion flow is rather unstable and that the solution has not yet converged at this point of time in the simulation. The accretion rates $\dot{M}_{\text{acc}}^{\text{t}}$ computed from the Maxwell stresses furthermore seem to agree better with the directly measured rates at earlier times in the inner region of the cavity.

Although the calculation involving the Maxwell stresses can not perfectly recover the actual accretion rates in the simulation, they clearly indicate the vertical Maxwell stresses dominate over the radial Maxwell stresses by almost one order of magnitude and are thus the driving factor of the accretion flow. Given that the magnetic field stays predominantly vertical before the secondary wind emerges in the cavital region, as visible in Fig. 4.4 and Fig. 4.5, it is intuitive that the contribution of the vertical Maxwell stress should be significantly larger than the radial one. The accretion mechanism can thus be regarded as a sort of vertical magnetic breaking.

4.3.4 Parameter study

In the following the sensitivity of the accretion rate in the cavity with respect to the initial disk mass and the plasma beta will be examined. The variation in disk mass was realized by changing the initial surface density $\Sigma(r = 1 \text{ au})$ (denoted by Σ_0 in the subsequent paragraphs) to multiples of $\Sigma_0 = 200 \text{ g/cm}^2$ in the simulation runs b4c50npm2, b4c50npm4, b4c50npm6 and b4c50npm8 up to a value of $\Sigma_0 = 1600 \text{ g/cm}^2$, which is close to the typical surface density assumed in the MMSN-model with $\Sigma_0 = 1700 \text{ g/cm}^2$.

Both the direct accretion rate $\dot{M}_{\text{acc}}^{\text{s}}$ and the accretion rate computed from the Maxwell stresses $\dot{M}_{\text{acc}}^{\text{t}}$ for the various initial gas surface densities are plotted in Fig. 4.9. The results were averaged over $\Delta t = 90 T_0$ starting from $t = 600 T_0$ which corresponds to the time frame when most of the cavital region of the disk is wind-free for all simulations. Additionally, the accretion rates were radially averaged in the range of $15 \text{ au} \leq r \leq 25 \text{ au}$ in order to smooth out radial fluctuations. It should be noted that these accretion flows are not necessarily in a steady-state, as shown previously in Fig. 4.8.

The data points in the left panel of Fig. 4.9 show a clear positive trend towards higher surface density since naturally a larger mass reservoir and density at the inner rim of disk would be expected to funnel more material into the cavity. This is especially the case because of the same value of $\beta = 10^4$ for all simulations with the variation in surface density listed above. To obtain the same value of β the ratio of thermal pressure

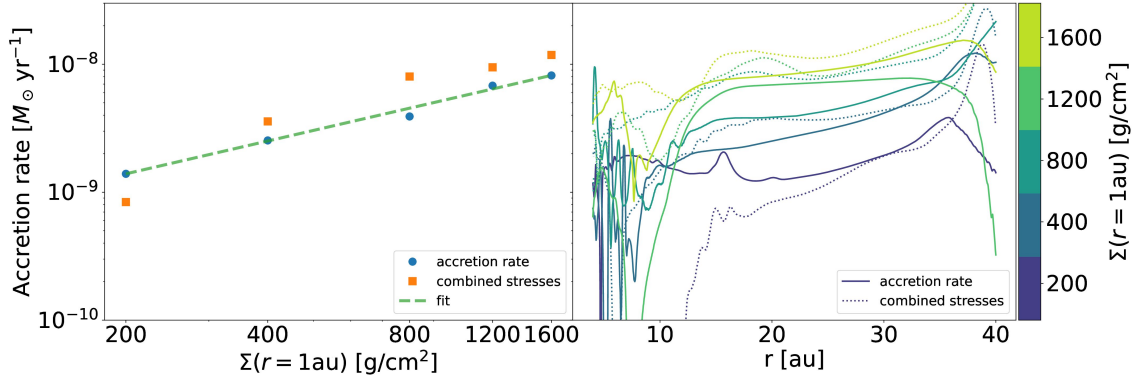


Figure 4.9: *Left panel:* Accretion rate in solar masses per year and stresses versus the initial surface density at $r = 1$ au of the simulation runs b4c50np, b4c50npm2, b4c50npm4, b4c50npm6 and b4c50npm8 with a cavity of 50 au. The simulation outputs were averaged over a time span of $\Delta t = 90 T_0$ starting from $t = 600 T_0$. The blue dots represent the direct accretion rate $\dot{M}_{\text{acc}}^{\text{s}}$ and the squared markers the accretion rate $\dot{M}_{\text{acc}}^{\text{t}}$ computed by the Maxwell stresses. The results of $\dot{M}_{\text{acc}}^{\text{s}}$ were fitted in logarithmic space, represented by the dashed green line.

Right panel: Accretion rate $\dot{M}_{\text{acc}}^{\text{s}}$ (solid lines) and the accretion rate computed by the Maxwell stresses $\dot{M}_{\text{acc}}^{\text{t}}$ (dotted lines) for different initial disk masses, calculated with the same procedure as described for the left panel.

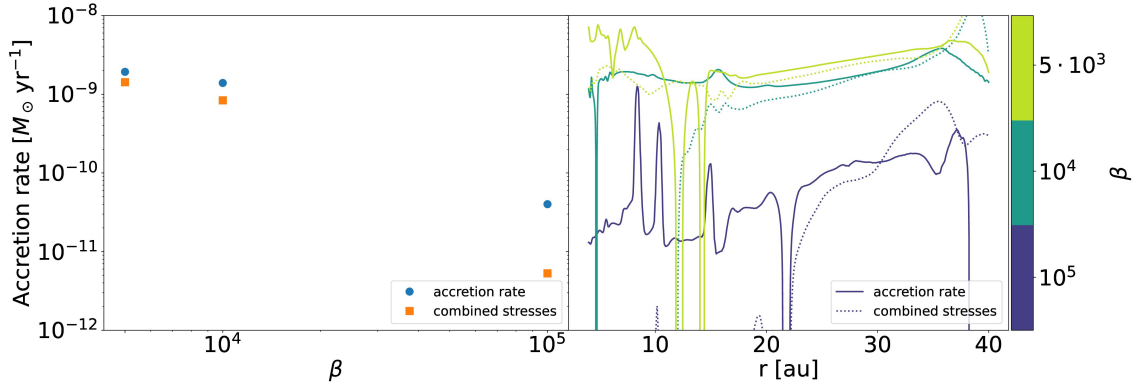


Figure 4.10: *Left panel:* Accretion rate in solar masses per year and stresses versus plasma beta for the simulation runs b3c50np, b4c50np and b5c50 with a cavity of 50 au. The simulation outputs were averaged over a time span of $\Delta t = 90 T_0$ starting from $t = 600 T_0$. The blue markers represent the direct accretion rate $\dot{M}_{\text{acc}}^{\text{s}}$ and the squared markers the accretion rate $\dot{M}_{\text{acc}}^{\text{t}}$ computed by the Maxwell stresses.

Right panel: Accretion rate $\dot{M}_{\text{acc}}^{\text{s}}$ (solid lines) and the accretion rate computed by the Maxwell stresses $\dot{M}_{\text{acc}}^{\text{t}}$ (dotted lines) depending on β . The values were averaged in the same manner as the results in the left panel.

and magnetic pressure needs to remain constant and the magnetic field strength thus has to increase quadratically compared to the increase in density, leading to stronger magnetic forces and accretion flows.

Numerical values for the accretions rates are $\dot{M}_{\text{acc}}^{\text{s}} \approx 1.9 \times 10^{-9} M_{\odot} \text{ yr}^{-1}$, $2.5 \times 10^{-9} M_{\odot} \text{ yr}^{-1}$, $3.9 \times 10^{-9} M_{\odot} \text{ yr}^{-1}$, $6.8 \times 10^{-9} M_{\odot} \text{ yr}^{-1}$ and $8.2 \times 10^{-9} M_{\odot} \text{ yr}^{-1}$ for the initial surface densities $\Sigma_0 = 200 \text{ g/cm}^2$, 400 g/cm^2 , 800 g/cm^2 , 1200 g/cm^2 , 1600 g/cm^2 , respectively. The accretion rate data of $\dot{M}_{\text{acc}}^{\text{s}}$ presented in Fig. 4.9 fits well to a power law with an exponent of the value of ≈ 0.85 . Depending on the initial surface density, we obtain the following scaling relation for the accretion rate:

$$\dot{M}_{\text{acc}}^{\text{s}}(\Sigma_0) \approx \left(\frac{\Sigma_0}{200 \text{ g/cm}^2} \right)^{0.85} 1.4 \times 10^{-9} M_{\odot} \text{ yr}^{-1} \quad (4.14)$$

Extrapolating the result to the density of the MMSN-model, an accretion rate of $\dot{M}_{\text{acc}} \approx 8.6 \times 10^{-9} M_{\odot} \text{ yr}^{-1}$ would be expected.

To estimate the impact of the plasma beta on the accretion flow, the accretion rates $\dot{M}_{\text{acc}}^{\text{s}}$ and $\dot{M}_{\text{acc}}^{\text{t}}$ depending on β are plotted in Fig. 4.10 for the simulation runs b3c50np, b4c50np and b5c50np with $\beta = 5 \cdot 10^3$, 10^4 and 10^5 , respectively. The accretion rate decreases significantly for the case with $\beta = 10^5$ and presents strong radial fluctuations in the plot on the right hand side of Fig. 4.10. This result can be considered to be caused by numerical artifacts and what is displayed here, mostly originates from the infalling background gas that continuously becomes replenished due to the floor density in the code. Moreover, the magnetic field does not seem strong enough to cause a strong accretion flow towards the star. It could however be possible that a comparatively weak accretion flow could form if the numerical floor density could be lowered further. Considering these drawbacks, the accretion rate of b5c50np can not be interpreted as a physical result.

The numerical value of the accretion rate resulting from b3c50np with $\beta = 5 \cdot 10^3$ $\dot{M}_{\text{acc}}^{\text{s}} = 1.93 \times 10^{-9} M_{\odot} \text{ yr}^{-1}$ is about 39 % higher compared to the simulation run with $\beta = 10^4$.

4.4 Discussion

The results of the simulation runs with cold magnetic wind with a plasma beta of $\beta = 10^4$ and below presented gas accretion flows in the inner cavity, driven into the gap by the magnetic wind. Accretion rates were found to be in the range of $\dot{M}_{\text{acc}}^{\text{s}} \approx 1 \times 10^{-9} M_{\odot} \text{ yr}^{-1}$ to $\dot{M}_{\text{acc}} \approx 8 \times 10^{-9} M_{\odot} \text{ yr}^{-1}$, which are completely compatible with the observed accretion rates in Manara et al. (2014), Manara et al. (2016) and Mulders et al. (2017).

We furthermore yield the result of a scaling relation between the accretion rate $\dot{M}_{\text{acc}}^{\text{s}}$ and the initial extrapolated surface density Σ_0 with a power law exponent of ≈ 0.85 . Since the initial surface density Σ_0 can be taken as a proxy for the total disk mass and assuming that the gas mass scales with the observed dust mass, the result of the power law fits well into the results by Manara et al. (2016) and Mulders et al. (2017), being $\approx 0.7 \pm 0.2$ and $\approx 0.8 \pm 0.2$. Interestingly, the trend is shallower than linear, as the observations indicate as well, differing from the expected result from viscous accretion theory. Considering that it can not be statistically excluded that the correlation could be shallower than linear, this result could give a hint towards the presence of wind-driven accretion in cTTs.

These results should however be expected to be affected by significant uncertainties. The simulations only showed a clear wind-free accretion funnel for several hundreds orbits at the inner boundary, which corresponds to only a few dynamical time scales at the location where the accretion rate was determined (15 au to 25 au). The accretion rates were determined at this stage of the evolution since the development of the secondary wind in the cavity could potentially be of artificial origin. At the radially inner simulation boundary gas piles up and does not accrete through the boundary. Further simulation would be necessary to model this part of the system in more detail and to implement a more sophisticated treatment of the radially inner boundary conditions. In this study the buffer zone with an elevated value of Ohmic diffusion identical to the one in chapter 3 was implemented. The decoupling of the magnetic field and the gas by this measure prevents further accretion.

In a real system the accretion would most probably continue much further inwards down to the radius of magnetospheric accretion r_m close to the star, which can be situated at several stellar radii (Bouvier et al., 2007). Putting the inner boundary close enough to model this part of the system would be computationally challenging in the current code. Other than the small time step limited by the small cell size in this region, an additional challenge would be the need of a better ionization model due to thermal ionization this close to the star.

In the hot wind model including photoevaporation, no accretion stream was able to form since all the material almost directly evaporates and joins the wind flow. For the case of $\beta = 10^4$ and $\Sigma_0 = 200 \text{ g/cm}^2$ the picture of non-accretion transition disks with large cavities put forward in Owen (2016) can be confirmed. It is however possible that a combination of photoevaporation and magnetically driven winds in a more massive disk would again accrete, due to the higher accretion rate. Further studies would be necessary to test this hypothesis.

Dust was not included in these models since numerical instabilities were encountered close to the inner boundary with the fluid description of dust. In the cold wind models a large part of the simulation domain is not supported by the wind flow and collapses towards the radially inner region. Including dust as a pressureless fluid proved to be difficult and further improvements have to be made.

The estimation of the accretion rate \dot{M}_{acc}^t by evaluation of the radial and vertical Maxwell stresses resulted in significant deviations from the direct computation of \dot{M}_{acc}^s . A reason for this could be that the system is not in a completely steady state and that the Maxwell stresses can only be taken as a rough indicator which part is predominantly driving the accretion process, which was the vertical Maxwell stress in this case.

The initial distribution of the magnetic field is rather unconstrained and here the assumption of a radially constant plasma beta was chosen. Inside the cavity this choice lead to small values of β below unity. It is debatable whether these initial conditions are most suitable for examining the accretion flows but tests with different conditions lead to more chaotic behavior due to the lack of equilibrium of the magnetic pressure, as presented in Sec. 4.3.1.

4.5 Conclusion

In this chapter the fully dynamic, non-ideal magnetohydrodynamical simulations of a transition disk with a large inner cavity were presented. Simulations with and without

internal XEUV-photoevaporation were carried out. The impact of the size of the inner cavity r_c was tested for the values $r_c = 10$ au and $r_c = 50$ au. In the following the main results are summarized:

- Cold magnetically winds are able to drive significant accretion flows into the inner cavity of the transition disk, even with a gap of $r_c = 50$ au. The accretion rates are on the order of $\approx 1 \times 10^{-9} M_\odot \text{ yr}^{-1}$ to $\approx 1 \times 10^{-8} M_\odot \text{ yr}^{-1}$, depending on the initial disk mass and an initial plasma beta of $\beta = 10^4$.
- By varying the initial disk mass, a correlation between the accretion rate and the initial surface density was found, resulting in

$$\dot{M}_{\text{acc}}^s(\Sigma_0) \approx \left(\frac{\Sigma_0}{200 \text{ g/cm}^2} \right)^{0.85} 1.4 \times 10^{-9} M_\odot \text{ yr}^{-1} \quad (4.15)$$

The scaling relation is shallower than viscous accretion theory would predict and the result of the power law exponent of 0.85 is consistent with recent observational surveys of transition disks (Manara et al., 2016; Mulders et al., 2017).

- Photoevaporation completely shuts off any accretion flow since the wind rates are large enough to evaporate away the material inside the cavity of the transition disk. Thus, even in the presence of a magnetically driven wind, a combination with photoevaporation can lead to a non-accreting transition disk with a large cavity.
- The accretion flow is mostly dominated by magnetic breaking inside the cavity caused by the vertical Maxwell stress $T_{\phi z}$. Secondary magnetic winds form within the cavity, but an artificial numerical origin cannot be excluded at this point.

All in all, this study showed that magnetically driven winds are capable to explain some of the key observations of transition disks with large inner cavities and thus provided thus a viable alternative to the viscous accretion model usually applied.

Conclusions and Outlook

In these thesis multiple projects discussing signatures of planet-disk interaction and disk winds were presented. Identifying these kind of signatures are important to further constrain the planet formation process and the evolution of protoplanetary disks. The presence of the crescent-shaped asymmetry in the HD 163296 disk located at the innermost large gap (Huang et al., 2018a) invited to take a closer look whether this feature could be a signpost of an embedded planet, as also discussed in (Zhang et al., 2018). Going further than the results in Zhang et al. (2018), the work presented in chapter 2 aims to quantify this feature with the help of hydrodynamic simulations including dust as a pressureless fluid in more detail. By modeling the system with three planets we could qualitatively reproduce the observed substructures of the system, using eight distinct dust fluids with a MRN grain size distribution ranging from $a_{\min} = 0.19 \mu\text{m}$ to $a_{\max} = 19 \mu\text{m}$. The crescent shaped asymmetry could be identified to be at the location of the trailing Lagrange point L5 of an embedded planet in the inner gap of the system at 48 au. Dust also accumulated at the leading L4 point but diffuses completely away during the evolution of the system. In the case of significant dust feedback onto the gas, the L4 point efficiently traps dust and both asymmetries fragment after a few hundred local orbits. A large dust-to-gas ratio would thus be incompatible with the observations.

We found that by normalizing the intensity of ring 1 to the observed values, 10 to 15 earth masses could be trapped in the asymmetry located at the L5 point. This results was mostly insensitive to variation of viscosity, aspect ratio, planet mass and eccentricity. We determined that a planet mass of at least 0.25 Jupiter masses of planet 1 would be necessary to cause a persisting asymmetry in the dust as observed. The best fit compared to the observations could be achieved by choosing $0.5 M_{\text{jup}}$ and $0.25 M_{\text{jup}}$ for planet 1 and planet 2, respectively.

The simulations could however not explain the vicinity of the asymmetry to the radially outer edge of the gap. This discrepancy could not be resolved by increasing the eccentricity of the planet. This measure would only disrupt the feature lifetime, or even prevent the formation of the asymmetry entirely. It is thus unclear how the position of the feature could be explained. Further studies including planetary migration could shed light on this issue. It is also unclear whether the dynamics of the asymmetry would persist if full 3D simulations would be performed. To date, no such study has been carried out and it would be an interesting future project to investigate this issue further. Gaining more insight into the nature of such asymmetries would also add the advan-

tage of predicting the azimuthal location of embedded planets by observing the dust continuum.

In chapter 3 we could successfully demonstrate that dust entrainment in both photoevaporative winds and magnetically driven winds is possible, depending on the grain size. Whereas in the warm wind case including photoevaporation the maximum entrainable grain size a_{\max} would be ranging from $3\ \mu\text{m}$ to $6\ \mu\text{m}$, a cold magnetic wind would only be able to carry away sub-micron sized grains.

Further radially outward the dust entrainment efficiency significantly drops. This phenomenon seems to be caused entirely by the smaller ratio of dust scale height to gas scale height at larger radii, which could be furthermore confirmed by the result that the Stokes number of the dust stays approximatively constant at the wind base beyond $r = 8\ \text{au}$ in the case of warm, ionized winds.

A significant difference between wind including photoevaporation and cold magnetic winds was found to be the dust flow angle θ_d . For cold winds the dust flow angle is much smaller with $\theta_d \approx 25^\circ$ compared to $67^\circ \leq \theta_d \leq 69^\circ$ for the warm, ionized winds. The cold magnetic wind showed a lower wind velocity on the order of $\approx 5\ \text{km s}^{-1}$ compared to the $\approx 15\ \text{km s}^{-1}$ for warm winds. The mass loss rate however was approximatively equal and the wind density is thus higher in the cold wind case. The effect of lower wind speeds but higher densities would cancel out and allow dust entrainment with a limiting grain size equal to the warm wind case. The only factor decreasing the dust entrainment efficiency is thus the temperature. Lowering the temperature decreases the thermal velocity of the gas particles and consequently increases the Stokes number of the dust grains embedded in the flow, leading to less dust entrainment.

Observationally, the dust entrained in the winds could be identified as a faint conical emission signature above and below the disk. To further determine whether these signatures are luminous enough to be detected by current instruments, further studies similar to the one in Franz et al. (2021) would be necessary. It would also be of interest to extend this wind model to three dimensional simulations. Azimuthal asymmetries in the dust flow passing by the observed column could perhaps explain sudden variations in the stellar flux, as seen in FU Orionis type events. One could furthermore increase the plasma beta in order to aim for a clear distinction between pure photoevaporative winds without magnetic fields and magnetothermal disk winds. The computational limitations did however not allow for such a study in this thesis.

In Chapter 4 we presented fully dynamic MHD-Simulations of magnetically disk wind driven accretion flows in a transition disk with a larger inner cavity ranging from $r_c = 10\ \text{au}$ to $r_c = 50\ \text{au}$. The accretion rates extracted from the simulation outputs were in a range roughly between $\dot{M}_{\text{acc}} \approx 1 \times 10^{-9}\ M_\odot\ \text{yr}^{-1}$ to $\dot{M}_{\text{acc}} \approx 1 \times 10^{-8}\ M_\odot\ \text{yr}^{-1}$, compatible with recent observations of transition disk (Manara et al., 2016; Mulders et al., 2017).

We could furthermore demonstrate a correlation between the accretion rate and the initial disk mass with a power law exponent of ≈ 0.85 . From traditional viscous accretion theory a linear relation would be expected. Interestingly, recent observations hinted towards similar power laws with exponents ranging from 0.7 to 0.8. These results were however subject to significant statistical uncertainty and a linear scaling could not be excluded. Since the simulations presented here were not in a completely steady state and secondary wind flows originating from the cavity formed at later times, our results would need further verification in future projects. The main issue would be the exten-

sion of the inner boundary and lowering the numerical floor density. The computational cost accompanied with these measures would be challenging.

Considering the accretion rates measured for the cold magnetic wind, we found that photoevaporation completely quenches the accretion flow. In future studies it would thus be interesting to decrease β further and hence increase the magnetic field strength in order to reach accretion rates that would persist under the influence of XEUV-heating.

To conclude, the results of this thesis provided additional information of signatures of planets embedded in protoplanetary disks and the presence of photoevaporation as well as magnetically driven disk winds. Especially the subject of MHD-winds still needs a considerable amount of theoretical work and observational confirmation and the extension of the models presented here could thus provide valuable insight into the nature of these phenomena for future studies.

Acknowledgements

First of all, I would like to thank my supervisor Kees Dullemond for giving me the opportunity to carry out my doctoral studies in his group, for all the nice discussions and for his support and encouragement throughout my PhD.

I express my deepest gratitude to my wife Imane for her love, her endless support and encouragement and I want to thank her for always being by my side.

I would also like to thank my parents for have given me the chance to pursue my studies and for supporting me throughout my whole life.

I also thank Pablo Benitez-LLambay, Martin Pessah and Christopher Andersen for the opportunity of the research visit in Copenhagen and the lively discussions.

I thank my colleagues at ITA for the nice conversations, pizza evenings and running events.

List of Figures

1.1 β -Pictoris	3
1.2 Protoplanetary disks in the Orion nebula	3
1.3 Observations of HL Tau & IM Lup	4
1.4 Dust drift speeds	16
1.5 Jets and outflows in HH-30 and DG Tau	21
1.6 Magnetic disk wind sketch	25
1.7 Photoevaporation and magnetically driven winds	26
2.1 Sketch of HD 163296 system	35
2.2 Stokes number & α -viscosity profiles	40
2.3 Dust opacities used in the HD 163296 model	41
2.4 Dust density maps depending on aspect ratio	44
2.5 Dust density maps depending on α -viscosity	44
2.6 Averaged densities and normalized optical depth	47
2.7 Ring width comparison with observed values	48
2.8 Dust density map comparison between planet 2 mass	50
2.9 Dust surface density maps of fiducial model in polar coordinates	51
2.10 Radial and azimuthal cut through asymmetries at L5 and L4	52
2.11 Radial and azimuthal cut through asymmetries at L5 and L4 with dust feedback	52
2.12 Asymmetry time evolution depending on α -viscosity	54
2.13 Asymmetry trapped dust mass parameter study	55
2.14 Asymmetry trapped dust mass planet mass dependence	55
2.15 Evolution of trapped dust mass depending on planet growth time scale	57
2.16 Dust density map comparison between fiducial and feedback model	58
2.17 Synthetic ALMA images	59
2.18 Synthetic ALMA images with different degrees of vertical dust mixing	60
2.19 Synthetic ALMA images depending on planet growth time scale	61
2.20 Asymmetry trapped dust mass resolution study	62
2.21 Computed dust temperatures compared to analytical solution	63
3.1 Numerical test results of the ionization model	74
3.2 Ambipolar diffusion STS test for $\langle\sigma v\rangle_i = 1000$	77
3.3 Ambipolar diffusion STS test for $\langle\sigma v\rangle_i = 100$	78
3.4 Photoevaporation temperature curves	79
3.5 Opacities used for the dust entrained in the wind	80

3.6	Gas density maps of phc2, b5c2 and b4c2 after 500 orbits	82
3.7	Wind mass loss rates of phc2, b5c2, b4c2 and b4c2np	82
3.8	Dust density maps with velocity streamlines of phc2, b5c2 and b4c2	84
3.9	Dust density maps with velocity streamlines of b4c2np	85
3.10	Cumulative mass loss rates of phc2, b5c2, b4c2 and b4c2a3	86
3.11	Numerically integrated dust trajectories of phc2, b5c2 and b4c2	88
3.12	Asymptotic dust flow inclination depending on grain size	89
3.13	Vertical dust and gas density slices with Stokes number	90
3.14	Vertical density slice depending on grain size	90
3.15	Physical quantities at wind launching surface	91
3.16	Physical quantities along streamline	93
3.17	Vertical slices of dust and gas temperatures	94
3.18	Vertical slices of ionization fraction and dust densities	95
3.19	Optical depth in H-band	96
3.20	Synthetic images with inclination of 70°	96
3.21	Synthetic images with inclination of 90°	97
4.1	Plasma parameter evolution comparison	105
4.2	Magnetic field evolution comparison radial	106
4.3	Magnetic field and density evolution comparison in 2D	107
4.4	Accretion flow with cavity of 10 au	108
4.5	Accretion flow with cavity of 50 au	108
4.6	Density and temperature map of b4c50np	109
4.7	Density map of b10c10np	110
4.8	Accretion rates and stresses of b4c50np	111
4.9	Accretion rates and stresses varying with initial surface density	113
4.10	Accretion rates and stresses varying with β	113

List of Tables

2.1	List of simulations and parameters of the HD 163296-model	42
2.2	Surface densities, grain sizes and optical depths of HD 163296	46
2.3	Ring width & position fits	46
2.4	Ring dust masses	46
3.1	List of disk wind simulation parameters including dust	69
4.1	List of simulations & parameters of disk wind accretion in transition disks	104

List of publications

Chapter 2 and chapter 3 are based on the first and the third publication listed below.

Rodenkirch, P. J. and Dullemond, C. P. (2022). Dust entrainment in magnetically and thermally driven disk winds. *A&A*, 659:A42.

Rodenkirch, P. J., Klahr, H., Fendt, C., and Dullemond, C. P. (2020). Global axisymmetric simulations of photoevaporation and magnetically driven protoplanetary disk winds. *A&A*, 633:A21.

Rodenkirch, P. J., Rometsch, T., Dullemond, C. P., Weber, P., and Kley, W. (2021). Modeling the nonaxisymmetric structure in the HD 163296 disk with planet-disk interaction. *A&A*, 647:A174.

Rometsch, T., Rodenkirch, P. J., Kley, W., and Dullemond, C. P. (2020). Migration jumps of planets in transition discs. *A&A*, 643:A87.

Weber, M. L., Ercolano, B., Picogna, G., Hartmann, L., and Rodenkirch, P. J. (2020). The interpretation of protoplanetary disc wind diagnostic lines from X-ray photoevaporation and analytical MHD models. *MNRAS*, 496(1):223–244.

Bibliography

- Adams, F. C., Hollenbach, D., Laughlin, G., & Gorti, U. 2004, *ApJ*, 611, 360
- Adams, F. C., Hollenbach, D., Laughlin, G., & Gorti, U. 2004, *The Astrophysical Journal*, 611, 360
- Akeson, R. L., Chen, X., Ciardi, D., et al. 2013, *PASP*, 125, 989
- Alcalá, J. M., Manara, C. F., Natta, A., et al. 2017, *A&A*, 600, A20
- Alcalá, J. M., Gangi, M., Biazzo, K., et al. 2021, *A&A*, 652, A72
- Alexander, R. D., & Armitage, P. J. 2007, *MNRAS*, 375, 500
- Alexander, R. D., Clarke, C. J., & Pringle, J. E. 2005, *MNRAS*, 358, 283
- . 2006, *MNRAS*, 369, 216
- Alexiades, V., Amiez, G., & Gremaud, P.-A. 1996, *Communications in Numerical Methods in Engineering*, 12, 31
- ALMA Partnership, Brogan, C. L., Pérez, L. M., et al. 2015, *ApJ*, 808, L3
- Andre, P., Ward-Thompson, D., & Barsony, M. 1993, *ApJ*, 406, 122
- Andrews, S. M., Huang, J., Pérez, L. M., et al. 2018, *ApJ*, 869, L41
- Armitage, P. J. 2020, *Astrophysics of Planet Formation* (Cambridge University Press)
- Artymowicz, P. 1993, *ApJ*, 419, 155
- Aumann, H. H. 1985, *PASP*, 97, 885
- Aumann, H. H., Gillett, F. C., Beichman, C. A., et al. 1984, *ApJ*, 278, L23
- Avenhaus, H., Quanz, S. P., Garufi, A., et al. 2018, *ApJ*, 863, 44
- Ayliffe, B. A., Laibe, G., Price, D. J., & Bate, M. R. 2012, *MNRAS*, 423, 1450
- Bae, J., & Zhu, Z. 2018, *ApJ*, 859, 118
- Bae, J., Zhu, Z., & Hartmann, L. 2017, *ApJ*, 850, 201
- Baehr, H., Klahr, H., & Kratter, K. M. 2017, *ApJ*, 848, 40

- Bai, X.-N. 2011, *Astrophysical Journal*, 739, arXiv:1107.2935
- Bai, X.-N. 2013, *ApJ*, 772, 96
- . 2017a, *ApJ*, 845, 75
- . 2017b, *ApJ*, 845, 75
- Bai, X.-N., & Goodman, J. 2009, *ApJ*, 701, 737
- Bai, X.-N., & Stone, J. M. 2013, *ApJ*, 769, 76
- . 2017, *ApJ*, 836, 46
- Bai, X.-N., Ye, J., Goodman, J., & Yuan, F. 2016, *ApJ*, 818, 152
- Balbus, S. A., & Hawley, J. F. 1991, *ApJ*, 376, 214
- . 1998, *Reviews of Modern Physics*, 70, 1
- Baruteau, C., & Zhu, Z. 2016, *MNRAS*, 458, 3927
- Benítez-Llambay, P., Krapp, L., & Pessah, M. E. 2019, *ApJS*, 241, 25
- Benitez-Llambay, P., Krapp, L., & Pessah, M. E. 2019, *ApJS*, 241, 25
- Benítez-Llambay, P., & Masset, F. S. 2016, *ApJS*, 223, 11
- Benitez-Llambay, P., & Masset, F. S. 2016, *ApJS*, 223, 11
- Béthune, W., Lesur, G., & Ferreira, J. 2017, *Astronomy & Astrophysics*, 600, A75
- Beuzit, J. L., Vigan, A., Mouillet, D., et al. 2019, *A&A*, 631, A155
- Bird, R., Lightfoot, E., & Stewart, W. 2002, *Transport Phenomena* (J. Wiley)
- Birnstiel, T., Dullemond, C. P., & Brauer, F. 2010, *A&A*, 513, A79
- Birnstiel, T., Klahr, H., & Ercolano, B. 2012, *A&A*, 539, A148
- Birnstiel, T., Dullemond, C. P., Zhu, Z., et al. 2018, *ApJ*, 869, L45
- Bitsch, B., Lambrechts, M., & Johansen, A. 2015, *A&A*, 582, A112
- Bjorkman, J. E., & Wood, K. 2001, *ApJ*, 554, 615
- Blaes, O. M., & Balbus, S. A. 1994, *Astrophysical Journal*, 421, 163
- Blanco, D., Ricci, L., Flock, M., & Turner, N. 2021, arXiv e-prints, arXiv:2108.00907
- Blandford, R. D., & Payne, D. G. 1982, *Monthly Notices of the Royal Astronomical Society*, 199, 883
- Bouvier, J., Alencar, S. H. P., Harries, T. J., Johns-Krull, C. M., & Romanova, M. M. 2007, in *Protostars and Planets V*, ed. B. Reipurth, D. Jewitt, & K. Keil, 479
- Brown, P. N., Byrne, G. D., & Hindmarsh, A. C. 1989, *Siam Journal on Scientific and Statistical Computing*, 10, 1038

- Burrows, C. J., Stapelfeldt, K. R., Watson, A. M., et al. 1996, *ApJ*, 473, 437
- Calvet, N., D'Alessio, P., Watson, D. M., et al. 2005a, *ApJ*, 630, L185
- . 2005b, *ApJ*, 630, L185
- Casse, F., & Keppens, R. 2002, *The Astrophysical Journal*, 581, 988
- Cazzoletti, P., van Dishoeck, E. F., Pinilla, P., et al. 2018, *A&A*, 619, A161
- Chandrasekhar, S. 1960, *Proceedings of the National Academy of Science*, 46, 253
- Chiang, E. I., & Goldreich, P. 1997, *ApJ*, 490, 368
- Choi, E., Kim, J., & Wiita, P. J. 2009, *ApJS*, 181, 413
- Clarke, C. J., Gendrin, A., & Sotomayor, M. 2001, *MNRAS*, 328, 485
- Crida, A., Morbidelli, A., & Masset, F. 2006, *Icarus*, 181, 587
- Cui, C., & Bai, X.-N. 2021, *MNRAS*, arXiv:2106.10167 [astro-ph.EP]
- de Val-Borro, M., Edgar, R. G., Artymowicz, P., et al. 2006, *MNRAS*, 370, 529
- de Valon, A., Dougados, C., Cabrit, S., et al. 2020, *A&A*, 634, L12
- Dipierro, G., Price, D., Laibe, G., et al. 2015, *MNRAS*, 453, L73
- Dominik, C., Min, M., & Tazaki, R. 2021, *Astrophysics Source Code Library*, ascl:2104.010
- Dong, R., Li, S., Chiang, E., & Li, H. 2017, *ApJ*, 843, 127
- Dong, R., Zhu, Z., & Whitney, B. 2015, *ApJ*, 809, 93
- Draine, B. T., Roberge, W. G., & Dalgarno, A. 1983, *ApJ*, 264, 485
- Drake, J. J., Ercolano, B., Flaccomio, E., & Micela, G. 2009, *ApJ*, 699, L35
- Drażkowska, J., Li, S., Birnstiel, T., Stammer, S. M., & Li, H. 2019, *ApJ*, 885, 91
- Dubrulle, B., Morfill, G., & Sterzik, M. 1995, *Icarus*, 114, 237
- Dullemond, C., Isella, A., Andrews, S., Skobleva, I., & Dzyurkevich, N. 2019, arXiv e-prints, arXiv:1911.12434
- Dullemond, C. P., & Dominik, C. 2004, *A&A*, 421, 1075
- Dullemond, C. P., Hollenbach, D., Kamp, I., & D'Alessio, P. 2007, in *Protostars and Planets V*, ed. B. Reipurth, D. Jewitt, & K. Keil, 555
- Dullemond, C. P., Juhasz, A., Pohl, A., et al. 2012a, *RADMC-3D: A multi-purpose radiative transfer tool*
- . 2012b, *RADMC-3D: A multi-purpose radiative transfer tool*
- Dullemond, C. P., Natta, A., & Testi, L. 2006, *ApJ*, 645, L69

- Dullemond, C. P., Birnstiel, T., Huang, J., et al. 2018, *ApJ*, 869, L46
- Durisen, R. H., Boss, A. P., Mayer, L., et al. 2007, in *Protostars and Planets V*, ed. B. Reipurth, D. Jewitt, & K. Keil, 607
- Dzyurkevich, N., Flock, M., Turner, N. J., Klahr, H., & Henning, T. 2010, *A&A*, 515, A70
- Dzyurkevich, N., Turner, N. J., Henning, T., & Kley, W. 2013, *ApJ*, 765, 114
- Edwards, S., Hartigan, P., Ghandour, L., & Andrulis, C. 1994, *AJ*, 108, 1056
- Ercolano, B., Clarke, C. J., & Drake, J. J. 2009, *Astrophysical Journal*, 699, 1639
- Ercolano, B., Picogna, G., Monsch, K., Drake, J. J., & Preibisch, T. 2021, arXiv e-prints, arXiv:2109.04113
- Espaillet, C., Muzerolle, J., Najita, J., et al. 2014, in *Protostars and Planets VI*, ed. H. Beuther, R. S. Klessen, C. P. Dullemond, & T. Henning, 497
- Evans, C. R., & Hawley, J. F. 1988, *ApJ*, 332, 659
- Fang, M., Pascucci, I., Edwards, S., et al. 2018, *ApJ*, 868, 28
- Fendt, C., & Sheikhnezami, S. 2013, *Astrophysical Journal*, 774, arXiv:1305.1263
- Ferreira, J., & Pelletier, G. 1993, *A&A*, 276, 625
- Ferreira, J., & Pelletier, G. 1995, *Astronomy & Astrophysics*, 295, 807
- Flaherty, K. M., Hughes, A. M., Rosenfeld, K. A., et al. 2015, *ApJ*, 813, 99
- Flaherty, K. M., Hughes, A. M., Rose, S. C., et al. 2017, *ApJ*, 843, 150
- Flock, M., Dzyurkevich, N., Klahr, H., Turner, N. J., & Henning, T. 2011, *Astrophysical Journal*, 735, arXiv:1104.4565
- Flock, M., Ruge, J. P., Dzyurkevich, N., et al. 2015, *A&A*, 574, A68
- Flock, M., Turner, N. J., Nelson, R. P., et al. 2020, *ApJ*, 897, 155
- Font, A. S., McCarthy, I. G., Johnstone, D., & Ballantyne, D. R. 2004, *ApJ*, 607, 890
- Fouchet, L., Gonzalez, J. F., & Maddison, S. T. 2010, *A&A*, 518, A16
- Fouchet, L., Maddison, S. T., Gonzalez, J. F., & Murray, J. R. 2007, *A&A*, 474, 1037
- Frank, A., Ray, T. P., Cabrit, S., et al. 2014, in *Protostars and Planets VI*, ed. H. Beuther, R. S. Klessen, C. P. Dullemond, & T. Henning, 451
- Frank, J., King, A., & Raine, D. J. 2002, *Accretion Power in Astrophysics: Third Edition*
- Franz, R., Ercolano, B., Casassus, S., et al. 2021, arXiv e-prints, arXiv:2110.10637
- Franz, R., Picogna, G., Ercolano, B., & Birnstiel, T. 2020, *A&A*, 635, A53
- Fromang, S., Latter, H., Lesur, G., & Ogilvie, G. I. 2013, *A&A*, 552, A71
- Fromang, S., & Nelson, R. P. 2009, *A&A*, 496, 597

- Fromang, S., & Papaloizou, J. 2007, *A&A*, 476, 1113
- Gaia Collaboration, Brown, A. G. A., Vallenari, A., et al. 2018, *A&A*, 616, A1
- Gammie, C. F. 1996, *ApJ*, 457, 355
- Garufi, A., Podio, L., Bacciotti, F., et al. 2019, *A&A*, 628, A68
- Giacalone, S., Teitler, S., Königl, A., Krijt, S., & Ciesla, F. J. 2019, *ApJ*, 882, 33
- Goldreich, P., & Tremaine, S. 1979, *ApJ*, 233, 857
- . 1980, *ApJ*, 241, 425
- Goldreich, P., & Ward, W. R. 1973, *ApJ*, 183, 1051
- Gombosi, T. I., Nagy, A. F., & Cravens, T. E. 1986, *Reviews of Geophysics*, 24, 667
- Gorti, U., & Hollenbach, D. 2009, *Astrophysical Journal*, 690, 1539
- Gorti, U., Hollenbach, D., Najita, J., & Pascucci, I. 2011, *ApJ*, 735, 90
- Gressel, O., Ramsey, J. P., Brinch, C., et al. 2020, *ApJ*, 896, 126
- Gressel, O., Turner, N. J., Nelson, R. P., & McNally, C. P. 2015, *Astrophysical Journal*, 801, arXiv:1501.05431
- Haisch, K. E., Lada, E. A., & Lada, C. J. 2001, *The Astrophysical Journal*, Volume 553, Issue 2, pp. L153-L156., 553, L153
- Hallam, P. D., & Paardekooper, S. J. 2020, *MNRAS*, 491, 5759
- Hammer, M., Kratter, K. M., & Lin, M.-K. 2017, *MNRAS*, 466, 3533
- Hammer, M., Pinilla, P., Kratter, K. M., & Lin, M.-K. 2019, *MNRAS*, 482, 3609
- Hartmann, L., Calvet, N., Gullbring, E., & D'Alessio, P. 1998, *ApJ*, 495, 385
- Hawley, J. F., & Stone, J. M. 1995, *Computer Physics Communications*, 89, 127
- Haworth, T. J., Clarke, C. J., & Owen, J. E. 2016, *MNRAS*, 457, 1905
- Hayashi, C. 1981, *Progress of Theoretical Physics Supplement*, 70, 35
- Hayashi, C., Nakazawa, K., & Nakagawa, Y. 1985, in *Protostars and Planets II*, ed. D. C. Black & M. S. Matthews, 1100
- Hennebelle, P., & Inutsuka, S.-i. 2019, *Frontiers in Astronomy and Space Sciences*, 6, 5
- Heney, L. G., & Greenstein, J. L. 1941, *ApJ*, 93, 70
- Hester, J. J., Scowen, P. A., Sankrit, R., et al. 1996, *AJ*, 111, 2349
- Holland, W. S., Greaves, J. S., Zuckerman, B., et al. 1998, *Nature*, 392, 788
- Hollenbach, D., Johnstone, D., Lizano, S., & Shu, F. H. 1994, *The Astrophysical Journal*, 428, 654

- Hourigan, K., & Ward, W. R. 1984, *Icarus*, 60, 29
- Huang, J., Andrews, S. M., Dullemond, C. P., et al. 2018a, *ApJ*, 869, L42
- Huang, J., Andrews, S. M., Pérez, L. M., et al. 2018b, *ApJ*, 869, L43
- Hughes, A. M., Andrews, S. M., Espaillat, C., et al. 2009, *ApJ*, 698, 131
- Hutchison, M. A., Laibe, G., & Maddison, S. T. 2016a, *MNRAS*, 463, 2725
- Hutchison, M. A., Price, D. J., Laibe, G., & Maddison, S. T. 2016b, *MNRAS*, 461, 742
- Igea, J., & Glassgold, A. E. 1999, *ApJ*, 518, 848
- Ilgner, M., & Nelson, R. P. 2006, *A&A*, 445, 205
- Isella, A., Guidi, G., Testi, L., et al. 2016, *Phys. Rev. Lett.*, 117, 251101
- Isella, A., Huang, J., Andrews, S. M., et al. 2018, *ApJ*, 869, L49
- Jeans, J. 1902, *Philosophical Transactions of the Royal Society of London. Series A, Containing Papers of a Mathematical or Physical Character*, 199, 1
- Johnstone, C. P., Jardine, M., Gregory, S. G., Donati, J. F., & Hussain, G. 2014, *MNRAS*, 437, 3202
- Johnstone, D., Hollenbach, D., & Bally, J. 1998, *ApJ*, 499, 758
- Jones, M. G., Pringle, J. E., & Alexander, R. D. 2012, *MNRAS*, 419, 925
- Kanagawa, K. D., Muto, T., Okuzumi, S., et al. 2018, *ApJ*, 868, 48
- Kant, I. 1755, *Allgemeine Naturgeschichte und Theorie des Himmels*
- Keppler, M., Benisty, M., Müller, A., et al. 2018, *A&A*, 617, A44
- Keppler, M., Teague, R., Bae, J., et al. 2019, *A&A*, 625, A118
- Klaassen, P. D., Juhasz, A., Mathews, G. S., et al. 2013, *A&A*, 555, A73
- Klahr, H., & Hubbard, A. 2014, *The Astrophysical Journal*, Volume 788, Issue 1, article id. 21, 8 pp. (2014)., 788, arXiv:1403.6721
- Klahr, H. H., & Bodenheimer, P. 2003a, *ApJ*, 582, 869
- . 2003b, *ApJ*, 582, 869
- Kley, W., & Nelson, R. P. 2012, *ARA&A*, 50, 211
- Königl, A. 1989, *ApJ*, 342, 208
- Korycansky, D. G., & Papaloizou, J. C. B. 1996, *ApJS*, 105, 181
- Kratter, K., & Lodato, G. 2016, *ARA&A*, 54, 271
- Krumholz, M. R., & Federrath, C. 2019, *Frontiers in Astronomy and Space Sciences*, 6, 7
- Kulsrud, R. M., & Zweibel, E. G. 2008, *Reports on Progress in Physics*, 71, 046901

- Lada, C. J., & Wilking, B. A. 1984, *ApJ*, 287, 610
- Lambrechts, M., & Johansen, A. 2012, *A&A*, 544, A32
- Laplace, P. S. 1796, *Exposition du systeme du monde* (De l'Imprimerie du Cercle-Social Paris)
- Lesur, G. 2020, arXiv e-prints, arXiv:2007.15967
- Li, H., Finn, J. M., Lovelace, R. V. E., & Colgate, S. A. 2000, *ApJ*, 533, 1023
- Liffman, K. 2003, *PASA*, 20, 337
- Lin, D. N. C., & Papaloizou, J. 1986, *ApJ*, 309, 846
- Liu, H. B. 2019, *ApJ*, 877, L22
- Liu, S.-F., Jin, S., Li, S., Isella, A., & Li, H. 2018, *ApJ*, 857, 87
- Louvet, F., Dougados, C., Cabrit, S., et al. 2018, *A&A*, 618, A120
- Lovelace, R. V. E., Li, H., Colgate, S. A., & Nelson, A. F. 1999, *ApJ*, 513, 805
- Lynden-Bell, D. 1996, *MNRAS*, 279, 389
- . 2003, *MNRAS*, 341, 1360
- Lynden-Bell, D., & Pringle, J. E. 1974, *MNRAS*, 168, 603
- Lyra, W., Johansen, A., Klahr, H., & Piskunov, N. 2009, *A&A*, 493, 1125
- Macías, E., Anglada, G., Osorio, M., et al. 2016, *ApJ*, 829, 1
- Maddison, S. T., Fouchet, L., & Gonzalez, J. F. 2007, *Ap&SS*, 311, 3
- Mamajek, E. E., Meyer, M. R., Hinz, P. M., et al. 2004, *The Astrophysical Journal*, Volume 612, Issue 1, pp. 496-510., 612, 496
- Manara, C. F., Testi, L., Natta, A., et al. 2014, *A&A*, 568, A18
- Manara, C. F., Rosotti, G., Testi, L., et al. 2016, *A&A*, 591, L3
- Manger, N., & Klahr, H. 2018, *MNRAS*, 480, 2125
- Marzari, F., & Scholl, H. 1998, *Icarus*, 131, 41
- Masset, F. 2000, *A&AS*, 141, 165
- Masset, F., & Snellgrove, M. 2001, *MNRAS*, 320, L55
- Masset, F. S. 2002, *A&A*, 387, 605
- Masset, F. S., & Papaloizou, J. C. B. 2003, *ApJ*, 588, 494
- Mathis, J. S., Rumpl, W., & Nordsieck, K. H. 1977, *ApJ*, 217, 425
- Matsuyama, I., Johnstone, D., & Hartmann, L. 2003, *ApJ*, 582, 893
- Mayor, M., & Queloz, D. 1995, *Nature*, 378, 355

- McCaughrean, M. J., & O'dell, C. R. 1996, *AJ*, 111, 1977
- McMullin, J. P., Waters, B., Schiebel, D., Young, W., & Golap, K. 2007, *Astronomical Society of the Pacific Conference Series*, Vol. 376, *CASA Architecture and Applications*, ed. R. A. Shaw, F. Hill, & D. J. Bell, 127
- McNally, C. P., Nelson, R. P., Paardekooper, S.-J., & Benítez-Llambay, P. 2019, *MNRAS*, 484, 728
- Meru, F., Rosotti, G. P., Booth, R. A., Nazari, P., & Clarke, C. J. 2019, *MNRAS*, 482, 3678
- Mestel, L. 1965a, *QJRAS*, 6, 161
- . 1965b, *QJRAS*, 6, 265
- Mestel, L. 2012, *Stellar Magnetism: Second Edition (International Series of Monographs on Physics)*, hardcover edn. (Oxford University Press), 754
- Miranda, R., Lai, D., & Méheut, H. 2016, *MNRAS*, 457, 1944
- Miranda, R., & Rafikov, R. R. 2019a, *ApJ*, 875, 37
- . 2019b, *ApJ*, 878, L9
- Miyake, T., Suzuki, T. K., & Inutsuka, S.-i. 2016, *ApJ*, 821, 3
- Montesinos, B., Eiroa, C., Mora, A., & Merín, B. 2009, *A&A*, 495, 901
- Montesinos, M., Garrido-Deutelmöser, J., Olofsson, J., et al. 2020, arXiv e-prints, arXiv:2009.10768
- Mulders, G. D., Pascucci, I., Manara, C. F., et al. 2017, *ApJ*, 847, 31
- Müller, T. W. A., Kley, W., & Meru, F. 2012, *A&A*, 541, A123
- Muzerolle, J., Hillenbrand, L., Calvet, N., Briceño, C., & Hartmann, L. 2003, *ApJ*, 592, 266
- Nakagawa, Y., Sekiya, M., & Hayashi, C. 1986, *Icarus*, 67, 375
- Nakatani, R., Hosokawa, T., Yoshida, N., Nomura, H., & Kuiper, R. 2018a, *ApJ*, 857, 57
- . 2018b, *ApJ*, 865, 75
- Natta, A., Testi, L., Muzerolle, J., et al. 2004, *A&A*, 424, 603
- Nelson, R. P., Gressel, O., & Umurhan, O. M. 2013, *MNRAS*, 435, 2610
- Nelson, R. P., Papaloizou, J. C. B., Masset, F., & Kley, W. 2000, *MNRAS*, 318, 18
- Newton, I. 1687, *Philosophiæ naturalis principia mathematica*
- O'dell, C. R., Wen, Z., & Hu, X. 1993, *ApJ*, 410, 696
- Okuzumi, S. 2009, *ApJ*, 698, 1122
- Oppenheimer, M., & Dalgarno, A. 1974, *ApJ*, 192, 29

- Owen, J. E. 2016, *PASA*, 33, e005
- Owen, J. E., Clarke, C. J., & Ercolano, B. 2012, *Monthly Notices of the Royal Astronomical Society*, 422, 1880
- Owen, J. E., Ercolano, B., & Clarke, C. J. 2011, *MNRAS*, 411, 1104
- Owen, J. E., Ercolano, B., Clarke, C. J., & Alexander, R. D. 2010, *Monthly Notices of the Royal Astronomical Society*, 401, 1415
- Owen, J. E., & Kollmeier, J. A. 2019, *MNRAS*, 487, 3702
- Paardekooper, S. J., Baruteau, C., & Kley, W. 2011, *MNRAS*, 410, 293
- Paardekooper, S. J., & Mellema, G. 2004, *A&A*, 425, L9
- . 2006, *A&A*, 453, 1129
- Padgett, D. L., Brandner, W., Stapelfeldt, K. R., et al. 1999, *AJ*, 117, 1490
- Parker, E. N. 1958, *ApJ*, 128, 664
- . 1979, *Cosmical magnetic fields. Their origin and their activity*
- Pascucci, I., & Sterzik, M. 2009, *ApJ*, 702, 724
- Pascucci, I., Sterzik, M., Alexander, R. D., et al. 2011, *ApJ*, 736, 13
- Pérez, S., Casassus, S., Baruteau, C., et al. 2019, *AJ*, 158, 15
- Pfeil, T., & Klahr, H. 2021, *ApJ*, 915, 130
- Picogna, G., Ercolano, B., & Espaillat, C. C. 2021, *MNRAS*, 508, 3611
- Picogna, G., Ercolano, B., Owen, J. E., & Weber, M. L. 2019, *MNRAS*, 487, 691
- Picogna, G., Ercolano, B., Owen, J. E., & Weber, M. L. 2019, 12, 1
- Picogna, G., & Kley, W. 2015, *A&A*, 584, A110
- Pinilla, P., Benisty, M., & Birnstiel, T. 2012, *A&A*, 545, A81
- Pinilla, P., Flock, M., Ovelar, M. d. J., & Birnstiel, T. 2016, *A&A*, 596, A81
- Pinte, C., Price, D. J., Ménard, F., et al. 2020, *The Astrophysical Journal Letters*, 890, L9
- Podio, L., Medves, S., Bacciotti, F., Eisloffel, J., & Ray, T. 2009, *A&A*, 506, 779
- Pohl, A., Pinilla, P., Benisty, M., et al. 2015, *MNRAS*, 453, 1768
- Pollack, J. B., Hollenbach, D., Beckwith, S., et al. 1994, *ApJ*, 421, 615
- Preibisch, T., Kim, Y.-C., Favata, F., et al. 2005, *ApJS*, 160, 401
- Pringle, J. E. 1981, *ARA&A*, 19, 137
- Purser, S. J. D., Lumsden, S. L., Hoare, M. G., et al. 2016, *MNRAS*, 460, 1039
- Rafikov, R. R. 2002, *ApJ*, 572, 566

- Ray, T. 2012, *Astronomy and Geophysics*, 53, 5.19
- Ray, T. P., & Ferreira, J. 2021, *New A Rev.*, 93, 101615
- Ribas, Á., Bouy, H., & Merín, B. 2015, 52, 1
- Rice, W. K. M., Lodato, G., Pringle, J. E., Armitage, P. J., & Bonnell, I. A. 2004, *MNRAS*, 355, 543
- . 2006, *MNRAS*, 372, L9
- Riols, A., & Lesur, G. 2018, 117, arXiv:1805.00458
- Rodenkirch, P. J., & Dullemond, C. P. 2022, *A&A*, 659, A42
- Rodenkirch, P. J., Klahr, H., Fendt, C., & Dullemond, C. P. 2020, *A&A*, 633, A21
- Rodenkirch, P. J., Rometsch, T., Dullemond, C. P., Weber, P., & Kley, W. 2021, *A&A*, 647, A174
- Rometsch, T., Rodenkirch, P. J., Kley, W., & Dullemond, C. P. 2020, *A&A*, 643, A87
- Safronov, V. S. 1972, *Evolution of the protoplanetary cloud and formation of the earth and planets.*
- Scally, A., & Clarke, C. 2001, *MNRAS*, 325, 449
- Schatzman, E. 1962, *Annales d'Astrophysique*, 25, 18
- Schreiber, A., & Klahr, H. 2018, *ApJ*, 861, 47
- Shakura, N. I., & Sunyaev, R. A. 1973, *A&A*, 500, 33
- Sheikhnezami, S., Fendt, C., Porth, O., Vaidya, B., & Ghanbari, J. 2012, *Astrophysical Journal*, 757, arXiv:1207.6086
- Shmidt, O. 1944, *AN SSSR*, 45(6), 245
- Shu, F., Najita, J., Ostriker, E., et al. 1994, *ApJ*, 429, 781
- Shu, F. H. 1991, in *NATO Advanced Study Institute (ASI) Series C, Vol. 342, The Physics of Star Formation and Early Stellar Evolution*, ed. C. J. Lada & N. D. Kylafis, 365
- Shu, F. H., Johnstone, D., & Hollenbach, D. 1993, *Icarus*, 106, 92
- Simon, J. B., Bai, X.-N., Stone, J. M., Armitage, P. J., & Beckwith, K. 2013, *ApJ*, 764, 66
- Simon, M. N., Pascucci, I., Edwards, S., et al. 2016, *ApJ*, 831, 169
- Smith, B. A., & Terrile, R. J. 1984, *Science*, 226, 1421
- Snell, R. L., Loren, R. B., & Plambeck, R. L. 1980, *ApJ*, 239, L17
- Spruit, H. C. 1996, in *NATO Advanced Study Institute (ASI) Series C, Vol. 477, Evolutionary Processes in Binary Stars*, ed. R. A. M. J. Wijers, M. B. Davies, & C. A. Tout, 249

- Spruit, H. C. 2013, arXiv e-prints, arXiv:1301.5572
- Stammler, S. M., & Dullemond, C. P. 2014, *Icarus*, 242, 1
- Stepanovs, D., & Fendt, C. 2014, *ApJ*, 793, 31
- Stepanovs, D., & Fendt, C. 2016, *The Astrophysical Journal*, 825, 14
- Stoll, M. H. R., & Kley, W. 2014, *A&A*, 572, A77
- . 2016, *A&A*, 594, A57
- Stone, J. M., & Norman, M. L. 1992, *ApJS*, 80, 753
- Strom, K. M., Strom, S. E., Edwards, S., Cabrit, S., & Skrutskie, M. F. 1989, *AJ*, 97, 1451
- Strom, S. E., Edwards, S., & Skrutskie, M. F. 1993, in *Protostars and Planets III*, ed. E. H. Levy & J. I. Lunine, 837
- Suriano, S. S., Li, Z.-Y., Krasnopolsky, R., & Shang, H. 2018, *MNRAS*, 477, 1239
- Suzuki, T. K., & Inutsuka, S. I. 2009, *Astrophysical Journal*, 691, L49
- Suzuki, T. K., Muto, T., & Inutsuka, S.-i. 2010, *ApJ*, 718, 1289
- Tarter, C. B., Tucker, W. H., & Salpeter, E. E. 1969, *ApJ*, 156, 943
- Teague, R., Bae, J., Bergin, E. A., Birnstiel, T., & Foreman-Mackey, D. 2018a, *ApJ*, 860, L12
- . 2018b, *ApJ*, 860, L12
- Toomre, A. 1964, *ApJ*, 139, 1217
- Tzeferacos, P., Ferrari, A., Mignone, A., et al. 2009, *MNRAS*, 400, 820
- Umebayashi, T., & Nakano, T. 2009, *ApJ*, 690, 69
- Ustyugova, G. V., Koldoba, A. V., Romanova, M. M., Chechetkin, V. M., & Lovelace, R. V. E. 1999, *ApJ*, 516, 221
- van der Marel, N., van Dishoeck, E. F., Bruderer, S., et al. 2013, *Science*, 340, 1199
- Vernet, J., Dekker, H., D’Odorico, S., et al. 2011, *A&A*, 536, A105
- Wang, L., Bai, X.-N., & Goodman, J. 2019, *ApJ*, 874, 90
- Wang, L., & Goodman, J. 2017a, *ApJ*, 847, 11
- Wang, L., & Goodman, J. J. 2017b, *ApJ*, 835, 59
- Ward, W. R. 1986, *Icarus*, 67, 164
- Ward, W. R. 1992, in *Lunar and Planetary Science Conference*, Vol. 23, *Lunar and Planetary Science Conference*, 1491
- . 1997, *Icarus*, 126, 261

- Wardle, M. 2007, *Ap&SS*, 311, 35
- Wardle, M., & Koenigl, A. 1993, *ApJ*, 410, 218
- Wardle, M., & Ng, C. 1999, *MNRAS*, 303, 239
- Weber, M. L., Ercolano, B., Picogna, G., Hartmann, L., & Rodenkirch, P. J. 2020, *MNRAS*, 496, 223
- Weber, P., Benítez-Llambay, P., Gressel, O., Krapp, L., & Pessah, M. E. 2018, *ApJ*, 854, 153
- Weber, P., Pérez, S., Benítez-Llambay, P., et al. 2019a, *ApJ*, 884, 178
- 2019b, *ApJ*, 884, 178
- Weidenschilling, S. J. 1977, *Ap&SS*, 51, 153
- Whipple, F. L. 1972, in *From Plasma to Planet*, ed. A. Elvius, 211
- Winter, A. J., Clarke, C. J., Rosotti, G., et al. 2018, *MNRAS*, 478, 2700
- Woitke, P., Min, M., Pinte, C., et al. 2016, *A&A*, 586, A103
- Wolszczan, A., & Frail, D. A. 1992, *Nature*, 355, 145
- Woolfson, M. M. 1964, *Proceedings of the Royal Society of London Series A*, 282, 485
- Wyatt, M. C. 2008, *ARA&A*, 46, 339
- Yoshida, F., & Nakamura, T. 2005, *AJ*, 130, 2900
- Youdin, A. N., & Lithwick, Y. 2007a, *Icarus*, 192, 588
- 2007b, *Icarus*, 192, 588
- Zanni, C., Ferrari, A., Rosner, R., Bodo, G., & Massaglia, S. 2007, *Astronomy & Astrophysics*, 828, 20
- Zhang, S., Zhu, Z., Huang, J., et al. 2018, *ApJ*, 869, L47
- Zhu, Z., Nelson, R. P., Hartmann, L., Espaillat, C., & Calvet, N. 2011, *ApJ*, 729, 47
- Zhu, Z., Stone, J. M., Rafikov, R. R., & Bai, X.-n. 2014, *ApJ*, 785, 122
- Zhu, Z., Zhang, S., Jiang, Y.-F., et al. 2019, *ApJ*, 877, L18
- Ziampras, A., Kley, W., & Dullemond, C. P. 2020, *A&A*, 637, A50